PSA SYSTEM DESIGN FOR SEPARATION OF ETHYLENE FROM LIGHT HYDROCARBON GAS STREAMS

A Dissertation
Presented to
The Academic Faculty

by

Trisha Sen

In Partial Fulfillment
Of the Requirements for the Degree
Doctor of Philosophy in the
School of Chemical and Biomolecular Engineering

Georgia Institute of Technology
August 2020

PSA SYSTEM DESIGN FOR SEPARATION OF ETHYLENE FROM LIGHT HYDROCARBON GAS STREAMS

Approved by:

Dr. Matthew J. Realff, Advisor
School of Chemical & Biomolecular Engineering
Georgia Institute of Technology

Dr. Yoshiaki Kawajiri, Advisor
School of Chemical & Biomolecular Engineering
Georgia Institute of Technology

Dr. David S. Sholl
School of Chemical & Biomolecular Engineering
Georgia Institute of Technology

Dr. Ryan P. Lively
School of Chemical & Biomolecular Engineering
Georgia Institute of Technology

Dr. Roshan V. Joseph
School of Industrial & Systems Engineering
Georgia Institute of Technology

Date Approved: April 25, 2020

To my family, Awsa Rakka and Hudu Mofra

ACKNOWLEDGEMENTS

Looking back at my time spent during my PhD, I realize that I have come to know a lot of people who have made this journey possible. I would first like to thank my advisors, Dr. Matthew J. Realff and Dr. Yoshiaki Kawajiri who have been extremely supportive of me throughout. I will always aspire to be as knowledgeable, patient and understanding as them. Their inputs have always pushed me to be more rigorous and creative in my research. They have also played a key role in building my scientific communication skills, which will always remain with me throughout my career. I am extremely grateful for having had this opportunity to work with them, and hope to never stop learning.

During my PhD I have had the unique opportunity to work on a collaborative project funded by the Dow Chemical Company. I am grateful to Dr. Eric Stangland for his interest in our work and his patient support throughout the course of this project. I am also grateful to my collaborators, Dr. Wenqin You, Yutao Gong and Dr. Richelle Lyndon. I really enjoyed getting to know their work and having the opportunity to learn more about the experimental and molecular simulation areas of research. Comments and questions from Dr. Ryan P. Lively and Dr, David S. Sholl were always very insightful and opened up new avenues for research which would may have been otherwise remained not taken.

I cannot forget the contributions of Dr. Lalit L. Darunte and Dr. Wenqin You who have both collaborated with me on separate projects during my PhD. I am grateful for them for approaching me with challenging problems, and their team spirit which has made working with them great learning experiences. I was able to look at research approaches of two excellent groups of Dr. Christopher W. Jones and Dr. David S. Sholl, which has greatly

diversified my work. Apart from their scientific contributions, Dr. Darunte and Dr. You are great friends who have given more fulfilment and meaning to my research.

I am also grateful for having worked alongside excellent people in my research lab who have guided me throughout, particularly in my first two years. Dr. Jayashree Kalyanaraman was the first person who introduced me to PSA cycle modeling and has greatly influenced my work. Apart from that I would also like to thank Dr. Anshuman Sinha, Dr. Sewei Guo and Dr. Shan Tie for their company and discussions throughout their time at Georgia Tech. I want to thank the current group members for making my time memorable here, Dr. Hector Rubiera, Seongbin Ga, Gordon Hullen, Akshaya Nair, Youngjo Kim and Dr. Donghwi Kim. The group dinners/lunches were always fun. I would especially lie to thank Dr. Rubiera for his time in explaining complex concepts and always pointing me to great literature sources relevant to my work.

My time here at Gerogia Tech would not have been as enjoyable without all my friends. Dr. Ushasi Roy, Somrita Sarkar, and Bahar Asgari have been great roommates who have always looked out for me. I hope to meet you again sometime. Dr. Jihyeon Song and Dr. Kyungjin Kim were always fun to hang out with. I am also grateful to have found close friends in my department, Simple Kumar, Dr. Qandeel Almas, Gamze Eris, Kavita Matange and Akshay Korde. I am extremely thankful for all the coffee breaks, dinners and trips together. I hope we keep in touch. I have shared innumerable trips and memories with Simple Kumar and Akshay Korde which have defined my experience here. I would like to thank Akshay Korde especially for being extremely supportive and understanding and helping me through the difficult days.

I cannot forget the ChBE Indian gang, who have made my time in Atlanta memorable through the dinners, movies game nights and birthdays. I am thankful to Dr. Dharam Kumar, Dr. Achintya Sujan, Dr. Pradnya Samant, Dr. Jaya Arya, Dr. Rohan Awati, Dr. Sireesha Aluri, Dr. Mayank Agrawal, Shivesh Chowdhury, Nikhil Raj, Arvind Ganesan, Udita Ringania, Pavithra Narayanan, Geetanjali Pendyala, Dhrumil Shah, Jagriti Sahoo, Shubham Jamdade, Roshan Shetty and Vaibhav Joshi.

Finally, I would never have been here at Georgia Tech without the support of my parents, uncle and sister. I am also grateful to Shikha Rajouria, Sanjana Banerjee, Sinjini Banerjee and Soma Banerjee for their support and friendship. They have always been there for me and have always had unquestioning faith and love for me. I am especially grateful to my parents who have always put my needs before theirs. I am happiest to share my success with them.

TABLE OF CONTENTS

LIST OF TABLES

LIST OF FIGURES

SUMMARY

The primary goal of this study is the synthesis, design, modeling and simulation of gas adsorption separation processes. In particular, those where differences in the transport or reaction of gas species in materials are important for separation as opposed to equilibrium adsorption properties. Two applications are used for illustration, purification of ethylene from a mixture of light hydrocarbon gases, and the capture of CO_2 from air. *Chapter 2* is primarily focused on quantifying the differences in optimal performance of a traditional packed bed to that of a novel hollow fiber bed. The hollow fiber bed showed a 5 times higher productivity (for similar product purity and recovery). *Chapter 3 (equal contribution from Dr. L. A. Darunte - experiments)* is concerned with understanding the impact of mass transfer on separation performance of MMEN-Mg_2(dopbpdc) for CO_2 capture. We showed that the co-operative insertion mechanism which provides thermodynamic advantages to this material, significantly hampers its separation process kinetics. *Chapter 4 (equal contribution from W. You – molecular simulations)* is concerned with understanding the impact of binding energy of M-BTC MOFs for ethylene-ethane separation. Temperature was shown to have a significant non-monotonic impact on process performance. We also found mixed metal MM'-BTCs that can outperform the constituent pure metal M-BTCs. *Chapter 5* is concerned with understanding the impact of adsorbent property parameters on kinetic separation at a PSA scale (packed bed), therefore bridging the gap between lab scale experiments and PSA design. An illumination algorithm (SAIL) was able to efficiently predict similar results with greater computational efficiency. *Overall,* my thesis advances the understanding of (a) the impact of bed configuration on PSA performance (b) how inherent material property parameters translate to a process scale performance.

CHAPTER 1. INTRODUCTION

Separation processes account for 45-55% of all industrial energy consumption of which, distillation accounts for nearly 49% of the energy consumed[1]. Techniques such as membrane permeation and pressure/temperature-swing adsorption (PSA/TSA) are more energy-efficient and could be used to debottleneck separation trains[1–6]. Adsorption is a separation process in which certain components of a mixture are transferred (adsorbed) onto "adsorption sites" of a material. In this thesis, I will focus exclusively on gas adsorption in highly porous crystalline solids. Adsorption based processes broadly rely on very specific (i) equilibrium, (ii) kinetics, (iii) conformational/entropic effects and (iv) molecular sieving, to enable molecular separation[4,7]. Adsorption has become one of the commonly used industrial techniques for fluid (gas/liquid) separation, mostly fueled by the invention of tunable synthetic zeolites in the 1940s and the development of cyclic schemes which allowed for product recovery and adsorbent regeneration[8]. Some basic concepts in adsorptive separation have been outlined in Appendix A.

1.1 Adsorbents and techniques for adsorptive separation

Equilibrium or thermodynamic driven adsorption is currently the most widely used mechanism for adsorptive separation. It exploits the difference in affinity the components of a mixture towards an adsorbent material to facilitate separation[9]. Some common applications include paraffin/olefin separation, desulfurization, natural gas upgrading, H_2O removal[10,11] etc.

Kinetic separation exploits the capability of a material to differentiate between two or more components owing to significant differences in their diffusivities, i.e. the ability/difficulty to move along the cages/channels of the porous materials and not their equilibrium loading amounts[2–4]. Such a mechanism is generally encountered for molecules that display similar size and functionality such as low molecular weight straight chain alkane and alkene hydrocarbons. Major separations of interest using kinetic separation are nitrogen/oxygen separations[12], carbon dioxide separation from methane or nitrogen[13–15] and hydrocarbon separations such as propylene/propane[2,16].

Commercial adsorbents for gas separation include zeolites, carbon molecular sieves, activated carbons, activated alumina, silica gel[17]. Metal-organic Frameworks (MOFs) have emerged as a new class of adsorbents in the past few decades, due to their tunability in terms of pore size and environment. MOFs are hybrid crystalline materials, where appropriate inorganic and organic building blocks can be assembled into a net-like hybrid material with a targeted topology[4,18], with the appropriate pore aperture size and shape for the envisioned/targeted separation.

1.2 Applications of Adsorptive separation

Two emerging applications of adsorptive separation are the separation of light hydrocarbons[19–21] and the removal CO_2 from the atmosphere/flue gas streams[22–25].

1.2.1 Ethylene purification from oxidative coupling of methane

Ethylene is a high value raw material which also holds a large volume of the organic chemical market. It is a raw material in the production of detergents, cosmetics, polymers

and lies at the base of many chemical supply chains. On the other hand, methane has gradually gained attention as a source of clean fossil energy and a feedstock for chemicals. Due to the difficulty of transportation of methane itself, enabling conversion of methane directly into higher value products such as ethylene has been of key interest[26,27]. One of the reactions of interest for this conversion is oxidative coupling of methane (OCM). However, current catalysts can convert only around 20% of the methane to ethylene, the rest of the by-products include ethane and CO_x. Apart from trying to improve conversion of the reaction itself, another approach could be the use of an energy efficient separation process to purify ethylene obtained from this reaction and recycling of the unconverted methane.

One of the major bottlenecks of this multi-component separation process is the separation of ethylene from ethane due to the close molecular weight of these two hydrocarbons. Paraffin olefin separation is also economically important when considering reduction in hydrocarbon losses, to avoid environmental penalties. Traditional separation scheme involves low temperature distillation[28], which is typically highly heat integrated to provide the very low temperatures while minimizing the energy cost. These systems have high capital and operational cost and are only attractive when the volume of ethylene production is large. One of the alternatives is to use an adsorption-based separation technique. A major portion of the work in the following chapters (Chapters 2, 3 and 4) was performed with this as the target application. Two routes for adsorptive separation of olefin/paraffin involves thermodynamic separation through reversible π-complexation of ethylene and kinetic separation[6]. One specific group of adsorbents with π-complexation property are the open metal site (OMS) MOFs[29–32]. Zeolites, ZIFs and MOFs have all been investigated for kinetic separation of olefins and praffins[2,33–35]. Among these ZIFs have

gained special attention since like zeolites they have a highly tuneable pore morphology which can control intra-crystalline diffusion.

1.2.2 Direct Air Capture

Rising atmospheric CO_2 levels are one of the main contributors to global climate change. Removal of CO_2 from anthropogenic sources such as flue gas has been augmented with research into direct capture of CO_2 from the air (DAC). This has advantages such as addressing issues with mobile sources, bypassing the need for a specific CO_2 feed stream, and is a negative emission technology (NET). One key technical challenge to direct air capture is the ultradilute CO_2 concentration in the atmosphere, in the range of 400 ppm as opposed to point sources such as power plants that range from 4 to 12v% CO_2. Supported amines, which are popular adsorbent materials for flue-gas capture, have also gained significant attention as key separation materials in air capture[22–24,36]. Another class of materials that have gained significant interest for direct air capture are amine-functionalized MOFs[37,38]. Chapter 5 focuses on the application of one of these MOFs for DAC processes.

1.3 Cyclic Operation of Adsorption-Desorption Process

In an adsorption process, the adsorbent used is normally shaped into spherical pellets or extruded[39]. The feed stream is put into contact with the adsorbent that is normally packed in fixed beds. A typical industrial process using adsorptive separation has two basic stages of operating a single bed. The “feed step” where, the feed gas is fed through the inlet, the “heavier” component is adsorbed and the relatively pure “lighter” component is collected at the outlet of the bed. Once the bed is saturated, the feed is stopped and either

the pressure is reduced (Pressure Swing Adsorption, PSA) or the temperature is increased (Temperature Swing Adsorption, TSA) to allow most of the *heavier* component to desorb.

To compare performance of two cycles some common Performance Indicators (PIs) are used, which are described here. Continuous cyclic operation starting form an initially clean bed, (q_i=0) for example, leads to a condition where the final bed concentration after desorption is the same as the initial bed condition prior to feed. The process is said to have reached a "cyclic steady state (CSS)" of operation and the performance of the process in terms of "purity" and "recovery" of the desired components is evaluated at this operating condition. Once these basic performance criteria are satisfied, other important considerations are the bed productivity and energy consumption.

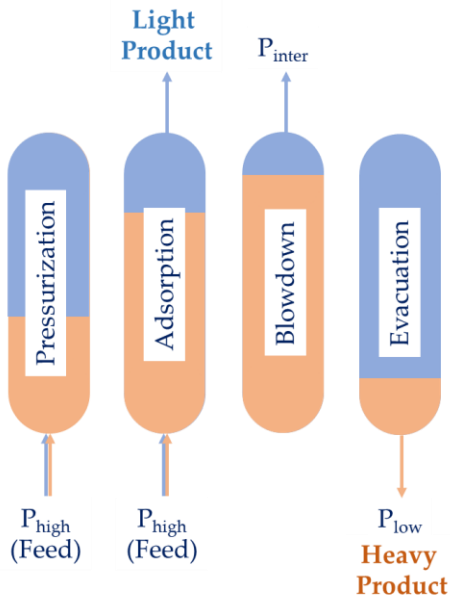

Figure 1-1 – Schematic of a simple PSA cycle with 4-steps and a single bed

It has been shown that PSA processes have tremendous flexibility in terms of cycle design. More than onecolumn can be used and a large number of cycles are possible[39].

Figure 1-1 shows the schematic of a very simple PSA cycle with 4 steps and a single bed. Modifications include using the separation products as purge or rinse to push product recovery or purity, increasing the number of beds to incorporate pressure equalizations in between the pressurization and blowdown steps.

1.4 Impact of PSA/TSA cycle on adsorbent selection

There are two main avenues for improving separation performance of an adsorbent: (1) improving inherent property parameters of the adsorbent itself and (2) improving performance of the PSA cycle through cycle design. Independent analysis of adsorbent property parameters[9] and cycle design[40] has been well studied in literature. In recent years there has been a growing interest in combining these two fields to develop an integrated approach towards materials and process development.

Material development for adsorption relies on a few characterizations such as isotherm parameters (selectivity, working capacity etc). Selection of adsorbents best suited for separation based on these simple metrics have been widely shown to be inaccurate when full PSA cycle optimizations are performed and performance metrics compared[41–44]. This has led to the development of several hierarchical approaches for adsorbent selection which takes into account both the simple metrics as well as the fully optimized PSA parameters[41,42]. Apart from this, development of simplified models that cut down on computational cost of the full cycle PSA optimization while still capturing similar information about relative performance of adsorbents, has also gained a lot of attention particularly in the area of CO_2 capture[43–45].

Another approach has been to improve inherent parameters at the single bed itself without changing properties of either the adsorbent or the cycle. Traditionally industrial PSA cycles operate in packed beds where, pellets of adsorbent material are randomly packed. Understanding that even for similar adsorbents, structure of the bed plays a crucial role in determining performance of the separation process, has gained significant interest[46–48]. Adsorbent packing affects parameters such as, heat and mass transfer which are crucial in determining quality of separation. Proposed structures include foams, monoliths[47], corrugated sheets[48] and hollow fiber beds[46].

1.5 Thesis objectives

The subsequent chapters specifically look at application of some of these concepts for integration of material and process discovery in the areas of ethylene/ethane separation and CO_2 capture. Both equilibrium and kinetic adsorptive separations have been studied in detail. The work was performed with inputs from experiments and molecular simulations by collaborators. The overarching aim was to use PSA cycle and other simulations to guide material discovery given the significantly higher time consumed in experimental synthesis and molecular dynamic calculations. A brief description of the specific objectives is outlined in the following subsections.

1.5.1 Quantifying improvement when a hollow fiber bed is used instead of a packed bed

A hollow fiber bed for an adsorptive separation provides an additional degree of improvement over existing structured contactors such as monoliths and foams.[49–51] While the previously proposed contractors result in reduction in pressure drop and increase in mass transfer profiles over the packed bed, the hollow fiber bed additionally improves heat

transfer properties of the bed. The hollow fiber bed constitutes solid sorbents embedded in a porous polymeric hollow fiber matrix. Several identical fibers are assembled inside a module which resembles a shell and tube heat exchanger. The bore of the hollow fiber has an impermeable lumen layer which allows the flow of a cooling/heating medium to mitigate the temperature of operation of the process despite heat of adsorption/desorption. However, due to the incorporation of a polymer matrix and the presence of a hollow bore, adsorbent density per unit volume is lower than the packed bed.

The aim of chapter 2 is to study whether the advantages posed by the use of the hollow fiber bed out-weigh the disadvantage mentioned above and to come up with a specific quantification for this comparison. Equivalent models for the packed bed and the hollow fiber bed are developed to enable unbiased comparison. A preliminary parametric comparison of properties such as heat and mass transfer co-efficients, adsorbent density, and pressure drop is demonstrated using these models. This is followed by a detailed PSA analysis for an equimolar mixture of propylene/propane with zeolite 13X as the adsorbent. We determine which configuration had a performance indicators under constraint of a minimum required purity.

1.5.2 Selection of metal site for OMS MOFs for ethylene/ethane separation

Open metal site (OMS) MOFs are very good candidates for the adsorptive separation of ethylene/ethane due to π-π interaction with the ethylene double bond. It has been established that properties of the metal center have a stronger impact on separation efficiency of these MOFs as opposed to nature of the organic linker used.[52,53] The aim of Chapter 3 is two-fold. We wish to understand how binding affinity of the metal center

impacts overall separation performance in a PSA cycle and whether simplified models can be used to speed up this analysis.

Once we have a general understanding of the impact of metal center properties in pure metal MOFs using BTC as the organic linker, the subsequent analysis looks at heterogeneous MM'-BTCs (which is a combination of two different metal centers M and M'). General thinking dictates that introduction of heterogeneity will inevitably reduce overall separation performance. This chapter aims to understand whether this statement is always true. Using a combination of molecular dynamic simulations of 11 mixed-metal BTCs and simplified process models we identify candidates for successful mixed metal combinations, which have been analyzed in detail using the full PSA model thus providing evidence that heterogeneity does not always reduce separation performance.

1.5.3 Kinetic Separation

Although equilibrium adsorptive separation has become one of the commonly used industrial techniques for gas and liquid separation, kinetic adsorptive separation has not received equal attention. Kinetic separation exploits the differences in diffusion coefficients of the different adsorbates in the mixture irrespective of their equilibrium loading amounts. This may even result in the selective adsorption of the weakly adsorbing component for a certain duration.

Using the traditional Fickian model for gas diffusion is, however, not adequate for predicting this transient overshoot. Instead, we have used the Maxwell-Stefan transport model which has been proposed and extensively validated with crystal diffusion experiments by Krishna et al.[54] A few past studies have attempted to screen materials and

subsequently develop PSA cycles for kinetic separations incorporating this more accurate description of crystal diffusion[16], but there remain significant unanswered questions.

There is no straight forward method of screening adsorbents for kinetic separation from diffusion coefficients and isotherm data alone. This is mostly due to the complex coupling between the kinetics and equilibrium. Chapter 4 presents a parametric study of the influence of isotherm shape and diffusion coefficient on the uptake within a single crystal and light component transient overshoot. These results have been used to screen materials which have better potential for kinetic separation. The selected adsorbents are incorporated into a PSA cycle model to determine the effectiveness of the primary screening using crystal level data. The goal is a systematic method to co-design materials and adsorption cycles for kinetic adsorption processes.

1.5.4 Impact of mass transfer on CO_2 capture

CO_2 uptake in amine-functionalized MOFs, such as Mg_2(dobpdc), follows a tunable stepped isotherm behavior. The stepped nature enables unprecedented high equilibrium as well as pressure-swing capacities for CO_2 capture under DAC conditions (< 0.4 mbar). Majority of the analysis of these class of materials have focused primarily on their equilibrium behavior. In Chapter 4, I analyze the kinetics associated with DAC using these materials and determine whether this limits their practical application.

An adsorption breakthrough setup with ultra-dilute (0.4 mbar) and dilute (1 mbar, 5 mbar and 10 mbar) feed was used as a proxy to simulate practical CO_2 feeds . Local equilibrium theory for stepped isotherms predicts a simple single shock breakthrough for feed concentrations of CO_2 above 1% (or 10 mbar). Below 10 mbar however, we expect

two shocks separated by a plateau corresponding to the isotherm step pressure. The predicted shapes of the breakthrough profiles matched the experimentally observed results only qualitatively. Attempts to fit a traditional linear driving force mass transfer model to match the observed data were unsuccessful.

The aim of Chapter 5 is therefore two-fold. Firstly, to understand and quantify the system kinetics of amine functionalized adsorbents with stepped isotherms. It was found that established models for co-operative uptake such as, the Avrami model for crystallization and the Michaelis-Menten model for enzymatic reactions, were successful in predicting breakthrough of CO_2 using Mg_2(dopbdc). Secondly, this chapter also shows that moving beyond equilibrium or swing capacity of these adsorbents, and looking at their kinetics is crucial to assess their efficiency in practical DAC applications.

1.6 References

[1] Sholl, D. S.; Lively, R. P. Seven Chemical Separations to Change the World. *Nature* **2016**, *532* (7600), 435–437. https://doi.org/10.1038/532435a.

[2] Pimentel, B. R.; Lively, R. P. Enabling Kinetic Light Hydrocarbon Separation via Crystal Size Engineering of ZIF-8. *Ind. Eng. Chem. Res.* **2016**, *55* (48), 12467–12476. https://doi.org/10.1021/acs.iecr.6b03199.

[3] Wang, Y.; Zhao, D. Beyond Equilibrium: Metal-Organic Frameworks for Molecular Sieving and Kinetic Gas Separation. *Cryst. Growth Des.* **2017**, *17* (5), 2291–2308. https://doi.org/10.1021/acs.cgd.7b00287.

[4] Adil, K.; Belmabkhout, Y.; Pillai, R. S.; Cadiau, A.; Bhatt, P. M.; Assen, A. H.; Maurin, G.; Eddaoudi, M. Gas/Vapour Separation Using Ultra-Microporous Metal-Organic Frameworks: Insights into the Structure/Separation Relationship. *Chem. Soc. Rev.* **2017**, *46* (11), 3402–3430. https://doi.org/10.1039/c7cs00153c.

[5] Koros, W. J.; Zhang, C. Materials for Next-Generation Molecularly Selective Synthetic Membranes. *Nat. Mater.* **2017**, *16* (3), 289–297. https://doi.org/10.1038/nmat4805.

[6] Rege, S. U.; Yang, R. T. Propane/Propylene Separation by Pressure Swing

Adsorption: Sorbent Comparison and Multiplicity of Cyclic Steady States. *Chem. Eng. Sci.* **2002**, *57* (7), 1139–1149. https://doi.org/10.1016/S0009-2509(01)00440-7.

[7] Li, J.-R.; Kuppler, R. J.; Zhou, H.-C. Selective Gas Adsorption and Separation in Metal–Organic Frameworks. *Chem. Soc. Rev.* **2009**, *38* (5), 1477–1504.

[8] Dąbrowski, A. Adsorption—from Theory to Practice. *Adv. Colloid Interface Sci.* **2001**, *93* (1–3), 135–224.

[9] Geier, S. J.; Mason, J. A.; Bloch, E. D.; Queen, W. L.; Hudson, M. R.; Brown, C. M.; Long, J. R. Selective Adsorption of Ethylene over Ethane and Propylene over Propane in the Metal–Organic Frameworks M 2 (Dobdc)(M= Mg, Mn, Fe, Co, Ni, Zn). *Chem. Sci.* **2013**, *4* (5), 2054–2061.

[10] Long, J.; Yaghi, O. Reviewing the Latest Developments across the Interdisciplinary Area of Metal–Organic Frameworks from an Academic and Industrial Perspective. *Chem. Soc. Rev* **2009**, *38*, 1257–1283.

[11] Yang, R. T. *Adsorbents: Fundamentals and Applications*; John Wiley & Sons, 2003.

[12] Effendy, S.; Xu, C.; Farooq, S. Optimization of a Pressure Swing Adsorption Process for Nitrogen Rejection from Natural Gas. *Industrial and Engineering Chemistry Research*. American Chemical Society May 10, 2017, pp 5417–5431. https://doi.org/10.1021/acs.iecr.7b00513.

[13] Nandi, S. P.; Walker, P. L. Separation of Oxygen and Nitrogen Using 5A Zeolite and Carbon Molecular Sieves. *Sep. Sci.* **1976**, *11* (5), 441–453. https://doi.org/10.1080/01496397608085334.

[14] Majumdar, B.; Bhadra, S. J.; Marathe, R. P.; Farooq, S. Adsorption and Diffusion of Methane and Nitrogen in Barium Exchanged ETS-4. *Ind. Eng. Chem. Res.* **2011**, *50* (5), 3021–3034. https://doi.org/10.1021/ie1014124.

[15] Erden, L.; Ebner, A. D.; Ritter, J. A. Separation of Landfill Gas CH4 from N2 Using Pressure Vacuum Swing Adsorption Cycles with Heavy Reflux. *Energy and Fuels* **2018**, *32* (3), 3488–3498. https://doi.org/10.1021/acs.energyfuels.7b03534.

[16] Bhadra, S. J.; Farooq, S. Separation of Methane-Nitrogen Mixture by Pressure Swing Adsorption for Natural Gas Upgrading. *Ind. Eng. Chem. Res.* **2011**, *50* (24), 14030–14045. https://doi.org/10.1021/ie201237x.

[17] Sircar, S. Basic Research Needs for Design of Adsorptive Gas Separation Processes. *Ind. Eng. Chem. Res.* **2006**, *45* (16), 5435–5448.

[18] Férey, G. Hybrid Porous Solids: Past, Present, Future. *Chem. Soc. Rev.* **2008**, *37* (1), 191–214.

[19] Bao, Z.; Chang, G.; Xing, H.; Krishna, R.; Ren, Q.; Chen, B. Potential of Microporous Metal–Organic Frameworks for Separation of Hydrocarbon Mixtures. *Energy Environ. Sci.* **2016**, *9* (12), 3612–3641.

[20] He, Y.; Krishna, R.; Chen, B. Metal–Organic Frameworks with Potential for Energy-Efficient Adsorptive Separation of Light Hydrocarbons. *Energy Environ. Sci.* **2012**, *5* (10), 9107–9120.

[21] Bloch, E. D.; Queen, W. L.; Krishna, R.; Zadrozny, J. M.; Brown, C. M.; Long, J. R. Hydrocarbon Separations in a Metal-Organic Framework with Open Iron (II) Coordination Sites. *Science (80-.).* **2012**, *335* (6076), 1606–1610.

[22] Choi, S.; Drese, J. H.; Jones, C. W. Adsorbent Materials for Carbon Dioxide Capture from Large Anthropogenic Point Sources. *ChemSusChem Chem. Sustain. Energy Mater.* **2009**, *2* (9), 796–854.

[23] Chaffee, A. L.; Knowles, G. P.; Liang, Z.; Zhang, J.; Xiao, P.; Webley, P. A. CO2 Capture by Adsorption: Materials and Process Development. *Int. J. Greenh. gas Control* **2007**, *1* (1), 11–18.

[24] Plaza, M. G.; Pevida, C.; Arenillas, A.; Rubiera, F.; Pis, J. J. CO2 Capture by Adsorption with Nitrogen Enriched Carbons. *Fuel* **2007**, *86* (14), 2204–2212.

[25] Yu, C.-H.; Huang, C.-H.; Tan, C.-S. A Review of CO2 Capture by Absorption and Adsorption. *Aerosol Air Qual. Res* **2012**, *12* (5), 745–769.

[26] Schwach, P.; Pan, X.; Bao, X. Direct Conversion of Methane to Value-Added Chemicals over Heterogeneous Catalysts: Challenges and Prospects. *Chem. Rev.* **2017**, *117* (13), 8497–8520.

[27] Lunsford, J. H. The Catalytic Oxidative Coupling of Methane. *Angew. Chemie Int. Ed. English* **1995**, *34* (9), 970–980.

[28] Eldridge, R. B. Olefin/Paraffin Separation Technology: A Review. *Ind. Eng. Chem. Res.* **1993**, *32* (10), 2208–2212.

[29] Mei, L.; Wu, Y.; Zhou, X.; Yan, J.; Xu, F.; Li, Z. Adsorption Performance of MIL-100 (Fe) for Separation of Olefin–Paraffin Mixtures. *J. Taiwan Inst. Chem. Eng.* **2017**, *70*, 74–78.

[30] Luna-Triguero, A.; Vicent-Luna, J. M.; Becker, T. M.; Vlugt, T. J. H.; Dubbeldam, D.; Gómez-Álvarez, P.; Calero, S. Effective Model for Olefin/Paraffin Separation Using (Co, Fe, Mn, Ni)-MOF-74. *ChemistrySelect* **2017**, *2* (2), 665–672.

[31] Luna-Triguero, A.; Vicent-Luna, J. M.; Gómez-Álvarez, P.; Calero, S. Olefin/Paraffin Separation in Open Metal Site Cu-BTC Metal–Organic Framework. *J. Phys. Chem. C* **2017**, *121* (5), 3126–3132.

[32] Kulkarni, A. R.; Sholl, D. S. Screening of Copper Open Metal Site MOFs for Olefin/Paraffin Separations Using DFT-Derived Force Fields. *J. Phys. Chem. C* **2016**, *120* (40), 23044–23054.

[33] Ramachandran, R.; Dao, L. Separation of Hydrocarbon Mixtures. *Zeolites* **1995**, *4* (15), 384.

[34] Li, K.; Olson, D. H.; Seidel, J.; Emge, T. J.; Gong, H.; Zeng, H.; Li, J. Zeolitic Imidazolate Frameworks for Kinetic Separation of Propane and Propene. *J. Am. Chem. Soc.* **2009**, *131* (30), 10368–10369.

[35] Bereciartua, P. J.; Cantín, Á.; Corma, A.; Jordá, J. L.; Palomino, M.; Rey, F.; Valencia, S.; Corcoran, E. W.; Kortunov, P.; Ravikovitch, P. I. Control of Zeolite Framework Flexibility and Pore Topology for Separation of Ethane and Ethylene. *Science (80-.).* **2017**, *358* (6366), 1068–1071.

[36] Didas, S. A.; Kulkarni, A. R.; Sholl, D. S.; Jones, C. W. Role of Amine Structure on Carbon Dioxide Adsorption from Ultradilute Gas Streams Such as Ambient Air. *ChemSusChem* **2012**, *5* (10), 2058–2064.

[37] McDonald, T. M.; Lee, W. R.; Mason, J. A.; Wiers, B. M.; Hong, C. S.; Long, J. R. Capture of Carbon Dioxide from Air and Flue Gas in the Alkylamine-Appended Metal–Organic Framework Mmen-Mg2 (Dobpdc). *J. Am. Chem. Soc.* **2012**, *134* (16), 7056–7065.

[38] Darunte, L. A.; Oetomo, A. D.; Walton, K. S.; Sholl, D. S.; Jones, C. W. Direct Air Capture of CO2 Using Amine Functionalized MIL-101 (Cr). *ACS Sustain. Chem. Eng.* **2016**, *4* (10), 5761–5768.

[39] Grande, C. A. Advances in Pressure Swing Adsorption for Gas Separation. *ISRN Chem. Eng.* **2012**, *2012*.

[40] Agarwal, A.; Biegler, L. T.; Zitney, S. E. A Superstructure-based Optimal Synthesis of PSA Cycles for Post-combustion CO2 Capture. *AIChE J.* **2010**, *56* (7), 1813–1828.

[41] Liu, T.; First, E. L.; Hasan, M. M. F.; Floudas, C. A. A Multi-Scale Approach for the Discovery of Zeolites for Hydrogen Sulfide Removal. *Comput. Chem. Eng.* **2016**, *91*, 206–218.

[42] Hasan, M. M. F.; First, E. L.; Floudas, C. A. Cost-Effective CO 2 Capture Based on in Silico Screening of Zeolites and Process Optimization. *Phys. Chem. Chem. Phys.* **2013**, *15* (40), 17601–17618.

[43] Rajagopalan, A. K.; Avila, A. M.; Rajendran, A. Do Adsorbent Screening Metrics Predict Process Performance? A Process Optimisation Based Study for Post-Combustion Capture of CO2. *Int. J. Greenh. Gas Control* **2016**, *46*, 76–85.

[44] Maring, B. J.; Webley, P. A. A New Simplified Pressure/Vacuum Swing Adsorption Model for Rapid Adsorbent Screening for CO2 Capture Applications. *Int. J. Greenh. Gas Control* **2013**, *15*, 16–31.

[45] Ga, S.; Jang, H.; Lee, J. H. New Performance Indicators for Adsorbent Evaluation Derived from a Reduced Order Model of an Idealized PSA Process for CO2 Capture. *Comput. Chem. Eng.* **2017**, *102*, 188–212.

[46] Rezaei, F.; Subramanian, S.; Kalyanaraman, J.; Lively, R. P.; Kawajiri, Y.; Realff, M. J. Modeling of Rapid Temperature Swing Adsorption Using Hollow Fiber Sorbents. *Chem. Eng. Sci.* **2014**, *113*, 62–76.

[47] Rezaei, F.; Webley, P. Structured Adsorbents in Gas Separation Processes. *Sep. Purif. Technol.* **2010**, *70* (3), 243–256.

[48] Amalraj, P. B. C. A.; Ebner, A. D.; Ritter, J. A. Effective Radial Thermal Conductivity of a Parallel Channel Corrugated Metal Structured Adsorbent. *Ind. Eng. Chem. Res.* **2019**, *58* (36), 16922–16933.

[49] Sen, T.; Kawajiri, Y.; Realff, M. J. Adsorption Process Intensification through Structured Packing: A Modeling Study Using Zeolite 13X and a Mixture of Propylene and Propane in Hollow-Fiber and Packed Beds. *Ind. Eng. Chem. Res.* **2019**, *58* (15), 5750–5767. https://doi.org/10.1021/acs.iecr.8b02189.

[50] DeWitt, S. J. A.; Sinha, A.; Kalyanaraman, J.; Zhang, F.; Realff, M. J.; Lively, R. P. Critical Comparison of Structured Contactors for Adsorption-Based Gas Separations. *Annu. Rev. Chem. Biomol. Eng.* **2018**, *9*, 129–152.

[51] Kalyanaraman, J.; Fan, Y.; Lively, R. P.; Koros, W. J.; Jones, C. W.; Realff, M. J.; Kawajiri, Y. Modeling and Experimental Validation of Carbon Dioxide Sorption on Hollow Fibers Loaded with Silica-Supported Poly (Ethylenimine). *Chem. Eng. J.* **2015**, *259*, 737–751.

[52] You, W.; Liu, Y.; Howe, J. D.; Sholl, D. S. Competitive Binding of Ethylene, Water, and Carbon Monoxide in Metal–Organic Framework Materials with Open Cu Sites. *J. Phys. Chem. C* **2018**, *122* (16), 8960–8966. https://doi.org/10.1021/acs.jpcc.8b00909.

[53] You, W.; Liu, Y.; Howe, J. D.; Tang, D.; Sholl, D. S. Tuning Binding Tendencies of Small Molecules in Metal–Organic Frameworks with Open Metal Sites by Metal Substitution and Linker Functionalization. *J. Phys. Chem. C* **2018**, *122* (48), 27486–27494.

[54] Krishna, R.; van Baten, J. M. Using Molecular Dynamics Simulations for Elucidation of Molecular Traffic in Ordered Crystalline Microporous Materials. *Microporous and Mesoporous Materials*. Elsevier March 1, 2018, pp 151–169. https://doi.org/10.1016/j.micromeso.2017.09.014.

CHAPTER 2. ADSORPTION PROCESS INTENSIFICATION THROUGH STRUCTURED PACKING: A MODELING STUDY USING ZEOLITE 13X AND A MIXTURE OF PROPYLENE AND PROPANE IN HOLLOW FIBER AND PACKED BED

Parts of this chapter have been adapted from 'Sen, T., Kawajiri, Y., & Realff, M. J. (**2018**). Adsorption Process Intensification through Structured Packing: A Modeling Study Using Zeolite 13X and a Mixture of Propylene and Propane in Hollow-Fiber and Packed Beds. *Ind. Eng. Chem. Res.*, *58*(15), 5750-5767.'

2.1 Introduction

Process intensification has been identified as one of the most promising development paths for the chemical process industry. In their comprehensive vision for process intensification, Gerven and Stankiewicz1 have described four fundamental principles and approaches. An optimally intensified process should aim to alter and improve inherent kinetics, provide a uniform processing history to each molecule involved (maximize mixing and minimize temperature gradients), optimize driving force through improved specific surface area and, seek and optimize synergistic processes (like reactive separation). The scope of process intensification spans the macro, meso and the molecular scales. This aim may be achieved by introducing structure to reduce spatial randomness, optimizing targeted energy transfer from source to recipient, performing synergistic integration of processes or by the manipulation of process time scales and periodicity. The

current work focuses on the intensification of the adsorptive separation process, particularly for a gaseous mixture, and employs several of the strategies outlined.

The phenomenon of adsorption was discovered by the Swedish chemist Carl Wilhelm Scheele in 1773. Since then adsorption has become one of the commonly used industrial techniques for fluid (gas/liquid) separation, mostly fueled by the invention of tunable synthetic zeolites in the 1940s and the development of cyclic schemes which allowed for product recovery and adsorbent regeneration. [2] Adsorption relies on very specific surface interaction properties of solids (adsorbents) with the different components of a fluid mixture to achieve separation, by exploiting either equilibrium or kinetic behavior. [3]

Traditionally, adsorbent crystals are formed into pellets (with or without a binder) and then packed into beds. A single bed, or multiple-beds in parallel, cycle through a series of steps which usually switches either the temperature (TSA) or the pressure (PSA, VSA) of the system between two levels. However, pressure drops are usually incurred due to the random and tortuous nature of the packing void space which influences the cost of pressurizing the feed gas and the feasible gas velocity which influences the shape of the adsorption front through the mass transfer coefficient. Heat transfer is inefficient for operating a TSA cycle and there is scope for improvement of fluid to adsorbent mass transfer coefficient. [4-6]

To overcome these difficulties, several structured configurations including, monoliths, laminates and foams, have been developed. Detailed reviews and comparisons of these configurations are available in literature [4,5,7,8]. Rezai et al. compared the

performance of ceramic cordierite monoliths to a packed bed for CO_2 separation[4]. Optimal geometry for different classes of structured adsorbent from a process point of view were also studied[5]. The role of improved heat transfer characteristics in structured adsorbents for enhancing a 2-step PSA process performance was also explored.[7] More recently, a novel hollow fiber-based solid sorbent system has been proposed and experimentally validated[6,9,10]. Not only does this provide the improvements in system parameters that have been targeted by the existing emerging technologies, it provides an additional degree of control over the heat transfer efficiency as described below.

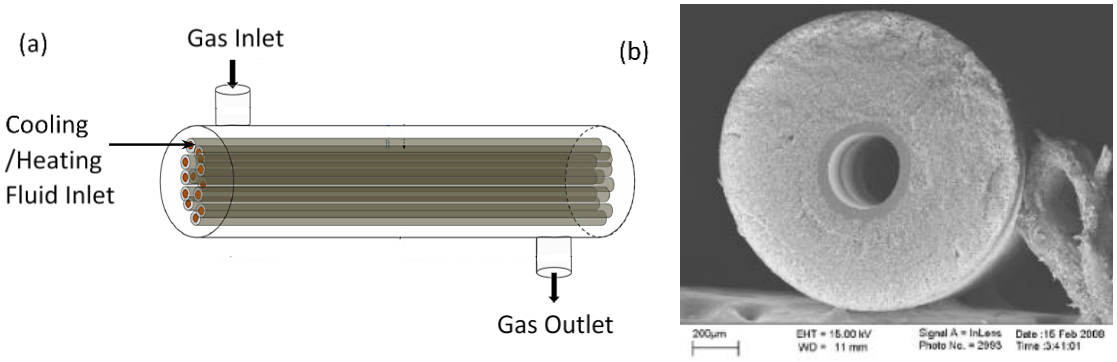

Figure 2-1 - (a) Schematic of a hollow fiber bed (b) SEM image of a single hollow fiber with impermeable lumen layer [6]

The hollow fiber configuration relies on solid sorbents embedded in a porous polymeric hollow fiber matrix. Several identical fibers are assembled inside a module which resembles a shell and tube heat exchanger (Figure 2-1). The bore of the hollow fiber has an impermeable lumen layer which allows the flow of a cooling/heating medium to mitigate the temperature of operation of the process despite heat of adsorption/desorption.[6]

Compared to the traditional packed bed, the configuration of the hollow fiber bed offers several advantages:[11] (1) the structured packing has a significantly lower pressure drop (2) the diffusion length for the fluid to the interior of the hollow fibers is significantly

lower than the spherical packed bed (3) the bore allows for a heating/cooling medium to efficiently transfer heat to/from the adsorbent phase. However there are also certain drawbacks in using the hollow fiber bed configuration. The manufacture of hollow fibers requires at least 25% by weight of the polymer matrix [11], but pellets may require minimal binder material or possibly be binderless. The presence of the bore in the hollow fiber reduces the quantity of adsorbent that can be packed inside a given bed volume. Therefore, in terms of adsorbent density per unit bed volume, the hollow fiber bed has a clear disadvantage.

It has been hypothesized that the advantages will outweigh the disadvantages of using a hollow fiber bed, but testing and understanding the drivers of the relative performance is needed. The aim of the computational study in this chapter is to perform a detailed comparison of the properties and separation performance of the novel hollow fiber bed configuration with that of the traditionally used packed bed. To enable unbiased comparison, the initial part of the study focuses on the development of an equivalent model for the packed bed and the hollow fiber bed. A preliminary parametric comparison of properties such as heat and mass transfer co-efficients, adsorbent density, and pressure drop was then performed on the basis of these models. Then the efficiency of separation of an equimolar mixture of propylene/propane using zeolite 13X was used as a case study. A detailed grid search optimization was performed to determine which configuration had a better performance under the constraint of a minimum required purity and use of products for different steps within the cycle.

2.2 Isotherm model

The separation of a 50:50 mixture of propylene and propane using adsorbent zeolite 13X was chosen as the case study for comparison between the hollow fiber bed and the packed bed. The feed temperature was 100^0 C at all times. The adsorption and desorption pressures were 1.5 bar and 0.1 bar respectively. The values were chosen since a complete VPSA cycle had been experimentally validated by Narin et al [12] under these operating conditions. Temperature swing was not employed.

Experimental measures of the propylene/propane isotherm parameters were obtained by Narin et al [12] at the temperatures of 50 ^{0}C, 100 ^{0}C and 150 ^{0}C. The experiments obtained single component data in the range of 0-6 bar and multi-component data at 100 ^{0}C and 1.5 bar. They used the competitive Dual-Site Langmuir (DSL) equation to model the multi-component adsorption equilibrium isotherms:

$$q_i^* = \frac{q_{A_{sat,i}} b_{A,i} p_i}{1+\sum_i b_{A,i} p_i} + \frac{q_{B_{sat,i}} b_{B,i} p_i}{1+\sum_i b_{B,i} p_i} \tag{2.1}$$

The estimates of the DSL model parameters obtained by Narin et al were used in the current study. Other studies, by Mathias et al [13] for example, have demonstrated that the DSL model provides enough mathematical flexibility to describe mixed-gas competitive adsorption for a range of mixtures.

The DSL model assumes two different adsorption sites (A and B) on the adsorption surface. q_i^* is the equilibrium adsorbed amount of a component, p_i is the partial pressure. The terms $q_{A_{sat,i}}$ and $q_{B_{sat,i}}$ are the saturation capacities on site A and B respectively.

Parameters $b_{A,i}$ and $b_{B,i}$ are the respective affinity constants which have a temperature dependence as represented by:

$$b_{A,i} = b_{A\infty,i}\, exp\left(\frac{-\Delta H_{A,i}}{RT_g}\right) \tag{2.2}$$

$$b_{B,i} = b_{B\infty,i}\, exp\left(\frac{-\Delta H_{B,i}}{RT_g}\right) \tag{2.3}$$

where $b_{A\infty,i}$ and $b_{B\infty,i}$ are the frequency factors for each affinity constants and $\Delta H_{A,i}$ and $\Delta H_{B,i}$ are the heats of adsorption for each site.

At low coverages, the equilibrium loading has a linear dependence on pressure which can be represented by using the Henry' constant, $K_{H,i}$:

$$q_i^* = K_{H,i} p_i \tag{2.4}$$

The temperature dependence of the Henry's constant is represented by the van't Hoff equation:

$$K_{H,i} = K_{0,i}\, exp\left(-\frac{\Delta H_{0,i}}{RT_g}\right) \tag{2.5}$$

where $K_{0,i}$ is the pre-exponential factor. This provides a means to estimate the enthalpy of adsorption at zero coverage (ΔH_0). Table B1 in Appendix B is a complete list of all the operating parameters needed in the isotherm model.

As a measure for the separation effectiveness, selectivity, $\alpha_{i/j}$ of the adsorbent for one component over the other is defined as:

$$\alpha_{i/j} = \frac{q_i^*/q_j^*}{p_i/p_j} \tag{2.6}$$

A more useful measure of selectivity ($S_{i/j}$) is one which accounts for the difference in product working capacities as well (difference in equilibrium adsorption capacities at adsorption and desorption pressures (1.5 bar and 0.1 bar respectively), at the temperature of operation of the PSA (373 K) and the composition of the feed (0.5:0.5):

$$S_{i/j} = \frac{K_{H_i}}{K_{H_j}} \frac{\Delta q_i^*}{\Delta q_j^*} \tag{2.7}$$

2.2.1 Equilibrium behavior

The single component adsorption isotherms on 13X zeolite crystals are plotted for propylene and propane in Figure 2-2(a) and (b), respectively. It is evident that the adsorbent has a stronger affinity towards propylene than propane. This is more pronounced at the lower temperatures of 50^0C and 100^0C where there is a sharp rise in equilibrium adsorption of propylene at low pressures. The ideal selectivity of 13X, calculated from single component isotherms, for a 50/50 mixture of propylene/propane at several pressures are also shown in Figure 2-2 (c). High selectivities are observed at the lower pressures up to nearly 2 bar, but as the pressure is increased the values approaches unity.

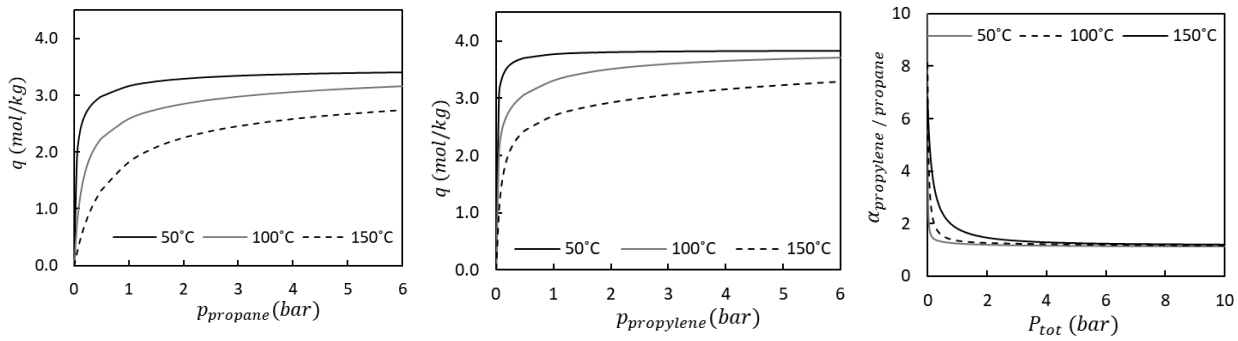

Figure 2-2: Single component isotherms for adsorption of a) propane, b) propylene on zeolite 13X and c) Ideal non-competitive selectivity of propylene/propane adsorption from a 50-50 mixture over a range of pressures (as calculated using single component isotherm measurements only)

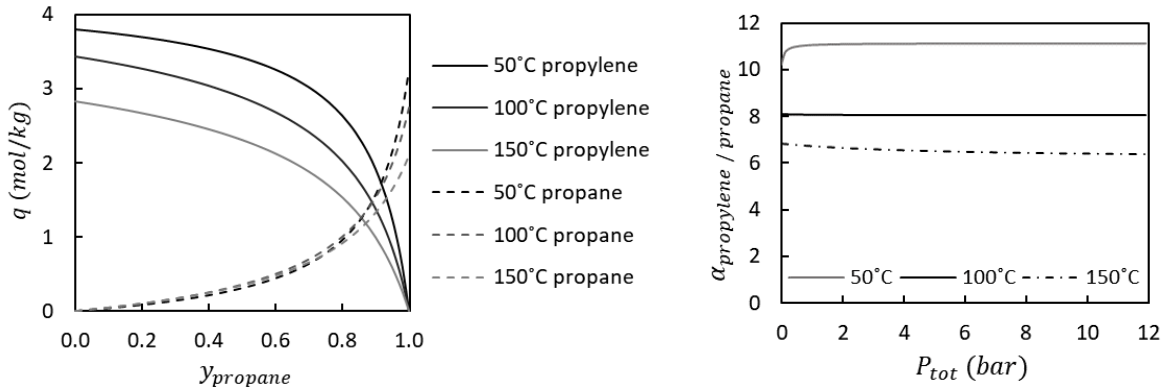

Figure 2-3 - (a) Binary adsorption isotherms for proylene/propane on zeolite 13X estimated using the DSL model at a constant total pressure of 1.5 bar. (b) Competetive selectivities of propylene/propane adsorption from a mixture with 50% propylene over a range of pressures (as calculated from two-component isotherm measurements).

The isotherms and selectivities for competitive adsorption between propylene/propane at different temperatures are plotted in Figure 2-3 (a) and (b) respectively. It is observed in Figure 2-3 (b) that, selectivity is mostly independent of pressure and high selectivity for propylene is maintained even at high pressures. Temperature however, has a significantly negative impact in the mixture selectivity of

zeolite 13X. It is worth mentioning that the selectivity was also observed to be mostly unaffected by the actual composition of the gas.

2.3 Parametric comparison

2.3.1 Equivalent mathematical models for hollow fiber bed and packed bed

Several assumptions are needed to effectively simulate the performance of an adsorption bed. Similar assumptions were made in modeling both the packed bed and the hollow fiber bed, to make as unbiased a comparison as possible.

2.3.1.1 Packed bed assumptions

The adsorbent pellets which pack the bed, are comprised of adsorbent crystals which are compacted together into a single larger sized solid (with or without the aid of a binder material). This results in voids called “macropores” inside the pellets themselves. The adsorbent crystals are also heterogeneous, with voids termed “micropores.” There are therefore two separate resistances to mass transfer from the pellet surface to the adsorption sites inside the crystals *(Figure 2-4).*

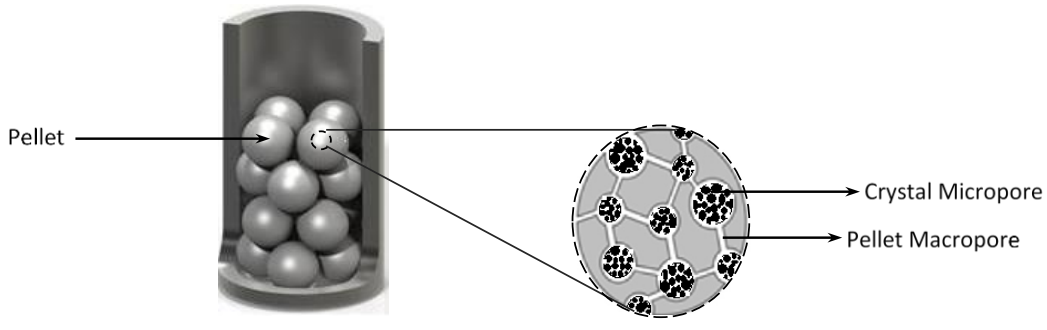

Figure 2-4 - Schematic of the mass transfer resistances inside a single pellet of the packed bed

The packed bed adsorption kinetics were described using a one-dimensional model with bi-disperse mass-transfer control, heterogeneous heat balance equations, local pressure drop and axial dispersion. The Ergun equation simplifies the momentum balance equation. The basic assumptions made while formulating the model are as follows [12]:

1. Radial gradients in concentration, velocity and temperature were neglected in the bed
2. The ideal gas equation describes the state of the gas phase in the bed.
3. The void fraction in the bed was considered uniform with no variability in the axial direction
4. External heat and mass transfer resistance were described by film diffusion.

2.3.1.2 Hollow fiber bed assumptions

The polymer commonly used for spinning the hollow fibers is cellulose acetate (CA). Similar to the packed bed, there are two main resistances to the diffusion of gas from the surface of the fiber to the adsorption sites inside the crystals. One is due to the presence of "micropores" in the crystals. The "macropore" resistance arises due to the presence of void spaces in the crystal-polymer matrix *(Figure 2-5).*

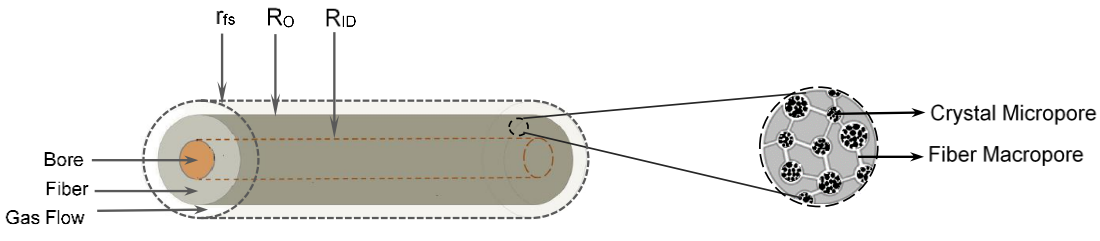

Figure 2-5 - Schematic of mass transfer resistances inside a single hollow fiber

It was assumed that each fiber is identical to every other fiber and also that the fibers are distributed evenly inside the module. This allowed for the assumption of a hypothetical gas shell surrounding each fiber, such that the gas to fiber ratio inside these hypothetical shells is the same as that of the module as a whole. Happel [14] used this free surface approach to find an analytical expression for pressure drop within the hollow fiber module, which was incorporated in this study. In exactly the same manner as the packed bed adsorption, a one-dimensional model with bi-disperse mass-transfer control, heterogeneous heat balance equations, local pressure drop and axial dispersion was used to describe the hollow fiber bed adsorption kinetics. The major assumptions pertaining to the hollow fiber bed model are as follows:

1. Radial gradients in concentration, velocity and temperature are neglected within the fiber
2. The ideal gas equation can describe the state of the gas phase in the bed.
3. The CA polymer is impermeable to the gas, and the gas can travel through the voids present in the matrix to reach the crystal surfaces. The weight percent of the fiber solids made up of CA is a known input to the process.
4. External heat and mass transfer resistance were described by film diffusion.

2.3.1.3 Mathematical models

The set of equations that describe adsorption dynamics in a packed bed were adopted from Da Silva and Rodrigues [17]. The accuracy of these equations in predicting adsorption equilibrium kinetics had been proven through several case studies reported in literature [12,15-18]. Experimental validation for this specific case involving the adsorption of

propylene/propane on zeolite 13X had been reported by Narin et al [12]. A similar set of equations were also used to describe the adsorption dynamics in the hollow fiber bed. Experimental validation for this model had been reported by Kalyanaraman et al [19]. PEI impregnated silica distributed in a CA matrix had been used as the adsorbent in the aforementioned case. For the current study, the crystal diffusion model was simplified to the volume averaged LDF model traditionally used in packed bed adsorption. The uniform distribution of the adsorption sites throughout the 13X crystal volume allowed for this simplification.

Table 2-1 shows in complete detail all the equations that were used to model the packed bed and the hollow fiber bed adsorption processes. The propylene and propane are distributed among three phases in both the beds – the bulk gas phase, the gas phase present in the macropores of the pellets and the adsorbed phase inside the crystals. The models are differential mass and heat balances for these three phases. Both the packed bed as well as the hollow fiber bed models have separate mass balances accounting for the mass transfer across all the interfaces rather than looking at a simplified overall mass transfer coefficient. The volume-averaged LDF (linear driving force) mass transfer coefficients were derived following the same principles and assumptions in both cases and have been included in *Appendix B*. The temperature of the solid crystals and the gas in the macropores of the pellets/fibers were assumed to be at equilibrium at all times and only the bulk gas phase temperature (T_g) and a single solid phase temperature (T_p/T_f) were modeled.

Table 2-1 - Model Equations used to simulate the packed bed and the hollow fiber bed adsorption processes

Packed Bed	**Hollow Fiber Bed**
Units: Concentrations: mol/m^3 , Pressure: bar, time: sec, velocity: m/s, Temperature: K	
Mass Balance Equations: *i. Bulk Gas Phase* $\frac{\partial Cg_i}{\partial t} = D_{ax,i}\frac{\partial^2 Cg_i}{\partial z^2} - \frac{\partial (Cg_i u_{g0}/\varepsilon)}{\partial z} - N_i$ $N_i = \frac{(1-\varepsilon)}{\varepsilon} k_{gas,i}(Cg_i - Cp_i)\frac{1}{1+Bi_i}$ *ii. Macropore Gas Phase* $\frac{\partial Cp_i}{\partial t} = k_{macro,i}(Cg_i - Cp_i)\frac{Bi_i}{1+Bi_i} - \frac{\rho_p}{\varepsilon_p}\frac{\partial q_i}{\partial t}$ *iii. Micropore Adsorbed Phase* $\frac{\partial q_i}{\partial t} = k_{micro,i}(q_i^* - q_i)$ where $u_{g0} = \frac{Q_{vol}}{Area}, \quad Area = \pi {R_{bed}}^2$ Mass Transfer Coefficients: $k_{gas,i} = ak_{g,i}$ $a = \frac{3}{R_p}, \; Bi_i = {ak_{g,i}}\Big/{\frac{15D_{p,i}\varepsilon_p}{R_p^2}}$ $k_{macro,i} = \frac{15D_{p,i}}{R_p^2}$ $k_{micro,i} = \frac{15D_{c,i}}{R_c^2}$	Mass Balance Equations: *i. Bulk Gas Phase* $\frac{\partial Cg_i}{\partial t} = D_{ax,i}\frac{\partial^2 Cg_i}{\partial z^2} - \frac{\partial (Cg_i u_{gi})}{\partial z} - N_i$ $N_i = \frac{R_{OD}^2 - R_{ID}^2}{r_{fs}^2 - R_{OD}^2} k_{gas,i}(Cg_i - Cp_i)\left[\frac{1}{1+Bi_i}\right]$ *ii. Macropore Gas Phase* $\frac{\partial Cp_i}{\partial t} = k_{macro,i}(Cg_i - Cp_i)\frac{Bi_i}{1+Bi_i} - \frac{\rho_f w_s}{\varepsilon_f}\frac{\partial q_i}{\partial t}$ *iii. Micropore Adsorbed Phase* $\frac{\partial q_i}{\partial t} = k_{micro,i}(q_i^* - q_i)$ where $u_{gi} = \frac{Q_{vol}}{Area}, \; Area = \pi {R_{bed}}^2(1 - v_{fib})$, $v_{fib}\pi r_{fs}^2 = \pi R_{OD}^2, \therefore r_{fs} = \frac{R_{OD}}{\sqrt{v_{fib}}}$ Mass Transfer Coefficients: $k_{gas,i} = ak_{g,i}$ $a = \frac{2R_{OD}}{(R_{OD}^2 - R_{ID}^2)}, \quad Bi_i = {ak_{g,i}}\Big/{\frac{8D_{fp,i}R_{OD}^2\varepsilon_f}{(R_{OD}^2 - R_{ID}^2)^2}}$ $k_{macro,i} = \frac{8D_{fp,i}R_{OD}^2}{(R_{OD}^2 - R_{ID}^2)^2}$ $k_{micro,i} = \frac{15D_{c,i}}{R_c^2}$

Ideal Gas Equation[12,13,17]:

$$p_i = Cg_i RT_g,\ P_{tot} = \sum p_i,\ C_{g,tot} = \sum Cg_i,\ C_{p,tot} = \sum Cp_i$$

Table 2-1 continued

Ergun Equation (Pressure Drop):

$$-\frac{\partial P_{tot}\times 10^5}{\partial z} = 150\frac{\mu_g(1-\varepsilon)^2}{\varepsilon^3(2R_p)^2}u_{g0} + 1.75\frac{(1-\varepsilon)\rho_g}{2R_p\varepsilon^3}|u_{g0}|u_{g0}$$

Heat Balance Equations:

$$c_{p,T} = \sum_i y_i c_{p,i},\ c_{v,T} = \sum_i y_i c_{v,i}$$

i. Bulk Gas Phase

$$\varepsilon C_{g,tot}c_{v,T}\frac{\partial T_g}{\partial t} = \lambda\frac{\partial^2 T_g}{\partial z^2} - u_{g0}C_{g,tot}c_{p,T}\frac{\partial T_g}{\partial z} + \varepsilon RT_g\frac{\partial C_{g,tot}}{\partial t} - (1-\varepsilon)a\,h_f(T_g - T_p) - \frac{2h_w}{R_{bed}}(T_g - T_w)$$

ii. Pellet

$$(1-\varepsilon)\left(\varepsilon_p\sum_i C_{p,i}\,c_{v,i} + \rho_p\left(\sum_i q_i\,c_{v,ads,i} + c_p\right)\right)\frac{\partial T_p}{\partial t} = (1-\varepsilon)a\,h_f(T_g - T_p) + \rho_b\sum_i\left(-\Delta H_{ads,i}\frac{\partial q_i}{\partial t}\right)$$

iii. Wall

$$\rho_w C_{p,w}\frac{\partial T_w}{\partial t} = \alpha_w h_w(T_g - T_w) - \alpha_{wl}U(T_w - T_{amb})$$

$$\alpha_w = \frac{D_{bed}}{t_w(D_{bed}+t_w)},\qquad \alpha_{wl} = \frac{1}{(D_{bed}+t_w)\ln\left(\frac{D_{bed}+t_w}{D_{bed}}\right)}$$

Happel's Equation (Pressure Drop):

$$-\frac{\partial P_{tot}\times 10^5}{\partial z} = \frac{u_{gi}\mu_g}{r_{OD}^2 - 3r_{fs}^2/8 + \ln\left(\frac{r_{fs}}{r_{OD}}\right)r_{fs}^4/2\left(r_{fs}^2 - r_{OD}^2\right)}$$

Heat Balance Equations:

$$c_{p,T} = \sum_i y_i c_{p,i},\ c_{v,T} = \sum_i y_i c_{v,i}$$

i. Bulk Gas Phase

$$\left(r_{fs}^2 - r_{OD}^2\right)C_{g,tot}c_{v,T}\frac{\partial T_g}{\partial t} = \lambda\frac{\partial^2 T_g}{\partial z^2} - \left(r_{fs}^2 - r_{OD}^2\right)\left[u_{gi}C_{g,tot}c_{p,T}\frac{\partial T_g}{\partial z} + RT_g\frac{\partial C_{g,tot}}{\partial t}\right] - \left(r_{OD}^2 - r_{ID}^2\right)a\,h_f(T_g - T_f)$$

ii. Fiber

$$\left(\varepsilon_f\sum_i C_{p,i}\,c_{v,i} + \rho_f\left(\sum_i q_i\,c_{v,ads,i} + c_{p_f}\right)\right)\frac{\partial T_f}{\partial t} = \lambda_f\frac{\partial^2 T_f}{\partial z^2} + a\,h_f(T_g - T_f) + \rho_f\sum_i\left(-\Delta H_{ads,i}\frac{\partial q_i}{\partial t}\right) - a_{f_{int}}h_{wat}(T_f - T_{wat}) \qquad where\ \ a_{f_{int}} = \frac{2R_{ID}}{R_{OD}^2 - R_{ID}^2}$$

iii. Bore Fluid

$$\rho_{bf}C_{p,bf}\frac{\partial T_{bf}}{\partial t} = -u_{bf}\rho_{bf}C_{p,bf}\frac{\partial T_{bf}}{\partial z} + \frac{2}{R_{ID}}h_{bf}(T_f - T_{bf})$$

2.3.2 Estimation of adsorbent bed specific property parameters

The same crystals of zeolite 13X (size, crystal diffusion properties) were assumed to form the pellets and the fibers. As suggested in literature [12] it was assumed that 13X can form binderless pellets. However, the hollow fibers were assumed to contain 40% by weight of the polymer cellulose acetate (CA), which is necessary to form the matrix to embed 13X crystals. Experimental studies have found that spinning of stable fibers with any kind of adsorbent crystal is possible up to a limit of as little as 25% of CA by weight[11]. The diameter and porosity of the pellets and that of the fibers in the hollow fiber bed, were set at values which had been generally used in experimental work in literature [19]. These are reported in *Table A2 Appendix B*. The bed packing fraction for both the packed bed as well as the hollow fiber bed were assumed to be 0.68 (i.e. a bed void fraction of 0.32).

The properties of the 13X crystals were taken from the experimental measurements that had been made by Narin et al [12]. Some of the properties of the solid phase had been reported as bulk values for the packed bed pellet phase as a whole (i.e. including the macropores and the crystals). Crystal property values were back calculated. The bulk fiber property values including the crystal, CA as well as the macropores were subsequently calculated. The detailed calculations are included in *Appendix B.* The final values are reported in *Table B2* in *Appendix B.*

Table B3 in *Appendix B* is a complete list of all the correlations that have been used to estimate the transport and physical property parameters in both models[12,20,21]. The Wakao and Funazkri correlations for axial dispersion in the packed bed model is well known [20]. However, such detailed studies on the axial dispersion in a hollow fiber bed are missing in literature. As an approximation the same correlation is used for both beds. This does not affect any results presented since, the operation regime was chosen such that

dispersion has negligible influence, as has been elaborated in the "Optimization procedure" section. *Table B4* in *Appendix B* lists the property details for propylene, propane and the non-adsorbing component helium which was assumed to fill the bed when not under operation.

2.4 Results - parametric comparison

At this stage a few preliminary comparisons may be made between the properties of the packed bed and the hollow fiber bed, without carrying out simulation of an actual separation process, as elaborated below.

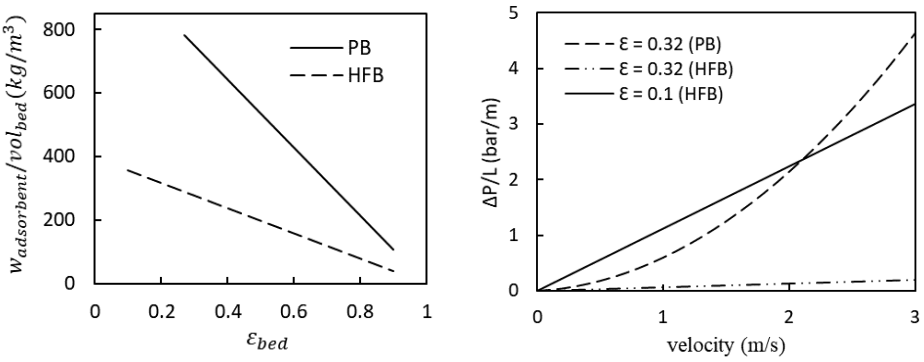

Figure 2-6 - (a) Amount of adsorbent available per unit volume of the bed with varying bed packing fraction for both the packed bed and the hollow fiber bed. (b) Pressure drop variation in the packed bed and hollow fiber bed with superficial velocity. ε is the bed void fraction.

Figure 2-6 (a) shows that the amount of adsorbent in a given volume of the packed bed is approximately 2.7 times larger than that in the same volume of the hollow fiber bed. This disadvantage can be attributed to the presence of the bore which reduces the actual volume that is available for the solid phase in the hollow fibers, and the need to have a porous polymer as the fiber material. On the other hand, for the packed bed, a very low quantity of binder material is required to form pellets (binderless pellets in this study). This

difference is partially offset by the higher packing fraction of the fibers in the bed compared to the pellets. The minimum possible ε for packed bed is 0.27, and for hollow fiber bed is 0.10.

Figure 2-6 (b) shows the variation of pressure drop per unit length of the bed with superficial gas velocity for both configurations. With similar bed velocities and bed void fraction of 0.32, the pressure drop in the hollow fiber bed almost appears negligible compared to the packed bed, for the same bed length. The pressure drop in the hollow fiber bed is so low that the equivalent pressure drop is achieved only with a solid packing fraction of almost 90% of the total volume (ε=0.1). Such a high packing fraction is the highest theoretically possible value for circles in a plane. The lower pressure drop in the hollow fiber bed may be attributed to the structured nature of its packing.

Table 2-2 shows the values of the three mass transfer coefficients for the same external gas volumetric flow rate and the same bed void fraction. Multiplying these coefficients by the adsorbed phase concentration driving force (Δq) gives the molar uptake rate per unit volume of the pellet (moles/sec/m^3 pellet). Detailed derivations are provided in Appendix B. In both configurations, the macropore mass transfer coefficient (k'_{macro}) has the smallest value. This indicates that macropore diffusion is the dominant resistance to the overall mass transfer from the bulk gas to the adsorption sites on the crystals. The resistance offered by gas film and crystal diffusion is comparatively negligible.

It can also be seen in Table 2-2 that k'_{macro} for the hollow fiber bed is nearly twice that of the packed bed. This indicates that the overall mass transfer performance of the

hollow fiber bed would be significantly better than that of the packed bed. This may be attributed to the fact that the diffusion length in the hollow fiber bed is from the outer radius only to the bore (inner radius), $R_{OD} - R_{ID}$ = 0.378 mm. On the other hand, the packed bed requires diffusion from the surface of the pellet to the center of the pellet, R_p = 0.8 mm.

Table 2-2 - Mass transfer coefficients in the packed bed and the hollow fiber bed for same interstitial bulk gas velocity (1.05 m/s) and same bed void fraction (0.32). The coefficients are calculated on the basis of a unit volume of the pellet (or hollow fiber) and the difference between the actual and the equilibrium adsorbed phase (q*) as the driving force

Mass transfer coefficients $\frac{mol/sec}{m^3_{pellet}\left(\frac{mol}{kg_{adsorbent}}\right)}$	C_3H_{10}		C_3H_8	
	Packed Bed	Hollow Fiber Bed	Packed Bed	Hollow Fiber Bed
k'_{gas}	93.53	17.98	11.17	2.06
k'_{macro}	**2.80**	**5.40**	**0.13**	**0.62**
k'_{micro}	5.39×10^5	2.42×10^5	8.89×10^4	3.99×10^4

Table 2-3 shows that the overall heat transfer coefficient per unit volume of adsorbent material for the hollow fiber bed, $h_{overall}$ = 1.15 × 10^7 W/K.m^3-fiber, is significantly higher than that of the packed bed, 3.89 × 10^3 W/K.m^3-pellet. This is due to the structural difference of the two beds. In the packed bed the heat is transferred through three media in series as follows: (1) from the pellet to the gas ($h_{adsorbent-gas}$), (2) the gas to the wall ($h_{gas-wall}$), and (3) from the wall to the surroundings ($h_{wall-ambient}$). On the other hand, in the hollow fiber bed the heat transfer occurs in parallel to the gas mixture

through the following two media: (1) from the adsorbent to the gas ($h_{adsorbent-gas}$), and (2) from the gas to the fluid in the bore of the fiber($h_{adsorbent-H/C\ medium}$). Detailed derivations for each of these heat transfer coefficients are provided in Appendix B.

Table 2-3 - Heat transfer coefficients in the packed bed and the hollow fiber bed for same interstitial bulk gas velocity (1.05 m/s) and same bed void fraction (0.32). Units: (Watt/K) / (m^3 of solid phase i.e. pellet or fiber. Detailed derivation: Appendix B

	$h_{adsorbent-H/C\ medium}$		$h_{adsorbent-gas}$	$h_{gas-wall}$	$h_{wall-ambient}$		$h_{overall}$
	$W/m^2.K$	$W/m^3.K$	$W/m^3.K$	$W/m^3.K$	$W/m^2.K$	$W/m^3.K$	$\mathbf{W/m^3.K}$
Hollow Fiber Bed	7,268 [19]	1.15×10^5	1.14×10^7				$\mathbf{1.15 \times 10^7}$
Packed Bed			1.57×10^5	1.16×10^4	30.0 [12]	6.09×10^3	$\mathbf{3.89 \times 10^3}$
					7,268 (artificially increased)	1.47×10^6	$\mathbf{1.07 \times 10^4}$

The overall heat transfer co-efficient ($h_{overall}$) for the hollow fiber bed was found to be 1.2×10^7 W/K.(m^3 of fiber). The $h_{overall}$ for the packed bed was found to be significantly smaller, 3.9×10^3 W/K.(m^3 of pellet). It can be confirmed that the significant difference in the overall heat transfer coefficient between the two beds is not due to the heat transfer utility (cooling fluid versus air). Even if $h_{wall-ambient}$ of the packed bed was artificially increased to match $h_{adsorbent-H/C\ medium}$ of water in the hollow fiber (7,268 W/m^2K), the overall heat transfer coefficient for the packed bed would be only 1.07×10^4

W/K.(m^3 of pellet), which is smaller than that of the hollow fiber bed by three orders of magnitude The high surface to volume ratio due to the presence of the bore gives a very significant advantage to the hollow fiber bed.

The properties in favor of the hollow fiber bed are the better mass and heat transfer coefficients and, the lower pressure drop. The comparative disadvantage of having a lower packing efficiency in the hollow fiber bed is, however, not clear. Further conclusions regarding the relative performance of both configurations requires process simulation.

2.5 Process performance comparison

For further insight into the relative performance of the hollow fiber bed and the packed bed, the models of section 2.4 were simulated to represent similar single-bed, multi-step VPSA processes in both configurations. The aim of the processes was to obtain a purified stream of propylene (which has a stronger affinity towards 13X) from a 50:50 mixture of propylene/propane. The effectiveness of the desired separation that was achieved at the cyclic steady state (CSS) for each process was used for the comparison.

The aim was to provide conditions that allowed the beds to remain as close to feed temperature as possible by choosing boundary conditions, as summarized in section 2.5.2. As stated previously, the adsorption pressure, P_{ads} is 1.5 bar while the desorption pressure, P_{des} is 0.1 bar. All inlets to the process are at 100^0 C. Both the T_{amb} for the packed bed and the inlet temperature of the bore fluid (T_{bf}) for the hollow fiber bed were 100^0 C.

2.5.1 Operation scheme for separation process

Figure 2-7 is a representation of the steps that were used in the VPSA scheme. The process begins with counter-current (to the process feed inlet) *pressurization* to adsorption pressure (P_{ads}), with the weakly adsorbed component (propane). This is followed by the *adsorption* step with the feed mixture and a rinse step with the strongly adsorbed component (propylene) both at P_{ads}. Both these steps produce propane (weakly adsorbed component) at the product end. Then the *rinse* step is carried out to improve the purity of the propylene that will be recovered in the subsequent steps. The loss in recovery of propylene as a result of rinsing was accounted for during the performance parameter calculations. At this point the bed is mostly filled with the strongly adsorbed propylene which needs to be recovered. Then a counter-current blowdown operation is carried out to decrease the pressure to the desorption pressure (P_{des}) and simultaneously recover the propylene at the product end. Finally in the *purge* step, the bed was counter-currently purged with propane (weakly adsorbed component) at P_{des} to further improve the recovery of propylene. This improvement in recovery is however at the cost of purity of the propylene product.

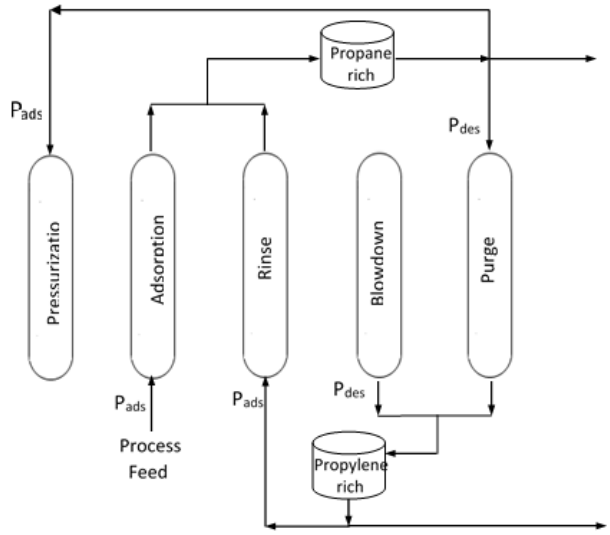

Figure 2-7 - Schematic of the VPSA cycle for the production high-purity propylene (storage tanks added to modify cycle from Narin et al [12])

The process schematic includes two additional holding tanks apart from the single bed that is used for the separation. These are necessary for a more realistic representation of the process operation allowing the product composition to be consistent with the operation as opposed to assuming that completely pure product is available. The outflow from the adsorption and rinse processes is stored in the "propane product" holding tank while that from the blowdown and purge steps is stored in the "propylene product" holding tank. The process was simulated such that the composition of the inlet of the rinse step and the "propylene product" and, that of the inlet of the pressurization and the purge steps and the "propane product" were the same at cyclic steady state. We employed this realistic assumption instead of using pure products in the rinse and purge steps, so that we can avoid over-estimation of the separation efficiency of the process. The mass balance of the products in the tanks are given by:

$$\mathrm{N}^{\mathrm{i,end}}_{\mathrm{tank_{propane}}} = \int_0^{\mathrm{t_{adsorption}+rinse}} \mathrm{A_{bed}}(\mathrm{C_{C_3H_8}} + \mathrm{C_{C_3H_6}})\mathrm{u_{g0}}|_{\mathrm{z=L}}\,\mathrm{dt} \tag{2.8}$$

$$\mathrm{N}^{\mathrm{i,end}}_{\mathrm{tank_{propylene}}} = \int_0^{\mathrm{t_{blowdown}+purge}} \mathrm{A_{bed}}(\mathrm{C_{C_3H_8}} + \mathrm{C_{C_3H_6}})\mathrm{u_{g0}}|_{\mathrm{z=0}}\,\mathrm{dt} \tag{2.9}$$

$$\mathrm{N}^{\mathrm{i}}_{\mathrm{product}} = \mathrm{N}^{\mathrm{i,end}}_{\mathrm{tank_{propane}}} - \mathrm{N}^{\mathrm{i+1}}_{\mathrm{purge}} \tag{2.10}$$

$$N^{i}_{\mathrm{product}} = N^{i,end}_{\mathrm{tank_{propylene}}} - N^{i+1}_{\mathrm{rinse}} \qquad \mathrm{N = total\ moles} \tag{2.11}$$

At CSS, the following equations are satisfied:

$$N_{rinse}^{i} = N_{rinse}^{i+1} \quad (2.12)$$

$$N_{purge}^{i} = N_{purge}^{i+1} \quad (2.13)$$

2.5.2 Boundary conditions

To simulate the VPSA process, the boundary conditions (BC's) are changed in each step. In this study, Danckwerts' BCs were used and have been reported in Table 2-4 for each of the five steps. We found that instead of simply specifying inlet or outlet pressure of the bed, pseudo-valve equations must be implemented to simulate the blowdown and the pressurization steps (Table 2-4) to avoid unrealistic velocities. Implementing the constant pressure boundary conditions (i.e. $P_{z=0} = P_{des}$), resulted in a maximum velocity of ~110 m/s (Figure 2-8 (a)) in the hollow fiber bed outlet during blowdown, which is not practical. To avoid such high flow rates, we chose the valve constants M_b and M_p to be 0.8 for both beds to restrict the flow rates below 25 m/s in the hollow fiber bed.

Figure 2-8 (b) indicates that the highest velocity in the packed bed (length = 1.2 m) is much smaller, at 10% of that in the hollow fiber bed (length = 3 m), during blowdown. This is due to the higher pressure drops in the unstructured configuration of the packed bed.

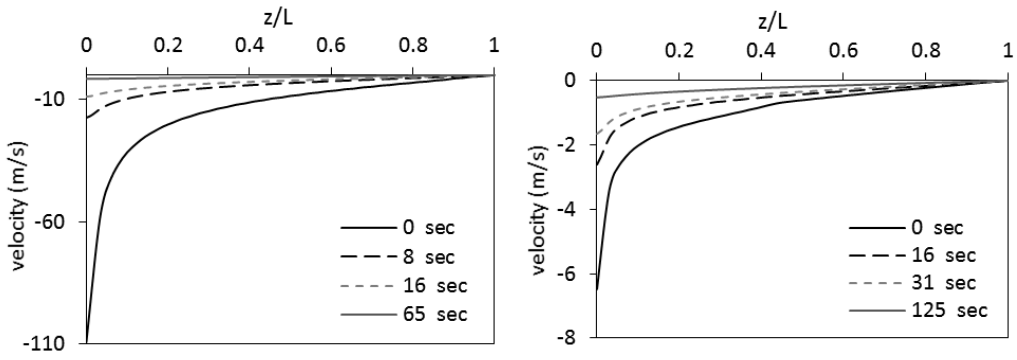

Figure 2-8 - Velocity profiles at different times for (a) a hollow fiber bed of length 3 m (b) a packed bed of length 1.2 m, during blowdown from an initial pressure of 1.5 bar to a final pressure of 0.1 bar. The simulations were run such that the outlet pressure was constantly held at 0.1 bar during the entire blowdown.

Table 2-4 - Boundary conditions for the 5-step single bed VPSA process

Units: Concentrations: mol/m^3 , Pressure: bar, time: sec, velocity: m/s, Temperature: K

Pressurization with weakly adsorbed component (Counter-current)

$$\left.\frac{\partial T_g}{\partial z}\right|_{0^+} = 0 \qquad -\lambda \left.\frac{\partial T_g}{\partial z}\right|_{L^-} = u_g C_{p,T}\Big|_{L^-} \sum_i C_{g,i_{in}} \left(T_{g_{in}} - T_{g_{L^-}}\right)$$

$$\left.\frac{\partial C_{g,i}}{\partial z}\right|_{0^+} = 0 \qquad -\varepsilon D_{ax,i} \left.\frac{\partial C_{g,i}}{\partial z}\right|_{L^-} = u_g\Big|_{L^-} \sum_i C_{g,i_{in}} \left(C_{g,i_{in}} - C_{g,i_{L^-}}\right)$$

where $C_{g,i_{in}} = 10^5 \times y_{press,i} \left.\frac{P_{tot}}{RT_g}\right|_{L^-}$

$$u_g\Big|_{0^+} = 0 \qquad P_{tot}\Big|_{z=L^-} = P_{tot}\Big|_{z=L^-}^{0} + \left(P_{ads} - P_{tot}\Big|_{z=L^-}^{0}\right)\left(1-\exp\left(-M_p t\right)\right)$$

Adsorption (Feed)

$$-\boldsymbol{\lambda}\left.\frac{\partial T_g}{\partial z}\right|_{0^+} = \boldsymbol{u_g C_{p,T}}\Big|_{0^+} \sum_i \boldsymbol{C_{g,i_{in}}} \left(\boldsymbol{T_{g_{in}}} - \boldsymbol{T_{g_0^+}}\right) \qquad \left.\frac{\partial T_g}{\partial z}\right|_{L^-} = \mathbf{0}$$

$$-\boldsymbol{\varepsilon D_{ax,i}} \left.\frac{\partial C_{g,i}}{\partial z}\right|_{0^+} = \boldsymbol{u_g}\Big|_{0^+} \left(\boldsymbol{C_{g,i_{in}}} - \boldsymbol{C_{g,i0}^+}\right) \qquad \left.\frac{\partial C_{g,i}}{\partial z}\right|_{L^-} = \mathbf{0}$$

Table 2-4 continued

where $C_{g,i_{in}} = 10^5 \times y_{ads,i} \left.\frac{P_{tot}}{RT_g}\right\|_{0^+}$	
$u_{g0^+} = v_{ads}$	$P_{tot}\|_{L^-} = P_{ads}$
Rinse (Co-current)	
$-\lambda \left.\frac{\partial T_g}{\partial z}\right\|_{0^+} = u_g C_{p,T} \Big\|_{0^+} \sum_i C_{g,i_{in}} \left(T_{g_{in}} - T_{g_0^+}\right)$	$\left.\frac{\partial T_g}{\partial z}\right\|_{L^-} = 0$
$-\varepsilon D_{ax,i} \left.\frac{\partial C_{g,i}}{\partial z}\right\|_{0^+} = u_g\|_{0^+} \left(C_{g,i_{in}} - C_{g_{,i0}^+}\right)$	$\left.\frac{\partial C_{g,i}}{\partial z}\right\|_{L^-} = 0$
where $C_{g,i_{in}} = 10^5 \times y_{rinse,i} \left.\frac{P_{tot}}{RT_g}\right\|_{0^+}$	
$u_{g0^+} = v_{rinse}$	$P_{tot}\|_{L^-} = P_{ads}$
Blowdown (Counter-current)	
$\left.\frac{\partial T_g}{\partial z}\right\|_{0^+} = 0$	$\left.\frac{\partial T_g}{\partial z}\right\|_{L^-} = 0$
$\left.\frac{\partial C_{g,i}}{\partial z}\right\|_{0^+} = 0$	$\left.\frac{\partial C_{g,i}}{\partial z}\right\|_{L^-} = 0$
$P_{tot}\|_{z=0^+} = P_{tot}\|_{z=0^+}^0 - \left(P_{tot}\|_{z=0^+}^0 - P_{des}\right)\left(1 - exp(-M_b t)\right)$	$u_{g_{L^-}} = 0;$
Purge (Counter-current)	
$\left.\frac{\partial T_g}{\partial z}\right\|_{0^+} = 0$	$-\lambda \left.\frac{\partial T_g}{\partial z}\right\|_{L^-} = u_g C_{p,T} \Big\|_{L^-} \sum_i C_{g,i_{in}} \left(T_{g_{in}} - T_{g_L^-}\right)$
$\left.\frac{\partial C_{g,i}}{\partial z}\right\|_{0^+} = 0$	$-\varepsilon D_{ax,i} \left.\frac{\partial C_{g,i}}{\partial z}\right\|_{L^-} = u_g\|_{L^-} \left(C_{g,i_{in}} - C_{g,i_L^-}\right)$
where $C_{g_{,i_{in}}} = 10^5 \times y_{purge,i} \left.\frac{P_{tot}}{RT_g}\right\|_{L^-}$	
$P_{tot}\|_{z=0^+} = P_{des}$	$u_{gL^-} = v_{purge}$

2.5.3 Performance parameters

The metrics that were used to compare the overall separation performance of the two different configurations over the above mentioned cycle are, the purity and recovery of the propylene product, and the productivity of the bed producing propylene. The purity, recovery and the productivity of the beds for propane stream are also important parameters that were monitored. The definitions used for each parameter are listed below:

Propylene:

$$\text{Purity}_{C_3H_6} = 100 \times \frac{\text{blowdown}_{\text{out},C_3H_6} + \text{purge}_{\text{out},C_3H_6}}{\sum_{i=\text{components}} (\text{blowdown}_{\text{out},i} + \text{purge}_{\text{out},i})} \quad (2.14)$$

$$\text{Recovery}_{C_3H_6} = 100 \times \frac{\text{blowdown}_{\text{out},C_3H_6} + \text{purge}_{\text{out},C_3H_6} - \text{rinse}_{\text{in},C_3H_6}}{\text{ads}_{\text{in},C_3H_6}} \quad (2.15)$$

Propane:

$$\text{Purity}_{C_3H_8} = 100 \times \frac{\text{ads}_{\text{out},C_3H_8} + \text{rinse}_{\text{out},C_3H_8}}{\sum_{i=\text{components}} (\text{ads}_{\text{out},i} + \text{rinse}_{\text{out},i})} \quad (2.16)$$

$$\text{Recovery}_{C_3H_8} = 100 \times \frac{\text{ads}_{\text{out},C_3H_8} + \text{rinse}_{\text{out},C_3H_8} - \text{purge}_{\text{in},C_3H_8} - \text{press}_{\text{in},C_3H_8}}{\text{ads}_{\text{in},C_3H_8}} \quad (2.17)$$

Productivity (moles/kg adsorbent/hr, velocity in m/sec, t_{cycle} in sec)

Packed Bed:

$$\text{Productivity}_{C_3H_6} = 3600 \times \frac{\text{blowdown}_{\text{out},C_3H_6} + \text{purge}_{\text{out},C_3H_6} - \text{rinse}_{\text{in},C_3H_6}}{\rho_b \, L \, \text{time}_{\text{cycle}}} \quad (2.18)$$

$$\text{Productivity}_{C_3H_8} = 3600 \times \frac{\text{ads}_{\text{out},C_3H_8} + \text{rinse}_{\text{out},C_3H_8} - \text{purge}_{\text{in},C_3H_8} - \text{press}_{\text{in},C_3H_8}}{\rho_b \, L \, \text{time}_{\text{cycle}}} \tag{2.19}$$

Hollow Fiber Bed:

$$\text{Productivity}_{C_3H_6} = 3600 \times \frac{(\text{blowdown}_{\text{out},C_3H_6} + \text{purge}_{\text{out},C_3H_6} - \text{rinse}_{\text{in},C_3H_6})}{\rho_f w_f (r_{OD}^2 - r_{ID}^2)/(r_{fs}^2 - r_{OD}^2) \, L \, \text{time}_{\text{cycle}}} \tag{2.20}$$

$$\text{Productivity}_{C_3H_8} = 3600 \times \frac{\text{ads}_{\text{out},C_3H_8} + \text{rinse}_{\text{out},C_3H_8} - \text{purge}_{\text{in},C_3H_8} - \text{press}_{\text{in},C_3H_8}}{\rho_f w_f (r_{OD}^2 - r_{ID}^2)/(r_{fs}^2 - r_{OD}^2) \, L \, \text{time}_{\text{cycle}}} \tag{2.21}$$

The terms ads_{in} , $rinse_{in}$, $purge_{in}$, $press_{in}$ represent the total molar flow rates into the bed during the entire duration of the respective cycle step. The subscript *out* represents total molar outlet flow during an entire cycle step. The total molar flow of a given component is calculated by a time integral. For example:

$$\text{ads}_{\text{out},C_3H_8} = \int_0^{t_{\text{adsorption}}} C_{C_3H_8} u_{g0}|_{z=L} \, dt \tag{2.22}$$

The molar flows for the hollow fiber bed are calculated in terms of interstitial velocity (u_{gi}), rather than the superficial velocity (u_{g0}) for convenience. For example:

$$\text{blowdown}_{\text{out},C_3H_6} = \int_0^{t_{\text{blowdown}}} C_{C_3H_6} u_{gi}|_{z=0} \, dt \tag{2.23}$$

2.5.4 Simulation procedure

To simplify the flowsheet shown in Figure 2-7, the compositions of the rinse and purge streams were provided as independent inputs to the system, rather than attempting to solve a recycle loop. There are two constraints that should be satisfied by this decoupled system at cyclic steady state (CSS).

$$x^{in}_{press,C_3H_8} \times 100 = x^{in}_{ads,C_3H_8} \times 100 = \text{Purity}_{C_3H_8} \quad (2.24)$$

$$x^{in}_{rinse,C_3H_6} \times 100 = \text{Purity}_{C_3H_6} \quad (2.25)$$

The terms x^{in}_{press,C_3H_8} , x^{in}_{ads,C_3H_8} and x^{in}_{rinse,C_3H_6}represent the mole fraction of the respective components in the inlet stream for the pressurization, adsorption and rinse steps. The constraints were met after several iterations with varying inlet compositions of the rinse and purge, allowing each iteration to reach the CSS. Further details are included in section 2.5.5.4.

The process simulations were performed using gPROMS [22]. The OCFEM (orthogonal collocation) scheme was used to discretize all axially varying parameters and variables. Time integration was performed using the default solver DASOLV. The bed was assumed to be filled with the non-adsorbing gas helium at feed temperature and pressure as the initial condition. The steps were cyclically simulated using the final conditions of the previous cycle as the initial conditions for the next one. The procedure was repeated until the squared sum of errors between the initial and final concentration profile in a cycle reached a specified tolerance value. The number of discretization points used were varied

such that the numerical dispersion had negligible effect and the cyclic simulations were numerically robust.

2.5.5 Optimization procedure

The purity, recovery and productivity, in terms of the desired product, in this case propylene, determine the efficiency and a significant fraction of the cost of mixture separation by a cyclic adsorption process. The objective of the optimization problem was to maximize the recovery of propylene using each of the fiber and packed bed configurations. A certain level of minimum purity was imposed for the propylene product. The variation of productivity as an outcome of this optimization was then studied as a performance indicator which will reflect tradeoffs in recovery and other cycle parameters.

For fixed process pressures (high: 1.5 bar, low 0.1 bar) and inlet temperatures (100^0C), the variables which determine the optimum performance are: length of the bed (L), velocity of the process stream (v), velocity of the heating/cooling fluid in the bore (v_{bore}) of the hollow fiber bed and, the cycle times for each of the individual process steps involved in the separation (t_{ads}, t_{rinse} , $t_{blowdown}$, t_{purge}, $t_{pressurization}$). As a base case, the inlet velocities for the rinse and purge steps were the same as the feed velocity.

2.5.5.1 Process stream velocity and bed length

Since energy consumption is an important consideration in implementing a VPSA process, we tried to set conditions that ensure equivalent upstream compression cost for both process configurations. Specifically, these conditions ensured that, the bed pressure drop as well as the volumetric flowrate of the feed gas, were kept the same in the two beds.

Table 2-5 lists the values of the bed length and diameters used along with the corresponding stream velocities. The pressure drop (ΔP) was fixed at $0.1P_{ads}$ (0.15 bar) and the volumetric flow rate was set to 16 standard liter per minute (SLPM). In this study, the length of the hollow fiber bed is fixed to 3.0m to avoid unrealistically long fibers.

For the packed bed, the bed diameter was varied to maintain the same volumetric flow rate and pressure drop. Varying the diameter of the packed bed did not affect cycle performance significantly, since radial distributions of concentration and temperature were ignored. Nevertheless, the diameter did have a small impact on the heat transfer area between the packed bed and the surroundings. The radial independence assumption was justified for all combinations of the packed bed length and diameter since, the rate of radial heat conduction from the center to the outer surface of the bed was fast, compared to the rate of heat transferred away from the bed surface to the exterior.

Table 2-5 - Dimensions of the packed bed and hollow fiber bed

Configuration	Length (m)	Bed Dia. (cm)	Volumetric flow (SLPM)	$Vel_{interstitial}$ (m/s)
Packed Bed	1.0	2.68	16	1.35
	1.5	3.04	16	1.04
	2.0	3.34	16	0.86
Hollow Fiber Bed	3.0	2.12	16	2.15

2.5.5.2 Negligible effect of dispersion

For the conditions of this chapter, dispersion had no significant impact on the cyclic purity and recovery of propylene at CSS, for the hollow fiber bed, as shown in Table 2-6. This justifies the adoption of the The Wakao-Funazkri correlation [20] for the packed bed, to also estimate the magnitude of dispersion in the hollow fiber bed. As mentioned previously, accurate knowledge of dispersion in a hollow fiber bed is not available in literature. The velocities for the packed bed were set in the range similar to the hollow fiber bed and dispersion is expected to have a negligible impact on its process performance as well, given the structured nature of the packing.

Table 2-6 - Sensitivity of overall process (with the same step lengths) purity and recovery of propylene to the magnitude of axial dispersion. (D_{base} represents the axial dispersion co-efficient obtained using the Wakao-Funazkri correlation [20] in the hollow fiber bed.)

Axial Dispersion co-efficient	Propylene purity (%)	Propylene recovery (%)
0.5 D_{base}	99.5	36.7
D_{base}	99.5	36.7
2 D_{base}	99.4	36.6
5 D_{base}	99.2	36.5

2.5.5.3 Velocity of cooling fluid through the bore

Velocity of the cooling/heating fluid through the bore of the hollow fiber bed, and consequently its heat transfer efficiency, is an important factor determining process

performance. To find an optimal value for v_{bore}, a sensitivity analysis was performed on cyclic purity and recovery. In this analysis, a hollow fiber bed cycle was fixed and the CSS purity and recovery were observed for the different cooling fluid velocities. We found that there was a limit to the process performance improvement that can be achieved by increasing cooling fluid velocity, which improves the heat transfer efficiency. Process purity reaches a plateau by increasing the bore fluid velocity beyond 0.5 m/s (Figure 2-9 (a)). This was therefore chosen as the optimal velocity of the bore fluid in the hollow fiber bed.

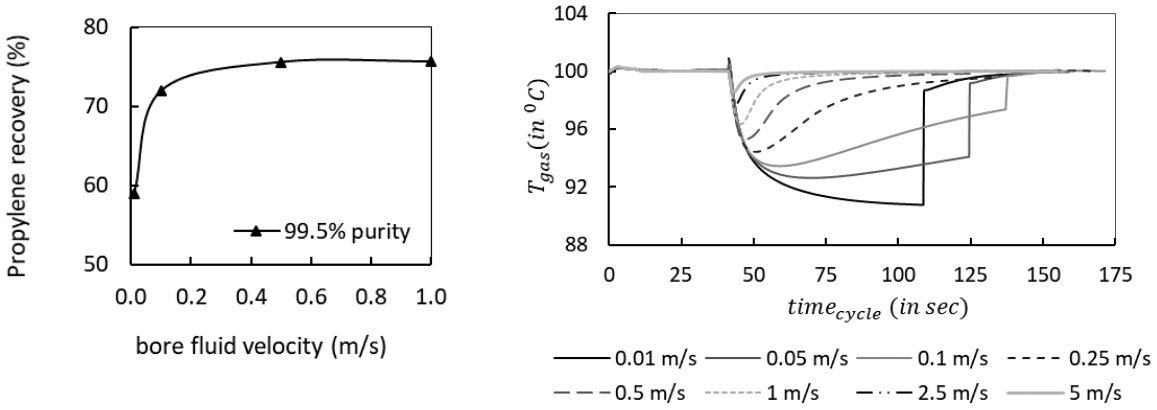

Figure 2-9 - (a) Propylene purity and recovery and (b) Cyclic gas phase temperature profiles, for different values of cooling fluid velocity in the hollow fiber bed, with the same process cycle

Cyclic temperature profiles of the gas at the center of the hollow fiber bed are plotted in Figure 2-9 (b) for different bore fluid velocities. It was observed that the heat of adsorption was completely removed during the pressurization, feed and rinse steps. The gas temperature does not rise very much from the feed temperature of 100^0 C, irrespective of the cooling fluid velocity. The velocity of the cooling fluid, however, has a significant impact on the temperature drop during the blowdown step. This is probably because during

blowdown there is no gas supply which can provide heat to the fiber, and thus water is the only heat source in this step.

2.5.5.4 Procedure for optimizing cycle times

The process cycle has five step lengths, t_{press}, $t_{blowdown}$, t_{ads}, t_{des}, t_{rinse}, and t_{purge}, which must be optimized. The following methodology has been used to perform a grid search to find the optimal combination. In this study, the pressurization and desorption times, t_{press} and $t_{blowdown}$, were determined in the following manner:

Pressurization: The pressurization time t_{press} was fixed at the time taken for the average bed pressure $\left(P_{bed_{avg}}\right)$ to reach 99% of the desired P_{ads} (1.5 bar) at CSS.

$$P_{bed_{avg}}|_{t=t_{press}} = 0.99\ P_{ads} \tag{2.26}$$

Blowdown: The blowdown time $t_{blowdown}$ was determined in a similar manner, but we define a tolerance $tol_{blw} > 0$ as follows:

$$P_{bed_{avg}}|_{t=t_{press}} = (1 + tol_{blw})\ P_{des} \tag{2.27}$$

We investigated the influence of tol_{blw} in section 2.6.1.

For the remaining 3 step lengths, t_{ads}, t_{rinse}, and t_{purge}, we employed a grid search approach. The details have been shown in the form of an algorithm below. The procedure will be referred to as *algorithm 5.1* in the remaining article.

Step 1: Let $i = 1$ and $j = 1$

Step 2: Let $t_{ads} = \mathrm{t}_{\mathrm{ads}}^{\mathrm{i}}$

Step 3: Let $t_{rinse} = t_{rinse}^{j}$

Step 4: To optimize t_{purge}, solve the following one-dimensional optimization problem:

$$Rec_{\mathrm{purge}}^{\mathrm{opt},j} = \max_{t_{\mathrm{purge}}} \left\{ Recovery_{C_3H_6} \mid Purity_{C_3H_6} \geq tol_{\mathrm{purity}} \right\}$$

where tol_{purity} is the minimum propylene purity required.

Step 5: Let $j = j+1$ and go to Step 3

Step 6: From the solutions in Steps 3-5, find optimal t_{rinse} *as follows:*

$$Rec_{\mathrm{purge,rinse}}^{\mathrm{opt}} = \max_{j} \left\{ Rec_{\mathrm{purge}}^{\mathrm{opt},j} \right\}$$

Step 7: Let i = i+*1,* j = *0, and go to Step 2*

where t_{ads}^{j} and t_{rinse}^{j} are discretized adsorption and rinse time, respectively.

To illustrate the grid search approach, an illustration for Steps 2-7 are shown in Figure 2-10 (a) and (b). In Step 4, the optimal purge time t_{purge} was found in the trade-off between purity and recovery, as shown in Figure 2-10 (a). In this example, the tolerance tol_{purity} was set to 99.5% (the point marked 'X' Figure 2-10 (a)), and the corresponding purge time t_{purge} was found to be 84 sec. This optimization step is repeated, changing the

rinse time t_{rinse} in the loop between Steps 3 and 5. After obtaining optimal t_{purge} at different values of t_{rinse}, we proceed to Step 6 where the optimal rinse time (t_{rinse}) is found to maximize the recovery (Figure 2-10 (b)). This sequence of steps is repeated by changing the adsorption time t_{ads} (Steps 2 and 7).

Inlet composition of purge and rinse: As mentioned in section 0, the inlet compositions of the rinse and purge should have the same purity as the product propylene and propane streams respectively (Eq. 5.17 – 5.18). The inlet composition of the rinse was set at the value of the constraint purity of propylene (99.5% here). An initial guess of 100% pure purge stream was used as a starting point. For each t_{ads} the optimal t_{rinse} and t_{purge} combination was found for this iteration. The purity of propane product, corresponding to the optimal point was used as the inlet purge composition in the next iteration. The procedure was repeated till the difference in the compositions of the purge inlet and the outlet propane rich stream at the optima were within ±1.0%.

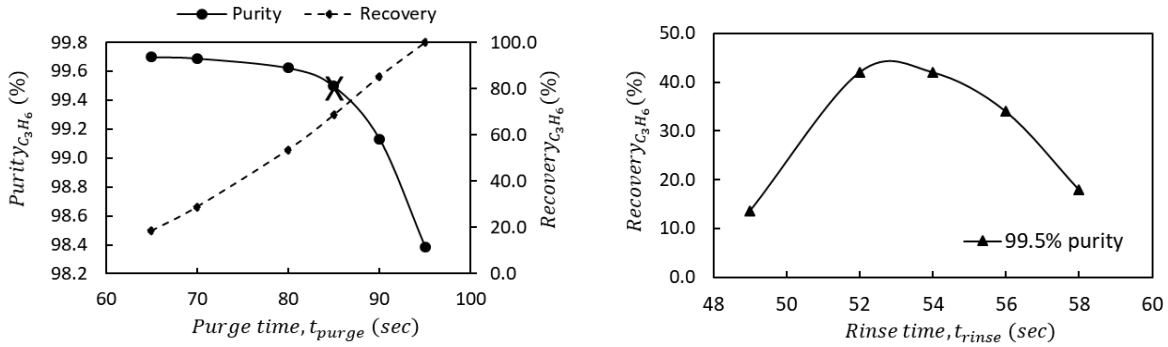

Figure 2-10 - An example of the behavior in a 1.5m packed bed of (a) CSS purity and recovery with increasing length of purge for constant adsorption (12 sec) and rinse times (50 sec) and (b) CSS recovery of propylene with increasing length of rinse for constant adsorption time (19 sec) with the constraint of a minimum purity requirement (99.5%)

2.6 Optimized results

2.6.1 Effect of blowdown time

For a fixed adsorption time, the optimal process performance was found to be significantly affected by the value of $tol_{blw} = (P_{bed_{avg}} - P_{des})/P_{des}$. Figure 2-11(a) shows a comparison of $t_{blowdown}$, the time required by each bed to reach the corresponding tol_{blw}, between the hollow fiber bed and the packed bed when P_{des} = 0.1 bar at the outlet. Figure 2-11(b) shows the same comparison when P_{des} = 0.3 bar. The length of the packed bed is 1.5 m and that of the hollow fiber bed is 3 m.

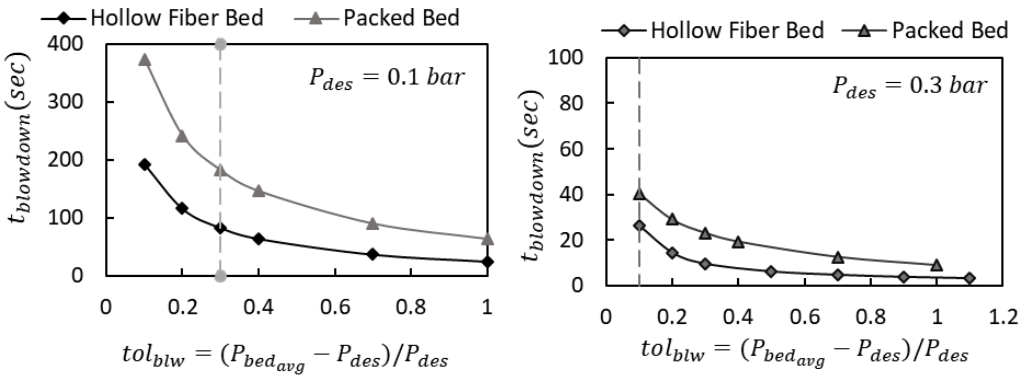

Figure 2-11 - Exponential decrease of time required to blowdown a 3m long hollow fiber bed with increasing gap between average bed pressure and the desired vacuum pressure (P_{des}) applied at the end of the bed. (a) P_{des} =0.1 bar and (b) P_{des} = 0.3 bar.

Irrespective of the P_{des}, there is an exponential increase in $t_{blowdown}$ with decreasing tol_{blw} (Figure 2-11(a)). On the other hand, at the higher value of P_{des} (0.3 bar), $t_{blowdown}$ can be reduced significantly, as can be seen by comparing the values of the vertical axes in Figure 2-11(a) and (b); the time needed to reach tol_{blw} = 0.1 increases by over 6 times (from 30 to 200 seconds) when P_{des} is decreased from 0.3 to 0.1 bar. Besides, the time required to reach the same $P_{bed_{avg}}$ is much higher, nearly twice, in the packed bed

than that in the hollow fiber bed. This can be attributed to the higher pressure drop for the unstructured packing in the packed bed.

Figure 2-12- (a) for the hollow fiber bed and (b) for the packed bed – are plots of the optimum recovery for different values of tol_{blw} Figure 2-12– (c) for the hollow fiber bed and (d) for the packed bed – show the plots for the corresponding productivity at different t_{ads} at P_{des} = 0.1 bar and tol_{purity} = 99.5%. It is observed in Figure 2-12(a) and (b) that decreasing tol_{blw} i.e. continuing the blowdown step for longer duration, the recovery increases. This recovery improvement becomes insignificant at shorter adsorption times when tol_{blw} is lower than 0.3. It can also be seen in Figure 2-12(c) and (d) that the corresponding productivity however, has a concave trend and there is a maximum. To maintain a balance between the improvement in recovery and a loss of productivity, tol_{blw} = 0.3 was chosen as a good trade-off point in all further calculations in this study.

For the case of P_{des} = 0.3 bar it was found that tol_{purity} = 99.5% could not be achieved with significant recovery. Therefore, tol_{purity} was relaxed to 97%. After performing the analysis described previously, it was found that tol_{blw} = 0.1 provided a good balance between the recovery and bed productivity.

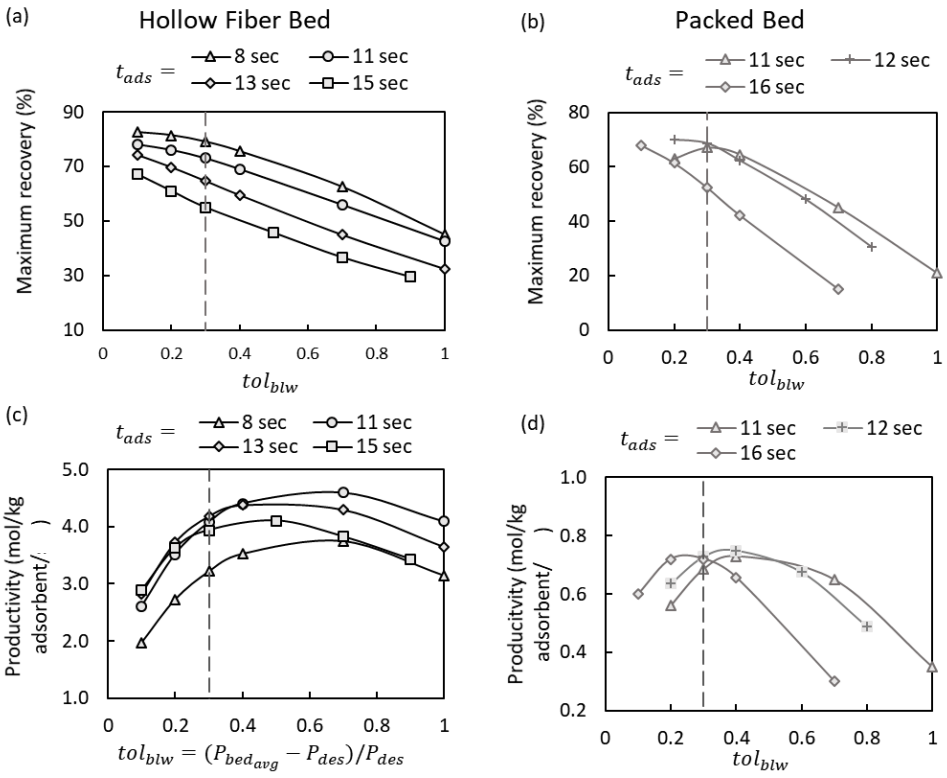

Figure 2-12 - For P_{des} = 0.1 bar with a purity requirement of 99.5%, the optimum recovery and the corresponding productivity is shown for different durations of adsorption, as indicated in the legend. (a), (c) Results for hollow fiber bed and (b),(d) results for packed bed. The length of the packed bed is 1.5 m and that of the hollow fiber bed is 3 m.

2.6.2 Comparison of optimal process performance

As discussed in the previous section, two cases have been considered for comparing the performance of the hollow fiber bed and the packed bed. In the remaining discussion, the two conditions shown in Table 2-7 are considered.

The length of the packed bed is fixed at 1.5m and the hollow fiber bed at 3m. The diameter of each is adjusted such that a volumetric flow rate of 16 SLPM gives a pressure drop of 0.15 bar (discussed previously). The rinse and purge velocities for both beds were the same as the corresponding feed velocity.

Table 2-7 - Conditions for case studies

	P_{des} (bar)	tol_{purity} (%)	tol_{blw}
Case 1	0.1	99.5	0.3
Case 2	0.3	97.0	0.1

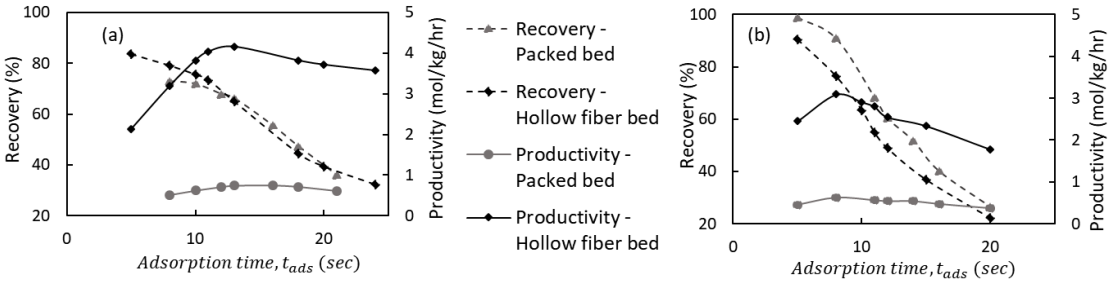

Figure 2-13 – Figure shows maximum recovery and corresponding productivity in the packed bed and the hollow fiber bed for varying adsorption times for (a) Case 1, and (b) Case 2

value of t_{ads} was not straightforward. It can be seen in these figures that decreasing t_{ads} resulted in higher values of propylene recovery. However, the productivity began to drop once a certain minimum t_{ads} had been reached. This is evident in these figures where the bed productivity shows a maximum despite the monotonic increase of recovery with decreasing t_{ads}. This behavior can be attributed to the observation that the requirement of the volume of rinse and purge relative to the feed volume increased as the t_{ads} reached very low values.

Figure 2-13(a) also shows a comparison of the performance of the hollow fiber bed with that of the packed bed for Case 1. We observe the same trend for both hollow fiber and packed beds that the recovery decreases with t_{ads}, while the productivity has a

maximum. However, the productivity of the hollow fiber bed is significantly higher. The maximum productivity of the packed bed is 0.75 mol/kg/hr for a purity of 99.5 % while it is 4.16 mol/kg/hr for the hollow fiber bed, a 5.5 times improvement. The improved performance may be attributed to several factors: the shorter blowdown time requirement (Figure 2-11), the improved mass transfer co-efficient and the ability to mitigate the heat of adsorption/desorption using a fluid through the bore of the hollow fiber bed.

Figure 2-13(b) is a comparison of the performance of the hollow fiber bed and the packed bed for Case 2. The trends observed in the productivity and the recovery with decreasing $t_{ads}$is similar to Case 1 despite the significantly reduced impact of the blowdown time on the overall process time (discussed in Section 2.6.1). The hollow fiber bed still outperforms the packed bed. The maximum value of the productivity is 0.63 mol/kg/hr in the packed bed compared to 3.09 mol/kg/hr for the hollow fiber bed, nearly a 5 fold improvement.

A comparison of Case 1 (Figure 2-13(a)) and 2 (Figure 2-13(b)) shows that the productivity is significantly higher in Case 1. This is because in Case 2 where the desorption pressure P_{des} is higher (0.3 bar), the volume of rinse and purge must be increased to compensate the incomplete desorption, while $t_{blowdown}$ can be reduced (Figure 2-11). On the other hand, the recovery achieved is higher in Case 2, possibly due to the lower purity requirement. The comparison of Figure 2-13(a) and (b) also shows that the maximum recovery also experiences a sharper drop with increasing t_{ads} in Case 2 where P_{des} is higher.

A similar comparison of productivity which is however based on total volume of the bed (mol/m^3-bed/hr) has been shown in Appendix B (Figure S1). Results in terms of volumetric productivity corresponding to Figure 2-14 and Figure 2-15 have also been included in Appendix B. In terms of volumetric productivity (mol/m^3-bed/hr) the hollow fiber bed still shows a nearly 2 fold improvement over the packed bed.

2.6.3 Impact of changing bed length and purge gas velocities on relative performance of packed bed and hollow fiber bed

The following discussion explores the impact of bed length and purge gas velocities on the performance of the packed bed and the hollow fiber bed.

2.6.3.1 Bed length

The recovery and productivity of the optimized process was studied for Case 1 while varying the length of the packed bed to 1m and 2m from the original value of 1.5m. The diameter was simultaneously varied to maintain equal pressure drop of 0.15 bar and volumetric flow rate of 16 SLPM for each case study.

For the packed bed, Pareto plots for optimum recoveries at different t_{ads} and their corresponding productivities are shown in Figure 2-14 (a) for the length of 1m, 1.5m and 2m. As can be seen in this figure, the productivity has a maximum for each bed length. Furthermore, the maximum recovey increases as the bed length increases; a bed length of 1m was found to be too small to allow sufficient separation of the propylene/propane mixture, giving very low recoveries. On the other hand, the longest bed of 2m suffers from low productivity.

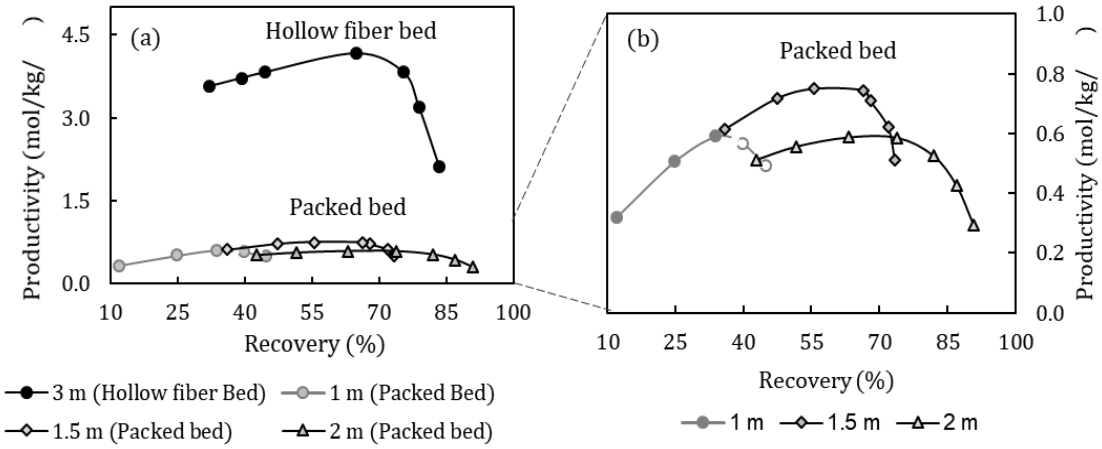

Figure 2-14 - Pareto plot for recovery and productivity tradeoff when desorption pressure is 0.1 bar and the minimum purity requirement is 99.5% for (a) different lengths of the packed bed and 3m long hollow fiber bed (b) magnified view of the packed bed pareto plot.

Figure 2-14 (a) also shows the Pareto plot for the hollow fiber bed (3 m), for comparision with the performance of the packed bed (which is also plotted separately in Figure 2-14(b)). As can be seen from this figure, the hollow fiber bed always achieves higher productivity than all of lengths of the packed bed considerd in this study (1, 1.5, and 2m). .

2.6.3.2 Purge velocity

We analyze the influence of purge velocity for both Case 1 and Case 2. These case studies were repeated for the packed bed and the hollow fiber bed after increasing purge velocity. In the previous sections, the ratio of the purge velocity to the feed velocity was one $\left(\frac{vel_{purge}}{vel_{feed}} = 1\right)$, while in this section, it is increased to two $\left(\frac{vel_{purge}}{vel_{feed}} = 2\right)$. The duration of time required to supply similar volumes of the purge gas decreased proportionately as a result of the increase in purge velocity. In a separate analysis which is not included here, it was observed that, for the same duration of the feed (adsorption) step, the maximum

recovery of propylene decreased significantly when the purge velocity is increased, while the optimum volume of purge gas required for maximum possible recovery did not change significantly.

Figure 2-15(a) shows, in a Pareto plot, the bed productivity versus the maximum recovery for Case 1 in the packed bed and hollow fiber bed. The Pareto plot was generated by varying durations of the feed step. It is seen that in both beds, for the same optimum recoveries the bed productivity is lower at $\frac{vel_{purge}}{vel_{feed}} = 2$ than at $\frac{vel_{purge}}{vel_{feed}} = 1$. Figure 2-15(b) shows the Pareto plot for the packed bed and hollow fiber bed for Case 2. Here, we observe the opposite trend to Case 1 (Figure 15(a)), where the productivity is higher at $\frac{vel_{purge}}{vel_{feed}} = 2$ than at $\frac{vel_{purge}}{vel_{feed}} = 1$. The opposite trend in productivity for Case 1 and 2 can be explained by two competing factors. One factor is that, the duration of the optimal purge step time decreases when the purge velocity is increased. This has the effect of reducing the overall cycle time, and therefore, has a positive effect on the bed productivity. The other factor is that, the maximum recovery achieved decreases when the purge velocity is increased, which has a negative impact on the bed productivity. In Case 1, the blowdown, which takes a long time, was already effective since the desorption pressure was very low ($P_{des} = 0.1\ bar$), and thus reduction in the purge time was insensitive to the overall cycle time. This is not the case in Case 2, where the blowdown was carried out in a shorter time at a higher pressure, and shortening the purge time has a significant impact on the productivity.

In both of Case 1 and 2, it was observed that the productivity of the hollow fiber bed was always substantially higher than that of the packed bed (Figure 2-15(a) and (b)).

The sensitivity analysis on the purge velocity discussed above indicates that nearly 5 times higher productivity is achieved by the hollow fiber bed in comparison to the packed bed.

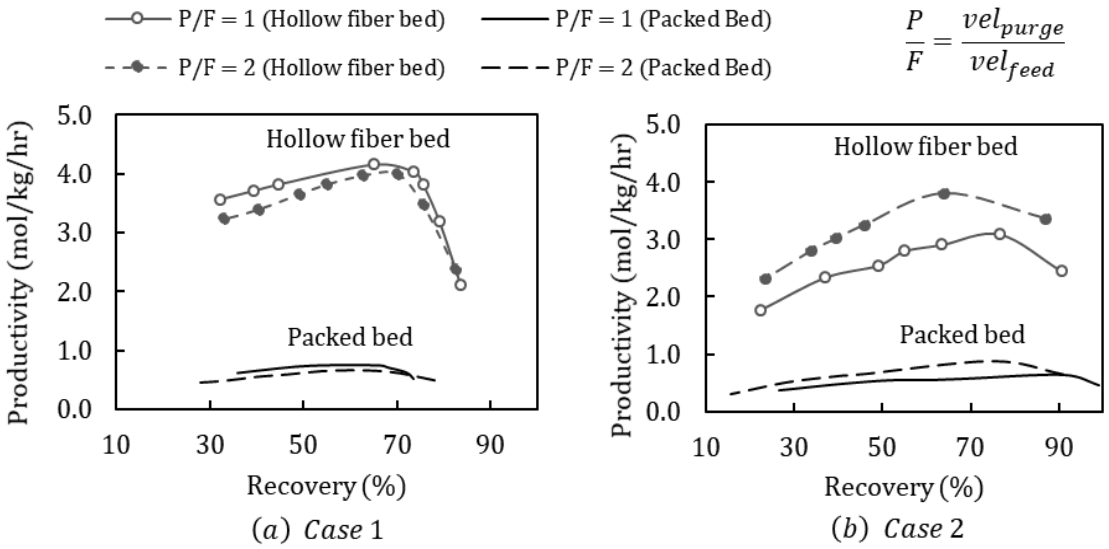

Figure 2-15 - Pareto plot for productivity and recovery tradeoff for different purge velocities in a 1.5m long packed bed and a 3m long hollow fiber bed when (a) desorption pressure is 0.1 bar and the purity requirement is 99.5% (b) desorption pressure is 0.3 bar and the purity requirement is 97%

2.6.4 Comparison of heat transfer efficiency

The efficient transfer of heat from the hollow fiber bed plays a significant role in its improved performance. Figure 2-16 shows the CSS temperature profiles for both beds on a normalized time scale. It is observed that the temperature rise during the adsorption and rinse steps is approximately 13 0C at t/tcycle = 0.18 for the packed bed, while the temperature rises nearly zero for the hollow fiber bed because of the heat removal. In both beds, the temperature decreases in the desorption step due to heat of desorption; in the packed bed, the minimum temperature is approximately 96 0C at t/tcycle = 0.78, while that for the hollow fiber bed is approximately 95 0C at t/tcycle = 0.28. While the temperature

drops sharply in the hollow fiber bed, it returns to the feed temperature of 100 ^{0}C more quickly.

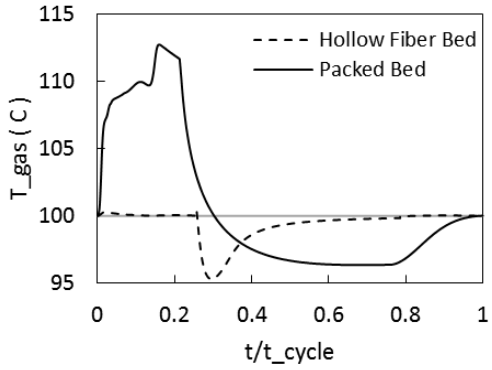

Figure 2-16 - CSS temperature profile at the center of the bed on a normalized time scale for a 1.5m long packed bed and a 3m long hollow fiber bed.

2.7 Conclusion

In this chapter, we compared packed adsorption bed and hollow fiber bed performance through numerical modeling case studies. The two bed models are compared matching the volumetric flowrate and pressure drop with the target of separating of a mixture of propylene and propane on zeolite 13X. A five step single bed cycle was used to compare the cyclic process performance of the two beds.

A detailed parametric comparison showed that the hollow fiber bed outperforms the packed bed in terms of heat and mass transfer coefficient as well as the pressure drop experienced by a flowing fluid. We found that the macropore diffusion was the controlling resistance in both beds, but was lower in the case of the fiber bed. Macropore diffusion control is usually expected for a typical equilibrium based separation such as the current study.

The presence of an impermeable lumen layer allowed for the use of a heating or cooling medium in the hollow fiber bed intensifying heat transfer by three orders of magnitude due to the small distances the heat has to travel in the fiber bed. However, this also means that the adsorbent packing density per unit volume of the hollow fiber bed, already lower due to the inactive polymer phase, was further reduced compared to the packed bed. We confirmed that this drawback would not reverse the advantages of the performance of the hollow fiber bed in our case studies.

For the same recovery and purity, the hollow fiber bed was found to have a productivity (per weight of adsorbent) which was 5 times higher than the packed bed, a significant intensification of the adsorption process. The hollow fiber bed always maintains the advantage of higher productivity, even when the recovery was sacrificed by increasing the purge velocity, for the case when extent of vacuum was lower (P_{des}=0.3 bar). It was also found that the 3m fiber bed always achieves higher productivity than the packed bed for three different lengths (1m, 1.5m, and 2m) considered in this study. Increased productivity per unit mass of adsorbent directly translates to proportionate reduction in the process capital cost when the adsorbent cost accounts for a majority of the expense. Even in terms of total volume of bed required to process similar volumetric flow of a gas mixture the hollow fiber bed consistently showed a 2 fold improvement over the packed bed. These case studies therefore indicate that the hollow fiber bed can intensify the process performance for the equilibrium separation of a gas mixture over the traditional packed bed, particularly when heat management is a critical issue.

2.8 Notation

$\Delta H_{ads,i}$	heat of adsorption of component i (J/mol)	P_{tot}	total pressure (bar)
a	area to volume ratio, pellet or fiber (1/m)	$P_{tot}\|_z^0$	pressure at position z at the beginning of respective step (bar)
Bi_i	Biot no. at the gas pellet (or fiber) interface	q_i	adsorbed phase concentration (mol/kg)
$C_{g,tot}$	total bulk gas phase concentration (mol/m^3)	q_i^*	equilibrium adsorbed phase concentration (mol/kg)
C_{gi}	bulk gas phase concentration (mol/m^3)	Q_{vol}	volumetric flow rate of gas (m^3/s)
$C_{interface,i}$	gas phase concentration at gas/pellet(or fiber) interface (mol/m^3)	R	ideal gas constant
$c_{p,i}$	heat capacity of component I (J/mol/K)	R_{bed}	radius of the bed, packed or hollow fiber (m)
$C_{p,T}$	total constant pressure heat capacity of gas (J/mol/K)	R_c	radius of crystal (m)
$C_{p,tot}$	total pellet gas phase concentration (mol/m^3)	Re	Reynold's number.
$C_{p,w}$	heat capacity of wall (J/kg/K)	r_{fs}	radius of Happel's free surface (m)
$C_{p,bf}$	heat capacity of fluid in the bore (J/kg/K)	R_{hyd}	hydraulic radius of fiber (m)
c_{pf}	heat capacity of fiber (J/kg/K)	R_{ID}	inner radius of a single fiber (m)
C_{pi}	macropore gas phase concentration (mol/m^3)	R_{OD}	outer radius of a single fiber (m)
$C_{v,ads,i}$	heat capacity of adsorbed phase (J/mol/K)	R_p	radius of pellet (m)
$c_{v,i}$	constant volume heat capacity of component i (J/mol/K)	Sc_i	Schmidt no.
$C_{v,T}$	total constant volume heat capacity of gas (J/mol/K)	Sh_i	Sherwood no.
$D_{ax,i}$	mass axial dispersion coefficient (m^2/s)	t	time (sec)
$D_{c,0A,I}$, $D_{c,0B,i}$	pre-exponential factors for crystal diffusivity (m2/s)	T_{amb}	temperature of ambient (K)
$D_{c,i}$	crystal diffusivity (m^2/s)	T_f	temperature of fiber (K)
$D_{fp,i}$	macropore diffusivity inside fiber (m^2/s)	T_g	gas temperature (K)
$D_{p,i}$	macropore diffusivity inside pellet (m^2/s)	$time_{cycle}$	total time to complete 1 cycle (sec)

$E_{A,}$, $E_{B,i}$	activation energy for crystal diffusion (J/mol)	T_p	solid phase temperature (pellet) (K)
h_f	Gas film heat transfer coefficient between gas and solid phase ($W/m^2/K$)	t_{step-x}	total time required for step x (x = adsorption, blowdown etc)
h_w	film heat transfer coefficient between gas and wall ($W/m^2/K$)	t_w	thickness of the wall (m)
h_{bf}	film heat transfer coefficient between fiber and fluid in the bore ($W/m^2/K$)	T_w	wall temperature (K)
$K_{baràPa}$	conversion factor for pressure (bar to Pa)	U	overall heat transfer coefficient from wall to ambient ($W/m^2/K$)
$K_{conductivity,i}$	thermal conductivity of pure component i (W/m2.K)	u_{g0}	superficial gas velocity (m/s)
$k_{g,i}$	gas film mass transfer coefficient (m/s)	u_{gi}	interstitial gas velocity (m/s)
$k_{gas,i}$, $k_{macro,i}$, $k_{micro,i}$, $k_{gas,j}$	LDF mass transfer coefficients (1/sec)	v_{fib}	volume fraction of bed occupied by the fibers
K_{mix}	thermal conductivity of gas mixture ($W/m^2.K$)	v_{purge}	velocity of the purge gas at inlet (m/s)
L	length of the bed (m)	v_{rinse}	velocity of the rinse gas at inlet (m/s)
M_p , M_b	pseudo-valve coefficients during pressurization, blowdown	w_s	weight fraction of adsorbent in the fiber
MW_i	molar weight of component i (kg/mole)	$y_{ads,i}$, $y_{rinse,i}$, $y_{purge,i}$	
N_i	flux of species i being removed from bulk gas phase (per unit volume of bulk gas)	$y_{ads,j}$	mole fraction in the inlet
P_{ads} , P_{des}	adsorption and desorption pressure (bar)	y_i	mole fraction
p_i	partial pressure (bar)	z	axial distance along column (m)
Pr	Prandtl no.		

2.8.1 Greek Letters

μ_g	viscosity of gas (Pa.s)	ρ_b	bulk density of the packed bed (kg/m^3)

α_w	ratio of internal surface area to the volume of the column wall (1/m)	ρ_f	total density of fiber (including fiber void volume) (kg/m^3)
α_{wl}	ratio of the logarithmic mean surface area of the column shell to the volume of the column wall (1/m)	ρ_g	density of gas (kg/m^3)
ε	porosity of bed	ρ_p	total density of fiber (including pellet void volume) (kg/m^3)
ε_f	porosity of fiber	ρ_w	density of wall (kg/m^3)
ε_p	porosity of pellet	ρ_{bf}	density of bore fluid (kg/m^3)
λ	axial heat dispersion (W/m.K)	τ	tortuosity of pellet
λ_f	thermal conductivity of fiber (W/m.K)	τ_f	tortuosity of fiber

2.9 References

[1] Van Gerven, T.; Stankiewicz, A. Structure, energy, synergy, time - The fundamentals of process intensification. *Ind. Eng. Chem. Res.* **2009**, *48*, 2465-2474.

[2] Dąbrowski, A. Adsorption—from theory to practice. *Adv. Colloid Interface Sci.* **2001**, *93*, 135-224.

[3] Li, J.-R.; Kuppler, R. J.; Zhou, H.-C. Selective gas adsorption and separation in metal–organic frameworks. *Chem. Soc. Rev.* **2009**, *38*, 1477-1504.

[4] Rezaei, F.; Mosca, A.; Webley, P.; Hedlund, J.; Xiao, P. Comparison of traditional and structured adsorbents for CO_2 separation by vacuum-swing adsorption. *Ind. Eng. Chem. Res.* **2010**, *49*, 4832-4841.

[5] Rezaei, F.; Webley, P. Optimum structured adsorbents for gas separation processes. *Chem. Eng. Sci.* **2009**, *64*, 5182-5191.

[6] Lively, R. P.; Chance, R. R.; Kelley, B.; Deckman, H. W.; Drese, J. H.; Jones, C. W.; Koros, W. J. Hollow fiber adsorbents for CO_2 removal from flue gas. *Ind. Eng. Chem. Res.* **2009**, *48*, 7314-7324.

[7] Rezaei, F.; Grahn, M. Thermal management of structured adsorbents in CO_2 capture processes. *Ind. Eng. Chem. Res.* **2012**, *51*, 4025-4034.

[8] Akhtar, F.; Andersson, L.; Ogunwumi, S.; Hedin, N.; Bergström, L. Structuring adsorbents and catalysts by processing of porous powders. *J. Eur. Ceram. Soc.* **2014**, *34*, 1643-1666.

[9] Lively, R., Chance, R.R., Koros, W.J., Deckman, H. and Kelley, B.T. Sorbent fiber compositions and methods of temperature swing adsorption *U.S. Patent 8133308* **2012**.

[10] Fan, Y.; Labreche, Y.; Lively, R. P.; Jones, C. W.; Koros, W. J. Dynamic CO_2 adsorption performance of internally cooled silica-supported poly (ethylenimine) hollow fiber sorbents. *AIChE J.* **2014**, *60*, 3878-3887.

[11] DeWitt, S. J.; Sinha, A.; Kalyanaraman, J.; Zhang, F.; Realff, M. J.; Lively, R. P. Critical Comparison of Structured Contactors for Adsorption-Based Gas Separations. *Annu. Rev. Chem. Biomol. Eng.* **2018** 9:1, 129-152.

[12] Narin, G.; Martins, V. F.; Campo, M.; Ribeiro, A. M.; Ferreira, A.; Santos, J. C.; Schumann, K.; Rodrigues, A. E. Light olefins/paraffins separation with 13X zeolite binderless beads. *Sep. Purif. Technol.* **2014**, *133*, 452-475.

[13] Mathias, P. M.; Kumar, R.; Moyer, J. D.; Schork, J. M.; Srinivasan, S. R.; Auvil, S. R.; Talu, O. Correlation of Multicomponent Gas Adsorption by the Dual-Site Langmuir Model. Application to Nitrogen/Oxygen Adsorption on 5A-Zeolite. *Ind. Eng. Chem. Res.* **1996**, *35*, 2477-2483.

[14] Happel, J. Viscous flow relative to arrays of cylinders. *AIChE J.* **1959**, *5*, 174-177.

[15] Lopes, F. V.; Grande, C. A.; Rodrigues, A. E. Activated carbon for hydrogen purification by pressure swing adsorption: Multicomponent breakthrough curves and PSA performance. *Chem. Eng. Sci.* **2011**, *66*, 303-317.

[16] Lopes, F. V. S.; Grande, C. A.; Ribeiro, A. M.; Loureiro, J. M.; Evaggelos, O.; Nikolakis, V.; Rodrigues, A. E. Adsorption of H2, CO_2, CH_4, CO, N_2 and H_2O in Activated Carbon and Zeolite for Hydrogen Production. *Separation Science and Technology* **2009**, *44*, 1045-1073.

[17] Da Silva, F. A.; Silva, J. A.; Rodrigues, A. E. A general package for the simulation of cyclic adsorption processes. *Adsorption* **1999**, *5*, 229-244.

[18] Da Silva, F. A.; Rodrigues, A. E. Propylene/propane separation by vacuum swing adsorption using 13X zeolite. *AIChE J.* **2001**, *47*, 341-357.

[19] Kalyanaraman, J.; Fan, Y.; Lively, R. P.; Koros, W. J.; Jones, C. W.; Realff, M. J.; Kawajiri, Y. Modeling and experimental validation of carbon dioxide sorption on hollow fibers loaded with silica-supported poly (ethylenimine). *Chem. Eng. J.* **2015**, *259*, 737-751.

[20] Wakao, N.; Funazkri, T. Effect of fluid dispersion coefficients on particle-to-fluid mass transfer coefficients in packed beds: correlation of Sherwood numbers. *Chem. Eng. Sci.* **1978**, *33*, 1375-1384.

[21] Asimakopoulou, A.; Karabelas, A. A study of mass transfer in hollow-fiber membrane contactors—The effect of fiber packing fraction. *J. Membr. Sci.* **2006**, *282*, 430-441.

[22] Process Systems Enterprise, gPROMS, www.psenterprise.com/gproms, **1997-2018**

CHAPTER 3. USING SITE HETEROGENEITY IN METAL-ORGANIC FRAMEWORKS WITH BIMETALLIC OPEN METAL SITES FOR OLEFIN/PARAFFIN SEPARATIONS

Parts of this chapter have been adapted from 'You, W.; Sen, T.; Kawajiri, Y.; Realff, M. J.; Sholl, D. S., Using Site Heterogeneity in Metal-Organic Frameworks with Bimetallic Open Metal Sites for Olefin/Paraffin Separations. Submitted to *ACS Appl. Nano Mater.*' This work was done in collaboration with Wenqin You, where she contributed to the molecular simulation aspects, whereas I contributed to the process simulation and optimization aspects. We both were equal contributors to the submitted manuscript.

3.1 Introduction

Adsorption in porous materials is a widely applicable technique for gas storage and chemical separations.[1-6] Adsorbents can be described as homogeneous if the adsorption energies of all their sites are (approximately) equivalent or heterogeneous if adsorption sites with a range of energies are available. Although common industrial adsorbents such as activated carbons are spatially and energetically heterogeneous, it is widely thought that homogeneous adsorbents can allow higher performance than heterogeneous materials. An influential study supporting this view was work by Bhatia and Myers[7], who showed in quite general terms that the storage capacity of an adsorbent is optimized for homogeneous adsorbents. Stated in a negative sense, Bhatia and Myers argued that heterogeneity is always detrimental for the storage capacity of an adsorbent. Energetic heterogeneity in an

adsorbent also leads to the heat of adsorption being temperature dependent, which can complicate process design.[8]

Metal-organic frameworks (MOFs) have drawn much attention as adsorbents because of their diverse and controllable structures. One strategy to diversify the range of MOFs that can be made is to synthesize materials that mix either organic linkers or metal centers.[9-15] Examples are known where mixed metal MOFs have enhanced stability relative to the pure metal materials.[16-17] Although these strategies can lead to large numbers of distinct materials, the discussion of homogeneous and heterogenous adsorbents above might suggest that mixed linker or metal MOFs will not perform as well as MOFs with a single linker and metal for adsorption applications. Our aim in this chapter is to examine whether this notion is correct. A specific application, adsorptive separation of ethylene and ethane by metal-organic frameworks (MOFs) with open metal sites (OMS), was chosen to study this question. The selective adsorption of ethylene over ethane can be achieved by MOFs with OMS because of the π-π interactions between olefin double bonds and OMS.[1, 18-25]

One family of MOFs with OMS available for ethylene/ethane separation is M-BTC, which has M_2 paddlewheel units with dimeric OMS.[26-29] Cu-BTC is the most well-known example of these materials. We have previously used Density Functional Theory (DFT) calculations to characterize the binding energy of ethylene, ethane and other small molecules in a wide range of M-BTC MOFs.[30-31] A key conclusion from that work was that the species of metals making up OMS plays a more important role than pore topology or linker functionality. A number of experimental studies have shown that M-BTC MOFs with mixed metals can be synthesized.[11, 32-33] Motivated by these observations and by the

large number of mixed metal M-BTC MOFs that can in principle exist, we aimed to understand whether mixed metal materials could ever outperform pure metal M-BTC MOFs for ethylene/ethane separations.

Evaluating the performance of an adsorbent for a desired separation is challenging. A variety of simplified metrics, typically based on single component adsorption isotherms, have been proposed for this task.[34-35] Shortcut models for specific processes such as pressure swing adsorption (PSA) have been developed.[36] Unfortunately, the success of these approaches in predicting the results of full process models, at least in the sense of correctly ranking a list of materials, is limited.[36-38] Park et al. demonstrated that gaps between the simplified and the full process models still exist after the process models haven been combined with molecular modeling strategies.[39] For this reason, we examined the performance of M-BTC MOFs for ethylene/ethane separations using both simplified models and detailed process models.

3.2 Methods (sections 3.2.1 to 3.2.3 are the contributions of W. You)

3.2.1 Geometry optimization for the modelled materials

For the homogeneous adsorbents, 12 metal-substituted M-BTCs (M = Cr, Mo, Fe, Ru, Ni, Cu, Mg, Ti, V, Mn, Co, and Zn) were studied, including seven experimentally reported materials (M = Cr,[40] Mo,[41] Fe,[42] Ru,[43] Ni,[44] Cu,[45] Zn[46]) and five hypothetical materials (M = Mg, Ti, V, Mn, and Co). The initial optimized structures for M-BTCs were taken from our previous work.[31] We constructed initial structures for mixed metal materials (MM'-BTC) by replacing one of the metals with another metal species (M') in each dimer

in M-BTC. Each mixed metal MM'-BTC was then energy-minimized in the absence of adsorbed molecules using Density Functional Theory (DFT) calculations.

During geometry relaxation of MOFs, both the lattice parameters and atomic positions were simultaneously optimized using a plane-wave cutoff energy of 520 eV and Γ-point sampling for Brillouin zone integration. All calculations of binding energy and geometry optimization of MOF materials were performed using spatially periodic DFT using the Vienna Ab initio Simulation Package (VASP)[47] with the PBE-D3 functional.[48] Hubbard U corrections are used for open shell 3d or 4d transition metals with the specific U value for each metal taken from earlier work.[49-51] Antiferromagnetic ordering and a high-spin electronic state were used for each dimer OMS.[28, 52] Our earlier work indicated by comparison with available experimental data that these choices lead to accurate predictions for the structure and molecular binding energies of these MOFs.[30] Using a quasi-Newton method, geometries were relaxed until the force on each atom is smaller than 0.03 eV/Å. The optimized lattice constants for 12 M-BTCs and 11 mixed-metal MM'-BTCs are tabulated in the Appendix C. During calculations of molecular binding energies, all atomic positions of the MOF material and guest molecules were relaxed. The binding energies of adsorbed molecules (ethylene and ethane) were defined by

$$-\Delta E = E_{ads+MOF} - E_{MOF} - E_{ads} \tag{3.1}$$

where $E_{ads+MOF}, E_{MOF},$ and E_{ads} represent the energy of a MOF with an adsorbed molecule, the energy of the empty MOF, and the energy of the adsorbate in the gas phase, respectively. With this convention, ΔE is positive when adsorption is exothermic.

3.2.2 Predicting adsorption isotherms in MOFs with OMS

The primary inputs for process models of equilibrium adsorption-based separations are the adsorption isotherms for species of interest. Grand Canonical Monte Carlo simulations (GCMC) using classical force fields (FFs) are a useful technique for generating isotherms in crystalline materials such as MOFs.[53-54] GCMC-simulated adsorption isotherms have generally given good agreement with experiments for small and non-polar adsorbates.[55-56] Generic FFs, however, are inadequate for describing adsorption in OMS MOFs.[57-58] Specialized force fields that address this problem for some specific molecules in Cu-BTC have been developed,[19, 22, 59] but force fields suitable for the full range of metal species for OMS MOFs of interest in this work are not currently available.

Since FF-based GCMC simulations cannot accurately describe OMS and are not useful for our materials, adsorption models derived primarily from DFT data were developed. The adsorption of small molecules in M-BTC can be divided into chemisorption on OMS and physisorption of small molecules in windows or cages. We therefore used a dual-site Langmuir (DSL) model for single component adsorption and the competitive DSL model for binary mixture adsorption:

$$n_A = \frac{n_{oms}^A * K_{oms}^A * P_A}{1 + K_{oms}^A * P_A + K_{oms}^B * P_B} + \frac{n_{phy}^A * K_{phy}^A * P_A}{1 + K_{phy}^A * P_A + K_{phy}^B * P_B} \tag{3.2}$$

Here $n_{oms}^{A(B)}$ and $n_{phy}^{A(B)}$ represent the saturation capacity of species A (B) at OMS and physisorption sites, respectively. $K_{oms}^{A(B)}$ and $K_{phy}^{A(B)}$ are the Langmuir equilibrium constants of species A (B) at the same two kinds of sites. For a unit cell of Cu-BTC, we

assume all OMS are available for chemisorption, so $n_{oms}^{A(B)}$ is 4.96 mmol/g. Since FFs of ethylene and ethane in Cu-BTC that accurately describe interactions with OMS are available,[22, 59] we used GCMC calculations with these FFs to predict the total adsorption uptake at saturation $n_{total}^{A(B)}$ in Cu-BTC. We then obtain $n_{phy}^{A(B)}$ by subtracting $n_{oms}^{A(B)}$ from $n_{total}^{A(B)}$ by assuming that one molecule adsorbs at each OMS at saturation and that the physisorption component of adsorption is the same as in Cu-BTC in every M-BTC MOF.

3.2.2.1 Adsorption Equilibrium Constant at OMS: $K_{oms}^{A(B)}$

To model adsorption at OMS, we adapt methods for using partition functions to derive Langmuir equilibrium constants that have been introduced in several studies.[60-63] Briefly, the Langmuir equilibrium constant is given by

$$K = e^{(-\frac{\Delta G}{RT})} \tag{3.3}$$

where ΔG is the Gibbs free energy of adsorption. The enthalpy change during adsorption, ΔH, is assumed to be equal to the binding energy of a species from DFT, *B.E.*, giving

$$\Delta G = \Delta H - T * \Delta S \approx -B.E. - T * \Delta S \tag{3.4}$$

The entropy change, ΔS, is

$$\Delta S = Rln\frac{Q_{adsorbed}}{Q_{gas}} \tag{3.5}$$

where Q_{gas} and $Q_{adsorbed}$ are the partition functions of the adsorbing species in the gas phase and the adsorbed phase, respectively. Q_{gas} takes all degrees of freedom (vibration, translation, and rotation) into account. $Q_{adsorbed}$ is calculated from the discrete vibrational energy levels available to the adsorbed molecule considered as a bound system.[63-65] This gives

$$K \approx b_0 * e^{\frac{B.E.}{RT}} \tag{3.6}$$

where $b_0 = \frac{Q_{adsorbed}}{Q_{gas}}$. Values of b_0 were calculated with DFT as described in Appendix C.

3.2.2.2 Adsorption Equilibrium Constant for Physisorption sites: $K_{phy}^{A(B)}$

Because physisorption includes contributions from multiple locations in the MOF's pores, it is challenging to reliably establish the physisorption parameters in Eq. (1) using DFT. Instead, we chose to fit K_{phy} using experimental adsorption data. We used experimental data for Cu-BTC from Jorge et al.[59] A complication in comparing Eq. (1) with experimental data is that we cannot assume all OMS are available (i.e. solvent-free) experimentally.[66] For the ethylene data from Jorge et al., $n_{oms}^{C_2H_4}$ in the experimental material was treated as an unknown, while $K_{oms}^{C_2H_4}$ and $n_{phy}^{C_2H_4}$ were calculated as described above. The same procedure was followed to compute parameters for ethane. Further details are given in Appendix C.

Table 3-1 lists the parameters of ethylene and ethane at OMS and physisorption sites calculated in Cu-BTC. We extended the information above to the full set of M-BTC

materials by making two assumptions. First, we ass umed that all OMS are available in every material. Second, we assumed that the physisorption parameters in every material are identical to those for Cu-BTC. Although this is an approximation, this assumption is reasonable because physisorption is dominated by dispersion interactions with the organic components of each MOF, not by specific interactions with metal sites. As described above, however, adsorption parameters for chemisorption on OMS were determined from DFT calculations for each distinct OMS.

Table 3-1 - Parameters of ethylene and ethane at OMS and physisorption sites calculated in Cu-BTC.

Adsorption Sites	OMS			Physisorption		
Parameters	n_{max} (mmol/g)	b_0	$B.E.$ (kJ/mol)	n_{max} (mmol/g)	b_0	$B.E.$ (kJ/mol)
C_2H_4	4.96	9.0E-7	40.0	7.84	4.4E-4	22.1
C_2H_6	4.96	5.8E-5	24.0	5.94	7.7E-5	24.9

3.2.3 Methods for Process Modelling

3.2.3.1 Full Process Model

To study the performance of different adsorbents at a process scale we used a hollow fiber-based solid sorbent configuration as described recently by Sen et al.[67-68] The hollow fiber configuration relies on solid sorbents embedded in a porous polymeric hollow fiber matrix. Several identical fibers are assembled inside a module, which resembles a shell and tube heat exchanger (shown in

Figure 3-1). This structured contactor results in improvements in pressure drop and mass transfer compared to a packed bed.[69] The bore of the hollow fiber has an impermeable

lumen layer that allows the flow of a cooling/heating medium to mitigate the temperature of operation of the process despite the heat of adsorption/desorption.[68]

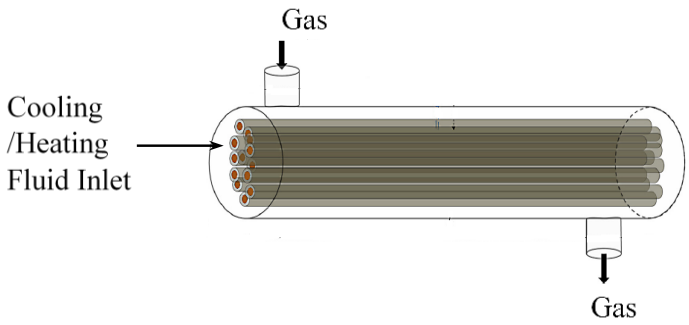

Figure 3-1 - Schematic of a hollow fiber module.[68]

To compare the performance of different adsorbents we used a standard 4-step Vacuum Pressure Swing Adsorption (VPSA) cycle as shown in Figure 3-2.[70] The steps include pressurization, high-pressure feed, intermediate pressure blowdown, and low-pressure evacuation. We assume the feed is an equimolar mixture of ethylene and ethane. The product of interest, ethylene, is collected during the evacuation step. Details of the process model are included in Appendix C.

Preliminary investigations revealed that the performance of OMS MOFs is sensitive to the temperature of adsorption but that the temperature swing during desorption and the adsorption pressure do not impact the overall performance as significantly. Therefore, we only considered pressure swings between 1 bar and partial vacuum with a constant temperature of operation for the entire cycle. The level of vacuum and operating temperature were variables that were optimized. Each process was evaluated based on purity, recovery, energy consumption and productivity of the ethylene as defined in the

Appendix C in Equations C12-C16. Three components of energy consumption were evaluated, namely the energy of pressurization-depressurization, the energy to heat the feed to the operating temperature, and the energy supplied/removed by the heating/cooling fluid in the hollow fiber bore. It was assumed that the feed is available at an ambient temperature of 25 ˚C.

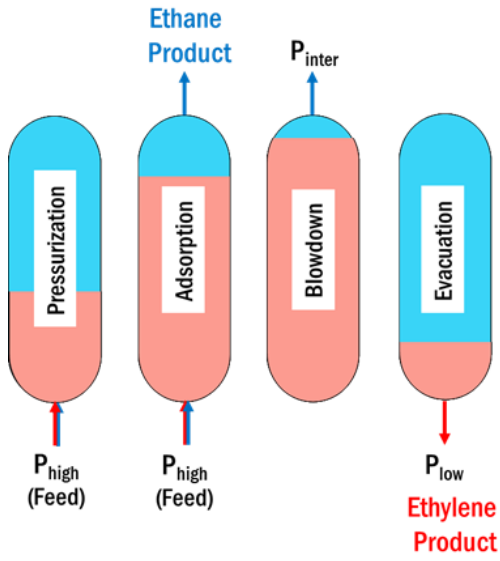

Figure 3-2. Schematic depiction of the 4-step Vacuum Pressure Swing Adsorption (VPSA) cycle.

3.2.3.2 Idealized Process Model

While the full-scale VPSA model provides a relatively accurate estimate of system performance, simulations with this model are time-consuming since it involves solving a system of partial differential algebraic equations and convergence to cyclic steady state (CSS). To generate a faster first-pass comparison of available adsorbents, an idealized simple process model has been proposed previously.[71] The idealized model assumes a simple two-step saturation-desaturation cycle with no mass transfer limitations (see Figure

3-3). It is assumed that the system is always at equilibrium and that the cycle allows 100% recovery of the adsorbed phase. These assumptions enable estimation of the purity and energy consumption of the adsorbed phase from a simple system of non-linear algebraic equations (shown in the Appendix C in the Equations E17-E20). We note that this idealized model is just one of several approaches that have been proposed recently as "shortcut" models for VPSA.[36, 72-73]

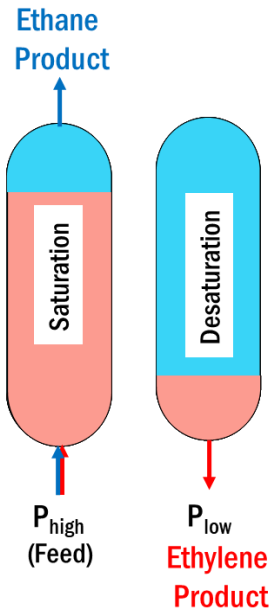

Figure 3-3 - Schematic depiction of the idealized process model.

3.3 Results and Discussion

3.3.1 Optimization of the Adsorption Process

The simplified model defined above only requires the operating conditions (temperature and pressure) and the isotherm of the material as input parameters. We

considered operating temperatures of 50-300 °C, low-pressure levels of 0.1-0.8 bar, and adsorption pressures of 1-1.5 bar. The high-pressure level did not have a strong impact on overall performance. From section 3.3.2 onwards, we restricted the maximum allowable operating temperature to 180 °C because temperatures above this could create issues of vaporization of the cooling/heating fluid in the bore of the fiber.

The simplified model assumes 100% recovery and full utilization of the bed (i.e. maximum productivity). The only process objectives are the process purity and energy consumption. We used a Non-dominated Sorting Algorithm (NSGA-II)[74] to compute a dual-objective Pareto front for each material that we evaluated. We ran the algorithm for a maximum of 10 generations with a population size of 200 per generation. NSGA-II is a stochastic approach whose results depend on the initial seed population. We have performed our analysis using a single seed population and have drawn conclusions based on the assumption that the initial seed has insignificant impact on the final Pareto plot obtained.

In addition to the operating conditions mentioned above, the detailed process model has other degrees of freedom, including the intermediate pressure level during blowdown and the duration of each cycle step. In addition to process purity and energy consumption, the process productivity and recovery are optimization objectives. We performed a three-objective Pareto optimization for all materials evaluated using the full-order cycle model. The optimization objectives are purity, recovery, and energy consumption. Due to increased model complexity, a surrogate-assisted optimization method (SOCEMO)[75] was used to reduce computational cost. The stopping criteria in this approach is the maximum number of function evaluations allowed, which was set to 300.

The following sections demonstrate the optimization procedure for both models, using the isotherm parameters of Zn-BTC (OMS binding energy of ethylene = 79 kJ/mol, ethane = 38 kJ/mol).

3.3.1.1 Case Study for the Simplified Model: Zn-BTC

Figure 3-4a shows the purity-energy consumption Pareto front obtained using the simplified model for Zn-BTC. The circles are color-coded from light to dark to indicate increasing purity. This enables easier visualization of estimated optimal value of the input parameters (P_{low}, T, and P_{high}) corresponding to each region of the Pareto curve (Figure 3-4b and Figure 3-4c). For this material, high purity can only be obtained with temperatures of 200-250 ˚C. Similar calculations showed that this optimal temperature range is highly metal-center dependent for OMS MOFs because of the large range of site binding energies among the materials we considered. As expected, energy consumption increases with increasing purity. Nearly 50% of the energy consumption for Zn-BTC is a result of heating the feed from an ambient temperature of 25 ˚C. The energy consumption due to de/re-pressurization is similar to results reported previously for a VSA cycle.[71] Although lowering the operating temperature reduces energy consumption, it also greatly affects the maximum purity that can be achieved for the simplified model using Zn-BTC.

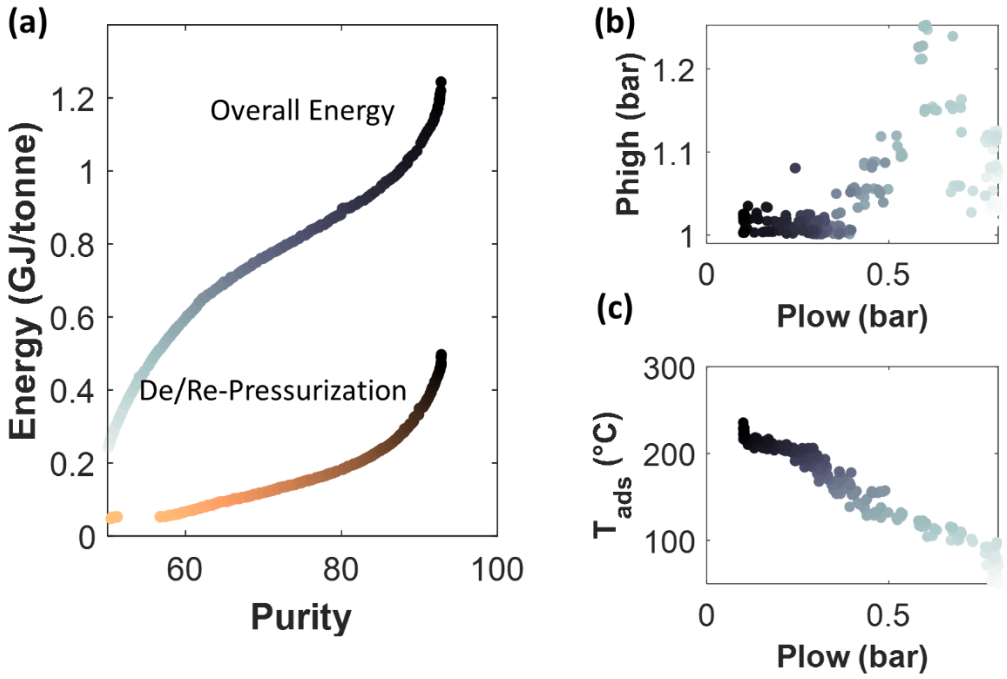

Figure 3-4 - (a) Energy - purity Pareto curve in the simple model for Zn-BTC, with the corresponding independent variables (b) high pressure and (c) temperature and low pressure. Darker circles represent a higher purity. In (a), the contribution of the energy of de/re-pressurization to the overall energy is shown.

3.3.1.2 Case Study for the Full Process Model: Zn-BTC

The results of applying the full process model to Zn-BTC are illustrated Figure 3-5. Optimization of the full process model results in a three-parameter Pareto front. For ease of visualization, we focused on a two-parameter view of purity and recovery (Figure 3-5a). As in section 3.3.1.1, we color-coded circles from light to dark to represent increasing purity. Figure 3-5b shows the two-parameter view of purity and energy consumption color-coded for increasing purity. Figure 3-5c shows the values of two of the input parameters, temperature and low pressure, corresponding to each point on the Pareto surface.

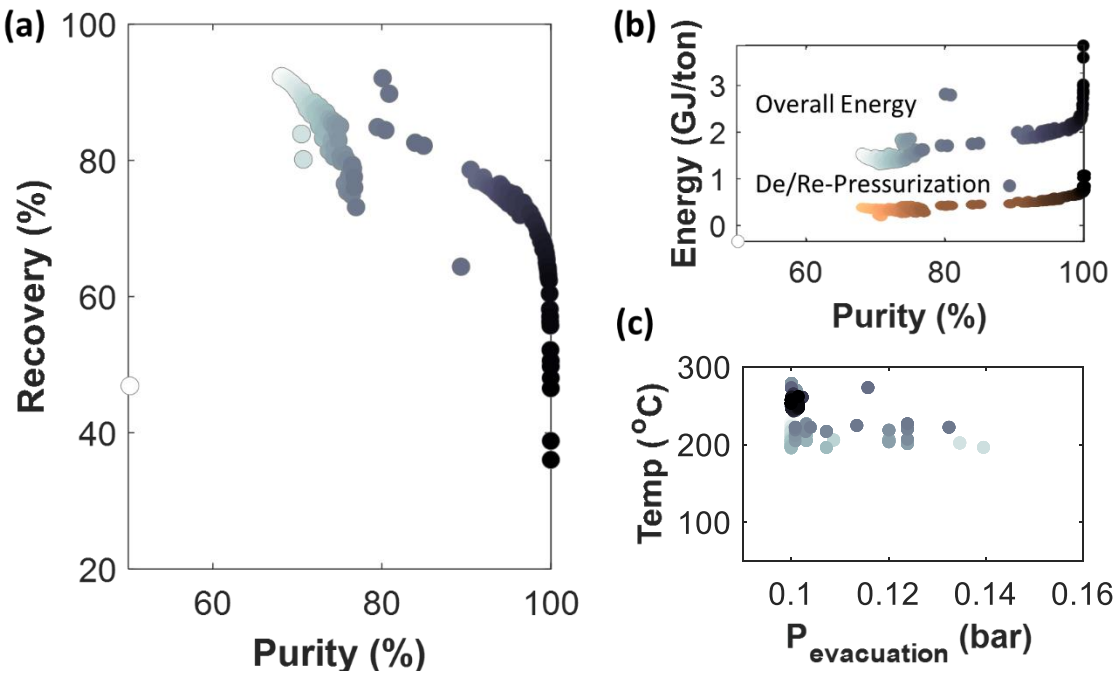

Figure 3-5 - Pareto front for (a) recovery-purity and (b) energy-purity optimization in the full process model for Zn-BTC, with the corresponding variables of (c) temperature and evacuation pressure. Darker circles represent a higher purity.

As predicted by the simple model, the highest purity in Zn-BTC is achieved at very high operating temperatures (200-280 ˚C). The energy consumption due to heating of the feed from an ambient temperature of 25 ˚C results accounts for ~50% of total energy consumed, similar to the simple model. Although the simple model provides a very good general estimate of optimal operating conditions and performance, it underestimates the maximum possible purity and the energy consumed.

3.3.2 Performance of Pure Metal MOFs

We investigated the impact of the binding strength of the metal centers on the separation performance of pure metal MOFs. It can be hypothesized that a weak binding of ethylene will result in poor selectivity and therefore poor performance. On the other

hand, a strong binding energy at the metal center will create problems for desorption and negatively impact separation performance. To visualize the effect of metal binding energy on MOF performance, we generated a map of separation performance for the entire range of feasible binding energies. The feasible binding energy range for the OMSs was estimated from DFT data of the 12 pure metal-substituted M-BTCs (Mo, Cr, Cu, Ni, Ru, Ti, V, Fe, Co, Mg, Mn, and Zn) giving 38-79 kJ/mol for ethylene and 20-41 kJ/mol for ethane, respectively. The reduced computational complexity of the simple model is beneficial for thoroughly mapping the entire range of possible binding energies. We used a grid of 30×30 uniformly distributed hypothetical binding energies of ethylene and ethane within the range specified above. Isotherms and subsequently optimal process performance for each of the 900 binding energy pairs were then evaluated using the simplified process model. The results are discussed in section 3.3.2.1.

It is necessary to check the conclusions drawn from the simple model against the more rigorous full-order process model. However, generating 900 optimized data points using the full model would be very time consuming. Therefore, we generated performance maps of a uniformly distributed 8×8 uniformly grid of binding energy pairs using the full model. The main aim of these calculations was to evaluate whether trends predicted by the simple model also hold under more rigorous evaluation. These results are discussed in section 3.3.2.2.

3.3.2.1 Purity Contour for 12 Pure MOFs in the Simple Model

Figure 3-6a is the optimum purity contour plot for the full range of binding energy combinations with the constraint of 1 GJ/ton energy consumption and an assumption of

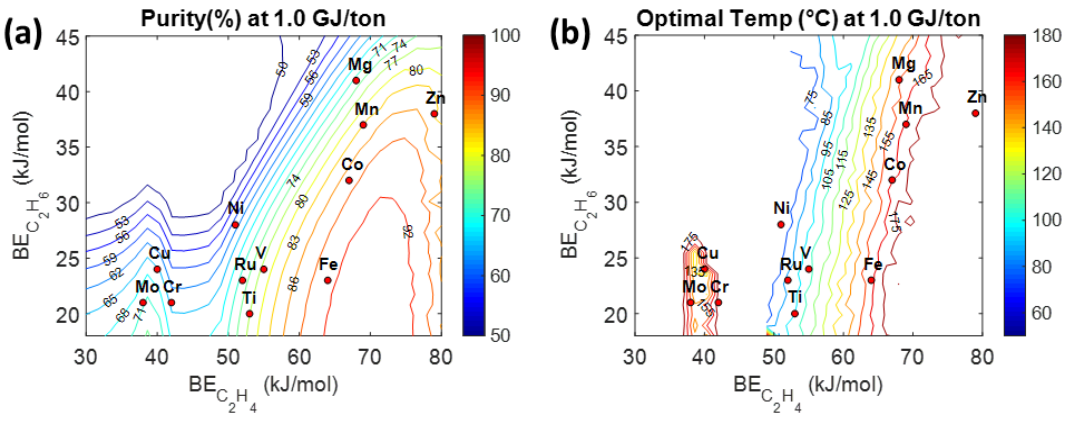

Figure 3-6 - (a) Purity and (b) optimal temperature contours for real and hypothetical pure M-BTCs in the simple model with constraints of 1 GJ/ton energy consumption and assumed 100% recovery. Red symbols indicate 12 pure M-BTCs materials.

100% recovery. The red dots represent the 12 pure M-BTC MOFs as defined by our DFT data, including with seven experimentally reported and five hypothetical materials. The highest and lowest purity is achieved by Fe-BTC and Ni-BTC with 90.4% and 60.7% purity, respectively. Figure 3-6b is a contour plot of the corresponding optimal temperatures of operation. For example, Co-BTC can achieve 87.5% purity for ethylene when the VPSA is operated at 150 °C, the optimal operating temperature for that adsorbent. The process performance shown in Figure 3-6 is nonmonotonic with respect to binding energy of ethylene and ethane (i.e. BE_{C2H4} and BE_{C2H6}) because the correlation between the OMS b_0 parameter and the identity of the metal species for ethylene is nonconvex (i.e. the S-shape shown in Figure D.1). The similar non-monotonic process performance can be observed in the full process model (Figure 3-7) for the same reason. The contour plots show the maximum separation efficiency is achieved approximately in the range of binding energies of iron (Fe). Unsurprisingly, the temperature needed for optimal performance

increases with increased binding energy of ethylene, as increasing temperature allows more efficient desorption performance.

3.3.2.2 Results for the Pure Metal MOFs using the Full Process Model

Figure 3-7a shows a scaled color plot for optimal purity calculated using the full process model with constraints of 2 GJ/ton energy consumption and 75% recovery. The energy constraint of 2 GJ/ton is used in the full model because the constraint of 1 GJ/ton is too low to get any meaningful purity improvement with the 75% recovery constraint. Similar to the simplified model, Fe-BTC achieves the highest purity among the 12 M-BTCs when evaluated using the full model. As mentioned above, the purity and the required energy consumption predicted using the full process model are somewhat higher than the simple model. It is encouraging, however, that the qualitative conclusions drawn from the simple model and the full process model are similar.

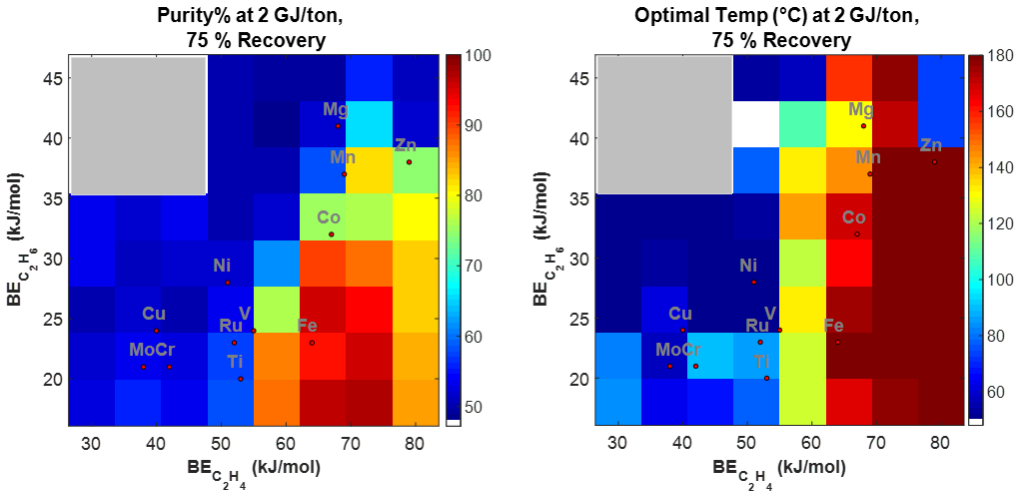

Figure 3-7 - (a) Purity and (b) optimal temperature scaled color plot of pure M-BTCs from the full process model with constraints of 2 GJ/ton energy consumption and 75% recovery. The purity and optimal temperature are color-coded. White indicates purity lower than 50% and grey means no numerical data is available.

Figure 3-7b shows the optimal temperatures corresponding to the purities shown in Figure 3-7a. As predicted by the simple model, the temperature of optimal operation of the pure metal MOFs increases as a function of ethylene binding energy. There is also good agreement between the temperatures predicted using the full process model and the simple model. These observations give us confidence that the simple model can be used to screen mixed-metal MOF candidates before rigorous evaluation of a limited number of candidate materials using the full process model, thereby cutting down on computational costs.

3.3.3 Performance of Mixed Metal MOFs

3.3.3.1 Purity for the mixed metal MM'-BTC in the Simple Model

For a given mixed-metal ratio in MM'-BTC, three kinds of metal dimers (MM, MM', and M'M') and four types of open metal sites (M in a MM dimer, M in a MM' dimer, and two similar M' sites) can exist. To evaluate the process performance of a mixed-metal MOF, knowledge of the relative concentrations of the three dimer pairs is necessary. We assume that the metals are distributed randomly among the available sites in a material, although we acknowledge that it is challenging to measure this distribution experimentally.[17] With this assumption, the population of each kind of site is defined once the metal ratio is defined. DFT calculations show that the binding energy of ethylene and ethane at M sites in MM dimers and MM' dimers are different, an observation that is important for understanding the results below. The binding energies of ethylene and ethane at MM and M'M' metal sites are given by data from the 12 pure metal MOFs. In all, the 12 metals we considered define 66 possible MM' combinations. We found that DFT calculations for dimers involving Ni, V, and Co were difficult to reliably converge because

of the spin states available to these species, so we did not consider them further. Rather than evaluating every possible pair, we performed DFT calculations for 11 metal pairs with a focus on combinations with Cr and Cu since they are the most feasible from the standpoint of experimental synthesis.[11, 76] The binding energies for these 11 metal pairs are listed in Appendix C.

Figure 3-8 shows the maximum purity achieved with three different energy constraints for the 11 MM'-BTC MOFs we considered as described by the simple process model. In each panel of the figure the horizontal axis represents the overall metal fraction in the mixed-metal MM'-BTC. If the general ideas described in the Introduction are correct, we would expect that the performance of mixed metal materials is always lower than at least one of the pure metal MOFs made from the same metals. For most of the MM'-BTC MOFs this is found to be the case. For example, higher purity can be achieved with Cr-BTC than with any mixed metal composition of Cr and Mo. There are two examples that are exceptions to this observation, however. Cr-Mg-BTC is found to give significantly higher purities than both Cr-BTC and Mg-BTC for a range of mixed metal compositions and Cr-Zn-BTC slightly outperforms Cr-BTC and Zn-BTC for a range of mixed metal compositions at an energy consumption of 0.5 GJ/ton. These examples demonstrate that in some circumstances homogeneous adsorbents are not necessarily better than heterogeneous adsorbents for adsorptive separations.

In the case of Cr-Mg-BTC example, not all mixed-metal ratios outperform the pure MOFs. Our calculation predicts that, when the Cr ratio is less than 0.6, the mixed-metal MOF can achieve higher purity than either pure metal material. It is helpful to consider this

situation in more detail. Figure 3-6a shows the purity performance not only for 12 M-BTCs but also 900 hypothetical structures.

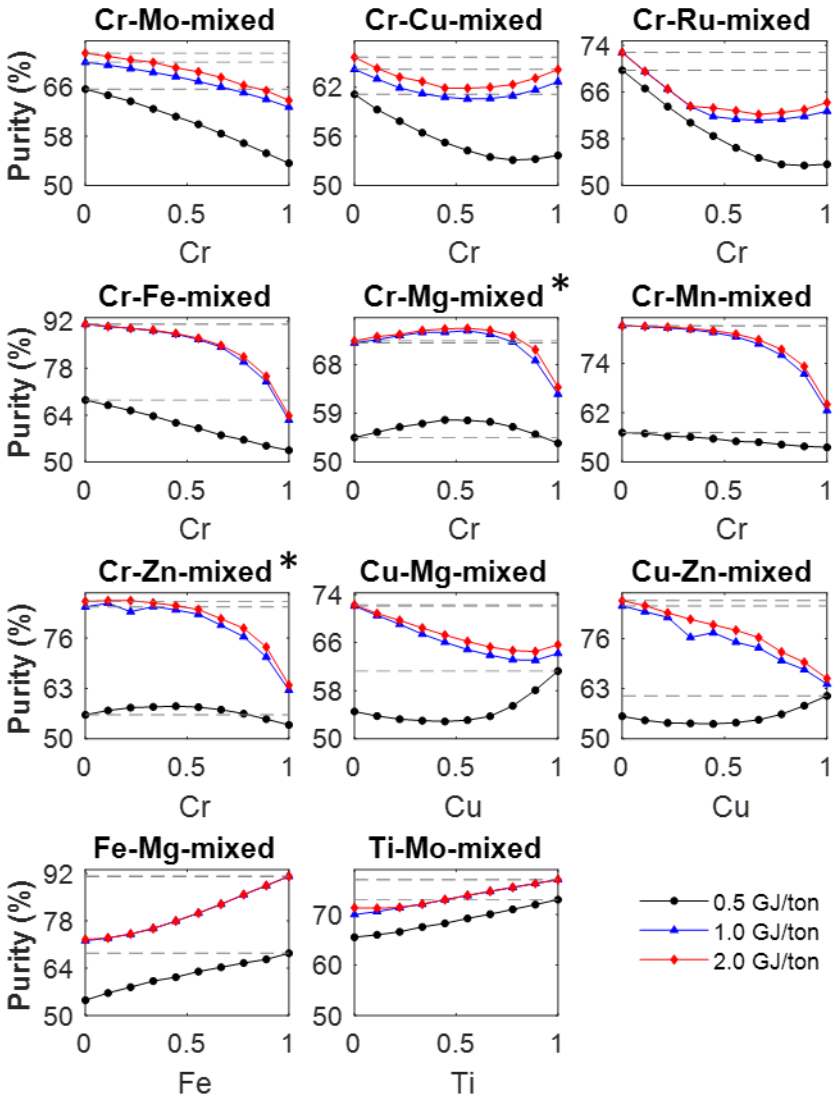

Figure 3-8 - Purity as a function of mixed-metal ratio as calculated with the simple process model for 11 MM'-BTC MOFs at three fixed levels of energy consumption. The dashed grey lines are the maximum purity the pure metal MOFs can achieve. The mixed-metal Cr-Mg- BTC and Cr-Zn-BTC materials, indicated with a *, outperform the pure metal MOFs for some metal compositions.

It is tempting to speculate that if a tie line drawn between the pure Cr and Mg metal values can cross a higher purity range then the mixed material would have improved

performance. This idea is not correct, however, for two reasons. First, the binding energies of mixed metal sites are not simple linear combinations of the pure metal sites. DFT calculations with the mixed metal dimers for Cr-Mg-BTC give ethylene (ethane) binding energies of 40.1 (20.0) kJ/mol on Cr and 68.7 (38.3) kJ/mol on Mg. The binding energies in the pure metal MOFs are for 42.0 (22.0) kJ/mol and 68.0 (41.0) kJ/mol for Cr and Mg, respectively. As seen in Figure D.3, the mixed site binding energies do not lie on the tie line between the pure metal states. The second complication with the tie line concept is that every point in Figure 3-6a correspond to different optimized process conditions. The process conditions that are optimal for a mixed-metal material must consider a weighted set of the four site energies shown in Figure D.3.

3.3.3.2 Optimization of Cr-Mg-BTC with the Full Process Model

Because of the interesting results for Cr-Mg-BTC with the simple process model the full process model was also applied to this material. Three objective functions, recovery, purity, and energy consumption are optimized in the full process model. Each recovery can be achieved by different combinations of the purity and the corresponding energy consumption. In Figure 3-9a only the point which maximized the purity is shown for each recovery, regardless of its energy consumption. Figure 3-9b shows the corresponding energy consumption. The process performance of Cr-Mg-BTC in full model is consistent with that in the simple model.

10 uniformly spaced mixed metal ratios were analyzed and a ratio of 40% Cr in Cr-Mg-BTC was found to be optimal. The performance of $Cr_{0.4}Mg_{0.6}BTC$ (red triangles) is considerably better than both the pure Cr-BTC (blue squares) and Mg-BTC (black circles).

However, not all metal ratios exceeded the pure metal performance; for example, $Cr_{0.9}Mg_{0.1}$BTC (green diamonds) has worse performance than the pure Mg-BTC. This observation is consistent with the prediction of the simple model. The corresponding energy consumption at each purity for these four mixed-metal ratios is shown in Figure 3-9b. The mixed metal material with 40% Cr is optimal since it has a higher purity with lower energy consumption when the purity is larger than 70%.

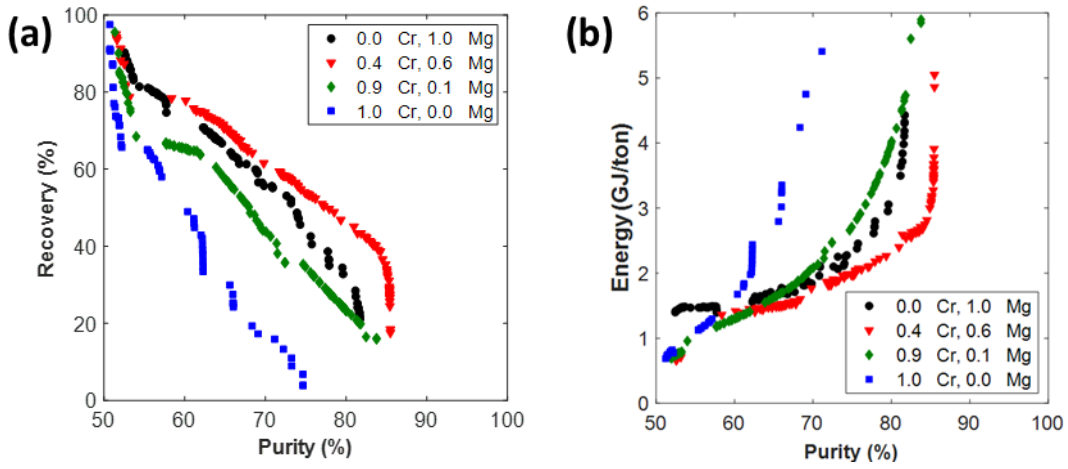

Figure 3-9 - (a) Recovery and (b) the corresponding energy consumption as a function of purity for these four mixed-metal ratios in Cr-Mg-BTC in the full model.

3.4 Summary

In this chapter, the aim was to understand whether mixed-metal materials (MM'-BTC) could ever outperform pure metal M-BTC MOFs for ethylene/ethane separations. Both simplified model (2-step saturation-desaturation cycle) and detailed full process model (4-step VPSA) were used to examine the process performance of M-BTC and MM'-BTC MOFs for ethylene/ethane separations. 12 metal-substituted M-BTCs were studied as the homogeneous adsorbents, and 11 mixed-metal pairs were evaluated as the energetically heterogeneous materials. The adsorption isotherms for species of interest are the primary

inputs for process models of equilibrium adsorption-based separations. Adsorption models derived primarily from DFT data were developed because FF-based GCMC simulations cannot accurately describe OMS and are not useful for our materials.

The optimization procedure was illustrated for both models with the isotherm parameters of Zn-BTC. The process purity and energy consumption are the optimized objectives for the simplified model, while process purity, energy consumption, and recovery are optimization objectives for full process model. For both models, the energy consumption increases with increasing purity. Although the simple model underestimates the maximum possible purity and the energy consumed, it still provides a useful general estimate of optimal operating conditions and performance.

We first investigated the impact of the binding strength of the metal centers on the separation performance of pure metal MOFs. 900 real and hypothetical materials were evaluated using the simplified ideal model, while 64 hypothetical binding energies pairs were examined with the full process model. The main aim is to evaluate whether trends predicted by the simple model also hold under more rigorous evaluation. Good agreement between the temperatures predicted using the full process model and the simple model was observed. Another observation is that the temperature of optimal operation of the pure metal MOFs increases as a function of ethylene binding energy in both models. These observations give us confidence that the simple model can be used to pre-screen mixed-metal MOF candidates before rigorous evaluation of a smaller number of candidate materials using the full process model.

Rather than evaluating every possible pair, 11 metal pairs were examined by the simple process model. For most of the MM'-BTC MOFs, the performance of mixed metal materials was found to be lower than at least one of the pure metal MOFs made from the same metals. However, we also found two examples that are exceptions to this rule. Cr-Mg-BTC gave significantly higher purities than both Cr-BTC and Mg-BTC and Cr-Zn-BTC slightly outperforms Cr-BTC and Zn-BTC at an energy consumption of 0.5 GJ/ton. The same conclusions also held when these two materials were more rigorously evaluated using the full model. These examples are, therefore, a demonstration that, in some circumstances, homogeneous (or pure) adsorbents do not necessarily outperform heterogeneous (or mixed) adsorbents for adsorptive separations.

We began this chapter by mentioning the work of Bhatia and Myers[7], which used a simple adsorption isotherm to show that the optimal adsorption-based storage capacity for an adsorbent is achieved when the adsorbent is energetically homogenous. Our results do not contradict this earlier work because we focused on the performance of adsorbents for separations of binary gas mixtures, not adsorption-based storage of a single component. Having a high swing capacity for the species being preferentially adsorbed in a separation is of course desirable, but the overall performance of a separation arises as the tradeoff between multiple factors in addition to this swing capacity.

3.5 References

[1] Bao, Z. B.; Alnemrat, S.; Yu, L.; Vasiliev, I.; Ren, Q. L.; Lu, X. Y.; Deng, S. G., Adsorption of Ethane, Ethylene, Propane, and Propylene on a Magnesium-Based Metal-Organic Framework. *Langmuir* **2011,** *27* (22), 13554-13562.

[2] 2. Liu, J.; Thallapally, P. K.; McGrail, B. P.; Brown, D. R.; Liu, J., Progress in adsorption-based CO_2 capture by metal-organic frameworks. *Chem. Soc. Rev.* **2012,** *41* (6), 2308-2322.

[3] Burtch, N. C.; Jasuja, H.; Walton, K. S., Water stability and adsorption in metal-organic frameworks. *Chem. Rev.* **2014,** *114* (20), 10575-612.

[4] Chen, B.; Ockwig, N. W.; Millward, A. R.; Contreras, D. S.; Yaghi, O. M., High H_2 Adsorption in a Microporous Metal-Organic Framework with Open Metal Sites. *Angew. Chem. Int.* **2005,** *117* (30), 4823-4827.

[5] Choi, S.; Watanabe, T.; Bae, T. H.; Sholl, D. S.; Jones, C. W., Modification of the Mg/DOBDC MOF with Amines to Enhance CO_2 Adsorption from Ultradilute Gases. *J. Phys. Chem. Lett.* **2012,** *3* (9), 1136-1141.

[6] RoqueMalherbe, R. M. A., Adsorption and Diffusion in Nanoporous Materials, 2nd Edition. *Adsorption and Diffusion in Nanoporous Materials, 2nd Edition* **2018**, 1-297.

[7] Bhatia, S. K.; Myers, A. L., Optimum conditions for adsorptive storage. *Langmuir* **2006,** *22* (4), 1688-1700.

[8] Hyla, A. S.; Fang, H.; Boulfelfel, S. E.; Muraro, G.; Paur, C.; Strohmaier, K.; Ravikovitch, P. I.; Sholl, D. S., Significant Temperature Dependence of the Isosteric Heats of Adsorption of Gases in Zeolites Demonstrated by Experiments and Molecular Simulations. *J Phys Chem C* **2019,** *123* (33), 20405-20412.

[9] Thompson, J. A.; Blad, C. R.; Brunelli, N. A.; Lydon, M. E.; Lively, R. P.; Jones, C. W.; Nair, S., Hybrid Zeolitic Imidazolate Frameworks: Controlling Framework Porosity and Functionality by Mixed-Linker Synthesis. *Chem. Mater.* **2012,** *24* (10), 1930-1936.

[10] Jayachandrababu, K. C.; Verploegh, R. J.; Leisen, J.; Nieuwendaal, R. C.; Sholl, D. S.; Nair, S., Structure Elucidation of Mixed-Linker Zeolitic Imidazolate Frameworks by Solid-State H^1 CRAMPS NMR Spectroscopy and Computational Modeling. *J. Am. Chem. Soc.* **2016,** *138* (23), 7325-7336.

[11] Dolgopolova, E. A.; Brandt, A. J.; Ejegbavwo, O. A.; Duke, A. S.; Maddumapatabandi, T. D.; Galhenage, R. P.; Larson, B. W.; Reid, O. G.; Ammal, S. C.; Heyden, A.; Chandrashekhar, M.; Stavila, V.; Chen, D. A.; Shustova, N. B.,

Electronic Properties of Bimetallic Metal-Organic Frameworks (MOFs): Tailoring the Density of Electronic States through MOF Modularity. *J. Am. Chem. Soc.* **2017,** *139* (14), 5201-5209.

[12] Hong, X. J.; Wei, Q.; Cai, Y. P.; Wu, B. B.; Feng, H. X.; Yu, Y.; Dong, R. F., Pillar-Layered Metal-Organic Framework with Sieving Effect and Pore Space Partition for Effective Separation of Mixed Gas C_2H_2/C_2H_4. *ACS Appl. Mater. Inter.* **2017,** *9* (34), 29374-29379.

[13] Villajos, J. A.; Orcajo, G.; Martos, C.; Botas, J. A.; Villacanas, J.; Calleja, G., Co/Ni mixed-metal sited MOF-74 material as hydrogen adsorbent. *Int. J. Hydro. Energy* **2015,** *40* (15), 5346-5352.

[14] Botas, J. A.; Calleja, G.; Sanchez-Sanchez, M.; Orcajo, M. G., Cobalt Doping of the MOF-5 Framework and Its Effect on Gas-Adsorption Properties. *Langmuir* **2010,** *26* (8), 5300-5303.

[15] Botas, J. A.; Calleja, G.; Sanchez-Sanchez, M.; Orcajo, M. G., Effect of Zn/Co ratio in MOF-74 type materials containing exposed metal sites on their hydrogen adsorption behaviour and on their band gap energy. *Int. J. Hydro. Energy* **2011,** *36* (17), 10834-10844.

[16] Jiao, Y.; Morelock, C. R.; Burtch, N. C.; Mounfield, W. P.; Hungerford, J. T.; Walton, K. S., Tuning the Kinetic Water Stability and Adsorption Interactions of Mg-MOF-74 by Partial Substitution with Co or Ni. *Ind. Eng. Chem. Res* **2015,** *54* (49), 12408-12414.

[17] Howe, J. D.; Morelock, C. R.; Jiao, Y.; Chapman, K. W.; Walton, K. S.; Sholl, D. S., Understanding Structure, Metal Distribution, and Water Adsorption in Mixed-Metal MOF-74. *J Phys Chem C* **2017,** *121* (1), 627-635.

[18] Herm, Z. R.; Bloch, E. D.; Long, J. R., Hydrocarbon Separations in Metal–Organic Frameworks. *Chem. Mater.* **2014,** *26* (1), 323-338.

[19] Fischer, M.; Gomes, J. R.; Froba, M.; Jorge, M., Modeling adsorption in metal-organic frameworks with open metal sites: propane/propylene separations. *Langmuir* **2012,** *28* (22), 8537-49.

[20] He, Y.; Krishna, R.; Chen, B., Metal–organic frameworks with potential for energy-efficient adsorptive separation of light hydrocarbons. *Energy Environ. Sci.* **2012,** *5* (10), 9107.

[21] Bloch, E. D.; Queen, W. L.; Krishna, R.; Zadrozny, J. M.; Brown, C. M.; Long, J. R., Hydrocarbon Separations in a Metal-Organic Framework with Open Iron(II) Coordination Sites. *Science* **2012,** *335* (6076), 1606-1610.

[22] Kulkarni, A. R.; Sholl, D. S., Screening of Copper Open Metal Site MOFs for Olefin/Paraffin Separations Using DFT-Derived Force Fields. *J Phys Chem C* **2016,** *120* (40), 23044-23054.

[23] Bohme, U.; Barth, B.; Paula, C.; Kuhnt, A.; Schwieger, W.; Mundstock, A.; Caro, J.; Hartmann, M., Ethene/Ethane and Propene/Propane Separation via the Olefin and Paraffin Selective Metal-Organic Framework Adsorbents CPO-27 and ZIF-8. *Langmuir* **2013,** *29* (27), 8592-8600.

[24] Bae, Y. S.; Lee, C. Y.; Kim, K. C.; Farha, O. K.; Nickias, P.; Hupp, J. T.; Nguyen, S. T.; Snurr, R. Q., High Propene/Propane Selectivity in Isostructural Metal-Organic Frameworks with High Densities of Open Metal Sites. *Angew Chem Int Edit* **2012,** *51* (8), 1857-1860.

[25] Wang, Q. M.; Shen, D. M.; Bulow, M.; Lau, M. L.; Deng, S. G.; Fitch, F. R.; Lemcoff, N. O.; Semanscin, J., Metallo-organic molecular sieve for gas separation and purification. *Micropor Mesopor Mat* **2002,** *55* (2), 217-230.

[26] Zang, J.; Nair, S.; Sholl, D. S., Prediction of Water Adsorption in Copper-Based Metal–Organic Frameworks Using Force Fields Derived from Dispersion-Corrected DFT Calculations. *J Phys Chem C* **2013,** *117* (15), 7519-7525.

[27] Watanabe, T.; Sholl, D. S., Molecular chemisorption on open metal sites in Cu_3(benzenetricarboxylate)$_2$: A spatially periodic density functional theory study. *J. Chem. Phys.* **2010,** *133* (9).

[28] Supronowicz, B.; Mavrandonakis, A.; Heine, T., Interaction of Small Gases with the Unsaturated Metal Centers of the HKUST-1 Metal Organic Framework. *J Phys Chem C* **2013,** *117* (28), 14570-14578.

[29] Rubes, M.; Wiersum, A. D.; Llewellyn, P. L.; Grajciar, L.; Bludsky, O.; Nachtigall, P., Adsorption of Propane and Propylene on CuBTC Metal-Organic Framework:

Combined Theoretical and Experimental Investigation. *J Phys Chem C* **2013,** *117* (21), 11159-11167.

[30] You, W.; Liu, Y.; Howe, J. D.; Sholl, D. S., Competitive Binding of Ethylene, Water, and Carbon Monoxide in Metal–Organic Framework Materials with Open Cu Sites. *J Phys Chem C* **2018,** *122* (16), 8960-8966.

[31] You, W. Q.; Liu, Y.; Howe, J. D.; Tang, D.; Sholl, D. S., Tuning Binding Tendencies of Small Molecules in Metal-Organic Frameworks with Open Metal Sites by Metal Substitution and Linker Functionalization. *J Phys Chem C* **2018,** *122* (48), 27486-27494.

[32] Song, X.; Jeong, S.; Kim, D.; Lah, M. S., Transmetalations in two metal-organic frameworks with different framework flexibilities: Kinetics and core-shell heterostructure. *CrystEngComm* **2012,** *14* (18), 5753-5756.

[33] Sava Gallis, D. F.; Parkes, M. V.; Greathouse, J. A.; Zhang, X. Y.; Nenoff, T. M., Enhanced O_2 Selectivity versus N_2 by Partial Metal Substitution in Cu-BTC. *Chem. Mater.* **2015,** *27* (6), 2018-2025.

[34] Rege, S. U.; Yang, R. T., A simple parameter for selecting an adsorbent for gas separation by pressure swing adsorption. *Sep. Sci. Technol.* **2001,** *36* (15), 3355-3365.

[35] Wiersum, A. D.; Chang, J. S.; Serre, C.; Llewellyn, P. L., An Adsorbent Performance Indicator as a First Step Evaluation of Novel Sorbents for Gas Separations: Application to Metal-Organic Frameworks. *Langmuir* **2013,** *29* (10), 3301-3309.

[36] Maring, B. J.; Webley, P. A., A new simplified pressure/vacuum swing adsorption model for rapid adsorbent screening for CO_2 capture applications. *Int. J. Greenh. Gas Con.* **2013,** *15*, 16-31.

[37] Rajagopalan, A. K.; Avila, A. M.; Rajendran, A., Do adsorbent screening metrics predict process performance? A process optimisation based study for post-combustion capture of CO_2. *Int. J. Greenh. Gas Con.* **2016,** *46*, 76-85.

[38] Farmahini, A. H.; Krishnamurthy, S.; Friedrich, D.; Brandani, S.; Sarkisov, L., From Crystal to Adsorption Column: Challenges in Multiscale Computational Screening of Materials for Adsorption Separation Processes. *Ind. Eng. Chem. Res* **2018**.

[39] Park, J.; Rubiera Landa, H. O.; Kawajiri, Y.; Realff, M. J.; Lively, R. P.; Sholl, D. S., How Well Do Approximate Models of Adsorption-based CO_2 Capture Processes Predict Results of Detailed Process Models? *Ind Eng Chem Res* **2019**.

[40] Murray, L. J.; Dinca, M.; Yano, J.; Chavan, S.; Bordiga, S.; Brown, C. M.; Long, J. R., Highly-Selective and Reversible O_2 Binding in Cr_3(1,3,5-benzenetricarboxylate)$_2$. *J. Am. Chem. Soc.* **2010,** *132* (23), 7856-+.

[41] Kramer, M.; Ulrich, S. B.; Kaskel, S., Synthesis and properties of the metal-organic framework $Mo_3(BTC)_2$ (TUDMOF-1). *J. Mater. Chem.* **2006,** *16* (23), 2245-2248.

[42] Xie, L. H.; Liu, S. X.; Gao, C. Y.; Cao, R. G.; Cao, J. F.; Sun, C. Y.; Su, Z. M., Mixed-valence Iron(II, III) trimesates with open frameworks modulated by solvents. *Inorg. Chem.* **2007,** *46* (19), 7782-7788.

[43] Kozachuk, O.; Yusenko, K.; Noei, H.; Wang, Y. M.; Walleck, S.; Glaser, T.; Fischer, R. A., Solvothermal growth of a ruthenium metal-organic framework featuring HKUST-1 structure type as thin films on oxide surfaces. *Chem. Commun.* **2011,** *47* (30), 8509-8511.

[44] Maniam, P.; Stock, N., Investigation of Porous Ni-Based Metal-Organic Frameworks Containing Paddle-Wheel Type Inorganic Building Units via High-Throughput Methods. *Inorg. Chem.* **2011,** *50* (11), 5085-5097.

[45] Chui, S. S. Y.; Lo, S. M. F.; Charmant, J. P. H.; Orpen, A. G.; Williams, I. D., A chemically functionalizable nanoporous material $[Cu_3(TMA)_2(H2O)_3]_n$ *Science* **1999,** *283* (5405), 1148-1150.

[46] Feldblyum, J. I.; Liu, M.; Gidley, D. W.; Matzger, A. J., Reconciling the Discrepancies between Crystallographic Porosity and Guest Access As Exemplified by Zn-HKUST-1. *J. Am. Chem. Soc.* **2011,** *133* (45), 18257-18263.

[47] Kresse, G.; Furthmuller, J., Efficient iterative schemes for ab initio total-energy calculations using a plane-wave basis set. *Phys Rev B* **1996,** *54* (16), 11169-11186.

[48] Grimme, S.; Antony, J.; Ehrlich, S.; Krieg, H., A consistent and accurate ab initio parametrization of density functional dispersion correction (DFT-D) for the 94 elements H-Pu. *J Chem Phys* **2010,** *132* (15).

[49] Dudarev, S. L.; Botton, G. A.; Savrasov, S. Y.; Humphreys, C. J.; Sutton, A. P., Electron-energy-loss spectra and the structural stability of nickel oxide: An LSDA+U study. *Phys Rev B* **1998,** *57* (3), 1505-1509.

[50] Wang, L.; Maxisch, T.; Ceder, G., Oxidation energies of transition metal oxides within the GGA+U framework. *Phys Rev B* **2006,** *73* (19).

[51] Mann, G. W.; Lee, K.; Cococcioni, M.; Smit, B.; Neaton, J. B., First-principles Hubbard U approach for small molecule binding in metal-organic frameworks. *J Chem Phys* **2016,** *144* (17).

[52] Watanabe, T.; Keskin, S.; Nair, S.; Sholl, D. S., Computational identification of a metal organic framework for high selectivity membrane-based CO_2/CH_4 separations: Cu(hfipbb)(H_2hfipbb)$_{0.5}$. *Phys Chem Chem Phys* **2009,** *11* (48), 11389-11394.

[53] Dubbeldam, D.; Calero, S.; Ellis, D. E.; Snurr, R. Q., RASPA: molecular simulation software for adsorption and diffusion in flexible nanoporous materials. *Mol Simulat* **2016,** *42* (2), 81-101.

[54] Garberoglio, G.; Skoulidas, A. I.; Johnson, J. K., Adsorption of gases in metal organic materials: Comparison of simulations and experiments. *J. Phys. Chem. B* **2005,** *109* (27), 13094-13103.

[55] Keskin, S.; Liu, J.; Rankin, R. B.; Johnson, J. K.; Sholl, D. S., Progress, Opportunities, and Challenges for Applying Atomically Detailed Modeling to Molecular Adsorption and Transport in Metal-Organic Framework Materials. *Ind. Eng. Chem. Res.* **2009,** *48* (5), 2355-2371.

[56] Babarao, R.; Hu, Z. Q.; Jiang, J. W.; Chempath, S.; Sandler, S. I., Storage and separation of CO_2 and CH_4 in silicalite, C-168 schwarzite, and IRMOF-1: A comparative study from monte carlo simulation. *Langmuir* **2007,** *23* (2), 659-666.

[57] Yazaydin, A. O.; Snurr, R. Q.; Park, T. H.; Koh, K.; Liu, J.; LeVan, M. D.; Benin, A. I.; Jakubczak, P.; Lanuza, M.; Galloway, D. B.; Low, J. J.; Willis, R. R., Screening of Metal-Organic Frameworks for Carbon Dioxide Capture from Flue Gas Using a Combined Experimental and Modeling Approach. *J. Am. Chem. Soc.* **2009,** *131* (51), 18198-18203.

[58] Krishna, R.; van Baten, J. M., In silico screening of metal-organic frameworks in separation applications. *Phys Chem Chem Phys* **2011,** *13* (22), 10593-10616.

[59] Jorge, M.; Fischer, M.; Gomes, J. R. B.; Siquet, C.; Santos, J. C.; Rodrigues, A. E., Accurate Model for Predicting Adsorption of Olefins and Paraffins on MOFs with Open Metal Sites. *Ind. Eng. Chem. Res* **2014,** *53* (40), 15475-15487.

[60] Kundu, A.; Sillar, K.; Sauer, J., Ab Initio Prediction of Adsorption Isotherms for Gas Mixtures by Grand Canonical Monte Carlo Simulations on a Lattice of Sites. *J. Phys. Chem. Lett.* **2017,** *8* (12), 2713-2718.

[61] Sillar, K.; Hofmann, A.; Sauer, J., Ab Initio Study of Hydrogen Adsorption in MOF-5. *J. Am. Chem. Soc.* **2009,** *131* (11), 4143-4150.

[62] Sillar, K.; Sauer, J., Ab Initio Prediction of Adsorption Isotherms for Small Molecules in Metal-Organic Frameworks: The Effect of Lateral Interactions for Methane/CPO-27-Mg. *J. Am. Chem. Soc.* **2012,** *134* (44), 18354-18365.

[63] Sillar, K.; Kundu, A.; Sauer, J., Ab Initio Adsorption Isotherms for Molecules with Lateral Interactions: CO_2 in Metal-Organic Frameworks. *J Phys Chem C* **2017,** *121* (23), 12789-12799.

[64] Wong, M. W., Vibrational frequency prediction using density functional theory. *Chem. Phys. Lett.* **1996,** *256* (4-5), 391-399.

[65] Shubina, T. E.; Hartnig, C.; Koper, M. T. M., Density functional theory study of the oxidation of CO by OH on Au(110) and Pt(111) surfaces. *Phys Chem Chem Phys* **2004,** *6* (16), 4215-4221.

[66] Bentley, J.; Foo, G. S.; Rungta, M.; Sangar, N.; Sievers, C.; Sholl, D. S.; Nair, S., Effects of Open Metal Site Availability on Adsorption Capacity and Olefin/Paraffin Selectivity in the Metal-Organic Framework $Cu_3(BTC)_2$. *Ind Eng Chem Res* **2016,** *55* (17), 5043-5053.

[67] Sen, T.; Kawajiri, Y.; Realff, M. J., Adsorption Process Intensification through Structured Packing: A Modeling Study Using Zeolite 13X and a Mixture of Propylene and Propane in Hollow-Fiber and Packed Beds. *Ind. Eng. Chem. Res* **2018,** *58* (15), 5750-5767.

[68] Lively, R. P.; Chance, R. R.; Kelley, B. T.; Deckman, H. W.; Drese, J. H.; Jones, C. W.; Koros, W. J., Hollow Fiber Adsorbents for CO_2 Removal from Flue Gas. *Ind. Eng. Chem. Res* **2009,** *48* (15), 7314-7324.

[69] DeWitt, S. J. A.; Sinha, A.; Kalyanaraman, J.; Zhang, F. Y.; Realff, M. J.; Lively, R. P., Critical Comparison of Structured Contactors for Adsorption-Based Gas Separations. *Annual Review of Chemical and Biomolecular Engineering, Vol 9* **2018,** *9*, 129-152.

[70] Haghpanah, R.; Majumder, A.; Nilam, R.; Rajendran, A.; Farooq, S.; Karimi, I. A.; Amanullah, M., Multiobjective Optimization of a Four-Step Adsorption Process for Postcombustion CO_2 Capture Via Finite Volume Simulation. *Ind. Eng. Chem. Res* **2013,** *52* (11), 4249-4265.

[71] Ga, S.; Jang, H.; Lee, J. H., New performance indicators for adsorbent evaluation derived from a reduced order model of an idealized PSA process for CO_2 capture. *Comput. Aided Chem. Eng.* **2017,** *102*, 188-212.

[72] Jung, W.; Lee, K. S., Novel short-cut estimation method for the optimum total energy demand of solid sorbents in an adsorption-based CO_2 capture process. *Energy* **2019,** *180*, 640-648.

[73] Kim, H.; Hwang, S. J.; Lee, K. S., Novel Shortcut Estimation Method for Regeneration Energy of Amine Solvents in an Absorption-Based Carbon Capture Process. *Environmental Science & Technology* **2015,** *49* (3), 1478-1485.

[74] Deb, K.; Pratap, A.; Agarwal, S.; Meyarivan, T., A fast and elitist multiobjective genetic algorithm: NSGA-II. *Ieee T Evolut Comput* **2002,** *6* (2), 182-197.

[75] Muller, J., SOCEMO: Surrogate Optimization of Computationally Expensive Multiobjective Problems. *Informs J. Comput.* **2017,** *29* (4), 581-596.

[76] Wade, C. R.; Dinca, M., Investigation of the synthesis, activation, and isosteric heats of CO2 adsorption of the isostructural series of metal-organic frameworks M3(BTC)2 (M = Cr, Fe, Ni, Cu, Mo, Ru). Dalton Transactions 2012, 41 (26), 7931-7938.

CHAPTER 4. INTEGRATION OF MATERIAL AND PROCESS DESIGN FOR KINETIC SEPARATION

Parts of this chapter are adapted from the paper 'Sen. T, Kawajiri Y. and Realff M. J., Integration of Material and Process Design for Kinetic Separation' which is in preparation.

4.1 Introduction

Separation processes account for 45-55% of all industrial energy consumption of which, distillation accounts for nearly 49% of the energy consumed[1]. Techniques such as membrane permeation and pressure/temperature-swing adsorption (PSA/TSA) are more energy-efficient and could be used to debottleneck separation trains.[1–6] Adsorption based processes broadly rely on (i) equilibrium, (ii) kinetics, (iii) conformational/entropic effects and (iv) molecular sieving, to enable molecular separation[4]. Kinetic separation exploits the capability of a material to differentiate between two or more components owing to significant differences in their diffusivities, and not their equilibrium loading amounts[2–4,7–12]. This may even result in the selective adsorption of the weakly adsorbing component for a certain duration. The transient loading of the weakly adsorbed component is usually higher than the final equilibrium loading in these cases.[10]

The first known commercial application of kinetic separation was nitrogen/oxygen separation using CMS[13]. Other major separations of interest using kinetic separation are carbon dioxide separation from methane or nitrogen[7,14,15] and hydrocarbon separations such as propylene/propane[2,16]. Performance of silicates, zeolites and CMS in kinetic separation

cycles has been well-studied from both materials and process perspectives[12,14,15,17]. Compared with these conventional adsorbents, the structure, pore environment, and pore size of MOFs and ZIFs can be readily tuned by crystal engineering to meet specific needs of gas separation[2–4,16,18,19]

For kinetic separation the micropore, or the intracrystalline, resistance is the controlling resistance[20].Capturing the dynamics of the intracrystalline diffusion process using a simple Fickian formulation has been shown to be inaccurate even at a qualitative level[9,10]. This complication arises due to the coupling of pore and surface diffusion which shows a strong dependence on surface occupancy.[21,22] A more realistic approach is to use the generalized Maxwell-Stefan diffusion equations which have been extensively studied and validated through experiments and Molecular Dynamic simulations to describe mass transfer phenomena in microporous materials[9–11,23–26]. The concentration gradient is replaced by a chemical potential gradient which allows prediction of multi-component mass transfer phenomena based only on single component mass transfer information.

Apart from an understanding of the fundamental phenomena of kinetic separation at a crystal level, it is equally important to study the phenomena in a bed configuration and analyze performance efficiency in terms of a complete process cycle[20]. Computational complexity associated with incorporating the fully discretized crystal model into cyclic simulations initially led to the development of approximations such as those introduced by Nakao Suzuki [27,28]. Some studies have been able to match PSA cycle experiments using the simple Glueckauf approximation[6,14,29]. However, these approximations are extremely sensitive to factors such as the system being studied, cycle times etc. and, have been shown

to be inadequate for most cases [22]. Improvement in computational efficiency has led more PSA cycle studies which fully incorporate crystal discretization into their cyclic models[15].

In the case of equilibrium separation it is now a well established fact that using simple metrics such as selectivity or working capacity alone is not a very good predictor of comparative process performance of materials[30–33]. Several in-silico screening studies have found interesting patterns/correlations that better capture adsorbent quality for a full-scale process separation[34–39]. The same is not true for kinetic separation. Simple metrics are used to translate measured property parameters into a metric that indicates relative separation efficiency of one adsorbent compared to others (equation 1).

$$\eta_{kinetic_{ij}} = \eta_{equlibrium_{ij}} \sqrt{\frac{D_{c,i}}{D_{c,j}}} \tag{4.1}$$

where, $\eta_{kinetic_{ij}}$ is the kinetic selectivity and $\eta_{equlibrium_{ij}}$ is the equilibrium selectivity. Comparison to experimental crystal uptake studies have shown limitations of using the above metric to compare materials[15]. True kinetic selectivity is a transient parameter as indicated by equation 4.2. It reduces to equation 4.1 under two major assumptions: (i) short contact times, (ii) uncoupled diffusion[15,17].

$$\eta_{kinetic}(i,j) = \frac{q_i^{avg}(t) / p_i}{q_j^{avg}(t) / p_j} \tag{4.2}$$

The objective of this study is to analyze the impact of material property parameters on kinetic separation potential of an adsorbent-gas combination. We have also tested the reliability of equation 4.1 when recommending materials for kinetic separation. We aim to provide guidelines for material comparison when only lab scale data such as isotherms and crystal diffusivity are available. The study is conducted in two parts. To locate high-performing materials in the property parameter space, we have looked at optimized purity-recovery pareto plots in 3-step packed bed PSA cycles. We have used a group of hypothetical materials with competitive Langmuir isotherms, no equilibrium selectivity (= 1) and, varying crystal diffusivity. Incorporation of fully discretized crystal model into the axial packed bed model results in longer computational times for the PSA optimization. To expand our analysis to include a wide range of equilibrium selectivities and other isotherm shapes such as Toth, we have explored prediction of optimal property parameters using a single crystal uptake model without using PSA optimization. For a more systematic and automated approach to the property parameter exploration using only the crystal uptake model, we have used SAIL (Surrogate Assisted Illumination)[40] algorithm. SAIL, described in Section 2.2, searches in a high-dimensional space to create a map of high-performing solutions at each point in a low-dimensional feature space defined by the user[41]. We compare predictions made using the single crystal model and the fully optimized PSA's to show the scalability of property comparisons from a single crystal uptake experiment/model to a full-scale kinetic PSA.

4.2 Methods

As mentioned in section 1, for kinetic separation the micropore, or the intracrystalline, resistance is the controlling resistance[20]. Here we briefly describe the

formulation for Maxwell-Stefan crystal diffusion model[9–11,23–26]. Its incorporation into packed bed simulations, which were used to generate optimal PSA pareto plots, is also described. Finally, we describe an algorithm, SAIL[40], which was used for systematic exploration of material property parameter space in conjunction with single crystal uptake predictions.

4.2.1 Modeling kinetic separation

4.2.1.1 Single Crystal Diffusion Model

The generalized Maxwell-Stefan (GMS) model for intracrystalline mass transfer[26,42,43] is as follows:

$$-\rho \frac{q_i}{RT} \frac{\partial \mu_i}{\partial r} = \sum_{j \neq i} \frac{x_j N_i - x_i N_j}{Đ_{ij}} + \frac{N_i}{Đ_i} \tag{4.3}$$

The boundary conditions are,

$$\begin{aligned} &\frac{\partial q_i}{\partial r} = 0 \quad \text{at} \quad r = 0 \\ &q_i = q_i^{eq} \quad \text{at} \quad r = R_c \end{aligned} \tag{4.4}$$

where, x_i is the component loading mole fraction, μ_i is the chemical potential, of component i in the adsorbed phase at constant temperature and spreading pressure π [22], $Đ$'s are the Maxwell-Stefan diffusivities. $Đ_i$ is the self-diffusivity of component i, representing component-crystal wall interactions, $Đ_{ij}$ is the cross-diffusion term in multi-component mixture diffusion. Local equilibrium between the adsorbed and gas phase

allows replacement of the adsorbed phase chemical potential with that of the gas phase finally giving the following set of equations:

$$-\rho\sum_{j}\Gamma_{ij}\frac{\partial q_j}{\partial r}=\sum_{j\neq i}\frac{x_jN_i-x_iN_j}{\mathcal{D}_{ij}}+\frac{N_i}{\mathcal{D}_i}$$
$$\text{where, } \Gamma_{ij}=\frac{q_i}{p_i}\frac{\partial p_i}{\partial q_j} \qquad (4.5)$$

Γ_{ij} is termed as the thermodynamic correction factor and can be obtained from knowledge of the multi-component isotherm[10,44].

The cross-diffusion term $\mathcal{D}_{ij}$ is dependent on the surface coverage as it reflects the relative ease of displacing one component in the presence of the other. Fundamental understanding of cross-diffusivity is not fully developed. The empirical Vignes[21,45] correlation that has been studied for multi-component diffusion in liquid mixtures is usually adopted.

$$\mathcal{D}_{ij}=[\mathcal{D}_i]^{\frac{\theta_i}{\theta_i+\theta_j}}[\mathcal{D}_j]^{\frac{\theta_j}{\theta_i+\theta_j}} \qquad (4.6)$$

where, $\mathcal{D}_i$ is the component self-diffusivity at high surface coverage. Non-dimensionalised forms of the above equations are listed in Appendix D.

In contrast the Fickian mass transfer model is as follows:

$$-\rho \frac{\partial q_i}{\partial r} = \frac{N_i}{D_i} \tag{4.7}$$

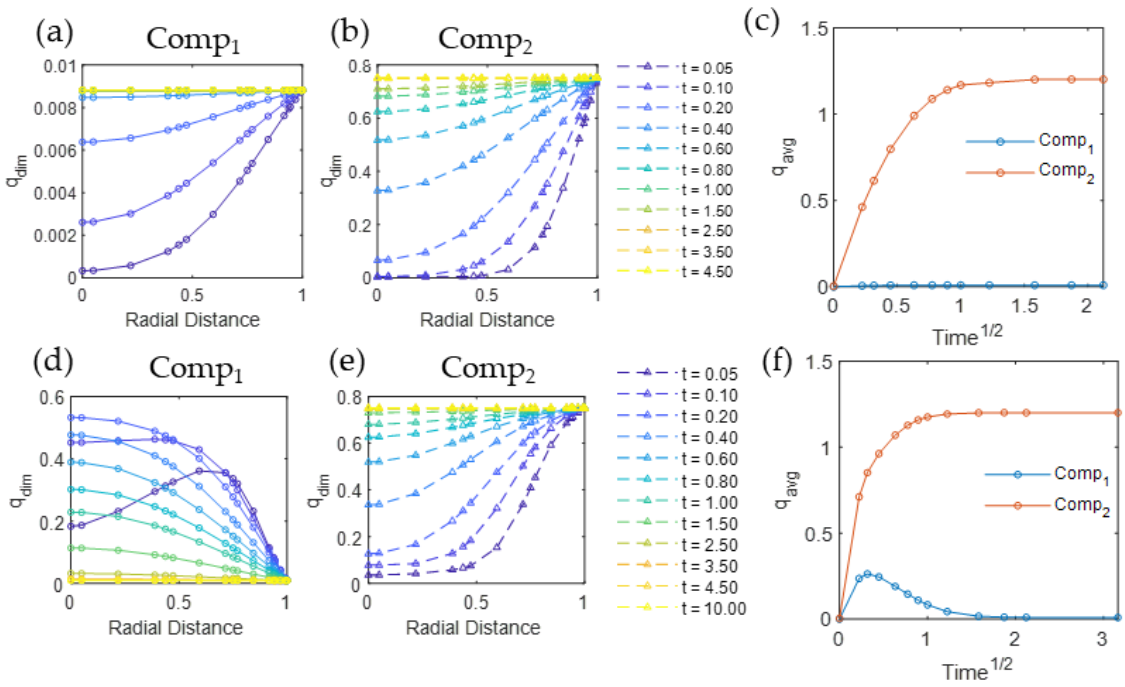

Figure 4-1 - These plots are radial profiles of component loadings on an adsorbent crystal as it changes with time. The initial state of the system is a nearly empty crystal devoid of either component 1 or 2. The diffusivity ratio of component 1 and 2 is 1: 0.314. At t = 0 the outer radius of the crystal is exposed to a 50:50 gas mixture whose equilibrium loadings on the crystal are [0.009 , 0.751] respectively. These loadings are non-dimensionless (w.r.t saturation loading of component 1). (a) & (b) are results of the simple Fickian diffusion equations (d) & (e) are the result of using Maxwell-Stefan diffusion equations. Fickian diffusion fails to capture the sharp increase in crystal loading of the fast component 1 above equilibrium. (c) & (f) show the average crystal loadings predicted by Fickian Diffusion and Maxwell-Stefan Diffusion respectively.

Figure 4-1 demonstrates the impact of using the thermodynamic correction factor and cross-diffusivity on the loading profiles inside the crystal with time. Component 1 is faster diffusing and weakly adsorbed when compared to component 2. The dimensionless equilibrium loadings are 0.009 and 0.751 respectively. The diffusivity ratio is (1 : 0.314).

The faster diffusing and weakly adsorbed component 1 rushes into the crystal in the initial stages resulting in a significant increase in its adsorbed concentration when compared to equilibrium. Figure 4-1 (c) demonstrates the temporal evolution of the radially averaged crystal loadings when there is simple Fickian diffusion, (f) shows the same plot when Maxwell-Stefan Diffusion is incorporated.

To generate the numerical results, the dimensionless Maxwell-Stefan crystal diffusion model (equation 4.5) was solved in MATLAB using Orthogonal Collocation of Finite Elements[46]. 5 finite elements with a 3 internal collocation points was found to be sufficient to capture the dynamics and spatial concentration profiles of the system. The internal collocation points were located at the roots of the Legendre Polynomial. Due to steeper fronts close to the outer radius of the crystal, the nodes were placed at squared distances from the outer radius.

4.2.1.2 Packed Bed Model

We have used the standard packed bed model with the average crystal loading at each axial point being accounted for by equating the flux out of the gas phase to the flux at the outer radius of the detailed crystal model described above. The detailed equations are provided in Appendix D.

$$\frac{\partial}{\partial t}c(z,i) = \left(D_{ax}(i)\frac{1}{{L_0}^2}\frac{\partial^2}{\partial z^2}c(z,i) - \frac{1}{L_0}\frac{\partial}{\partial z}\left(\frac{u_g(z)}{\varepsilon}c(z,i)\right) - N_{gas}(z,i)\right) \qquad (4.8)$$

$$N_{gas}(z,i) = \frac{(1-\varepsilon)}{\varepsilon}\frac{\partial}{\partial t}\left(q1_{avg}(z,i)\times\rho_p\right) \tag{4.9}$$

$$\frac{\partial}{\partial t}q_{avg}(z,i) = \frac{3}{R_c}N(z,R_c,i) \tag{4.10}$$

4.2.2 SAIL Algorithm

For systematic exploration of kinetic separation material property parameter space, in conjunction with single crystal uptake predictions, we used Surrogate Assisted Illumination (SAIL) [40] algorithm described here. SAIL is a modified version of the MAP-elites algorithm which we will describe first. Multi-dimensional Archive of Phenotypic Elites (MAP-Elites) algorithm searches in a high-dimensional space to create a map of high-performing solutions at each point in a low-dimensional feature space defined by the user[41]. Two main components of implementing this algorithm are to choose a performance measure f(x) to evaluate a solution x and a description of N dimensions of variation which define a *feature space* of interest. For example, in evolving robot morphologies, fitness could be the speed of a robot and features could be its height, weight and energy efficiency.[41]

Each dimension of the feature space is discretized according to user preference or computational budget (*Figure 4-2a).* MAP-elites algorithm searches for the highest performing solution in each bin of the discretized N-dimensional feature space (*Figure 4-2b*). This type of *illumination algorithm* allows for an understanding of how underlying parameters combine to affect the performance potential and trade-offs with features at each point. For example, in illuminating robot morphologies; MAP-elites finds the fastest robot

that is tall, light, energy efficient; the fastest robot that is tall, heavy, energy inefficient; the fastest robot that is short, heavy, energy inefficient; etc.

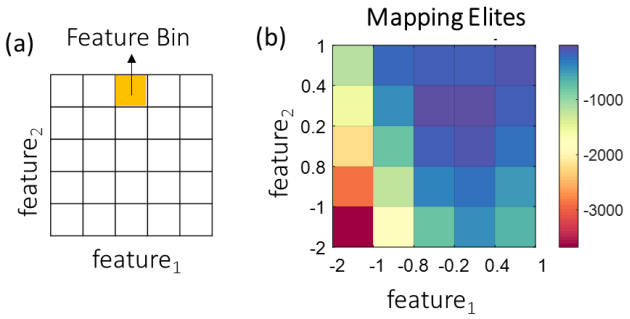

Figure 4-2 - (a) illustrates a (5 × 5) binned feature map used in the MAP-elites algorithm for a problem with n independent input parameters (genotypes) [x1 , x2, … , xn]. feature1 and feature2 are functions of these input parameters (phenotypes)and are values that capture features of interest of the system. (b) represents the result generated by the algorithm. The color-scale represents the value of performance measure (p) which is also a function of x. The final map is the estimated maxima of p per bin. The optimal values of x per bin can be similarly plotted from the algorithm output.

Feature vectors are not independent parameters, rather they are dependent parameters or *phenotypes* which are functions of an independent parameter set x of *genotypes*. The search is therefore conducted over the *genotype space* which contains values of all possible combinations of x. It is to be noted that, while some *phenotypes* require simulation of complex models, others may just have a simple correlation to the *genotype* such as robot height. Algorithmic details of MAP-Elites are provided in the SI.

Evolutionary approaches like MAP-elites typically requires several evaluations before a satisfactory solution can be reached. Even when the underlying system being explored is computationally inexpensive, the scale of the number of evaluations means that surrogate models can drastically speed up computation. SAIL is a surrogate assisted version of MAP-elites, which uses Gaussian Process (GP) to approximate the performance

measure[40]. It uses the framework of Bayesian Optimization which makes use of the concept of an *acquisition function* to balance exploration (high performance) and exploitation (high uncertainty). The acquisition function is Upper Confidence Bound estimate (UCB) shown in equation 4.11.

$$UCB(x) = \mu(x) + \kappa\sigma(x) \tag{4.11}$$

where, κ is the user-defined trade-off between mean (μ) and variance (σ) of the GP. Algorithmic details of SAIL are provided in the SI and the original MATLAB implementation is available at (github.com/agaier/sail_gecco2017)[40]. Specific details such as performance measures, genotypes and phenotypes in material exploration for kinetic separation are described in the Results and discussion section.

4.3 Results and discussion

To understand the impact of the interplay of crystal diffusion and adsorption thermodynamics, we have performed two analysis. One analysis looks at optimized simple 3-step PSA cycles in a packed bed with different adsorbent property parameters. The hypothetical adsorbents were all described using the simple competitive Langmuir isotherm, but had varying shapes of the isotherm. An equilibrium selectivity of close to 1 was considered, to eliminate the effect of equilibrium on separation efficiency. However, each optimization run takes around 3-6 hours which makes expanding our analysis to include other isotherms and selectivities unwieldy. Therefore, we have used the single crystal model with the systematic SAIL algorithm described in Section 4.2.2, to explore the isotherm and diffusion property parameter space more extensively.

4.3.1 Optimization procedure using full packed bed model

The packed bed model described in section 4.2.1.2 was used to simulate 3-step Pressure Swing Adsorption (PSA) cycles until cyclic steady state (CSS) was reached. The steps were pressurization with feed, adsorption and counter-current blowdown. The product of interest was the slower diffusing species which is obtained in pure form during the adsorption step. The multi-objective optimization problem was to obtain the purity-recovery pareto front for this component. Energy consumption and productivity were calculated, but not included as constraints in the optimization problem. The variables that were optimized were the step times, velocity of the feed, length of the bed and the operating pressures. Detailed description of the performance objectives and range of the decision variables are provided in the SI. We used surrogate assisted algorithm, SOCEMO[47] for efficient optimization with few model evaluations. In our analysis, the model evaluation budget for each optimization was set to 100. Each optimization took around 3-6 hours to complete. The evaluation budget was set to minimize time spent per sample material, while still getting a general idea about performance relative to others.

4.3.2 Application of SAIL to crystal uptake model

The isolated single crystal model is orders of magnitude faster to solve compared to optimizing the full bed model. Therefore, it is worthwhile to compare materials which perform well when looking at this simplified model to those that perform well in terms of a fully optimized PSA cycle. To explore impact of adsorbent property parameters in terms of crystal uptake performance, we used SAIL. To implement the algorithm we need to define the feature space or the *phenotypes* we want to explore and, some measure for

comparing relative *performance* of one material over another. The input parameter space to describe an adsorbent for kinetic separation (*genotype*) is described later.

The phenotype space that we have chosen comprises the equilibrium selectivity $\left(\eta_{equlibrium_{ij}}\right)$ and the diffusivity ratio $\left(D_1^c / D_2^c\right)$, since these are the parameters typically used to estimate the ideal kinetic selectivity of materials (Equation 4.1). Our performance evaluation metric is described next.

As shown in Figure 4-1 difference in crystal diffusion rates of two components in a mixture leads to supra-equilibrium loadings for the faster diffusing component. We are interested in understanding the impact of this supra-equilibrium loading on the potential separation efficiency. Specifically, we are interested in understanding how material property parameters such as isotherm shape and crystal diffusivity affects enhancement of transient selectivity above equilibrium. To facilitate this analysis, we have used the maximum *improvement in selectivity* as the performance metric to compare different materials.

Figure 4-3 represents the transient change in kinetic selectivity (equation 4.2) curves for four different materials. These have been normalized w.r.t. the respective equilibrium selectivity. This normalized metric can be interpreted as the contribution of crystal diffusion towards selectivity enhancement. The maximum height of these curves labelled 'A' in Figure 4-3 is what we refer to as the *improvement in selectivity* metric to compare performance of two different materials for kinetic separation. The width of these peaks could also be a parameter of interest but this is not in the scope of our current work.

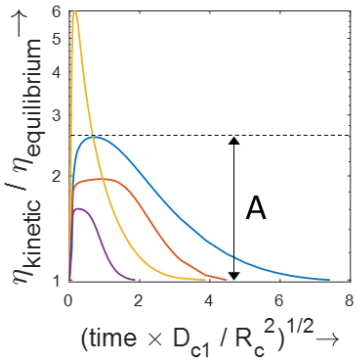

Figure 4-3 - The figure represents normalized transient curves for kinetic selectivity. The curves are normalized with respect to the equilibrium selectivity at the gas phase concentration at the crystal boundary. 'A' represents the improvement in selectivity metric used in our study. It is the maximum value of the normalized kinetic selectivity.

4.3.3 Independent property parameters impacting kinetic separation

Here we describe in detail, the set of independent property parameters of an adsorbent that can impact its kinetic separation performance. The property parameters are similar whether we analyze performance in terms of the full PSA analysis or just the crystal uptake. To understand this independent property parameter space, we need to look at the detailed Maxwell-Stefan crystal diffusion model, introduced in Section 2.1.1. Dimensionless forms of these equations have been included in Appendix D. The dimensionless variables are as follows:

$$\theta_i = \frac{q_i}{q_1^{sat}}; \quad \hat{r} = \frac{r}{R_c}; \quad \hat{\mathcal{D}}_{ij} = \frac{\mathcal{D}_{ij}}{\mathcal{D}_{11}}; \quad \hat{t} = \frac{t}{\mathcal{D}_{11} R_c^{\,2}} \tag{1}$$

The competitive Langmuir isotherm to describe equilibrium is as follows.

$$\theta_i = \theta_i^{sat} \frac{P_i b_i}{1 + \sum P_j b_j}; \quad b_i = b_i^0 \exp\left(-\frac{\Delta H_i}{RT}\right); \quad \theta_i^{sat} = \frac{q_i^{sat}}{q_1^{sat}} \tag{2}$$

$$\mathcal{D}_{ii} = \hat{D}_i^c \exp\left(\frac{E_i}{RT}\right); \quad \hat{D}_{c_i} = \frac{D_i^c}{D_2^c}; \quad D_i^c = D_i^{c0} \exp\left(-\frac{E_c}{RT}\right) \tag{3}$$

We have assumed a constant value of q_1^{sat}, E_i and ΔH_i in the all following analysis and have been listed Appendix D. Five independent material property parameters can be adjusted for a binary mixture, assuming Langmuir isotherm $b_1^0, \frac{b_2^0}{b_1^0}, \theta_2^{sat}, \frac{D_2^c}{{R_c}^2}, \hat{D}_1^c \left(= \frac{D_1^c}{D_2^c}\right)$.

4.3.4 Favorable materials for optimized PSA performance

Independent property parameters effecting kinetic separation performance are described above. In the full PSA analysis we have only considered cases with θ_2^{sat}=1. From a random sampling of Langmuir isotherms $\left(b_1^0, b_2^0/b_1^0\right)$ we selected those parameters which gave equilibrium selectivity close to 1 and; from that set, selected four that were sufficiently distinct from each other (Figure 4-4).

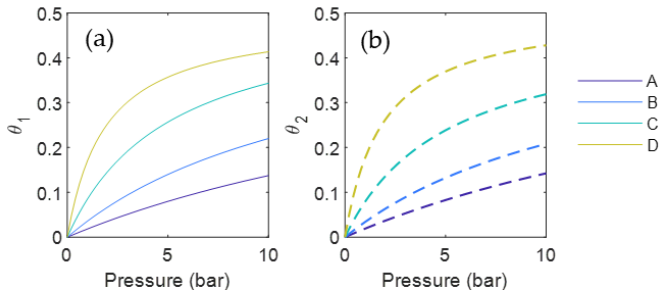

Figure 4-4 - (a & b) Show competitive Langmuir isotherms generated by the four sets of parameters selected for full PSA analysis, for components 1 and 2 respectively. Each pair has an equilibrium selectivity close to 1.

In the following sections we have analyzed the relative kinetic separation performance of these four isotherms and the impact of changing D_2^c / R_c^2 and $\hat{D}_1^c$. The comparison was based on optimized pareto fronts for PSA cycles as described in section 4.3.1. Throughout the analysis component 1 is the faster diffusing species, component 2 is the slower species.

4.3.4.1 Effect of crystal radius

Changing crystal radius changes the diffusion length for mass transfer when this is the controlling resistance. In a PSA cycle on the other hand, optimizing cycle step times might compensate for the changing diffusion distance. To understand how this impacts kinetic separation performance, we have analyzed how D_2^c / R_c^2 impacts PSA separation performance when all other material parameters are unchanged. Figure 4-5 shows pareto fronts for kinetic separation of a 50:50 mixture using materials with five diffusivity ratios of the two components ranging from 6.5 to 260, when equilibrium is described by isotherm C (in Figure 4-4). Similar results were also obtained for the other three isotherms as well.

The results show that there is an optimal range of crystal radius that maximizes the purity recovery trade-off in the packed bed. Product recovery suffers when the crystal radius is too small as evidenced by the convex shape of the pareto front. On the other hand, at too high a crystal radius, the maximum purity suffers heavily. The effect of crystal radius on PSA performance becomes increasingly mild as the difference between the diffusivity of the two components increases. We can conclude that the crystal radius is an inherent material property parameter that impacts optimal performance of the PSA cycle. External factors such as cycle step times are unable to compensate for its impact.

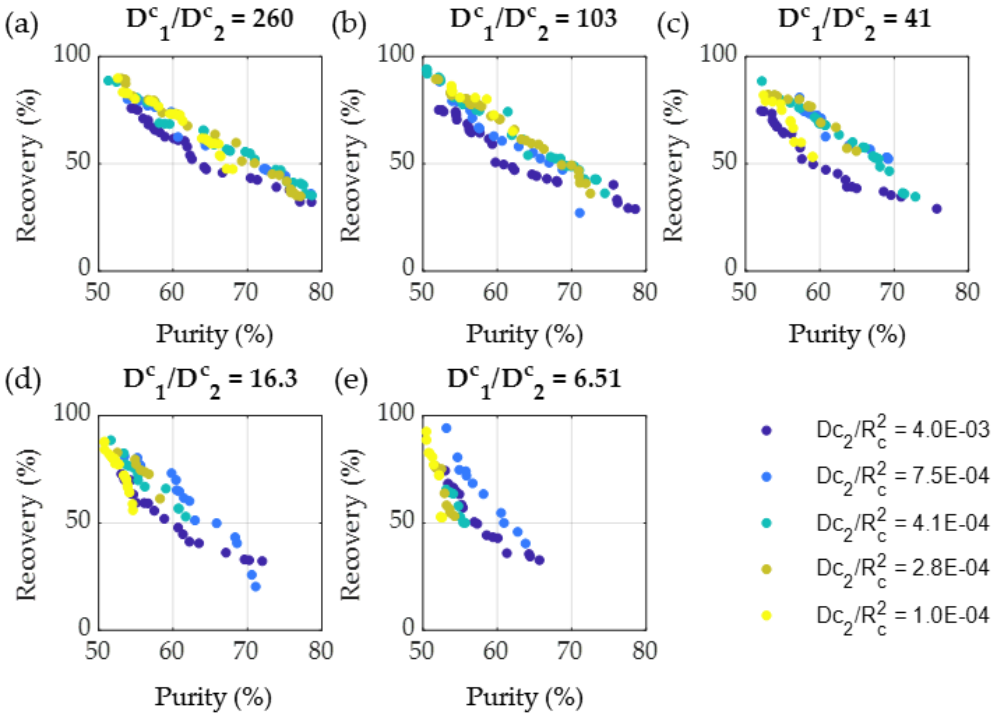

Figure 4-5 - Pareto plot of the separation of a 50:50 gas mixture on a hypothetical adsorbent with thermodynamic parameters corresponding to isotherm C in Figure 4-4 and kinetic property parameters as indicated on the plots. The aim of this plot is to show the existence of an optimal crystal radius (indicated by the parameter D_2^c/R_c^2.

4.3.4.2 Effect of isotherm parameters and diffusivity ratio

With a better understanding of the impact of crystal radius on kinetic separation performance, we next consider the relative impact of inherent material property parameters, the diffusivity ratio and the shape of the isotherm. Figure 4-6 shows the purity-recovery pareto fronts for kinetic separation of a 50:50 mixture of gases with material adsorption equilibrium represented by the four different isotherms shown in Figure 4-4. The analysis is performed for four different diffusivity ratios $\left(\text{i.e. } D_1^c/D_2^c\right)$ ranging from 16 to 260. Each pareto front is obtained in the optimal crystal radius $\left(\text{i.e. } D_2^c/R_c^2\right)$ as explained in the previous section. It is evident that for equal equilibrium selectivity

$\left(\text{here, } \eta_{equilibrium} = 1\right)$ and diffusivity ratio, there is a very significant impact of the isotherm shape on kinetic separation performance. Each plot shows that increased steepness of the isotherm slope (achieved mathematically by increasing affinity parameter *b*), leads to a better separation performance irrespective of other material property parameters.

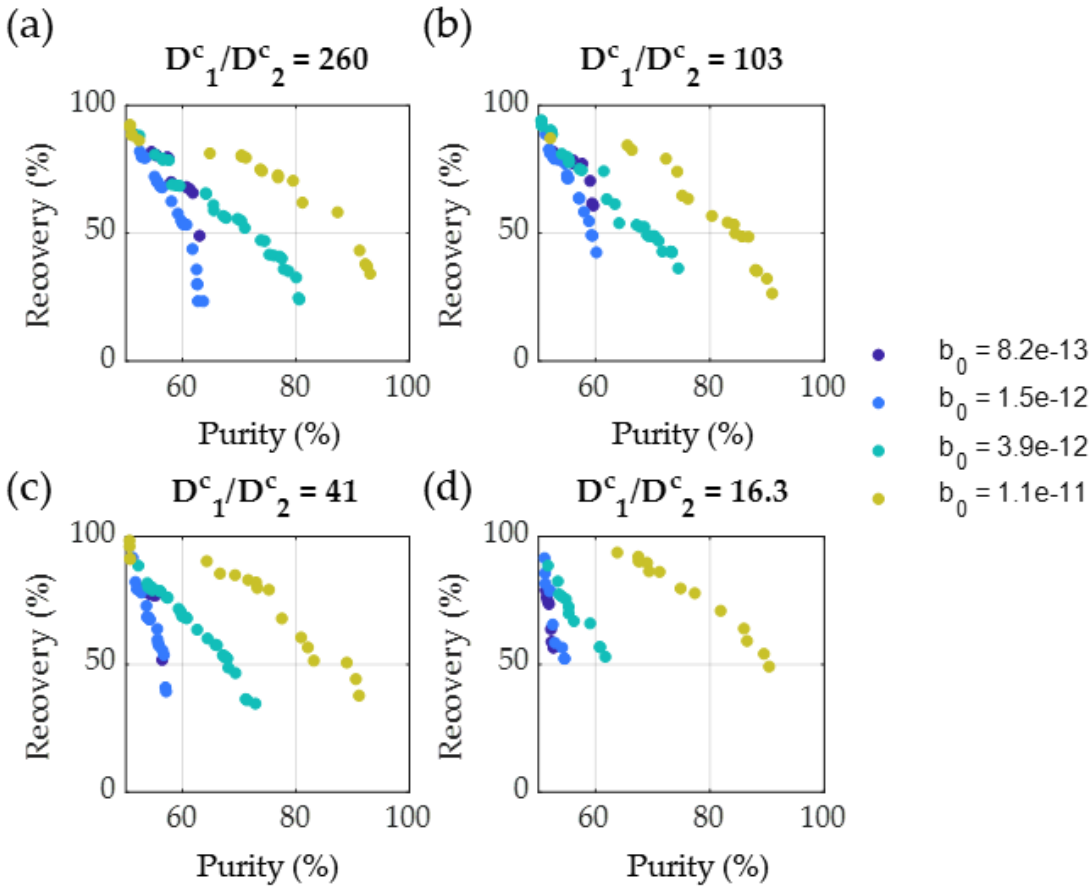

Figure 4-6 - Pareto plot of the separation of a 50:50 gas mixture on a hypothetical adsorbent with thermodynamic and kinetic property parameters as indicated on the plot. Higher slope of the isotherm leads to a better pareto trade-off between purity and recovery. (Plots of the isotherms are also shown in Figure 4-4.)

The following analysis investigates the relative importance of diffusivity ratio and the isotherm shape on kinetic separation efficiency. This is shown in Figure 4-7 and Figure

4-8 for isotherms D and B (refer to Figure 4-4) which are shallow and steep isotherms respectively. In both cases it is visible that significant changes in diffusivity ratio have relatively mild impact on the overall kinetic separation performance. The impact of changing the diffusivity ratio is especially low when the isotherm has a steeper slope (Figure 4-7). Improvement in performance can be achieved by increasing diffusivity ratio when the isotherm is shallow (Figure 4-8).

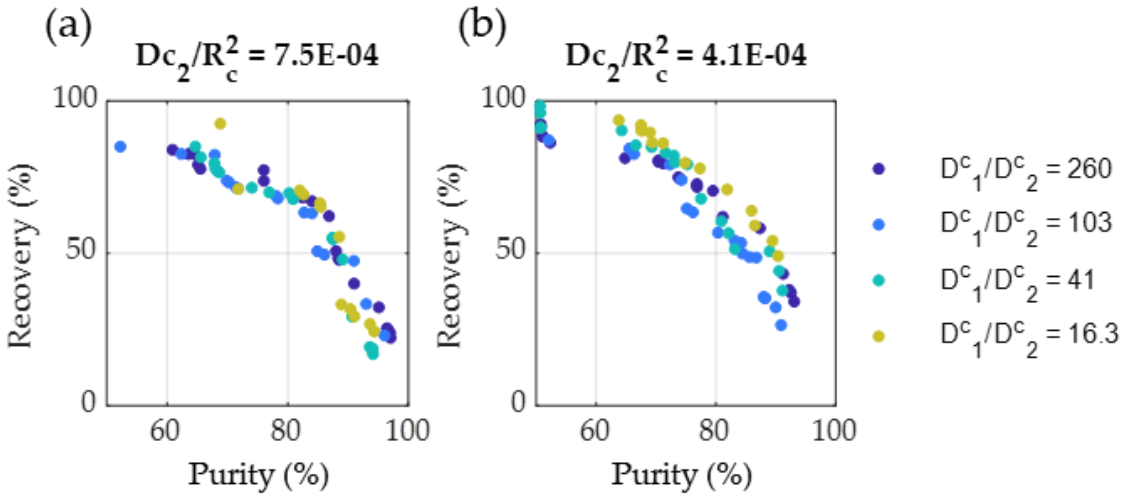

Figure 4-7 - Pareto plot of the separation of a 50:50 gas mixture on a hypothetical adsorbent with kinetic property parameters as indicated on the plot. Thermodynamic parameters match isotherm D in Figure 4-4.)

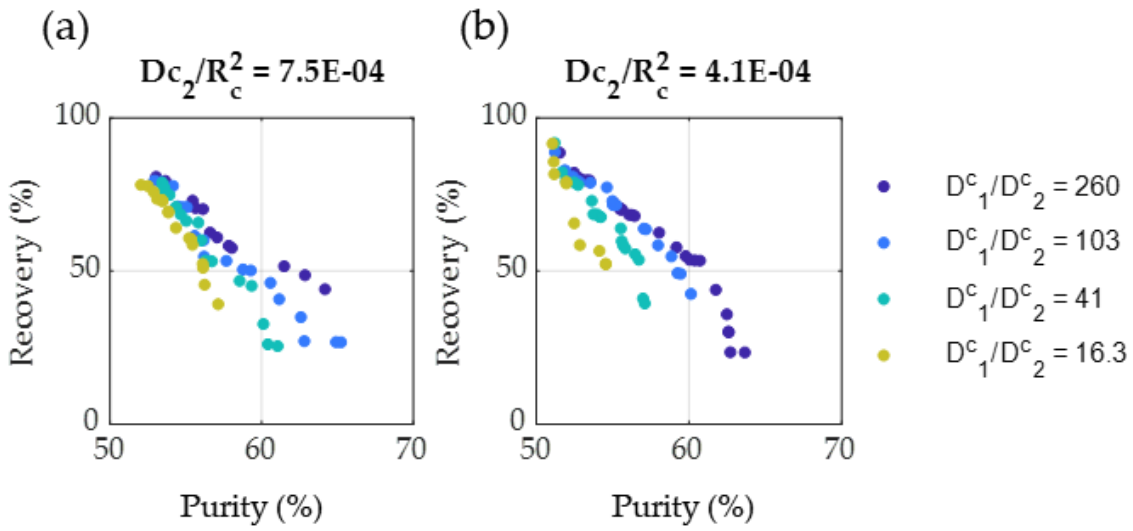

Figure 4-8 - Pareto plot of the separation of a 50:50 gas mixture on a hypothetical adsorbent with kinetic property parameters as indicated on the plot. Thermodynamic parameters match isotherm B in Figure 4-4.)

4.3.5 Exploring impact of property parameters through the simple crystal uptake model

In the previous section, full-scale PSA cycle optimizations have indicated a strong correlation between a material's isotherm parameters and its kinetic separation performance in the case where equilibrium selectivity was close to 1. However, each case required an optimization run which takes around 3-6 hours to complete. While this provides a detailed understanding of the system, a faster approach will enable expansion of our analysis to all possible equilibrium selectivities. In the following section therefore, we use the transient characteristics from single crystal uptake simulations, to explore the impact of varying material property parameters on kinetic separation effectiveness. We have used SAIL algorithm to facilitate systematic exploration as described in section 4.2.2. The performance metric is *maximum improvement in selectivity* as described in section 4.3.2. The features of interest i.e. the *phenotypes* are the equilibrium selectivity and the diffusivity ratio, also elaborated in section 4.3.2. We also compare our findings to the commonly used

measure to compare kinetic separation performance of materials, the ideal kinetic selectivity ($\eta_{kinetic_{ij}}$) as indicated in equation 4.1. The ideal kinetic selectivity is an analytical expression based on the assumption of short contact times and uncoupled crystal diffusion.

4.3.5.1 SAIL Results for Competitive Langmuir Isotherm

The input parameter space (*phenotype*) along with the isotherm equations have been described in section 4.3.3. In the following analysis we have only considered cases where the saturation capacities for both components in the gas mixture are identical (i.e. θ_2^{sat} =1.) as is appropriate for competitive Langmuir isotherm. As mentioned previously component 1 is the faster diffusing component and component 2 is the slower diffusing. We are only interested in cases where the maximum transient kinetic selectivity towards component 1 is greater than 1. Calculations that resulted in uptakes that had maximum kinetic selectivity towards the faster component less than 1 were discarded.

Figure 4-9 (a) & (b) show the final maps for the optimal input parameters predicted by SAIL. Since we have not included cases where kinetic selectivity towards the faster diffusing component 1 was unfavorable (< 1) there are some empty bin on the left-hand side of these plots. We notice that the affinity parameters (b_1 and b_2) are selected to be the maximum possible given the restriction on equilibrium selectivity which is represented on the x-axis. This observation is in agreement with what was observed for the full PSA optimizations for materials with equilibrium selectivity of 1. The SAIL algorithm took approximately 500 seconds to run with a precise evaluation budget of 150, which is

significantly lower than the PSA evaluations, which took 3-6 hours to evaluate a single point.

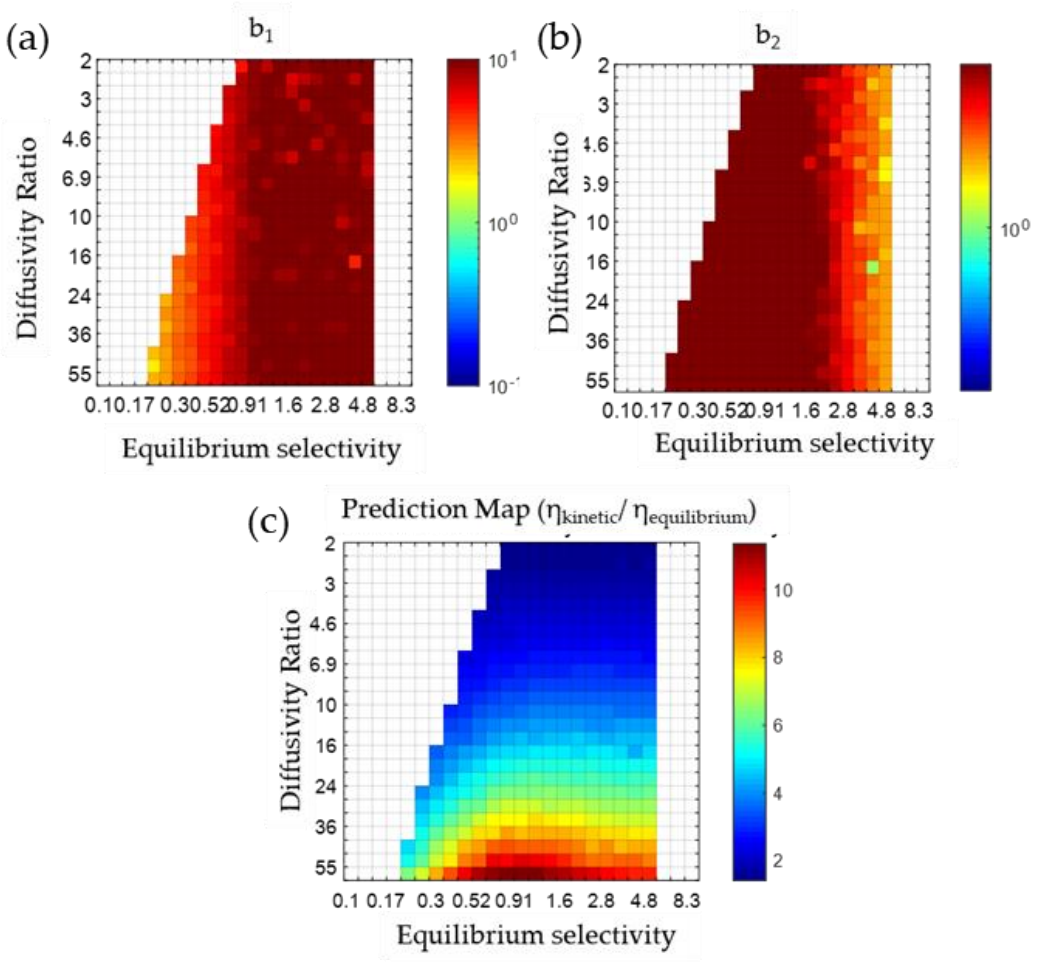

Figure 4-9 - SAIL results showing the predicted material parameters for high kinetic separation performance for competitive Langmuir isotherms and Maxwell-Stefan diffusion formulation. (c) shows the predicted values of maximum improvement in selectivity over equilibrium when separation is performed using these high-performing materials

Figure 4-9 (c) shows the *maximum improvement in selectivity* predicted by SAIL for different combinations of diffusivity ratio and equilibrium selectivity. The diffusivity ratios plotted vary from 2 (i.e. $\sqrt{D_1^c / D_2^c} = 1.42$) up to 55 ((i.e. $\sqrt{D_1^c / D_2^c} = 7.42$). If

equation 4.1 was accurate then the performance metric $\left(\eta_{kinetic}/\eta_{equilibrium}\right)$ would be correlated to the diffusivity ratio alone and vary from 1.4 to 7.4. However, we observe that there is also a strong positive correlation with the equilibrium selectivity, especially in the lower selectivity ranges (< 1). At higher equilibrium selectivities, the correlation with equilibrium selectivity is much weaker. However, the predicted maximum improvement in kinetic selectivity is still higher than just $\sqrt{D_1^c/D_2^c}$ which indicates a strong coupling of system kinetics and thermodynamics which cannot be captured by equation 4.1 which assumes Fickian diffusion. One drawback of the current analysis is that we do not have any metric that can predict the impact of changing diffusion length on separation performance, as was done in the full scale PSA analysis in section 4.3.4.

4.3.5.2 Discussion and comparison with Fickian diffusion

To further emphasize the impact of system thermodynamics on kinetic separation performance, we have also performed SAIL analysis on the same set of material property parameters, using Fickian diffusion formulation as opposed to Maxwell-Stefan. The results are shown in Figure 4-10. Two important observations can be made. (a) & (b) show the isotherm parameters (b_1 and b_2) predicted to maximize kinetic separation performance. There is no observable pattern in the parameters selected by the algorithm, they appear random which is in contrast to what we observed in Figure 4-9. This shows that the isotherm shape has no impact on separation performance predicted by Fickian diffusion which is to be expected. The other observation is in Figure 4-10 (c) where we plot the maximum $\eta_{kinetic}/\eta_{equilibirum}$ which shows a linear correlation with diffusivity ratio alone, and appears uncorrelated to the equilibrium selectivity. Moreover, the values go from 1.4

to 7.4 which is what we expect from the ideal selectivity prediction of equation 4.1 (i.e. $\eta_{kinetic}/\eta_{equilibirum} = \sqrt{D_1^c/D_2^c}$).

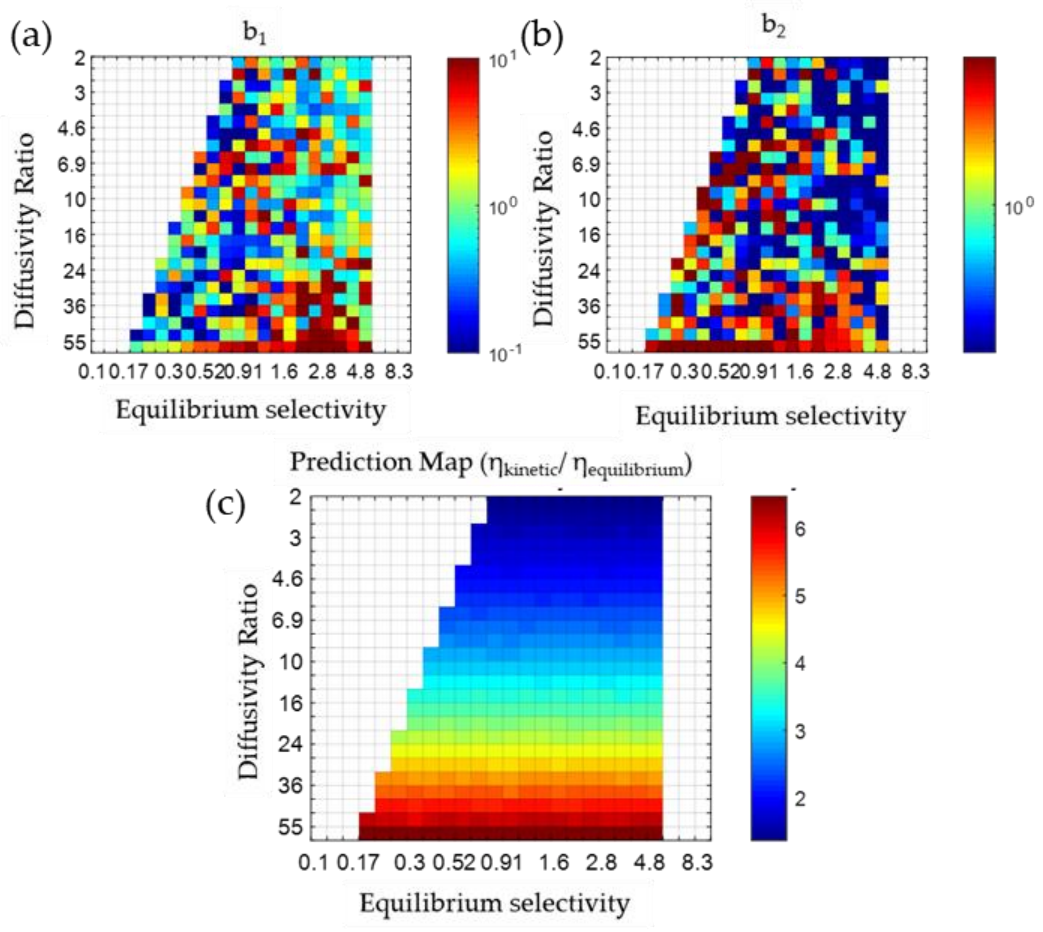

Figure 4-10 - SAIL results showing the predicted material parameters for high kinetic separation performance for competitive Langmuir isotherms and Fickian diffusion formulation. (c) shows the predicted values of maximum improvement in selectivity over equilibrium when separation is performed using these high-performing materials

4.3.5.3 Incorporating Toth isotherm into SAIL analysis

A limitation of using the competitive Langmuir isotherm to describe adsorption behavior is that it assumes equal saturation capacity of the adsorbent and site-

heterogeneity. To overcome this issue, we incorporated IAST calculations[48] for multi-component loadings, using single component Toth isotherms shown in equation 4.12.

$$\theta_i = \theta_i^{sat} \frac{b_i^{1/n_i} p_i}{\left(1 + b_i p_i^{n_i}\right)^{1/n_i}} = \theta_i^{sat} \frac{p_i}{\left(\frac{1}{b_i} + p_i^{n_i}\right)^{1/n_i}} \tag{4.12}$$

Where b_i is the temperature dependent affinity parameter and n_i is the temperature independent heterogeneity parameter[49]. $0 < n_i \leq 1$, and deviation from 1 indicates greater heterogeneity. $q^{sat}{}_i$ is the saturation loading of component *i*. Our focus here is on two component adsorption systems.

4.3.5.3.1 Calculation of Thermodynamic correction factor (Γ)

Whereas calculation of thermodynamic correction factor Γ_{ij} (equation 4.5) is analytical for the competitive Langmuir isotherm, typically, only a numerical estimate is possible when using IAST. This requires knowledge of equilibrium pressure corresponding to crystal loading at each radial node and at each time point, which greatly increases computational complexity. Landa et al[48] describe a procedure for analytical calculation of the Jacobian (*J*) form knowledge of loading and corresponding equilibrium pressure, without the need for an analytical multi-component isotherm (Appendix D). This has been used to enable analytical calculation of Γ (equation 4.13).

$$\Gamma = \left[\frac{q}{P}\right]\left[J\right]^{-1} \tag{4.13}$$

While these approaches were robust for a wide range of isotherm and diffusivity parameters, numerical failure was still unavoidable close to the boundary of our parameter range. This was attributed to the need for calculation of equilibrium pressure at each node of the crystal. To avoid this we approximated Γ form the multi-component Langmuir equation which has the following form (equation 4.14).

$$\Theta = \mathrm{col}\left(\theta_i\right) \quad \theta_{tot} = \sum_i \theta_i$$
$$\Gamma = \mathrm{I} + \left[\mathrm{I}\Theta\right] \left(\frac{1}{1-\theta_{tot}}\right) \tag{4.14}$$

Appendix D, Figure D-3 shows that this expression has very good qualitative agreement with the full calculation of Γ and was therefore found appropriate for the purpose of comparing relative performance of materials.

4.3.5.3.2 SAIL results

Figure 4-11 shows the results for running SAIL with isotherm parameters corresponding to single component Toth equation and the Maxwell-Stefan Diffusion formulation. The results are very similar to those described in section 4.3.5.1 using competitive Langmuir equations. The heterogeneity parameter was allowed to vary from 0.5 to 1. The algorithm shows preference for higher n values. This can be interpreted to mean a preference for steeper slopes in the isotherm. This cannot be correlated to a preference for site-heterogeneity simply due to the empirical nature of the Toth isotherm.

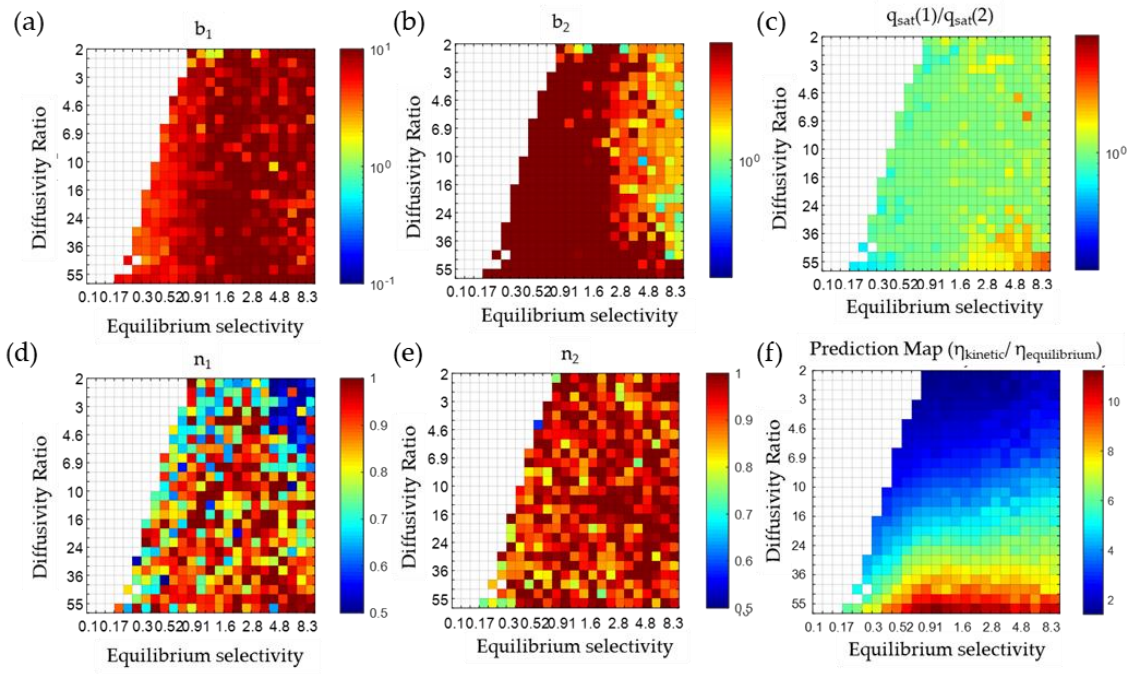

Figure 4-11 - SAIL results showing the predicted material parameters for high kinetic separation performance for Toth isotherms and Maxwell-Stefan diffusion formulation. (f) shows the predicted values of maximum improvement in selectivity over equilibrium when separation is performed using these high-performing materials

4.4 Summary

Kinetic separation exploits differences in diffusion coefficients of different adsorbates in the mixture irrespective of their equilibrium loading amounts. There is no straight forward method of screening adsorbents for kinetic separation based on diffusion coefficients and isotherm data alone. This is mostly due to the complex coupling between the kinetics and equilibrium. Our aim was to test the accuracy of the current standard approach of ranking material selectivity for particular kinetic gas-separation. It is denoted as a product of equilibrium selectivity and square-root of their diffusivity ratio. The study is conducted in two parts. Throughout our analysis we have used the extensively studied Maxwell-Stefan diffusion equation which has been shown to capture transient crystal

diffusion characteristics with far greater accuracy than the Fickian formulation. We have looked at optimized purity-recovery pareto curves in 3-step PSA cycles, for four Langmuir isotherms that have no equilibrium selectivity (=1). These hypothetical materials also varied in diffusivity ratio and crystal radius. The conclusion from our analysis was that for a given set of diffusivities, there exists an optimal range of crystal radius that can maximize separation performance. Smaller crystals result in poor process recovery whereas, larger crystals result in a reduction in optimal purity of the slow diffusing product. We also found that the slope of the isotherm has a very strong effect on separation performance, even for similar equilibrium selectivities. A higher slope of the isotherm resulted in higher purity of the slow product. The diffusivity ratio on the other hand had a milder impact on kinetic separation when compared to the isotherm slope. To expand our analysis to equilibrium selectivities other than 1, we have used a surrogate assisted illumination (SAIL) algorithm based on single crystal uptake simulations. As opposed to multiple hours spent in a PSA cycle optimization, a single crystal simulation takes a few seconds. Steep isotherm slopes were found to result in higher transient selectivities for similar equilibrium selectivity and diffusivity ratio. This correlates well with what we observed at the PSA cycle scale. Similar observations were made when we applied SAIL to hypothetical materials described by Toth isotherms. From these analysis we suggest that using the ideal kinetic selectivity metric mentioned earlier is inadequate for comparison of materials for kinetic separation of a target gas mixture. In addition, the combination of SAIL and single crystal uptake model was successfully able to replicate observations made using full PSA cycle optimizations. One shortcoming of our SAIL analysis was that we were not able to identify affect of crystal size on kinetic separation. This was mostly a limitation of our comparison

metric. Further work needs to be done to refine the performance metric used to compare materials using SAIL algorithm.

4.5 References

[1] Sholl, D. S.; Lively, R. P. Seven Chemical Separations to Change the World. *Nature* **2016**, *532* (7600), 435–437. https://doi.org/10.1038/532435a.

[2] Pimentel, B. R.; Lively, R. P. Enabling Kinetic Light Hydrocarbon Separation via Crystal Size Engineering of ZIF-8. *Ind. Eng. Chem. Res.* **2016**, *55* (48), 12467–12476. https://doi.org/10.1021/acs.iecr.6b03199.

[3] Wang, Y.; Zhao, D. Beyond Equilibrium: Metal-Organic Frameworks for Molecular Sieving and Kinetic Gas Separation. *Cryst. Growth Des.* **2017**, *17* (5), 2291–2308. https://doi.org/10.1021/acs.cgd.7b00287.

[4] Adil, K.; Belmabkhout, Y.; Pillai, R. S.; Cadiau, A.; Bhatt, P. M.; Assen, A. H.; Maurin, G.; Eddaoudi, M. Gas/Vapour Separation Using Ultra-Microporous Metal-Organic Frameworks: Insights into the Structure/Separation Relationship. *Chem. Soc. Rev.* **2017**, *46* (11), 3402–3430. https://doi.org/10.1039/c7cs00153c.

[5] Koros, W. J.; Zhang, C. Materials for Next-Generation Molecularly Selective Synthetic Membranes. *Nat. Mater.* **2017**, *16* (3), 289–297. https://doi.org/10.1038/nmat4805.

[6] Rege, S. U.; Yang, R. T. Propane/Propylene Separation by Pressure Swing Adsorption: Sorbent Comparison and Multiplicity of Cyclic Steady States. *Chem. Eng. Sci.* **2002**, *57* (7), 1139–1149. https://doi.org/10.1016/S0009-2509(01)00440-7.

[7] Kapoor, A.; Yang, R. T. Kinetic Separation of Methane-Carbon Dioxide Mixture by Adsorption on Molecular Sieve Carbon. *Chem. Eng. Sci.* **1989**, *44* (8), 1723–1733. https://doi.org/10.1016/0009-2509(89)80014-4.

[8] Ackley, M. W.; Yang, R. T. Kinetic Separation by Pressure Swing Adsorption: Method of Characteristics Model. *AIChE J.* **1990**, *36* (8), 1229–1238. https://doi.org/10.1002/aic.690360812.

[9] Krishna, R. Highlighting the Influence of Thermodynamic Coupling on Kinetic Separations with Microporous Crystalline Materials. *ACS Omega* **2019**, *4* (2), 3409–3419. https://doi.org/10.1021/acsomega.8b03480.

[10] Krishna, R. Tracing the Origins of Transient Overshoots for Binary Mixture Diffusion in Microporous Crystalline Materials. *Physical Chemistry Chemical Physics*. Royal Society of Chemistry 2016, pp 15482–15495. https://doi.org/10.1039/c6cp00132g.

[11] Krishna, R.; van Baten, J. M. Using Molecular Dynamics Simulations for Elucidation of Molecular Traffic in Ordered Crystalline Microporous Materials. *Microporous Mesoporous Mater.* **2018**, *258*, 151–169. https://doi.org/10.1016/j.micromeso.2017.09.014.

[12] Effendy, S.; Xu, C.; Farooq, S. Optimization of a Pressure Swing Adsorption Process for Nitrogen Rejection from Natural Gas. *Industrial and Engineering Chemistry Research*. American Chemical Society May 10, 2017, pp 5417–5431. https://doi.org/10.1021/acs.iecr.7b00513.

[13] Nandi, S. P.; Walker, P. L. Separation of Oxygen and Nitrogen Using 5A Zeolite and Carbon Molecular Sieves. *Sep. Sci.* **1976**, *11* (5), 441–453. https://doi.org/10.1080/01496397608085334.

[14] Erden, L.; Ebner, A. D.; Ritter, J. A. Separation of Landfill Gas CH_4 from N_2 Using Pressure Vacuum Swing Adsorption Cycles with Heavy Reflux. *Energy and Fuels* **2018**, *32* (3), 3488–3498. https://doi.org/10.1021/acs.energyfuels.7b03534.

[15] Majumdar, B.; Bhadra, S. J.; Marathe, R. P.; Farooq, S. Adsorption and Diffusion of Methane and Nitrogen in Barium Exchanged ETS-4. *Ind. Eng. Chem. Res.* **2011**, *50* (5), 3021–3034. https://doi.org/10.1021/ie1014124.

[16] Bárcia, P. S.; Zapata, F.; Silva, J. A. C.; Rodrigues, A. E.; Chen, B. Kinetic Separation of Hexane Isomers by Fixed-Bed Adsorption with a Microporous Metal - Organic Framework. *J. Phys. Chem. B* **2007**, *111* (22), 6101–6103. https://doi.org/10.1021/jp0721898.

[17] Bhadra, S. J.; Farooq, S. Separation of Methane-Nitrogen Mixture by Pressure Swing Adsorption for Natural Gas Upgrading. *Ind. Eng. Chem. Res.* **2011**, *50* (24), 14030–14045. https://doi.org/10.1021/ie201237x.

[18] Tanaka, S.; Fujita, K.; Miyake, Y.; Miyamoto, M.; Hasegawa, Y.; Makino, T.; Van Der Perre, S.; Cousin Saint Remi, J.; Van Assche, T.; Baron, G. V.; et al. Adsorption and Diffusion Phenomena in Crystal Size Engineered ZIF-8 MOF. *J. Phys. Chem. C* **2015**, *119* (51), 28430–28439. https://doi.org/10.1021/acs.jpcc.5b09520.

[19] Mendes, P. A. P.; Horcajada, P.; Rives, S.; Ren, H.; Rodrigues, A. E.; Devic, T.; Magnier, E.; Trens, P.; Jobic, H.; Ollivier, J.; et al. A Complete Separation of Hexane Isomers by a Functionalized Flexible Metal Organic Framework. *Adv. Funct. Mater.* **2014**, *24* (48), 7666–7673. https://doi.org/10.1002/adfm.201401974.

[20] Raghavan, N. S.; Hassan, M. M.; Ruthven, D. M. Numerical Simulation of a PSA System Using a Pore Diffusion Model. *Chem. Eng. Sci.* **1986**, *41* (11), 2787–2793. https://doi.org/10.1016/0009-2509(86)80010-0.

[21] Kirshna, R. Multicomponent Surface Diffusion of Adsorbed Species: A Description Based on the Generalized Maxwell-Stefan Equations. *Chem. Eng. Sci.* **1990**. https://doi.org/10.1016/0009-2509(90)87055-W.

[22] Hu, X.; Do, D. D. Multicomponent Adsorption Kinetics of Hydrocarbons onto Activated Carbon: Effect of Adsorption Equilibrium Equations. *Chem. Eng. Sci.* **1992**, *47* (7), 1715–1725.

[23] Krishna, R. A Unified Approach to the Modelling of Intraparticle Diffusion in Adsorption Processes. *Gas Sep. Purif.* **1993**, *7* (2), 91–104. https://doi.org/10.1016/0950-4214(93)85006-H.

[24] Kapteijn, F.; Moulijn, J. A.; Krishna, R. The Generalized Maxwell–Stefan Model for Diffusion in Zeolites:: Sorbate Molecules with Different Saturation Loadings. *Chem. Eng. Sci.* **2000**, *55* (15), 2923–2930. https://doi.org/10.1016/S0009-2509(99)00564-3.

[25] Farooq, S.; Rathor, M. N.; Hidajat, K. A Predictive Model for a Kinetically Controlled Pressure Swing Adsorption Separation Process. *Chem. Eng. Sci.* **1993**, *48* (24), 4129–4141. https://doi.org/10.1016/0009-2509(93)80259-S.

[26] Krishna, R. The Maxwell-Stefan Description of Mixture Diffusion in Nanoporous Crystalline Materials. *Microporous and Mesoporous Materials*. 2014. https://doi.org/10.1016/j.micromeso.2013.10.026.

[27] NAKAO, S.-I.; SUZUKI, M. Mass Transfer Coefficient in Cyclic Adsorption and Desorption. *J. Chem. Eng. Japan* **1983**, *16* (2), 114–119. https://doi.org/10.1252/jcej.16.114.

[28] Glueckauf, E.; Coates, J. I. 241. Theory of Chromatography. Part IV. The Influence of Incomplete Equilibrium on the Front Boundary of Chromatograms and on the Effectiveness of Separation. *J. Chem. Soc.* **1947**, No. 0, 1315. https://doi.org/10.1039/jr9470001315.

[29] Cavenati, S.; Grande, C. A.; Rodrigues, A. E. Separation of CH_4 / CO_2 / N_2 Mixtures by Layered Pressure Swing Adsorption for Upgrade of Natural Gas. *Chem. Eng. Sci.* **2006**, *61* (12), 3893–3906. https://doi.org/10.1016/j.ces.2006.01.023.

[30] Liu, T.; First, E. L.; Hasan, M. M. F.; Floudas, C. A. A Multi-Scale Approach for the Discovery of Zeolites for Hydrogen Sulfide Removal. *Comput. Chem. Eng.* **2016**, *91*, 206–218.

[31] Hasan, M. M. F.; First, E. L.; Floudas, C. A. Cost-Effective CO_2 Capture Based on in Silico Screening of Zeolites and Process Optimization. *Phys. Chem. Chem. Phys.* **2013**, *15* (40), 17601–17618.

[32] Rajagopalan, A. K.; Avila, A. M.; Rajendran, A. Do Adsorbent Screening Metrics Predict Process Performance: A Process Optimisation Based Study for Post-Combustion Capture of CO_2. *Int. J. Greenh. Gas Control* **2016**, *46*, 76–85.

[33] Maring, B. J.; Webley, P. A. A New Simplified Pressure/Vacuum Swing Adsorption Model for Rapid Adsorbent Screening for CO_2 Capture Applications. *Int. J. Greenh. Gas Control* **2013**, *15*, 16–31.

[34] Hao, P.; Shi, Y.; Li, S.; Zhu, X.; Cai, N. Correlations between Adsorbent Characteristics and the Performance of Pressure Swing Adsorption Separation Process. *Fuel* **2018**. https://doi.org/10.1016/j.fuel.2018.05.030.

[35] Braun, E.; Zurhelle, A. F.; Thijssen, W.; Schnell, S. K.; Lin, L.-C.; Kim, J.; Thompson, J. A.; Smit, B. High-Throughput Computational Screening of Nanoporous Adsorbents for CO_2 Capture from Natural Gas. *Mol. Syst. Des. Eng.* **2016**, *1* (2), 175–188.

[36] First, E. L.; Hasan, M. M. F.; Floudas, C. A. Discovery of Novel Zeolites for Natural Gas Purification through Combined Material Screening and Process Optimization. *AIChE J.* **2014**, *60* (5), 1767–1785.

[37] Leperi, K. T.; Chung, Y. G.; You, F.; Snurr, R. Q. Development of a General Evaluation Metric for Rapid Screening of Adsorbent Materials for Postcombustion CO_2 Capture. *ACS Sustain. Chem. Eng.* **2019**, *7* (13), 11529–11539.

[38] Krishna, R.; Long, J. R. Screening Metal-Organic Frameworks by Analysis of Transient Breakthrough of Gas Mixtures in a Fixed Bed Adsorber. *J. Phys. Chem. C* **2011**, *115* (26), 12941–12950. https://doi.org/10.1021/jp202203c.

[39] Krishna, R. Methodologies for Screening and Selection of Crystalline Microporous Materials in Mixture Separations. *Separation and Purification Technology*. 2018. https://doi.org/10.1016/j.seppur.2017.11.056.

[40] Gaier, A.; Asteroth, A.; Mouret, J.-B. Data-Efficient Exploration, Optimization, and Modeling of Diverse Designs through Surrogate-Assisted Illumination. In *Proceedings of the Genetic and Evolutionary Computation Conference*; GECCO '17; Association for Computing Machinery: New York, NY, USA, 2017; pp 99–106. https://doi.org/10.1145/3071178.3071282.

[41] Mouret, J.-B.; Clune, J. Illuminating Search Spaces by Mapping Elites. *arXiv Prepr. arXiv1504.04909* **2015**.

[42] Krishna, R. Describing the Diffusion of Guest Molecules inside Porous Structures. *J. Phys. Chem. C* **2009**, *113* (46), 19756–19781.

[43] Krishna, R. Occupancy Dependency of Maxwell–Stefan Diffusivities in Ordered Crystalline Microporous Materials. *ACS omega* **2018**, *3* (11), 15743–15753.

[44] Krishna, R.; van Baten, J. M. Using Molecular Dynamics Simulations for Elucidation of Molecular Traffic in Ordered Crystalline Microporous Materials. *Microporous and Mesoporous Materials*. Elsevier March 1, 2018, pp 151–169. https://doi.org/10.1016/j.micromeso.2017.09.014.

[45] Vignes, A. Diffusion in Binary Solutions. Variation of Diffusion Coefficient with Composition. *Ind. Eng. Chem. Fundam.* **1966**, *5* (2), 189–199.

[46] Finlayson, B. A. Orthogonal Collocation in Chemical Reaction Engineering. *Catal. Rev. Sci. Eng.* **1974**, *10* (1), 69–138.

[47] Müller, J. SOCEMO: Surrogate Optimization of Computationally Expensive Multiobjective Problems. *INFORMS J. Comput.* **2017**, *29* (4), 581–596.

[48] Landa, H. O. R.; Flockerzi, D.; Seidel-Morgenstern, A. A Method for Efficiently Solving the IAST Equations with an Application to Adsorber Dynamics. *AIChE J.* **2013**, *59* (4), 1263–1277.

[49] Jaroniec, M.; Töth, J. Adsorption of Gas Mixtures on Heterogeneous Solid Surfaces: I. Extension of Tóth Isotherm on Adsorption from Gas Mixtures. *Colloid Polym. Sci.* **1976**, *254* (7), 643–649. https://doi.org/10.1007/BF01753693.

CHAPTER 5. MOVING BEYOND ADSORPTION CAPACITY IN DESIGN OF ADSORBENTS FOR CO_2 CAPTURE FROM ULTRA-DILUTE FEEDS: KINETICS OF CO_2 ADSORPTION IN MATERIALS WITH STEPPED ISOTHERMS

Parts of this chapter are adapted from 'Darunte, L. A.; Sen, T.; Bhawanani, C.; Walton, K. S.; Sholl, D. S.; Realff, M. J.; Jones, C. W. Moving Beyond Adsorption Capacity in Design of Adsorbents for CO2 Capture from Ultradilute Feeds: Kinetics of CO2 Adsorption in Materials with Stepped Isotherms. *Ind. Eng. Chem. Res.* **2019**, *58* (1), 366–377.' Dr. Lalit A. Darunte performed the experiments, while I performed simulations in gPROMS. Model development to explain experimentally observed phenomena was equally contributed to by Dr. Lalit A. Darunte and Trisha Sen.

5.1 Introduction

CO_2 capture from ultra-dilute feeds is gaining attention as a key part of global and local carbon management programs.[1–3] Direct air capture (DAC) is one of the few carbon emissions mitigation technologies that has the potential to be carbon negative. Amine-functionalized adsorbents such as mesoporous silica,[3–5] carbon,[6] and metal organic frameworks (MOFs)[7,8] have attracted attention for DAC because of their high CO_2 capacities even at ultra-dilute CO_2 concentrations. Much of the work in this field has focused on the development of materials with large equilibrium adsorption capacities.[9–11]

Metal organic frameworks (MOFs) are a class of hybrid organic-inorganic materials that have generated significant interest for CO_2 capture. Several MOFs have been developed that strongly adsorb CO_2 at ultra-dilute concentrations.[12–14] One example is the amine-functionalized Mg_2(dobpdc) material reported by Long and co-workers.[13,15,16] The Mg_2(dobpdc) framework, when functionalized with N,N'-dimethyl ethylene diamine (MMEN) and ethylene diamine (ED), have room-temperature CO_2 uptakes of 3 mmol/g[15] and 2.83 mmol/g,[17]respectively, in the presence of 0.4 mbar of CO_2. The sigmoidal shape of the CO_2 isotherm in these materials has been explained in terms of a cooperative insertion mechanism in which capture of one CO_2 creates a facile pathway for capture of another CO_2. This mechanism has led to the creation of a series of materials with a sharply stepped CO_2 adsorption isotherm in which the variation in metal centers and diamines allows the pressure at which the step occurs to be tuned.[15]The existence of a sharp step in the CO_2 isotherm suggests that a high working capacity for CO_2 capture may be possible in a cyclic adsorption process using a relatively small change in pressure or temperature.[16,18]A key aim of this chapter is to explore whether factors extending beyond this conceptual description of equilibrium adsorption may be critical in practical applications of these materials.

Additional considerations such as an adsorbent's stability and suitable adsorption/desorption kinetics are required to develop adsorbents for a practical process.[3,8] While previous articles[18–20] discussed the stability of these materials under humid conditions, not much is known about the kinetics of CO_2 adsorption for a potentially practical process. Often, the CO_2 adsorption kinetics put limitations on the throughput possible in a practical process. In CO_2 purification, the adsorption process is typically

halted when CO_2 breakthrough is achieved, and this may be kinetically controlled. The kinetics of CO_2 adsorption can also limit the utilization of an adsorption bed, as slow adsorbing systems can have long mass transfer zones (MTZ), leaving some fraction of the bed unused.[21] In this work, we are primarily concerned DAC processes, which are typically operated as extractions rather than purifications, where the emphasis is on the rate of CO_2 extraction using the system (mmol/g-adsorbent/h), making efficient bed use is critical.

Practical adsorption-based separations require that the adsorbent be deployed in a fixed-bed, immobilized on a practical substrate such as a monolith[22,23] or hollow fibers,[24,25] or deployed in a fluidized bed.[26] Ultra-dilute systems require special attention to the design of the gas-solid contactor, necessitating designs that offer very low pressure drops such as fiber and monolith contactors.[11,27] Mass transfer in these systems can potentially be affected by a range of competing heat and mass transfer effects, including film, macropore, or micropore resistances and adsorption/desorption/reaction. Film and macropore resistances are relatively well understood.[28,29] Non-trivial components of system design include the estimation of micropore diffusion, surface resistances, and reaction (or adsorption/desorption) kinetics. Usually, one or more of these are the controlling resistances and limited studies exist for transport of CO_2 in supported amine materials.[30–38] In the absence of precise microscopic techniques, macroscopic techniques such as gravimetric uptake or pressure decay can be used to measure the kinetics of CO_2 adsorption.

Several different CO_2 adsorption kinetic models have been proposed to describe thermogravimetric gas (TGA) uptake analysis for amine-functionalized adsorbents. Pseudo-first order,[39,40] pseudo-second order,[41] Avrami's fractional-order,[42] and other

fractional-order[30] kinetic models have all been explored. Serna-Guerro et al.[31] studied TRI-PE-SBA-15 (an aminosilane-grafted mesoporous silica material) on a TGA using a first order, a pseudo-second order, and an Avrami model, and suggested the Avrami model fit the data best for the adsorption of CO_2 at 5% concentration in N_2 at elevated temperatures. Other examples where the Avrami model has been applied to CO_2 adsorption include amine-functionalized multi-walled carbon nanotubes,[43]TEPA-functionalized mesoporous silica,[33,34] and poly(ethyleneimine) (PEI) modified phenolic resin.[35] The application of Avrami model to adsorption of CO_2 in amine-functionalized materials is not without drawbacks; it lacks an underlying physical mechanism, and the rate constant becomes very large at long times. Other studies[32,36,37,44] in adsorption of CO_2 in polyamine-functionalized silica included the development semi-empirical models that attempted to utilize underlying mechanism of CO_2 adsorption.

The work summarized above used TGA experiments to assess CO_2 uptake. These experiments offer a useful initial assessment of an adsorbent but understanding mass transfer in packed beds or other supported adsorbent systems requires consideration of additional factors such as axial dispersion and heat effects. These factors are less important in TGA experiments, which typically use high flow rates. For example, Bollini et al.[45] analyzed CO_2 adsorption on 3-aminopropyl silane (APS) functionalized mesoporous SBA-15 silica using a packed-bed adsorber. They found that a single parameter LDF (Linear Driving Force) model is not sufficient to predict the long tail observed in the CO_2 breakthrough from a packed bed with material with high amine loadings and that heat effects were negligible at low flow rates for dilute feeds.

A well-designed experiment with a small bed can allow accurate predictions for larger beds if it can capture the dynamics of CO_2 adsorption satisfactorily. Some of the parameters of interest are the CO_2 concentration profile at the exit of the bed, the fractional bed usage, the overall CO_2 capture fraction, the breakthrough time, the productivity, and the adsorption rate constant, k_{ads}. Mass transfer of CO_2 in a packed bed can be modeled by equation 5.1,[46] which takes into account dispersive and mass transfer effects.

$$\frac{\partial C_g}{\partial t} = D_{ax}\frac{\partial^2 C_g}{\partial z^2} - \frac{u_g}{\varepsilon}\frac{\partial C_g}{\partial z} - \frac{(1-\varepsilon)\rho_p}{\varepsilon}\frac{dq}{dt} \tag{5.1}$$

Here C_g, D_{ax}, u_g, ρ_p, ε are the gas phase concentration, axial dispersion coefficient, gas phase superficial velocity, particle density, and porosity, respectively.

In the present work, CO_2 adsorption in packed beds was studied in materials with stepped isotherms using MMEN-Mg_2(dobpdc) as an example. Local equilibrium theory predicts the formation of a "Dual Shock" breakthrough profile with a plateau located at the concentration/pressure step in the sigmoidal isotherm. Our experimental results qualitatively followed this expected behavior, but showed significant deviations. Our results indicate a striking difference in the CO_2 uptake at different flowrates and concentrations. This work highlights the importance of kinetic models in understanding the full utility of adsorbents and develops a general framework that can be used to analyze other materials with stepped CO_2 isotherms.

5.2 Experimental Section (sections 5.2.1 to 5.2.4 are the contributions of L. Darunte)

5.2.1 Chemicals

$Mg(NO_3)_2$-6-H_2O (Fischer, reagent grade), N-N' dimethyl ethylene diamine (Fischer, reagent grade), dimethylformamide (Fischer, ACS grade), N-hexane (Fischer, anhydrous,) and methanol (BDH Chemicals, ACS grade) were used as received. N-hexane and MMEN were stored in an N_2 containing glovebox to keep them moisture free.

5.2.2 Material Synthesis

H_4(dobpdc) was synthesized using the approach of McDonald et al.[13] Mg_2(dobpdc) was then synthesized following the recipe of McDonald et al.[15] The synthesis was performed in a convection oven at 120 °C in sealed pressure tubes to achieve a narrow distribution of crystal sizes. Scanning electron microscopy (SEM) showed needle-shaped crystal with 3-5 μm length. Needle-shaped crystals are akin to those observed in Figure 3.4 of our previous publication.[22]

5.2.3 Characterization

N_2 Physisorption & Powder X-ray diffraction (PXRD) measurement details can be found in our previous publication.[22]

CO_2 adsorption isotherms were obtained using a Micromeritics 3 Flex at various temperatures (25 °C, 49 °C, and 69 °C). MOF samples (~70 mg) were activated at 100 °C under 10 μBar vacuum for 4h. The adsorption isotherm at 23 °C was obtained based on the modeling fit to experimental isotherms at three different temperatures.

5.2.4 Breakthrough Adsorption Experiments

A custom-built setup, shown schematically in Figure 5-1, was used to perform breakthrough adsorption measurements. Helium was used as the carrier gas. Pre-mixed He containing 400 ppm CO_2 was obtained from Matheson Trigas Ltd. Pre-mixed He containing 1000 and 10020 ppm CO_2 were obtained from Airgas Inc. The system consists of mass flow controllers (MFC, 0-200 SCCM/min N_2) to control the flowrate of He and pre-mixed mixtures of CO_2 in He. A LI-COR 840 analyzer was used to continuously measure the effluent gas concentration. The LI-COR 840 is an absolute non-dispersive infrared (IR) based analyzer with a measurement range of 0-20000 ppm CO_2. The temperature in the bed was recorded with a type K thermocouple. MOF powders containing small crystals agglomerated into larger particles were sieved to obtain particles in the size range of 153-425 μm. The packed bed system was well insulated, and the temperature was controlled using an Omega benchtop CSi32 PID based controller. The bed was regenerated at 115 °C for 4 h until the exit concentration was below 5 ppm CO_2 between cycles. The deadtime of the system was measured using a helium tracer and was found to be less than 1 min for the employed experimental conditions. Additional analysis of the impact of the dead volume on the spreading of the breakthrough curve (Figure E-7) suggested that negligible spreading of the breakthrough for the conditions used in the experiments. Correspondingly, the effect of dead volume on the breakthrough are neglected in the present analysis. Other properties of the bed are listed in Table 5-1.

Table 5-1 - Parameters of the packed bed adsorber and operating conditions.

Packed bed experiments parameters	Value
Length of the bed	5.5 cm
Internal radius	0.4 cm
Desorption Temperature	115 °C
Adsorption Temperature	23 °C, 49 °C, 70 °C
Particle size (d_p)	153 – 425 µm
MOF crystal length	3-5 µm
MOF crystal density	860 kg/m^3
Particle porosity	0.85
Bed porosity (ε)	0.32
Adsorbent weight	60 mg
Feed	
Pressure	1.1 Bar
Flow rate	17.2 NmL/min, 28.2 NmL/min, 48.6 NmL/min, & 100 NmL/min
Concentration of CO_2 in the feed	400 ppm, 1000 ppm, 5660 ppm, & 10020 ppm

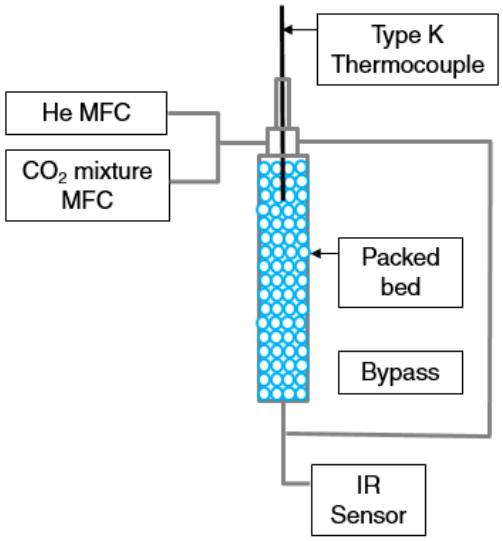

Figure 5-1 - Packed bed adsorption system schematic.

5.2.5 Adsorption Isotherm Fitting

The sigmoidal CO_2 isotherm of MMEN-Mg_2(dobpdc) is modeled using the method outlined by Hefti et al.[52] with some modifications. Total adsorption is the sum of two

adsorption mechanisms denoted by q_1^*, and q_2^*. The equilibrium adsorbed quantity at the step partial pressure, p_{step} is denoted by q_{sat}. Adsorption of CO_2 below p_{step} is represented by a Sips isotherm with a temperature dependent surface heterogeneity factor (n). A combination of Langmuir and Henry's isotherm is used after the transition step.

$$q_{total} = q_1^* + q_2^* \tag{5.2}$$

$$q_1^* = q_{low}(1-w) + q_{sat}w \tag{5.3}$$

$$q_2^* = \left(q_{high} - q_{sat}\right)w \tag{5.4}$$

$$q_{low} = \frac{q_L(b_L p)^n}{1+(b_L p)^n} \text{ For } p < p_{step} \tag{5.5}$$

$$q_{high} = \frac{q_H b_H p}{1+b_H p} + q_U p \text{ For } p > p_{step} \tag{5.6}$$

$$q_{sat} = \frac{q_L(b_L p_{step})^n}{1+\left(b_L p_{step}\right)^n} \tag{5.7}$$

A smooth function (w) is used to switch between the low pressure Sips and the high pressure Langmuir-Henry isotherms, shown here in equation 5.8. Parameters in the

isotherm are listed in Table C-1. Other details in isotherm are given in equation C.1-C.13 and Table C-1.

$$w = \left(\frac{exp\left(\frac{log(p) - log(p_{step})}{\sigma} \right)}{1 + exp\left(\frac{log(p) - log(p_{step})}{\sigma} \right)} \right)^{\gamma} \tag{5.8}$$

The temperature dependence of the transition pressure, p_{step} is modeled using equation 5.9. A reference state was assumed at 313 K for the p_{step} of 0.8 mbar[15]. The temperature dependence of various parameters was obtained based on isotherms at different temperatures.

$$p_{step}(T) = p_{step,0} \exp\left(-\frac{\Delta H_{step}}{R} \left(\frac{1}{T_0} - \frac{1}{T} \right) \right) \tag{5.9}$$

5.2.6 Linear Driving Force Parameter Model for Packed Bed Adsorption

A packed bed model for CO_2 adsorption was developed to simulate the temperature swing adsorption process. In a typical packed bed experiment, adsorbents were sieved to obtain adsorbent particles between 153-425 μm. This typically results in macropores and micropores inside each particle. The mass balance in the packed bed is modeled by equation 5.1, which accounts for mass transport by convection and diffusion in the gas phase. Equation 5.10 describes mass transfer for pressures below the step pressure (p_{step}) using a pseudo-first order (PFO) model. Equation 5.11 describes mass transfer with an Avrami model for pressures above the step pressure. The detailed mass transfer model in a

packed bed was adapted from Sen et al.[46], expressed in the appendix with equations C.14-C.29.

$$\frac{\partial q_1}{\partial t} = k_1(q_{eq1} - q_1) \text{ For } p < p_{step} \tag{5.10}$$

$$\frac{\partial q_2}{\partial t} = k_2^{n_A} t^{(n_A - 1)}(q_{eq2} - q_2) \text{ For } p > p_{step} \tag{5.11}$$

The initial and boundary conditions that account for zero loading at zero concentration of CO_2 in the bed are

$$C_{g,CO_2}\big|_z = 0, q_{CO_2}\big|_z = 0 \text{ At } t = 0 \tag{5.12}$$

$$-\varepsilon D_{ax,i} \left.\frac{\partial C_{g,i}}{\partial z}\right|_0 = u_{g_0}\left(C_{g,i_{in}} - C_{g,i}\big|_0\right), \text{ where}$$
$$\left(C_{g_{in}} = y_{ads}\frac{P_{tot}\big|_0}{RT\big|_0}\right) \tag{5.13}$$

$$\left.\frac{\partial C_{g,i}}{\partial z}\right|_L = 0 \tag{5.14}$$

where k_1, k_2, C_g, and q are the PFO model rate constant, Avrami model rate constant, gas phase concentration, and averaged adsorbed concentration, respectively. Axial dispersion coefficient, D_L was calculated using the Wakao & Funazkri empirical correlations[53] (Equations C.30, C.31). In all of our calculations, we assume that there are

no radial gradients in concentration, velocity, or temperature, that the gas phase in the bed can be described as an ideal gas, and the entry effects on heat and mass transfer are negligible. Breakthrough profiles were simulated using gPROMs[50] ModelBuilder for equations 5.1-5.12 and C.1-31.

5.3 Results and Discussion

5.3.1 Isotherm fit and temperature dependence of P_{step}

MMEN-Mg_2(dobpdc) samples were prepared and activated following the method by Long and workers.[15,16] Our measured equilibrium CO_2 adsorption isotherms in MMEN-Mg_2(dobpdc) at several temperatures (25 °C, 49 °C, and 69 °C) are shown in Figure 5-2. The solid curves in Figure 5-2 show fits to the experimental data using the isotherm model described above. As noted previously by Long and coworkers[15,16], the sharp step in the CO_2 isotherm is strongly temperature dependent. An additional predicted isotherm was also

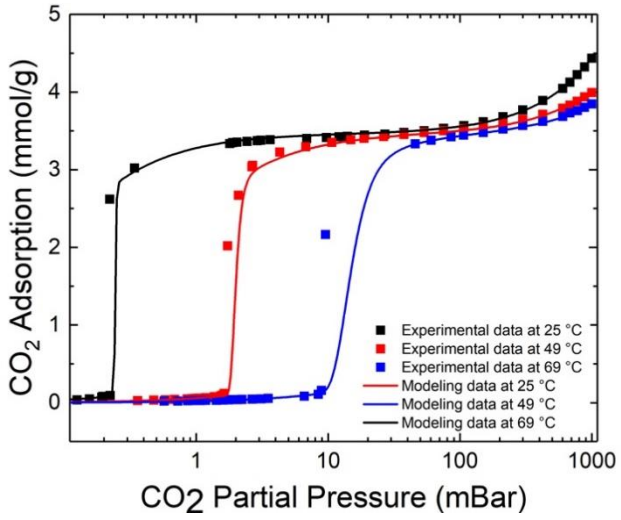

Figure 5-2 - Experimental data (symbols) and modeling fit (solid curves) at 25 °C (black), 49 °C (red) and 69 °C (blue) for CO2 adsorption in MMEN-Mg2(dobpdc). Parameters for the modeling fit are listed in Table C-1.

obtained at 23 °C to account for the temperature variation during breakthrough experiments.

We now consider the implications of the adsorption isotherms in MMEN-Mg_2(dobpdc) for packed beds filled with this material. Breakthrough profiles in a packed bed of MMEN-Mg_2(dobpdc) at a range of CO_2 partial pressures at 17.2 NmL/min flowrate were simulated in gProms[50], considering simple macropore diffusional resistance. Results of these simulations are shown in Figure 5-3 (left). We note that, for feeds with CO_2 partial pressures of 0.4 mBar, 1 mBar and 5.6 mBar, the breakthrough curves have behaviors that involve multiple steps or dual shock waves [51,52].

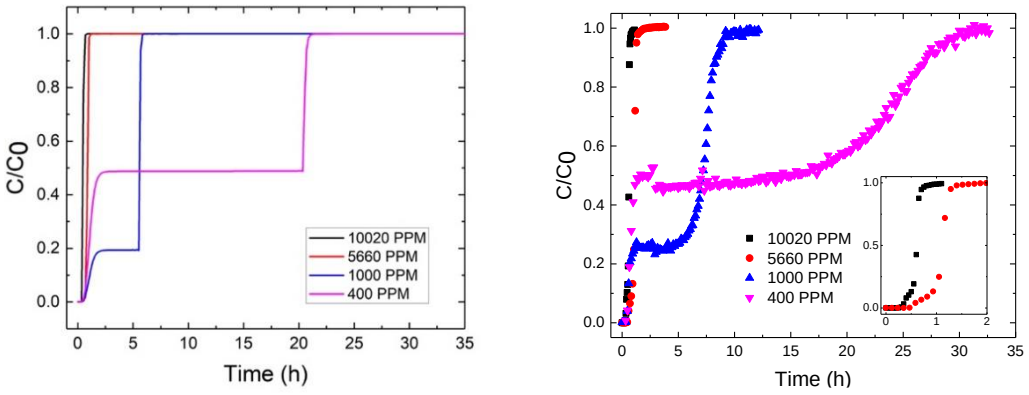

Figure 5-3 - Normalized breakthrough profiles for a packed bed of MMEN-Mg2(dobpdc) at 23 °C as a function of the partial pressure of CO_2 in the gas entering the bed. Simulations (left) and experiments (right) were carried out at the flow rate of 17.2 NmL/min. The results are shown in terms of the normalized CO_2 concentration at the exit of the bed.

To allow comparison of the predictions above with experimental data, breakthrough adsorption experiments for a packed bed with the parameters in Table 5-1 were performed at various concentrations, flowrates, and temperatures. Figure 5-3 (right) presents the normalized breakthrough adsorption data at the feed flowrate of 17.2 NmL/min

and various CO_2 concentrations. The experimental results match the predicted dual shock waves breakthrough profiles quite well. In particular, the profiles for feeds with CO_2 partial pressure of 0.4 mBar and 1 mBar show a relatively rapid initial shock wave breakthrough, followed by a longer dispersive wave to reach the feed concentration. Experimentally observed times for the second shock wave for feeds with CO_2 partial pressures of 0.4 mBar and 1 mBar are longer than the predictions from the simulations assuming simple macropore diffusion resistance. Additionally, the dispersive wave plateau concentrations were observed to be higher than expected. These observations suggest the presence of kinetic limitations, a point we return to below.

A sharp breakthrough curve is expected to improve the utilization of the bed. CO_2 capture from point sources such as coal or gas-fired power plants is typically operated as a purification process, where the operation of the bed is stopped when the effluent concentration of CO_2 exceeds a fraction (for example, 5%) of the feed concentration. DAC of CO_2, however, is expected to be performed as an extraction operation,[10] with the fraction of CO_2 extracted chosen based on process economics rather than regulatory constraints. For mmen-Mg_2(dobpdc), the stepped isotherm along with the very low capacity before the step signifies a relatively early breakthrough and a more useful metric in this case is the rate of CO_2 extraction. The rate of CO_2 extraction is calculated as moles of CO_2 captured per gram adsorbent per unit time. Quite often, the goal of DAC operation is to reduce otherwise long cycle times, even at the cost of a decrease in the fraction of CO_2 captured from the feed. The rate of CO_2 extraction is directly affected by the kinetics of CO_2 adsorption. Another metric that has been considered is the overall fraction of CO_2 captured when the CO_2 concentration at the exit of the bed is 95% of the feed concentration. Table

5-2 lists the net rate of CO_2 extraction using the bed along with the overall CO_2 capture fraction when 95% of the initial CO_2 concentration is detected in the effluent. A short first shock followed by a long wave leads to a poor utilization and lower rate of CO_2 extraction using the bed for feeds with a CO_2 partial pressure of 0.4 mBar or 1 mBar. As the breakthrough curve sharpens for higher concentrations of CO_2, both rate of CO_2 extraction and CO_2 capture fractions increase. The experimental CO_2 capture fraction is lower than the theoretical values, suggesting the existence of kinetic limitations.

Breakthrough adsorption experiments were conducted at a CO_2 partial pressure of 0.4 mBar and different flowrates. The resultant breakthrough profiles are shown in Figure 5-4. A typical dual shock wave breakthrough profile, such as those shown, has three important features, (i) the time of the first shock wave, (ii) the concentration of the dispersive wave, and (iii) the wave profile until the saturation.

Table 5-2 - Rate of CO_2 extraction and overall CO_2 capture fraction for the feed flow rate of 17.2 NmL/min and various concentrations.

Concentration/partial pressure of CO_2	Rate of CO_2 Extraction (mmol/g/h)	CO_2 Capture Fraction	Theoretical CO_2 Capture Fraction
400 ppm/0.4 mBar	0.11	44 %	52%
1000 ppm/ 1 mBar	0.44	64 %	81%
5660 ppm/ 5.67 mBar	3.34	83 %	97%
10020 ppm/ 10.02 mBar	5.86	83 %	98%

As expected, the breakthrough time for the first shock wave decreased as the flowrate of the gas mixture in the bed increased. A sharper breakthrough profile was

observed for higher flowrates. Unexpectedly, the concentration for the dispersive wave also increased along with a subsequent dip in the concentration, indicating non-equilibrium behavior. In the case of fast adsorption of CO_2, the dispersive wave concentration is expected to be at the effluent concentration corresponding to P_{step} for that particular temperature. For a concentration front entering the bed at 0.4 mBar, the concentration decreases as the bed adsorbs CO_2, and because of the step in the isotherm, a gas mixture with a partial pressure of less than P_{step} will slip through the bed with negligible adsorption.

The dual shock breakthrough behavior is most prominent at lower flowrates and the breakthrough profile broadens for higher flowrates. This has important implications for process design applications. Table 5-3 lists the rate of CO_2 extraction and CO_2 capture fraction for different flowrates at 400 ppm and 23 °C. As the flowrates are increased from 17.2 NmL/min to 100 NmL/min, the CO_2 capture fraction decreased from 44% to 17%, while the time needed to saturate the adsorbent also decreased. Again, the experimental CO_2 capture fraction was less than the theoretical CO_2 capture fraction. Net rate of CO_2 extraction using the bed increased from 0.11 mmol/g/h to 0.28 mmol/g/h. This indicates the tradeoff between rate of CO_2 extraction and CO_2 capture fraction while operating a practical process.

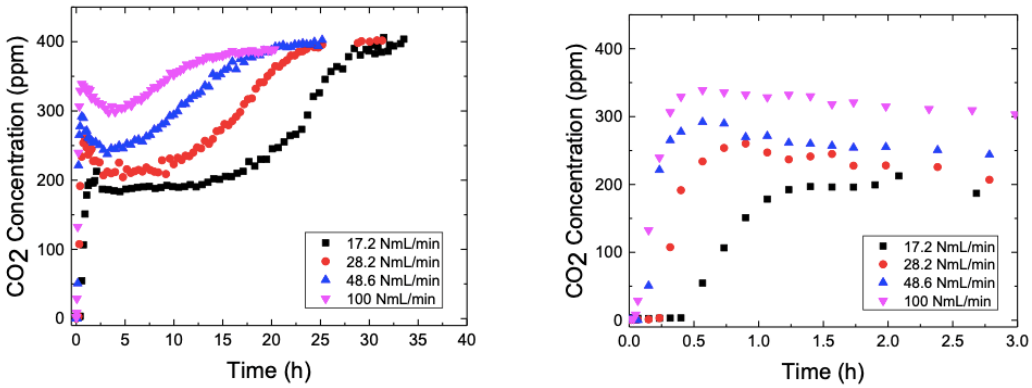

Figure 5-4 - Breakthrough adsorption experiments performed at 23 °C with the feed containing CO_2 at the partial pressure of 0.4 mBar and different flowrates of 17.2 NmL/min, 28.2 NmL/min, 48.6 NmL/min, and 100 NmL/min. Figure on the left shows full breakthrough profile while the figure on the right shows breakthrough profiles for first 3 hours.

Table 5-3 - Rate of CO_2 extraction and CO_2 Capture Fraction for the bed at different flowrates

Flowrate	Rate of CO_2 Extraction (mmol/g/h)	Experimental CO_2 Capture Fraction	Theoretical CO_2 Capture Fraction
17.2 NmL/min	0.11	44 %	52%
28.2 NmL/min	0.16	36 %	52%
48.6 NmL/min	0.21	27 %	52%
100 NmL/min	0.28	17 %	52%

5.3.2 Development of a kinetic model at 400 ppm CO_2

For DAC operations, the rate of CO_2 extraction is an important metric and a kinetic model accounting for the mass transfer of CO_2 inside the bed was developed. The rate of accumulation of CO_2 inside a particle is modeled using a linear driving force model. As shown in Figure E1, the breakthrough profiles for different flowrates were simulated at the

feed partial pressure of 0.4 mBar and 23 °C using a single linear driving force model. For all flowrates, the same plateau concentration and sharp shocks were predicted by the model. Figure E1 shows that a single linear driving force parameter model fails to explain the dispersive wave concentration and profile of the experimentally obtained breakthrough profiles. Further attempts were made by modeling CO_2 adsorption in MMEN-Mg_2(dobpdc) as a combination of two reactions, as described below.

At partial pressures below the step, CO_2 adsorption in MMEN-Mg_2(dobpdc) has been suggested to be associated with ammonium carbamate formation with a 2:1 amine-CO_2 stoichiometry.[55] This has been modeled as an PFO linear driving force model, as shown by equation 5.10 which accounts for ammonium carbamate pathway at partial pressures below the step pressure.

$$\frac{\partial q}{\partial t} = k_1(q_{eq1} - q_1) \text{ For } p < p_{step} \tag{5.10}$$

At pressures above p_{step}, cooperative insertion of CO_2 leads to the saturation of amine sites over a small change in the CO_2 partial pressure with a 1:1 amine-CO_2 stoichiometry.[15,16,55] Such cooperative transitions have been observed in a few biological systems.[56,57] In this mechanism, the binding of a second molecule to a multisite substrate is much faster than the binding of the first molecule. CO_2 uptake in a cooperative process can occur either as an insertion of CO_2 at a single site or as a part of the chain that has already formed. Net CO_2 uptake is then a weighted combination of both insertions (single site and chain). At the start of the cooperative insertion, net CO_2 adsorption is dominated by multiple single site insertions, which then set off propagating chains that capture

subsequent CO_2 molecules at faster rates. This particular type of CO_2 adsorption can be modeled by Avrami's fractional order rate model, shown in equation 5.11:

$$\frac{\partial q_2}{\partial t} = k_2^{n_A} t^{(n_A-1)}(q_{eq2} - q_2) \tag{5.11}$$

where k_2, t, q_{eq2}, n_A are the Avrami rate constant, time, saturation capacity, and Avrami fractional constant, respectively.

This hybrid PFO and Avrami model was applied to simulate the breakthrough profiles for different concentrations and flowrates. The initial breakthrough before the isotherm step, was fitted by a PFO linear driving force model and the later part was fitted with the Avrami model. Initially, a CO_2 concentration of 400 ppm at different flowrates was considered. As shown in Figure 5-5, the hybrid model exhibits the best fit for the data and explains many characteristics of the breakthrough curve. More specifically, it describes the first shock and dispersive wave concentrations well. It also predicts the dip in the dispersive wave at higher flowrates. As shown in Figure 5-5 (right), the PFO model for reaction 1 had the best prediction for the breakthrough. As the flowrate is increased, the breakthrough profile also sharpened. The majority of CO_2 adsorption in the bed happened after the breakthrough and the Avrami model for the cooperative insertion of CO_2 had a direct impact on the calculated dispersive wave concentration and the breakthrough profile until saturation. This suggests that the limiting resistance to the mass transfer lies inside the crystal, with the film and macropore resistances playing relatively less prominent roles in the mass transfer for the conditions used in our experiments. Given the small crystal (3-5 μm) lengths, we also expecting a smaller micropore diffusional

resistance to CO_2 transport. Indeed, previous PFG NMR diffusional studies suggest that micropore diffusion is quite rapid in these systems.[58]

However, this hybrid scheme consisting of the PFO and the Avrami model failed to predict breakthrough profiles at higher concentrations. This highlights some limitations of the Avrami model. While it captured system dynamics for different flowrates at 0.4 mBar partial pressure with reasonable accuracy, it failed to capture system dynamics at 1 mBar, 5.6 mBar, and 10.02 mBar CO_2 partial pressure. More specifically, it failed to capture the dispersive wave concentration at higher concentrations of CO_2 in the feed.

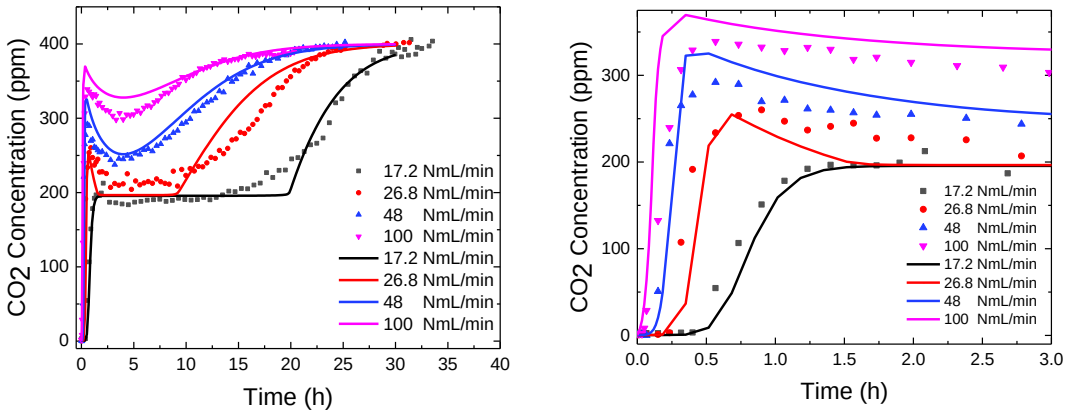

Figure 5-5 - Experimental (scatter) and simulated breakthrough profiles (solid lines) for CO_2 adsorption with the CO_2 partial pressure of 0.4 mBar in the feed. Simulated profiles were obtained at a flowrate of 17.2 NmL/min, 28.2 NmL/min, 48.6 NmL/min and 100 NmL/min at 23 ºC. Avrami model which was used in this analysis to account the cooperative CO_2 binding.

5.3.3 Development of a kinetic model at higher concentrations

McDonald et al.[15] drew an analogy with Rubisco, a Mg-based enzyme known for fixing CO_2 in plants, in early work on cooperative insertion of CO_2 in MMEN-Mg_2(dobpdc). The kinetics of the enzymatic reaction often follows the Michaelis-Menten model. Here attempts were made to model the kinetics of CO_2 adsorption based on

Michaelis-Menten kinetics by incorporating an additional coefficient, *n*, as an order for the CO_2 concentration. In this hybrid scheme, the initial breakthrough was modeled by the PFO model (equation 5.10). Cooperative CO_2 insertion was modeled by equation 5.12:

$$\frac{dq_2}{dt} = k_f \frac{C_g^n}{k_b + C_g^n}(q_{eq2} - q_2) \tag{5.12}$$

where k_f, k_b, n are the CO_2 consumption rate constant, half reaction rate constant and order of reaction, respectively. Figure 5-6 demonstrates the experimental data (black scatter) and modeling predictions (solid black lines) for 1 mBAr (Figure 5-6a), 5.6 mBar (Figure 5-6b) and 10.02 mBar (Figure 5-6c) conditions at 17.2 NmL/min flowrate. The initial part of the uptake was fitted with a PFO model corresponding to a low equilibrium capacity, and the latter part was fitted with equation 5.12, corresponding to a high equilibrium capacity. This hybrid empirical scheme fits the data well, even though it has a limited physical justification. Values obtained for k_f, k_b, n are 7.11×10^{-3} sec^{-1}, 2.36×10^{-3} sec^{-1}, and 2.5, respectively. Also, breakthrough profile predictions are plotted for comparison in Figure C.5 using both the Avrami and Michaelis-Menten models for the cooperative insertion of CO_2.

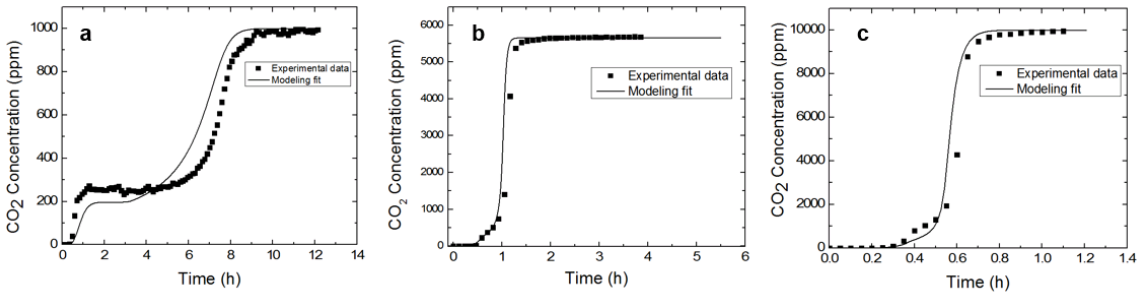

Figure 5-6 - Experimental breakthrough data (scatter) and modeling predictions (solid line) for 1 mBar (a), 5.6 mBar (b), and 10.02 mBar (c) CO_2 partial pressure conditions using the hybrid scheme consisting of the PFO linear driving force model and Michaelis-Menten model for the cooperative insertion of CO_2

It should also be noted that given the high heat of adsorption of CO_2 in this system, thermal effects can have a significant impact on the breakthrough. In our particular case, the adsorbent bed was assumed to be a near isothermal system given a small volume of the bed. Also, no significant increase in the bed temperature was detected during the adsorption process. To understand thermal effects, CO_2 adsorption in packed bed adsorption was simulated under both adiabatic and near isothermal conditions in Figures E4-E6 for two different CO_2 concentrations of 400 PPM and 5660 PPM. A small temperature (~0.6 °C) increase was predicted at 17.2 NmL/min feed with 400 PPM CO_2 concentration for the case of adiabatic bed. This resulted in a slightly higher concentration of the dispersive wave in the breakthrough than the isothermal case. At 100 NmL/min, the temperature rise was smaller than at 17.2 NmL/min for the case of an adiabatic bed and the breakthrough profile was almost identical with the near isothermal case. A higher increase in the bed temperature (~7 °C) was predicted in case of 17.2 NmL/min feed at 5660 PPM CO_2 concentration. This suggests that at higher concentrations, thermal effects are more prominent in this system.

The modeling scheme used here has the limitation that it fails to identify a single unifying model to predict breakthrough profiles, but it captures many features of this complex system such as the shape of the complex breakthrough curve, as well as the dispersive wave concentration. More importantly, it offers practical ways to study breakthrough adsorption of the MMEN-Mg_2(dobpdc) and related stepped isotherm systems. We believe our conclusions are also applicable to similar flow systems such as monolithic contactor/hollow fiber adsorbents because the resistance to the mass transfer comes from within the crystal. Further process studies should explore alternative gas-solid contactors that can overcome these limitations, in addition to the requirements of low pressure drop and effective heat removal at high concentrations.

5.4 Summary

The MOF MMEN-Mg_2(dobpdc) has shown unprecedented, high adsorption capacities and high amine-efficiencies at ultra-low partial pressures of CO_2 in equilibrium isotherm studies. This system shows a stepped isotherm that is tunable, and it has been suggested previously that such a system may be ideally suited for direct air capture (DAC) applications. In this work, CO_2 adsorption in MMEN-Mg_2(dobpdc) was studied under ultra-dilute conditions using a breakthrough adsorption setup as a proxy for practical flow systems. Dynamic CO_2 adsorption experiments were carried out at various flow rates, temperature and concentrations. Breakthrough simulations with the assumption of simple macropore diffusion resistance suggested a dual shock breakthrough for lower feed concentrations. This was confirmed through experiments where a shock wave - dispersive wave - shock wave breakthrough was observed in experiments simulating DAC conditions. A single shock breakthrough was observed for CO_2 concentrations above 1%. A higher

wave concentration was observed in adsorption experiments at higher flowrates compared to the feed concentration of 400 ppm, corresponding to DAC. The breakthrough adsorption behavior was further described through a kinetic model that accounted for two different reaction mechanisms, ammonium carbamate formation and cooperative CO_2 insertion. It was found that the hybrid rate law that consisted of a pseudo-first order and Avrami model gave a better prediction for the CO_2 fixed bed breakthrough profile at 400 ppm conditions. A kinetic model analogous to Michelis-Menten model of enzymatic reactions was proposed for higher feed concentration conditions. The system performance was further characterized by quantifying the rate of CO_2 extraction of the bed and the fraction of CO_2 captured at saturation. It was found that kinetic factors severely reduced the CO_2 capture fraction at low concentrations, reducing the viability of MMEN-Mg_2(dobpdc) for practical DAC applications. Improved rate of CO_2 extraction and the fraction of CO_2 captured makes the materials more suitable for adsorption applications where the CO_2 concentration in the feed is more than 1%.

5.5 References

[1] Jones, C. W. CO_2 Capture from Dilute Gases as a Component of Modern Global Carbon Management. *Annu. Rev. Chem. Biomol. Eng.* **2011**, *2* (1), 31–52.

[2] Lackner, K. S.; Brennan, S.; Matter, J. M.; Park, A. H.; Wright, A.; van der Zwaan, B. The Urgency of the Development of CO_2 Capture from Ambient Air. *Proc Natl Acad Sci U S A* **2012**, *109* (33), 13156–13162.

[3] Sanz-Pérez, E. S.; Murdock, C. R.; Didas, S. A.; Jones, C. W. Direct Capture of CO_2 from Ambient Air. *Chem. Rev.* **2016**, *116* (19), 11840–11876.

[4] Belmabkhout, Y.; Serna-Guerrero, R.; Sayari, A. Amine-Bearing Mesoporous Silica for CO_2 Removal from Dry and Humid Air. *Chem. Eng. Sci.* **2010**, *65* (11), 3695–3698.

[5] Choi, S.; Drese, J. H.; Eisenberger, P. M.; Jones, C. W. Application of Amine-Tethered Solid Sorbents for Direct CO_2 Capture from the Ambient Air. *Environ.*

Sci. Technol. **2011**, *45* (6), 2420–2427.

[6] Wang, J.; Wang, M.; Zhao, B.; Qiao, W.; Long, D.; Ling, L. Mesoporous Carbon-Supported Solid Amine Sorbents for Low-Temperature Carbon Dioxide Capture. *Ind. Eng. Chem. Res.* **2013**, *52* (15), 5437–5444.

[7] Sumida, K.; Rogow, D. L.; Mason, J. a; McDonald, T. M.; Bloch, E. D.; Herm, Z. R.; Bae, T.-H.; Long, J. R. Carbon Dioxide Capture in Metal-Organic Frameworks. *Chem. Rev.* **2012**, *112* (2), 724–781.

[8] Darunte, L. A.; Walton, K. S.; Sholl, D. S.; Jones, C. W. CO_2 Capture via Adsorption in Amine-Functionalized Sorbents. *Curr. Opin. Chem. Eng.* **2016**, *12*.

[9] Kulkarni, A. R.; Sholl, D. S. Analysis of Equilibrium-Based TSA Processes for Direct Capture of CO_2 from Air. *Ind. Eng. Chem. Res.* **2012**, *51* (25), 8631–8645.

[10] Sinha, A.; Darunte, L. A.; Jones, C. W.; Realff, M. J.; Kawajiri, Y. Systems Design and Economic Analysis of Direct Air Capture of CO_2 through Temperature Vacuum Swing Adsorption . *Ind. Eng. Chem.* **2016**.

[11] Lively, R. P.; Realff, M. J. On Thermodynamic Separation Efficiency: Adsorption Processes. *AIChE J.* **2016**, *62* (10), 3699–3705.

[12] Darunte, L. A.; Oetomo, A. D.; Walton, K. S.; Sholl, D. S.; Jones, C. W. Direct Air Capture of CO_2 Using Amine Functionalized MIL-101(Cr). *ACS Sustain. Chem. Eng.* **2016**, *4* (10), 5761–5768.

[13] McDonald, T. M.; Lee, W. R.; Mason, J. A.; Wiers, B. M.; Hong, C. S.; Long, J. R. Capture of Carbon Dioxide from Air and Flue Gas in the Alkylamine-Appended Metal–Organic Framework Mmen-Mg2(Dobpdc). *J. Am. Chem. Soc.* **2012**, *134* (16), 7056–7065.

[14] Choi, S.; Watanabe, T.; Bae, T.-H.; Sholl, D. S.; Jones, C. W. Modification of the Mg/DOBDC MOF with Amines to Enhance CO_2 Adsorption from Ultradilute Gases. *J. Phys. Chem. Lett.* **2012**, *3* (9), 1136–1141.

[15] Mcdonald, T. M.; Mason, J. A.; Kong, X.; Bloch, E. D.; Gygi, D.; Dani, A.; Crocellà, V.; Giordanino, F.; Odoh, S. O.; Drisdell, W. S.; et al. Cooperative Insertion of CO_2 in Diamine- Appended Metal-Organic Frameworks.

[16] Siegelman, R. L.; McDonald, T. M.; Gonzalez, M. I.; Martell, J. D.; Milner, P. J.; Mason, J. A.; Berger, A. H.; Bhown, A. S.; Long, J. R. Controlling Cooperative CO_2 Adsorption in Diamine-Appended Mg2(Dobpdc) Metal–Organic Frameworks. *J. Am. Chem. Soc.* **2017**, *139* (30), 10526–10538.

[17] Lee, W. R.; Jo, H.; Yang, L.-M.; Lee, H.; Ryu, D. W.; Lim, K. S.; Song, J. H.; Min, D. Y.; Han, S. S.; Seo, J. G.; et al. Exceptional CO_2 working Capacity in a Heterodiamine-Grafted Metal–Organic Framework. *Chem. Sci.* **2015**, *6* (7), 3697–

3705.

[18] Milner, P. J.; Siegelman, R. L.; Forse, A. C.; Gonzalez, M. I.; Runčevski, T.; Martell, J. D.; Reimer, J. A.; Long, J. R. A Diaminopropane-Appended Metal–Organic Framework Enabling Efficient CO_2 Capture from Coal Flue Gas via a Mixed Adsorption Mechanism. *J. Am. Chem. Soc.* **2017**, *139* (38), 13541–13553.

[19] Mason, J. A.; McDonald, T. M.; Bae, T. H.; Bachman, J. E.; Sumida, K.; Dutton, J. J.; Kaye, S. S.; Long, J. R. Application of a High-Throughput Analyzer in Evaluating Solid Adsorbents for Post-Combustion Carbon Capture via Multicomponent Adsorption of CO_2, N_2, and H_2O. *J Am Chem Soc* **2015**, *137* (14), 4787–4803.

[20] Darunte, L. A.; Terada, Y.; Murdock, C. R.; Walton, K. S.; Sholl, D. S.; Jones, C. W. Monolith-Supported Amine-Functionalized Mg 2 (Dobpdc) Adsorbents for CO_2 Capture. *ACS Appl. Mater. Interfaces* **2017**, *9* (20), 17042–17050.

[21] Yang, R. T. CHAPTER 5 - Adsorber Dynamics: Bed Profiles and Breakthrough Curves BT - Gas Separation by Adsorption Processes; Butterworth-Heinemann, 1987; pp 141–200.

[22] Rezaei, F.; Lawson, S.; Hosseini, H.; Thakkar, H.; Hajari, A.; Monjezi, S.; Rownaghi, A. A. MOF-74 and UTSA-16 Film Growth on Monolithic Structures and Their CO_2 Adsorption Performance. *Chem. Eng. J.* **2016**, *3*, http://dx.doi.org/10.1016/j.cej.2016.11.058.

[23] Labreche, Y.; Lively, R. P.; Rezaei, F.; Chen, G.; Jones, C. W.; Koros, W. J. Post-Spinning Infusion of Poly(Ethyleneimine) into Polymer/Silica Hollow Fiber Sorbents for Carbon Dioxide Capture. *Chem. Eng. J.* **2013**, *221*, 166–175.

[24] Lively, R. P.; Chance, R. R.; Kelley, B. T.; Deckman, H. W.; Drese, J. H.; Jones, C. W.; Koros, W. J. Hollow Fiber Adsorbents for CO_2 Removal from Flue Gas. *Ind. Eng. Chem. Res.* **2009**, *48* (15), 7314–7324.

[25] Zhang, W.; Liu, H.; Sun, C.; Drage, T. C.; Snape, C. E. Capturing CO_2 from Ambient Air Using a Polyethyleneimine–Silica Adsorbent in Fluidized Beds. *Chem. Eng. Sci.* **2014**, *116*, 306–316.

[26] Eisenberger, P. Carbon Dioxide Capture/Regeneration Aparatus. US 8696801 B2, 2014.

[27] Shafeeyan, M. S.; Wan Daud, W. M. A.; Shamiri, A. A Review of Mathematical Modeling of Fixed-Bed Columns for Carbon Dioxide Adsorption. *Chem. Eng. Res. Des.* **2014**, *92* (5), 961–988.

[28] Kärger, J.; Ruthven, D. M.; Theodorou, D. N. Sorption Kinetics. In *Diffusion in Nanoporous Materials*; Wiley-VCH Verlag GmbH & Co. KGaA, 2012; pp 143–189.

[29] Heydari-Gorji, A.; Sayari, A. CO_2 Capture on Polyethylenimine-Impregnated Hydrophobic Mesoporous Silica: Experimental and Kinetic Modeling. *Chem. Eng. J.* **2011**, *173* (1), 72–79.

[30] Serna-Guerrero, R.; Sayari, A. Modeling Adsorption of CO_2 on Amine-Functionalized Mesoporous Silica. 2: Kinetics and Breakthrough Curves. *Chem. Eng. J.* **2010**, *161* (1), 182–190.

[31] Suh, D.-M.; Sun, X. Particle-Scale CO_2 Adsorption Kinetics Modeling Considering Three Reaction Mechanisms. *Int. J. Greenh. Gas Control* **2013**, *17*, 388–396.

[32] Wang, X.; Guo, Q.; Kong, T. Tetraethylenepentamine-Modified MCM-41/Silica Gel with Hierarchical Mesoporous Structure for CO_2 Capture. *Chem. Eng. J.* **2015**, *273*, 472–480.

[33] Zhao, A.; Samanta, A.; Sarkar, P.; Gupta, R. Carbon Dioxide Adsorption on Amine-Impregnated Mesoporous SBA-15 Sorbents: Experimental and Kinetics Study. *Ind. Eng. Chem. Res.* **2013**, *52* (19), 6480–6491.

[34] Liu, F.; Chen, S.; Gao, Y.; Xie, Y. CO_2 Adsorption Behavior and Kinetics on Polyethylenimine Modified Porous Phenolic Resin. *J. Porous Mater.* **2017**, *24* (5), 1335–1342.

[35] Ebner, A. D.; Gray, M. L.; Chisholm, N. G.; Black, Q. T.; Mumford, D. D.; Nicholson, M. A.; Ritter, J. A. Suitability of a Solid Amine Sorbent for CO_2 Capture by Pressure Swing Adsorption. *Ind. Eng. Chem. Res.* **2011**, *50* (9), 5634–5641.

[36] Abdollahi-Govar, A.; Ebner, A. D.; Ritter, J. A. New Kinetic Model That Describes the Reversible Adsorption and Desorption Behavior of CO_2 in a Solid Amine Sorbent. *Energy & Fuels* **2015**, *29* (7), 4492–4502.

[37] Bollini, P.; Brunelli, N. A.; Didas, S. A.; Jones, C. W. Dynamics of CO_2 Adsorption on Amine Adsorbents. 1. Impact of Heat Effects. *Ind. Eng. Chem. Res.* **2012**, *51* (46), 15145–15152.

[38] Azizian, S. Kinetic Models of Sorption: A Theoretical Analysis. *J. Colloid Interface Sci.* **2004**, *276* (1), 47–52.

[39] Simonin, J.-P. On the Comparison of Pseudo-First Order and Pseudo-Second Order Rate Laws in the Modeling of Adsorption Kinetics. *Chem. Eng. J.* **2016**, *300*, 254–263.

[40] Ho, Y.-S. Review of Second-Order Models for Adsorption Systems. *J. Hazard. Mater.* **2006**, *136* (3), 681–689.

[41] Avrami, M. Kinetics of Phase Change. I General Theory. *J. Chem. Phys.* **1939**, *7* (12), 1103–1112.

[42] Liu, Q.; Shi, J.; Zheng, S.; Tao, M.; He, Y.; Shi, Y. Kinetics Studies of CO_2 Adsorption/Desorption on Amine-Functionalized Multiwalled Carbon Nanotubes. *Ind. Eng. Chem. Res.* **2014**, *53* (29), 11677–11683.

[43] Jung, W.; Park, J.; Lee, K. S. Kinetic Modeling of CO_2 Adsorption on an Amine-Functionalized Solid Sorbent. *Chem. Eng. Sci.* **2018**, *177*, 122–131.

[44] Bollini, P.; Brunelli, N. A.; Didas, S. A.; Jones, C. W. Dynamics of CO_2 Adsorption on Amine Adsorbents. 2. Insights Into Adsorbent Design. **2012**.

[45] Sen, T.; Kawajiri, Y.; Realff, M. J. Adsorption Process Intensification through Structured Packing: A Modeling Study Using Zeolite 13X and a Mixture of Propylene and Propane in Hollow-Fiber and Packed Beds. *Ind. Eng. Chem. Res.* **2018**.

[46] Mazzotti, M.; Rajendran, A. Equilibrium Theory–Based Analysis of Nonlinear Waves in Separation Processes. *Annu. Rev. Chem. Biomol. Eng.* **2013**, *4* (1), 119–141.

[47] Yun, J.-H. Unusual Adsorber Dynamics Due to S-Shaped Equilibrium Isotherm. *Korean J. Chem. Eng.* **2000**, *17* (5), 613–617.

[48] Inglezakis, V. J.; Fyrillas, M. M. Adsorption Fixed Beds Modeling Revisited: Generalized Solutions for S-Shaped Isotherms. *Chem. Eng. Commun.* **2017**, *204* (11), 1299–1317.

[49] Schweich, D.; Sardin, M. Adsorption, Partition, Ion Exchange and Chemical Reaction in Batch Reactors or in Columns — A Review. *J. Hydrol.* **1981**, *50*, 1–33.

[50] Cousin-Saint-Remi, J.; Denayer, J. F. M. Applying the Wave Theory to Fixed-Bed Dynamics of Metal-Organic Frameworks Exhibiting Stepped Adsorption Isotherms: Water/Ethanol Separation on ZIF-8. *Chem. Eng. J.* **2017**, *324*, 313–323.

[51] Rhee, H.-K.; Aris, R.; Amundson, N. R. On the Theory of Multicomponent Chromatography. *Philos. Trans. R. Soc. London. Ser. A, Math. Phys. Sci.* **1970**, *267* (1182), 419–455.

[52] Hefti, M.; Joss, L.; Bjelobrk, Z.; Mazzotti, M. On the Potential of Phase-Change Adsorbents for CO_2 Capture by Temperature Swing Adsorption. *Faraday Discuss.* **2016**, *192* (0), 153–179.

[53] Wakao, N.; Kaguei, S.; Funazkri, T. Effect of Fluid Dispersion Coefficients on Particle-to-Fluid Heat Transfer Coefficients in Packed Beds: Correlation of Nusselt Numbers. *Chem. Eng. Sci.* **1979**, *34* (3), 325–336.

[54] Process Systems Enterprise, gPROMS, W. psenterprise. com/gprom. ,1997-2018.

[55] Wu, D.; McDonald, T. M.; Quan, Z.; Ushakov, S. V; Zhang, P.; Long, J. R.; Navrotsky, A. Thermodynamic Complexity of Carbon Capture in Alkylamine-Functionalized Metal–Organic Frameworks. *J. Mater. Chem. A* **2015**, *3* (8), 4248–4254.

[56] Eaton, W. A.; Henry, E. R.; Hofrichter, J.; Mozzarelli, A. Is Cooperative Oxygen Binding by Hemoglobin Really Understood? *Nat. Struct. Biol.* **1999**, *6*, 351.

[57] Hunter, C. A.; Anderson, H. L. What Is Cooperativity? *Angew. Chemie Int. Ed.* **2009**, *48* (41), 7488–7499.

[58] Forse, A. C., Gonzalez, M. I., Siegelman, R. L., Witherspoon, V. J., Jawahery, S., Mercado, R., ... & Long, J. R. "Unexpected Diffusion Anisotropy of Carbon Dioxide in the Metal–Organic Framework Zn_2 (dobpdc). *J Am Chem Soc* **2018**, 140(5), 1663-1673.

CHAPTER 6. SUMMARY AND FUTURE WORK

6.1 Summary of current work

6.1.1 Chapter 2 – Hollow Fiber Bed

In this chapter we compared the separation performance of a hollow fiber bed to that of a packed bed using simulation studies. The analysis involved a detailed parametric comparison and was followed by a comparison of performance metrics in fully optimized PSA cycles. The target separation was an equimolar mixture of propylene and propane using zeolite 13X. Macropore diffusion was found to be nearly two times faster in the hollow fiber bed due to reduced diffusion length compared to a pellet in the packed bed. Heat transfer co-efficient per unit volume of adsorbent was intensified by three orders of magnitude in the hollow fiber bed due to the presence of an impermeable bore for heating/cooling medium. However, this also reduced the packing efficiency in the hollow fiber bed. We confirmed that this drawback would not reverse the advantages of the performance of the hollow fiber bed in our case studies.

In terms of a full PSA cycle, with similar purity and recovery requirements, the hollow fiber bed showed nearly 5 times better productivity (per unit weight of the adsorbent) as compared to a packed bed. Even in terms of volumetric productivity, the hollow fiber bed consistently showed a 2 fold improvement over the packed bed. Increased productivity directly indicates reduced capital cost when using expensive adsorbents that account for a significant portion of investment. Significant intensification can therefore, be

achieved by using the hollow fiber bed configuration over the packed bed, when the separation is equilibrium limited and specifically when heat management is of importance.

6.1.2 Chapter 3 – OMS MOFs for ethylene/ethane separation

In this chapter we aim to understand the impact of changing metal centers in open metal site (OMS) MOFs (with BTC as the representative linker) affects ethylene/ethane separation performance. We also investigated whether mixed-metal materials (MM'-BTC) could ever outperform pure metal M-BTC MOFs. DFT calculations (by a collaborator) for 12 pure metal BTCs and 11 mixed metal BTCs generated binding energy (BE) data for their respective metal centers.

The BE data was used to generate isotherms which could then be used directly for process evaluations. Pure metal BTCs were evaluated in terms of process performance metrics such as purity and energy consumption using both a simplified algebraic model as well as a fully optimized PSA cycle. While the simplified model under-predicts performance compared to the full model, trends observed in both evaluations is very similar. Interestingly both models predicted that the optimal operating temperature of operation of these OMS MOFs is a very strong function of the binding energy of ethylene.

When examining the heterogeneous MOFs, the performance was mostly found to be lower than those of their homogeneous pure metal counterparts. However, we also found two examples that are exceptions to this rule. Cr-Mg-BTC gave significantly higher purities than both Cr-BTC and Mg-BTC and Cr-Zn-BTC slightly outperforms Cr-BTC and Zn-BTC at an energy consumption of 0.5 GJ/ton. These examples are, therefore, a

demonstration that, in some circumstances, homogeneous (or pure) adsorbents do not necessarily outperform heterogeneous (or mixed) adsorbents for adsorptive separations.

6.1.3 Chapter 4 – Kinetic Separation

Kinetic separation exploits differences in diffusion coefficients of different adsorbates in the mixture irrespective of their equilibrium loading amounts. Our aim was to test the accuracy of the current standard approach of ranking material selectivity for a target kinetic gas-separation. It is denoted as a product of equilibrium selectivity and square-root of their diffusivity ratio. Throughout our analysis we have used the extensively studied Maxwell-Stefan diffusion equation which has been shown to capture transient crystal diffusion characteristics with far greater accuracy than the Fickian formulation. The study is conducted in two parts.

We have looked at optimized purity-recovery pareto curves in 3-step PSA cycles, for four Langmuir isotherms that have no equilibrium selectivity (=1), with varying diffusivity ratio and crystal radius. Additionally we also used a surrogate assisted illumination (SAIL) algorithm based on single crystal uptake simulations, to cover a wider range of equilibrium selectivities in a fraction of the time taken for full PSA simulations. We concluded that that for similar diffusivities and equilibrium selectivity, steeper isotherms show better kinetic separation performance. In addition, the size of the crystal also strongly impacts optimal performance whereas, diffusivity ratio was found to have a weaker than expected impact. Therefore, we suggest that using the ideal kinetic selectivity metric mentioned earlier is inadequate for comparison of materials for kinetic separation of a target gas mixture. . In addition, the combination of SAIL and single crystal uptake

model was successfully able to replicate observations made using full PSA cycle optimizations.

6.1.4 Chapter 5 – Impact of mass transfer on CO_2 capture using amine-functionalized Mg_2(dobpdc) MOF

The amine functionalized form of the MOF Mg_2(dobpdc) shows a stepped-isotherm behaviour that results in very high adsorption capacities even at low CO_2 concentrations. The location of the step is very temperature sensitive resulting in high TSA swing capacities as well. Therefore, this group of materials is an ideal candidate for Direct Air capture (DAC) i.e. removing CO_2 directly from the air. Despite strong interest, mass transfer properties remained an unknown aspect of these materials. Such knowledge is, however, crucial to its implementation in a practical system.

CO_2 breakthrough experiments were carried out at various flow rates and concentrations by a collaborator. The concentrations studies included both ultra-dilute (400 ppm) and dilute (1%) CO_2 in the feed. Breakthrough simulations using simple linear driving force model (LDF) and the isotherm parameters predicted a dual-shock breakthrough with the location of the step dependant only on the location of the pressure step in the isotherm at the operating temperature. However, in practice, these steps were shown to be dependent on feed velocity especially at 400 ppm CO_2, corresponding to DAC. The breakthrough curves however qualitatively looked similar to theoretical predictions.

Using a co-operative insertion model to describe mass transfer following the step change in isotherm was able to capture the observed system dynamics very well. The Avrami model, which is frequently used in crystallization theory, was well suited at low

CO_2 concentrations of 400 ppm while, at higher feed concentrations, a model similar to Michaelis-Menten used to describe enzyme kinetics was found to be more appropriate. We were therefore able to conclude that, the co-operative insertion mechanism which results in the highly-desirable stepped isotherm for MMEN-Mg_2(dobpdc) also severely impacts system kinetics. The impact in kinetics is negative since it leads to a widely-dispersed breakthrough profile which results in a much lower CO_2 capture fraction in the bed.

6.2 Future Work

6.2.1 Use of hollow fiber bed for kinetic separation

While use of structured contactors for equilibrium-based separations has been widely studied, the same is not true for kinetically limited separations. The limiting mass transfer in this case is the crystalline or micropore resistance as opposed to the macropore mass transfer. Major advantages of using structured contactors are reduction inexternal mass transfer resistance, improvement in pressure drop characteristics (allowing for higher velocity of feed) and improvement in heat transfer co-efficient. On the other hand, the hollow fiber bed has a lower volume of adsorbent due to the presence of the bore. While reduction in macropore diffusion length is not expected to affect kinetic separation in anyway, it is expected to be that the improvement in heat transfer and the velocity profile might still offer advantages in terms of productivity when the hollow fiber bed is used for kinetic separation. Future work can use the approach described in Chapter 2 to elucidate the impact of contactor design on kinetic separation.

6.2.2 Kinetic separation – use of more rigorous isotherm parameters, SAIL on full PSA cycle

Chapter 4 used SAIL on crystal uptake models to show the impact of isotherm parameters on the maximum improvement in kinetic selectivity. However, another important aspect of crystal uptake is the duration of time for which the supra-equilibrium selectivity is active. Constructing a metric to connect other measures of the shape of the crystal uptake curve to PSA separation performance could yield a metric that has a tighter correlation with PSA bed performance. The simple crystal model showed a dependence of kinetic separation performance on the original equilibrium selectivity of the material. This was not verified using the full PSA model. Running SAIL on the full PSA model might provide more direct insight into this behaviour.

While literature data was used to fix the ranges of the different materials property parameters, ranking of materials reported in literature based on the criteria established in our study has not been attempted. Further analysis in this direction will add to the understanding that has been developed in the current study on comparing performance of two different materials on their kinetic separation potential.

6.2.3 Design of PSA cycle for CO_2 capture using Mg_2(dobpdc)

While the analysis in Chapter 5 detailed an underlying model that can accurately capture kinetics of CO_2 capture, it also showed that the breakthrough characteristics especially at low CO_2 concentrations and high velocities were unfavourable when compared to the typical diffusion limited adsorbents. Further investigation of how characteristics of the PSA cycle such as changing bed length, time steps for adsorption/ desorption etc, might be adjusted to improve performance of this particular material.

Additionally, the mass transfer model used (Avrami) is empirical and has no direct physical basis. Attempts to understand kinetics of this process at a more fundamental level might result in a model which has a physical basis and can extrapolate experimental results with more confidence. Further, this model has not been tested on desorption curves for bed breakthrough. Understanding how the co-operative insertion mechanism impacts desorption is of primary interest if a PSA cycle is to be designed. It will be important to see whether the empirical model is still able to capture dynamics, or whether it fails to capture the physics of desorption sufficiently to enable useful predictions.

APPENDIX A. SUPPORTING INFORMATION FOR CHAPTER 1

In this section we describe some basic concepts that are essential in assessing separation potential of an adsorbent material.

A.1 Breakthrough Curves

Usually the adsorbent crystals (~μm dimensions) are formed into relatively larger particles (~mm dimensions) which are then packed into a bed. The fluid mixture is then passed continuously through the bed while the bed has the capacity to adsorb one of the components. The bed concentration profiles in the fluid and the solid phase continuously change with time as well as position, even if the process is operating at the "cyclic steady state". Initially the concentration of the strongly adsorbed component drops to zero exponentially, with distance from the inlet, as all the molecules are transferred to the solid phase in a small portion of the bed. After some time the front of the bed becomes saturated and the concentration profile move down the length of the bed. The position at which the components are being transferred from the fluid to the solid is known as the "mass-transfer zone".

Information about these concentration profiles is obtained by monitoring the concentration of the gas coming out from the outlet of the bed at different times, known as the breakthrough curve. The outlet gas concentration begins to rise from zero as more of the bed becomes saturated. The flow of the gas to the bed is stopped and regeneration started once the gas concentration in the outlet reaches a threshold, typically 5-10% of the original concentration at the inlet. *Figure A-1 (a)* shows the concentration profiles in the

fluid phase at different times and (b) shows the breakthrough curve for the same bed. The feed flow is stopped at t^*. C_0 is the concentration at the inlet.

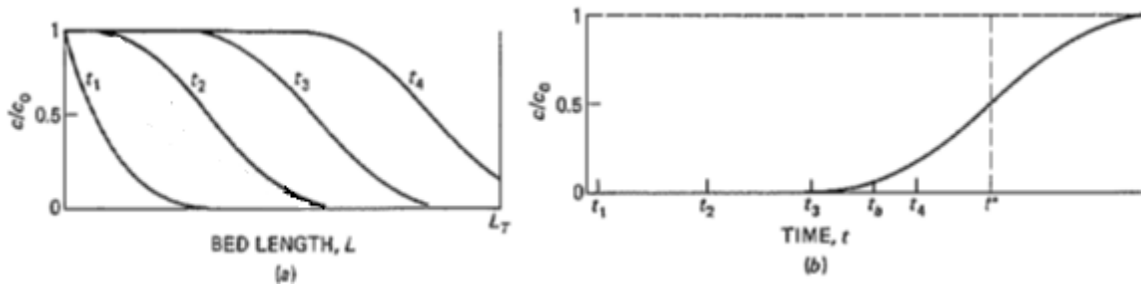

Figure A-1 - : (a) Fluid-phase concentration profiles along the bed length shown for 4 different times. (b) Breakthrough curve for the same bed. [25]

A.2 Non-idealities due to mass and heat transfer

For an ideal breakthrough curve, the concentration of the solid throughout the bed would have reached the equilibrium value w.r.t the inlet concentration and, the breakthrough curve will be a vertical line at t^*. The fluid has to move from the gas phase into the pores of the adsorbent particles and further into the adsorption surfaces inside the crystal pores. The kinetics of this transfer of mass determines how close to ideal the breakthrough curve will be and how efficiently the bed will be utilized. *Figure A-2* shows the shapes of the breakthrough curves for a "fast" and "slow" mass transfer respectively, for the same bed length.

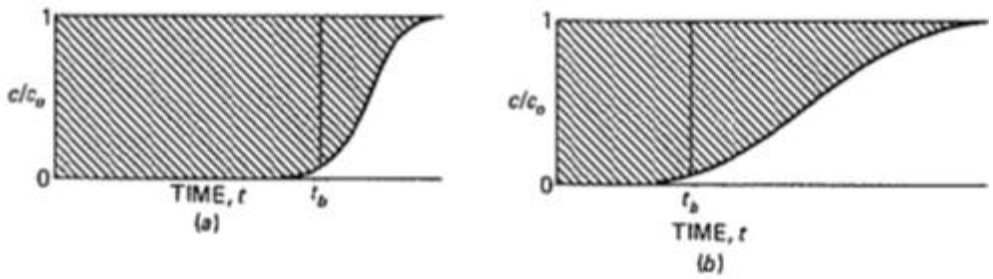

Figure A-2 Breakthrough curves for (a) fast mass transfer (b) slow mass transfer [25]

Non-idealities are also the result of accumulation of ΔH_{ads} which leads to an increase in temperature of the bed and consequently, a decrease in the equilibrium capacity of the adsorbent. The effectiveness with which heat can be removed from the "mass-transfer zone" also determines the effectiveness with which the bed capacity can be utilized.

APPENDIX B. SUPPORTING INFORMATION FOR CHAPTER 2

B.1 Supplementary Tables

Table B-1 - Isotherm parameters for the DSL model and Henry's law constants

	Propane	Propylene
$b_{A,}$, bar^{-1}	7.77×10^{-5}	1.52×10^{-4}
b_B , bar^{-1}	1.33×10^{-6}	1.25×10^{-7}
$q_{A,sat}$, mol/kg	2.79	2.71
$q_{b,sat}$, mol/kg	0.69	1.14
ΔH_{ads} , J/mol	-32×10^{3}	-37.8×10^{3}
ΔH_A , J/mol	-35.32×10^{3}	-39.82×10^{3}
ΔH_B , J/mol	-38.00×10^{3}	-50.2×10^{3}
K_0 , mol/kg.bar	3.52×10^{-4}	4.74×10^{-4}
ΔH_0, J/mol	-32.0×10^{3}	-37.8×10^{3}

Table B-2 - Properties of the adsorption bed and the adsorbent solid phase

Packed Bed		**Hollow Fiber Bed**	
R_p ,m	0.8×10^{-3}	R_{OD} ,m	0.653×10^{-3}
R_{pore} , µm	0.17	R_{ID} ,m	0.275×10^{-3}
ε_p	0.39	ε_f	0.48
τ	2.2	τ_f	2.5
R_c , µm	1	R_{pore} , µm	0.17

Table B-2 continued			
C_{ps} , J/kg.K	920	R_c , µm	1
ε	0.32	ρ_f ,kg/m^3	802
ρ_p , kg/m3	1072	w_f	0.6
ρ_b , kg/m^3	690	λ_f, W/m.K	0.05
ρ_w , kg/m^3	8238	C_{pf} , J/kg.K	1142.4
$C_{p,w}$, J/kg.K	500	v_{fib}	0.68
h_w , W/m^2.K	60	$C_{p,bf}$, J/kg.K	4178
U , W/m^2.K	30	h_{bf} , W/m^2.K	7268
t_w , m	3×10^{-3}	ρ_{bf} ,kg/m^3	1000

Table B-3 - Correlations for transport parameters and physical properties of gases

Packed Bed	**Hollow Fiber Bed**

Molecular Diffusivity: The diffusivity of pure components were calculated using the Chapman-Enskog equation

$$D_{mol,i} = 10^{-4} \times 1.8583 \times 10^{-3} \sqrt{\frac{2\,T_g^{\,3}}{(MW_i \times 10^3)(P\,\sigma_i^2\,\omega_i)}}$$

where P is in bar, $D_{\mathrm{mol,i}}$ is in m^2/s, σ_i (Å) and ω_i are the characteristic Lenard Jones length and energy of each component.

Knudsen Diffusivity: Kauzmann correlation

$$D_{knud,i} = \frac{2}{3} R_{pore} \sqrt{\frac{8RT_{g,i}}{\pi\, MW_i}}$$

Table B-3 continued

Pore Diffusivity: Bosanquet equation

$$\frac{1}{D_{p,i}} = \frac{\tau}{\varepsilon}\left(\frac{1}{D_{mol,i}} + \frac{1}{D_{knud,i}}\right)$$

[$D_{p,propane}$: $3.27 \times 10^{-6}\ m^2/s$; $D_{p,propylene}$: $3.41 \times 10^{-6}\ m^2/s$ are typical values]

Axial Mass and Heat Dispersion Coefficients: Wakao ansd Funazkri correlations [20] $D_{ax,i} = (20 + 0.5Sc_iRe)\ \frac{D_{mol,i}}{\varepsilon}$ $\lambda = (7 + 0.5PrRe)\ K_{mix}$ where $Re = \frac{\rho_g v_{ads} 2R_p}{\mu_g}$, $Sc_i = \frac{\mu_g}{\rho_g D_{mol,i}}$, $\Pr = \frac{\mu_g}{K_{mix}} \frac{c_{p,T}}{\sum_i y_i MW_i}$ $\left(c_{p,T}\ in\ J/mol\ \right)$, $K_{mix} = \sum_i y_i K_{conductivity,i}$ *Convective Mass and Heat Transfer Coefficients:* $k_{g,i} = Sh_i \frac{D_{mol,i}}{2R_p}$, $h_f = Nu \frac{K_{mix}}{2R_p}$	*Axial Mass and Heat Dispersion Coefficients:* (approximated using the Wakao and Funazkri correlation; found to have little impact in the regime of operation) $D_{ax,i} = (20 + 0.5Sc_iRe)\ \frac{D_{mol,i}}{\varepsilon}$ $\lambda = (7 + 0.5PrRe)\ K_{mix}$ where $Re = \frac{\rho_g u_{g0} 2r_{fs}}{\mu_g}$, $Sc_i = \frac{\mu_g}{\rho_g D_{mol,i}}$, $\Pr = \frac{\mu_g}{K_{mix}} \frac{c_{p,T}}{\sum_i y_i MW_i}$ $\left(c_{p,T}\ in\ J/mol\ \right)$ $K_{mix} = \sum_i y_i K_{conductivity,i}$ *Convective Mass and Heat Transfer Coefficients:* $k_{g,i} = Sh_i \frac{D_{mol,i}}{2R_{hyd}}$ $where\ R_{hyd} = \frac{r_{fs}^2 - R_{OD}^2}{2R_{OD}}$ $h_f = Nu \frac{K_{mix}}{2R_{hyd}}$

Table B-3 continued	
Wakao Correlations [20] $Sh_i = 2 + 1.1Re^{0.6}Sc_i^{0.33}$ $Nu = 2 + 1.1Re^{0.6}Pr^{0.33}$	Asimakapolou correlations [21] $Sh_i = 1.45\left(ReSc_i\frac{2R_{OD}}{L}\right)^{\frac{1}{3}}$ $Nu = 1.45\left(\mathrm{RePr}\frac{2\mathrm{R_{OD}}}{\mathrm{L}}\right)^{\frac{1}{3}}$

Crystal Diffusivity [12] *:* $D_{c,i} = D_{c0,A,i}exp\left(-\frac{E_{A,i}}{RT_g}\right) + D_{c0,B,i}exp\left(-\frac{E_{B,i}}{RT_g}\right)$

[$D_{c,propane}$: $3.35 \times 10^{-11}\ m^2/s$; $D_{c,propylene}$: $5.53 \times 10^{-12}\ m^2/s$ are typical values at T = 373 K

Density : $\rho_g = \frac{P_{tot}}{RT_g}\sum_i y_i MW_i$

The 2-site crystal diffusivity model [12] provides an empirical prediction for crystal diffusivity (which was confirmed to fall within the range of values reported in literature).

Table B-4: Property parameters for propylene, propane and inert gas helium

	He	C_3H_8	C_3H_6
D_{c0A} , m^2/sec	0	3.8×10^{-9}	3.6×10^{-9}
D_{c0B} , m^2/sec	0	3.1×10^{-9}	3.9×10^{-9}
E_A , J/mol	0	16.97×10^{3}	23.7×10^{3}
E_B , J/mol	0	16.05×10^{3}	21.5×10^{3}
C_p , J/mol	20.77	89.33	76.37
C_v , J/mol	12.49	81.01	68.06
$C_{v,ads}$, J/mol	90	120	112

Table B-4 continued			
$K_{conductivity}$, W/m.K	190.6×10^{-3}	28.9×10^{-3}	27.07×10^{-3}
σ	2.576	4.934	4.766
ω	0.6854	1.24	1.24
μ_g , Pa.s	1.53×10^{-5}		

B.2 Mass transfer coefficients

1. Micropore Mass Transfer Coefficient

The mass balance inside a single crystal is given by: (considering adsorbed phase to be the only phase inside the micropores of the crystal)

$$\frac{\partial q_i}{\partial t} = D_c \frac{1}{r^2}\frac{\partial}{\partial r}\left(r^2 \frac{\partial q_i}{\partial r}\right) \rightarrow \mathbf{A1}$$

BCs in the radial domain: $q = q^* \; at \; r = R_c$, $\frac{\partial q}{\partial r} = 0 \; at \; r = 0 \rightarrow \boldsymbol{A2}$

Integrating **A1** over crystal volume:

$$\frac{\partial q_{avg,i}}{\partial t}\frac{4}{3}\pi R_c^3 = 4\pi D_c \left(R_c^2 \frac{\partial q_i}{\partial r}\Big|_{R_c}\right), \quad \frac{\partial q_{avg,i}}{\partial t} = \frac{3D_c}{R_c}\frac{\partial q_i}{\partial r}\Big|_{R_c}$$

Assuming a quadratic profile across the crystal radius: $q(r) = A + Br^2 \rightarrow \boldsymbol{A3}$

Integrating **A3** over crystal volume:

$$q_{avg,i} = \frac{3}{4\pi r^2}\int_0^{R_c} 4\pi r^2 (A + Br^2) dr = A + \frac{3}{5}BR_c^2 \qquad \rightarrow \boldsymbol{A4}$$

Using **A2** & **A4** we can obtain B as: $\frac{5}{2}\frac{(q_i^* - q_{avg,i})}{R_C^2}$

$\left.\frac{\partial q_i}{\partial r}\right|_{r=R_c} = 2BR_c = 5\frac{(q_i^* - q_{avg,i})}{R_c}$

$\therefore \frac{\partial q_{avg,i}}{\partial t} = \frac{15D_c}{R_c^2}\left(q_i^* - q_{avg,i}\right)$

2. Macropore Mass Transfer Coefficient

The mass balance inside a single pellet at axial position z is given by:

$(1-\varepsilon_p)\rho_p \frac{\partial q_i}{\partial t} + \varepsilon_p \frac{\partial C_{p,i}}{\partial t} =$

$\varepsilon_p D_p \frac{1}{r^2}\frac{\partial}{\partial r}\left(r^2 \frac{\partial C_{p,i}}{\partial r}\right) \quad \rightarrow \boldsymbol{B1}$

$\frac{\partial q_i}{\partial t} = 0,$

$\because C_p is\ the\ rate - controlling\ phase$

BCs in the radial domain:

$C_{p_i} = C_{interface_i}\ at\ r = R_p$

$\frac{\partial C_{p_i}}{\partial r} = 0\ at\ r = 0 \rightarrow \boldsymbol{B2}$

Integrating **B1** over pellet volume:

$\frac{\partial C_{P_{avg,i}}}{\partial t}\frac{4}{3}\pi R_p^3 = 4\pi D_p\left(R_p^2 \left.\frac{\partial C_{p,i}}{\partial r}\right|_{R_p}\right)$

$\frac{\partial C_{p_{avg,i}}}{\partial t} = \frac{3D_p}{R_p}\left.\frac{\partial C_{p,i}}{\partial r}\right|_{R_p}$

Assuming a quadratic profile across the crystal radius: $C_p(r) = A_1 + B_1 r^2 \rightarrow \boldsymbol{B3}$

2. Macropore Mass Transfer Coefficient

The mass balance inside a single fiber at axial position z is given by:

$(1-\varepsilon_f)\rho_f w_f \frac{\partial q_i}{\partial t} + \varepsilon_f \frac{\partial C_{p,i}}{\partial t} =$

$\varepsilon_f D_{pf} \frac{1}{r}\frac{\partial}{\partial r}\left(r \frac{\partial C_{p,i}}{\partial r}\right) \quad \rightarrow \boldsymbol{B1}$

$\frac{\partial q}{\partial t} = 0,$

$\because C_p is\ the\ rate - controlling\ phase$

BCs in the radial domain:

$C_{p_i} = C_{interface_i}\ at\ r = R_{OD}$

$\frac{\partial C_{p_i}}{\partial r} = 0\ at\ r = R_{ID} \rightarrow \boldsymbol{B2}$

Integrating **B1** over fiber volume:

$\frac{\partial C_{P_{avg,i}}}{\partial t}\pi(R_{OD}^2 - R_{ID}^2) =$

$2\pi D_{pf}\left(R_{OD}\left.\frac{\partial C_{p,i}}{\partial r}\right|_{R_{OD}}\right)$

$\frac{\partial C_{p_{avg,i}}}{\partial t} = \frac{2D_{pf}R_{OD}}{(R_{OD}^2 - R_{ID}^2)}\left.\frac{\partial C_{p,i}}{\partial r}\right|_{R_{OD}}$

Integrating B**3** over crystal volume: $C_{p_{avg,i}} = A_1 + \frac{3}{5}B_1R_p^2 \qquad \rightarrow \boldsymbol{B4}$ Using **B2** & **B4** we can obtain B_1 as: $\frac{5}{2}\frac{\left(C_{interface_i} - C_{p_{avg,i}}\right)}{R_p^2}$, $\left.\frac{\partial C_{p_i}}{\partial r}\right\|_{R_p} = \frac{5}{R_p}\left(C_{interface_i} - C_{p_{avg,i}}\right)$ $\therefore \frac{\partial C_{P_{avg,i}}}{\partial t} = \frac{15D_p}{R_p^2}\left(C_{interface_i} - C_{p_{avg,i}}\right)$	Assuming a quadratic profile across the crystal radius: $C_p(r) = A_1 + B_1r^2 \rightarrow \boldsymbol{B3}$ Integrating B**3** over crystal volume: $C_{p_{avg,i}} = A_1 + \frac{1}{2}B_1(R_{OD}^2 + R_{ID}^2) \qquad \rightarrow \boldsymbol{B4}$ Using **B2** & **B4** we can obtain B_1 as: $\frac{2}{(R_{OD}^2 - R_{ID}^2)}\left(C_{interface_i} - C_{p_{avg,i}}\right)$, $\left.\frac{\partial C_{p_i}}{\partial r}\right\|_{R_{OD}} = \frac{4R_{OD}}{(R_{OD}^2 - R_{ID}^2)}\left(C_{interface_i} - C_{p_{avg,i}}\right)$ $\therefore \frac{\partial C_{P_{avg,i}}}{\partial t} = \frac{8D_{pf}R_{OD}^2}{(R_{OD}^2 - R_{ID}^2)^2}\left(C_{interface_i} - C_{p_{avg,i}}\right)$
3. <u>Gas to Pellet Phase Biot No.</u> $ak_g\left(C_g - C_{interface}\right) = \frac{15D_{p,i}}{R_p^2}\varepsilon_p\left(C_{interface} - C_p\right)$ $\rightarrow per\ unit\ volume\ of\ pellet$	3. <u>Gas to Fiber Phase Biot No.</u> $ak_g\left(C_g - C_{interface}\right) = \frac{8D_{fp,i}R_{OD}^2}{\left(R_{OD}^2 - R_{ID}^2\right)^2}\varepsilon_f\left(C_{interface} - C_p\right)$ $\rightarrow per\ unit\ volume\ of\ fiber$

$Bi(C_g - C_{interface}) = (C_{interface} - C_p)$, $C_{interface} = \frac{Bi\, C_g + C_p}{1+Bi}$

$\therefore (C_g - C_{interface}) = C_g - \frac{Bi\, C_g + C_p}{1+Bi} = \frac{C_g - C_p}{1+Bi}$ and $(C_{interface} - C_p) = \frac{Bi}{1+Bi}(C_g - C_p)$

B.3 Property parameters

1. $\rho_p \rightarrow$ weight of adsorbent/volume pellet = 1072 kg/m^3
   Pellet volume = pores (0.39) + crystals (0.61)
   $\rho_p = \rho_{crystal} \times 0.61 \rightarrow \rho_{crystal} = \frac{1072}{0.61} = 1757$ kg/m^3

2. $\rho_{fiber} \rightarrow$ weight of adsorbent/volume of the fiber
   Fiber volume = pores + crystals + cellulose acetate
   $(loading\ of\ crystals = 60\ wt\%\ and\ fiber\ porosity = 0.48)$
   Density of cellulose acetate = $1300\,\frac{kg}{m^3}$
   $\frac{wt_{crystal}}{0.6} = \frac{wt_{CA}}{0.4} \rightarrow \rho_{crystal} \times vol_{crystal} = 1.5\rho_{CA} \times (1 - vol_{crystal})$
   $vol_{crystal} = \frac{1.5\rho_{CA}}{1.5\rho_{CA} + \rho_{crystal}} = 0.53$
   $\rho_{solid} = 0.53\rho_{crystal} + 0.47\rho_{CA} = 1542\ kg/m^3$
   $\rho_{fib} = (1 - \varepsilon_f)\rho_{solid} = 802\ kg/m^3$

3. Packed Bed: $C_{P_s} = 920\ J/kgK$
   ε = 0.39, $\rho_s = 1757\ kg/m^3, \rho_{gas} = 1\ kg/m^3$
   $Cp_{gas} = 1000\ J/kg\ K$, $k_{gas} = 0.024$ W/m K
   $1072 * 920 = (0.61)1757x + 0.39 * 1 * 1000 = 920\ J/kgK$

4. Mixed
   $\rho_{fib} C_{p_{fib}} = \varepsilon_f \rho_{gas} C_{p_{gas}} + (1 - \varepsilon_f)[v_f \rho_{crystal} C_{crystal} + (1 - v_f)\rho_{CA} C_{CA}]$
   $C_{fib} = \frac{1}{802} * (0.48 * 1 * 1000 + 0.52 * (0.53 * 1757 * 920 + 0.47 * 1300 * 1480))$
   $C_{fib} = 1142.4\ J/kgK$
   $k_{fib} = k_{gas}^{\varepsilon_f} k_{solid}^{1-\varepsilon_f}$
   $k_{solid} = \left(\frac{0.05}{(0.024)^{0.5}}\right)^{\frac{1}{0.5}}$

APPENDIX C. SUPPORTING INFORMATION FOR CHAPTER 3

C.1 Geometry Optimization for the Modelled Materials

Table C-1 - Lattice constants for 12 optimized M-BTCs computed with PBE-D3

M-BTCs	Lattice constant (Å)		
	a	b	c
Mg (d^0)	18.84	18.87	18.86
Ti (d^2)	18.91	18.93	18.92
V (d^3)	19.04	19.01	19.04
Cr (d^4)	18.97	18.99	18.99
Mo (d^4)	18.91	18.93	18.93
Mn (d^5)	19.12	19.14	19.14
Fe (d^6)	18.96	18.93	18.93
Ru (d^6)	19.06	19.07	19.07
Co (d^7)	18.90	18.86	18.88
Ni (d^8)	18.58	18.62	18.61
Cu (d^9)	18.69	18.71	18.70
Zn (d^{10})	18.91	18.93	18.93

Table C-2 - Lattice constants for 11 optimized MM'-BTCs computed with PBE-D3

MM'-BTCs	Lattice constant (Å)		
	a	b	c
Cr-Mo-BTC	19.20	19.21	19.21
Cr-Cu-BTC	18.84	18.85	18.85
Cr-Ru-BTC	19.04	19.05	19.06

Table C-2 continued			
Cr-Fe-BTC	18.97	18.95	18.95
Cr-Mg-BTC	18.90	18.92	18.92
Cr-Mn-BTC	19.06	19.07	19.07
Cr-Zn-BTC	18.95	18.97	18.97
Cu-Zn-BTC	18.69	18.71	18.70
Cu-Mg-BTC	18.78	18.80	18.79
Fe-Mg-BTC	18.89	18.91	18.91
Ti-Mo-BTC	19.22	19.22	19.22
Cr-Mo-BTC	19.20	19.21	19.21

C.2 Adsorption Equilibrium Constant at OMS: $\mathbf{K_{oms}^{A(B)}}$

The Langmuir equilibrium constant K can be simplified defined by

$$K \approx \frac{Q_{adsorbed}}{Q_{gas}} e^{\frac{B.E.}{RT}} \approx b_0 * e^{\frac{B.E.}{RT}} \quad \text{(C1)}$$

where b_0, adsorption affinity parameter, is defined by $\frac{Q_{adsorbed}}{Q_{gas}}$. Q_{gas} and $Q_{adsorbed}$ are the partition functions of the adsorbing species in the gas phase and the adsorbed phase, respectively. Q_{gas} and $Q_{adsorbed}$ can be calculated with the following method.

C.2.1 Partition function in the gas phase: Q_{gas}

Q_{gas} takes all possible degrees of freedom (vibration, translation, and rotation) into account and is defined by

$$Q_{gas} = Q_{vib} * Q_{rot} * Q_{trans}\,(in\ the\ gas\ phase) \quad \text{(C2)}$$

where $Q_{vib}, Q_{rot}, and\ Q_{trans}$ are defined by

$$Q_{gas\_vib} = \prod \frac{1}{1 - e^{\frac{-\theta_v}{T}}} \quad \text{(C3)}$$

$$Q_{gas\_rot} = \frac{\pi^{0.5}}{\sigma} \frac{T^{1.5}}{\theta_x \theta_y \theta_z} \quad \text{(C4)}$$

$$Q_{gas\_trans} = \frac{kT}{P} \left(\frac{2\pi * M_{gas} * kT}{h^2}\right)^{1.5} \quad \text{(C5)}$$

where $\theta_v = {hv}/{k}$, which has units of temperature, is referred as the vibrational temperature; σ, symmetry number, is equal to 4 and 6 for ethylene and ethane; $\theta_x, \theta_y, and\ \theta_z$ are rotational temperatures; h and k are the Planck and Boltzmann constants, respectively. The specific values of rotational constants and partition function of ethylene and ethane are listed in the following Table C-3 and

Table C-4.

Table C-3 - Rotational constants of ethylene and ethane in the gas phase

Rotational constants (cm-1)	C_2H_4	C_2H_6
A	4.83	2.52
B	1.00	0.68
C	0.82	0.68

Table C-4 - Partition function of ethylene and ethane in the gas phase

Partition Function	C_2H_4	C_2H_6
Q_{gas_vib}	1.08	1.51
Q_{gas_rot}	743.79	1371.86
Q_{gas_trans}	7199612.45	7984614.52
Q_{gas}	5804023185	5986803878

C.2.2 Partition function in the adsorbed phase: $Q_{adsorbed}$

$Q_{adsorbed}$ is calculated from the discrete vibrational energy levels that consider the adsorbed molecules are characterized as bound system. In the adsorbed phase, the freedom of translation and rotation for the adsorbed molecules are constrained. The hindered motion of translation and rotation can be approximated by harmonic vibrations of the adsorbed molecule relative to the surface, which is perfect for ethylene adsorbed at OMS. However, for the adsorption of ethane at OMS, the harmonic approximation of translation and rotation is too constrained. Sauer and coworkers pointed out the rotational energy levels of CH_4 are very similar to those of the gas phase.[1] Therefore, in this chapter, for $Q_{adsorbed}$ of ethane at OMS, the gas-phase rotational partition function was used for the rotation term in the adsorbed ethane phase instead of harmonic oscillator.

$$Q_{adsorbed} = Q_{ads\_vib} * Q_{ads\_rot} * Q_{ads\_trans} \approx Q_{vib\_all} \approx \prod \frac{1}{1 - e^{\frac{-\theta_v}{T}}} \quad \text{(C6)}$$

C.2.3 DFT calculations for vibrational frequencies

DFT has become a popular approach for the calculation of vibrational frequencies, which was facilitated by analytical second-derivative techniques.[2-3] For the general set-up, the electronic minimization algorithm selected a robust mixture of the Davidson and

RMM-DIIS algorithms. Energy cutoff was set as 520 eV. The break condition for the electronic self-consistency loop was 10^{-6}. For the dynamic set-up, the Hessian matrix of the second derivatives of the energy concerning the atomic positions was determined, and the vibrational frequencies were calculated. To calculate the Hessian matrix, we selected the central difference to determine the number of ionic displacements and selected 0.015 as the step size for displacements. The vibrational frequencies are calculated only for the adsorbed molecules and their motions relative to the adsorbed surface (partial Hessian). To save the computational cost during the frequency calculation of ethylene and ethane in M-BTCs, we fixed the atomic positions of MOFs and only relaxed the adsorbed molecules. The step size of displacement was carefully tuned to avoid unphysical imaginary frequencies in the optimized structures.

C.2.4 The calculations for vibrational frequencies and b_0 for all metal centers

fter obtaining frequencies without imaginary values, the b_0 for ethylene and ethane at OMS was calculated, then $K_{oms}^{C_2H_4}$ and $K_{oms}^{C_2H_6}$ can be further calculated in Cu-BTC. The same procedure was followed to calculate b_0 at OMS in other M-BTCs to explore other metal species. Because the difficulty of eliminating the imaginary frequencies, only five b_0 pairs of ethylene and ethane at OMS were obtained in M-BTCs, which are listed in the Table C-5 and Table C-6. Since $\frac{b_{0\_max}}{b_{0\_min}} < 50$, the correlation shown in Figure C.1 was used to obtain b_0 values for other M-BTCs. The derived correlation of b_0 for ethylene at OMS is a function of the binding energy (B.E.) at the metal sites. The functions are written below and the calculated b_0 is shown in Table C-7.

$$b_{0_{C2H4}} \approx 10^{b} \tag{C7}$$

$$\text{with: b} = (1 - \text{w}) * \left(\left(\frac{40.23}{B.E.}\right)^{20.88} - 7.36\right) - 5.64 * \text{w}; \tag{C8}$$

$$\text{and with: w} = {}^{1}/_{(1 + e^{5*(B.E.-40.4)})} \tag{C9}$$

The same case for ethane and the derived correlation functions of b_0 at OMS are written below with the calculated b_0 for M-BTCs in Table C-8:

$$b_{0_{C2H6}} \approx 10^{(-3.38-0.033*B.E.)} \tag{C10}$$

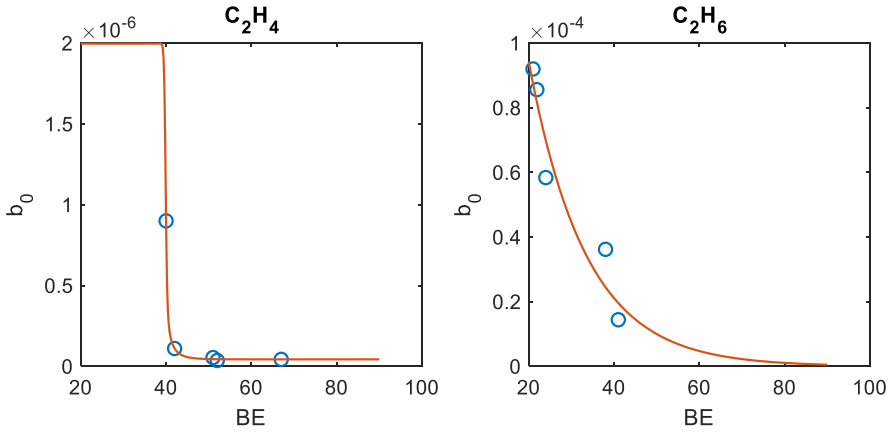

Figure C-1 - b_0 correlation of binding energy for ethylene and ethane in 12 metal species at OMS

Table C-5 - Binding energy and calculated b_0 of ethylene at OMS for five M-BTCs

Metals	Cu	Cr	Ni	Ru	Co
$B.E._{oms}^{C_2H_4}$	40	42	51	52	67
$b_{o,oms}^{C_2H_4}$ (calculated)	9.00E-07	1.10E-07	5.42E-08	3.60E-08	4.28E-08

Table C-6 - Binding energy and calculated b_0 of ethane at OMS for five M-BTCs

Metals	Mo	Cr	Cu	Zn	Mg
$B.E._{oms}^{C_2H_6}$	21	22	24	38	41
$b_{o,oms}^{C_2H_6}$ (calculated)	9.20E-05	8.56E-05	5.84E-05	3.62E-05	1.44E-05

Table C-7 - Calculated binding energy and fitted b_0 of ethylene at OMS for M-BTCs

Metals	Mg	Ti	V	Mo	Mn	Fe	Zn
$B.E._{oms}^{C_2H_4}$	68	53	55	38	69	64	79
$b_{o,oms}^{C_2H_4}$ (fitted)	4.37E-08	4.40E-08	4.38E-08	2.28E-06	4.37E-08	4.37E-08	4.37E-08

Table C-8 - Calculated binding energy and fitted b_0 of ethane at OMS for M-BTCs

Metals	Ni	Ti	V	Co	Mn	Fe	Ru
$B.E._{oms}^{C_2H_6}$	28	20	24	32	37	23	23
$b_{o,oms}^{C_2H_6}$ (fitted)	4.97E-05	9.12E-05	6.73E-05	3.66E-05	2.51E-05	7.26E-05	7.26E-05

C.3 Adsorption Equilibrium Constant at Physisorption Site: $K_{phy}^{A(B)}$

The approach of deriving K_{phy} is to fit with experimental adsorption data. Taking the fitting of ethylene as an example, since not all OMS are available in practical experiment, $n_{oms}^{C_2H_4}$ is treated as unknown, while $K_{oms}^{C_2H_4}$ and $n_{phy}^{C_2H_4}$ were known variables. The two unknown variables $K_{phy}^{C_2H_4}$ and $n_{oms}^{C_2H_4}$ could be obtained by fitting with Jorge's experimental data at three temperatures using a single-component DSL model, which was defined by

$$n_A = \frac{n_{oms}^A * K_{oms}^A * P_A}{1 + K_{oms}^A * P_A} + \frac{n_{phy}^A * K_{phy}^A * P_A}{1 + K_{phy}^A * P_A} \tag{C11}$$

The same procedure was followed to compute parameters for ethane. All the parameters of ethylene and ethane are listed in the Table C-9.

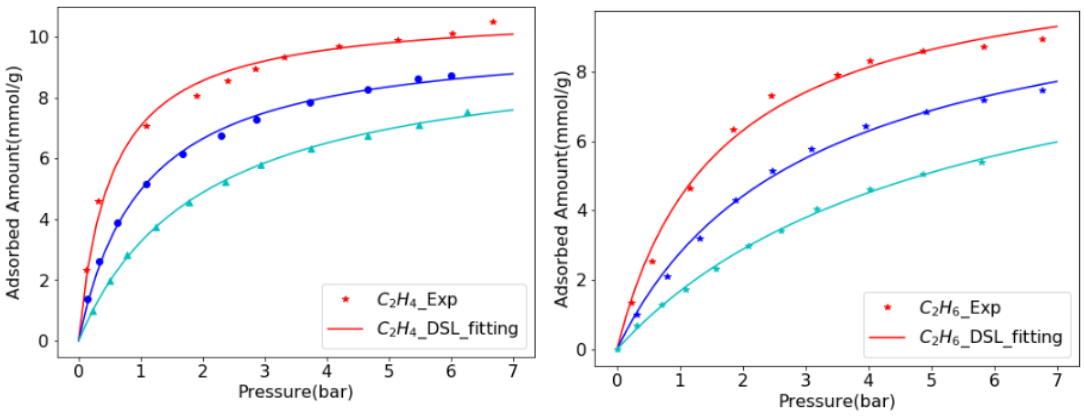

Figure C-2 - Comparison between model fitting (lines) and experimental adsorption isotherms (points) for ethylene (left) and ethane (right) on CuBTC at 323K (red), 348K (blue), and 373K (cyan).

Table C-9 - Fitted parameters of ethylene and ethane obtained at three tempetures.

Temperature (K)	$n_{oms}^{C_2H_4}$	$K_{phy}^{C_2H_4}$	R^2	$n_{oms}^{C_2H_6}$	$K_{phy}^{C_2H_6}$	R^2
323	3.049	1.597	0.986	5.637	0.801	0.991
348	2.254	0.965	0.998	5.259	0.430	0.995
373	1.958	0.528	0.999	4.780	0.231	0.999

C.4 Equations for Full Model

C.4.1 Hollow Fiber Bed Model

Table C-10 - Model Equations used to simulate the hollow fiber bed adsorption processes

Hollow Fiber Bed

Units: Concentrations: mol/m^3, Pressure: bar, time: sec, velocity: m/s, Temperature: K

Mass Balance Equations:

i. Bulk Gas Phase

$$\frac{\partial Cg_i}{\partial t} = D_{ax,i}\frac{\partial^2 Cg_i}{\partial z^2} - \frac{\partial (Cg_i u_{gi})}{\partial z} - N_i$$

$$N_i = \frac{R_{OD}^2 - R_{ID}^2}{r_{fs}^2 - R_{OD}^2} k_{gas,i}(Cg_i - Cp_i)\left[\frac{1}{1+Bi_i}\right]$$

ii. Macropore Gas Phase

$$\frac{\partial Cp_i}{\partial t} = k_{macro,i}(Cg_i - Cp_i)\frac{Bi_i}{1+Bi_i} - \frac{\rho_f w_s}{\varepsilon_f}\frac{\partial q_i}{\partial t}$$

iii. Micropore Adsorbed Phase

$$\frac{\partial q_i}{\partial t} = k_{micro,i}(q_i^* - q_i)$$

where

$$u_{gi} = \frac{Q_{vol}}{Area},\ Area = \pi {R_{bed}}^2\left(1 - v_{fib}\right),$$

$$v_{fib}\pi r_{fs}^2 = \pi R_{OD}^2, \therefore r_{fs} = \frac{R_{OD}}{\sqrt{v_{fib}}}$$

Table C-10 continued

Mass Transfer Coefficients:

$k_{gas,i} = ak_{g,i}$

$a = \frac{2R_{OD}}{(R_{OD}^2 - R_{ID}^2)}, \quad Bi_i = \left. ak_{g,i} \right/ \frac{8D_{fp,i}R_{OD}^2\varepsilon_f}{(R_{OD}^2 - R_{ID}^2)^2}$

$k_{macro,i} = \frac{8D_{fp,i}R_{OD}^2}{(R_{OD}^2 - R_{ID}^2)^2}$

$k_{micro,i} = \frac{15D_{c,i}}{R_c^2}$

Ideal Gas Equation:

$p_i = Cg_i RT_g,\ P_{tot} = \sum p_i,\ C_{g,tot} = \sum Cg_i,\ C_{p,tot} = \sum Cp_i$

Happel's Equation (Pressure Drop):

$$-\frac{\partial P_{tot} \times 10^5}{\partial z} = \frac{u_{gi}\mu_g}{r_{OD}^2 - 3r_{fs}^2 \Big/ 8 + ln\left(\frac{r_{fs}}{r_{OD}}\right) r_{fs}^4 \Big/ 2\left(r_{fs}^2 - r_{OD}^2\right)}$$

Heat Balance Equations:

$c_{p,T} = \sum_i y_i c_{p,i},\ c_{v,T} = \sum_i y_i c_{v,i}$

i. Bulk Gas Phase

$$\left(r_{fs}^2 - r_{OD}^2\right) C_{g,tot} c_{v,T} \frac{\partial T_g}{\partial t} = \lambda \frac{\partial^2 T_g}{\partial z^2} - \left(r_{fs}^2 - r_{OD}^2\right)\left[u_{gi} C_{g,tot} c_{p,T} \frac{\partial T_g}{\partial z} + RT_g \frac{\partial C_{g,tot}}{\partial t}\right] - (r_{OD}^2 - r_{ID}^2) a\, h_f (T_g - T_f)$$

ii. Fiber

$$\left(\varepsilon_f \sum_i C_{p,i}\, c_{v,i} + \rho_f \left(\sum_i q_i\, c_{v,ads,i} + c_{p_f}\right)\right)\frac{\partial T_f}{\partial t} = \lambda_f \frac{\partial^2 T_f}{\partial z^2} + a\, h_f (T_g - T_f) + \rho_f \sum_i \left(-\Delta H_{ads,i} \frac{\partial q_i}{\partial t}\right) - a_{f_{int}} h_{bf} (T_f - T_{bf}) \qquad where \quad a_{f_{int}} = \frac{2R_{ID}}{R_{OD}^2 - R_{ID}^2}$$

iii. Bore Fluid

$$\rho_{bf} C_{p,bf} \frac{\partial T_{bf}}{\partial t} = -u_{bf} \rho_{bf} C_{p,bf} \frac{\partial T_{bf}}{\partial z} + \frac{2}{R_{ID}} h_{bf} (T_f - T_{bf})$$

C.4.2 Boundary Conditions

Table C-11 - Boundary conditions for the 4-step single bed VPSA process

Units: Concentrations: mol/m^3, Pressure: bar, time: sec, velocity: m/s, Temperature: K

Pressurization with feed (Co-current)

$$-\lambda \frac{\partial T_g}{\partial z}\Big|_{0^+} = u_g C_{p,T}\Big|_{0^+} \sum_i C_{g,i_{in}} \left(T_{g_{in}} - T_{g_0^+}\right) \qquad \frac{\partial T_g}{\partial z}\Big|_{L^-} = 0$$

$$-\varepsilon D_{ax,i} \frac{\partial C_{g,i}}{\partial z}\Big|_{0^+} = u_g\Big|_{0^+} \left(C_{g,i_{in}} - C_{g_{,i0}^+}\right) \qquad \frac{\partial C_{g,i}}{\partial z}\Big|_{L^-} = 0$$

where $C_{g,i_{in}} = y_{ads,i} \frac{P_{tot}}{RT_g}\Big|_{0^+}$

$$P_{tot}\big|_{z=0^+} = P_{tot}\big|_{z=0^+}^{0} + \left(P_{ads} - P_{tot}\big|_{z=0^+}^{0}\right)\left(1 - \exp\left(-M_p t\right)\right) \qquad u_g\big|_{L^-} = 0$$

Adsorption (Feed)

$$-\lambda \frac{\partial T_g}{\partial z}\Big|_{0^+} = u_g C_{p,T}\Big|_{0^+} \sum_i C_{g,i_{in}} \left(T_{g_{in}} - T_{g_0^+}\right) \qquad \frac{\partial T_g}{\partial z}\Big|_{L^-} = 0$$

$$-\varepsilon D_{ax,i} \frac{\partial C_{g,i}}{\partial z}\Big|_{0^+} = u_g\Big|_{0^+} \left(C_{g,i_{in}} - C_{g_{,i0}^+}\right) \qquad \frac{\partial C_{g,i}}{\partial z}\Big|_{L^-} = 0$$

where $C_{g,i_{in}} = y_{ads,i} \frac{P_{tot}}{RT_g}\Big|_{0^+}$

$$u_{g0^+} = v_{ads} \qquad P_{tot}|_{L^-} = P_{ads}$$

Blowdown (Co-current)

$$\frac{\partial T_g}{\partial z}\Big|_{0^+} = 0 \qquad \frac{\partial T_g}{\partial z}\Big|_{L^-} = 0$$

$$\frac{\partial C_{g,i}}{\partial z}\Big|_{0^+} = 0 \qquad \frac{\partial C_{g,i}}{\partial z}\Big|_{L^-} = 0$$

$$u_{g_{0^+}} = 0; \qquad P_{tot}|_{z=L^-} = P_{tot}|_{z=L^-}^{0} - \left(P_{tot}|_{z=L^-}^{0} - P_{inter}\right)\left(1 - exp(-M_b t)\right)$$

Table C-11 continued

Evacuation (Counter-current)

$\left.\frac{\partial T_g}{\partial z}\right|_{0^+} = 0$ $\qquad$ $\left.\frac{\partial T_g}{\partial z}\right|_{L^-} = 0$

$\left.\frac{\partial C_{g,i}}{\partial z}\right|_{0^+} = 0$ $\qquad$ $\left.\frac{\partial C_{g,i}}{\partial z}\right|_{L^-} = 0$

$P_{tot}|_{z=0^+} = P_{tot}|^0_{z=0^+} - \left(P_{tot}|^0_{z=0^+} - P_{des}\right)\left(1 - exp(-M_b t)\right)$ $\qquad$ $u_{g_{L^-}} = 0;$

C.4.3 Correlations for transport parameters and physical properties of gases

Table C-12 - Equations used to determine heat and mass transfer co-efficients and physical properties of ethylene and ethane

Molecular Diffusivity: The diffusivity of pure components were calculated using the Chapman-Enskog equation

$$D_{mol,i} = 10^{-4} \times 1.8583 \times 10^{-3} \sqrt{\frac{2\,T_g{}^3}{(MW_i \times 10^3)(P\sigma_i^2\omega_i)}}$$

where P is in bar, $D_{\text{mol,i}}$ is in m^2/s, σ_i (Å) and ω_i are the characteristic Lenard Jones length and energy of each component.

Knudsen Diffusivity: Kauzmann correlation

$$D_{knud,i} = \frac{2}{3} R_{pore} \sqrt{\frac{8RT_{g,i}}{\pi\, MW_i}}$$

Pore Diffusivity: Bosanquet equation

$$\frac{1}{D_{p,i}} = \frac{\tau}{\varepsilon}\left(\frac{1}{D_{mol,i}} + \frac{1}{D_{knud,i}}\right)$$

Axial Mass and Heat Dispersion Coefficients:

(approximated using the Wakao and Funazkri correlation; found to have little impact in the regime of operation)

$$D_{ax,i} = (20 + 0.5 Sc_i Re)\,\frac{D_{mol,i}}{\varepsilon}$$

$$\lambda = (7 + 0.5 PrRe)\,K_{mix}$$

Table C-12 continued

where

$Re = \frac{\rho_g u_{g0} 2r_{fs}}{\mu_g}$, $Sc_i = \frac{\mu_g}{\rho_g D_{mol,i}}$, $\mathrm{Pr} = \frac{\mu_g}{K_{mix}} \frac{c_{p,T}}{\sum_i y_i MW_i}$ $\left(c_{p,T}\ in\ J/mol\ \right)$

$K_{mix} = \sum_i y_i K_{conductivity,i}$

Convective Mass and Heat Transfer Coefficients:

$k_{g,i} = Sh_i \frac{D_{mol,i}}{2R_{hyd}}$ $where\ R_{hyd} = \frac{r_{fs}^2 - R_{OD}^2}{2R_{OD}}$ $h_f = Nu \frac{K_{mix}}{2R_{hyd}}$

Asimakapolou correlations [21]

$Sh_i = 1.45 \left(ReSc_i \frac{2R_{OD}}{L} \right)^{\frac{1}{3}}$

$Nu = 1.45 \left(\mathrm{RePr} \frac{2\mathrm{R_{OD}}}{\mathrm{L}} \right)^{\frac{1}{3}}$

Crystal Diffusivity [12] *:* $D_{c,i} = D_{c0,A,i} exp\left(-\frac{E_{A,i}}{RT_g}\right) + D_{c0,B,i} exp\left(-\frac{E_{B,i}}{RT_g}\right)$

Density : $\rho_g = \frac{P_{tot}}{RT_g} \sum_i y_i MW_i$

The 2-site crystal diffusivity model [12] provides an empirical prediction for crystal diffusivity (which was confirmed to fall within the range of values reported in literature).

C.4.4 Purity, Recovery, Productivity

The following equations represent the calculated purity, recovery and productivity of ethylene (which is the selectively adsorbed component).

$$Purity_{C_2H_4} = 100 \times \frac{\int_{evacuation} u_g^{out} C_{g,C_2H_4}^{out}}{\sum_i \int_{evacuation} u_g^{out} C_{g,i}^{out}} \qquad \text{(C12)}$$

$$Recovery_{C_2H_4} = 100 \times \frac{\int_{evacuation} u_g^{out} C_{g,C_2H_4}^{out} dt}{\int_{\substack{adsorption \\ + pressurization}} u_g^{in} C_{g,C_2H_4}^{in} dt} \tag{C13}$$

$$Productivity_{C_2H_4} = 3600 \times \frac{\int_{evacuation} u_g^{out} C_{g,C_2H_4}^{out} dt}{\rho_f w_f L \left(\frac{r_{OD}^{\ 2} - r_{ID}^{\ 2}}{r_{fs}^{\ 2} - r_{OD}^{\ 2}} \right) t_{cycle}} \tag{C14}$$

C.4.5 Energy Consumption

Following equations represent the energy consumed due to (i) heating feed from its starting temperature to the temperature of operation of the PSA cycle, (ii) compression of feed gas from ambient to the higher pressure of operation and (iii) depressurizing the bed to the intermediate and low pressures of the blowdown and evacuation step respectively

$$Energy_{feed} = \int_{\substack{Feed + \\ Pressn}} \left(\sum_{i=comp} C_{g,i} c_{p,i} (T_{g,ads} - T_{feed}) u_g \Big|_{in} \right) dt \tag{C15}$$

$$Energy_{compression} = \frac{1}{\eta} \frac{\gamma}{\gamma - 1} \int_{press+\ feed} P_{tot}\ u_g \left(\left(\frac{P_{tot}}{P_{atm}} \right)^{\frac{\gamma-1}{\gamma}} - 1 \right) \Bigg|_{z=0,in} dt \tag{C16}$$

$$if \quad P_{tot} > P_{atm}$$

$$Energy_{depress} = \frac{1}{\eta}\frac{\gamma}{\gamma-1}\left(\int_{blowdown} P_{tot}\, u_g \left(\left(\frac{P_{atm}}{P_{tot}} \right)^{\frac{\gamma-1}{\gamma}} - 1 \right)\Bigg|_{z=L,out} dt + \int_{evacuation} P_{tot}\, u_g \left(\left(\frac{P_{atm}}{P_{tot}} \right)^{\frac{\gamma-1}{\gamma}} - 1 \right)\Bigg|_{z=0,out} dt \right) \qquad \text{(C17)}$$

$$if \quad P_{tot} < P_{atm}$$

$$Energy_{removed} = \left(\int_{\substack{Blowdown+\\Evacuation}} \rho_{bf} c_{p,bf} (T_{bf,in} - T_{bf,out}) \left\| u_{bf} \right\| dt \right) \frac{r_{ID}^2}{r_{fs}^2 - r_{OD}^2} \qquad \text{(C18)}$$

$$Energy_{supplied} = \left(\int_{\substack{Press+\\Feed}} \rho_{bf} c_{p,bf} (T_{bf,out} - T_{bf,in}) \left\| u_{bf} \right\| dt \right) \frac{r_{ID}^2}{r_{fs}^2 - r_{OD}^2} \qquad \text{(C19)}$$

C.5 Equations for Simple Model

C.5.1 Purity Estimate

The following equation was used to approximate ethylene purity in the simplified model

$$P_{TVSA} = \frac{q^*_{C_2H_4}(y_{feed,C_2H_4}, T, P_{high}) - q^*_{C_2H_4}(x_{prod,C_2H_4}, T, P_{low})}{\sum_{\substack{i=C_2H_6,\\ C_2H_4}} q^*_i(y_{feed,i}, T, P_{high}) - q^*_i(x_{prod,i}, T, P_{low})} \quad \text{(C20)}$$

C.5.2 Energy Estimate

Equation (23) was used to estimate the energy consumed per unit mass of ethylene product generated by the TVSA cycle (in the simplified model). Equations (21) and (22) show the calculations leading to the final form i.e. Equation (23)

Assuming $T_{ads} = T_{des}$ i.e. constant temperature of operation

$$E_{TVSA} = \frac{\left(\begin{array}{l} c_p\left(T_{ads} - T_{feed}\right)\int \dot{n}_{feed}\, dt + \frac{\gamma}{\gamma - 1} RT\left[\left(\frac{P_{high}}{P_{feed}}\right)^{\frac{\gamma-1}{\gamma}} - 1\right]\int n_{feed\,dt} \\ + \frac{\gamma}{\gamma - 1} RT\left[\left(\frac{P_{atm}}{P_{low}}\right)^{\frac{\gamma-1}{\gamma}} - 1\right]\int n_{prod\,dt} \end{array} \right)}{\eta \times MW_{C_2H_4} \times \left(y_{feed,C_2H_4}\int \dot{n}_{feed}\, dt\right)} \quad \text{(C21)}$$

$$y_{feed,C_2H_4}\int \dot{n}_{feed}\, dt = x_{prod,C_2H_4}\int \dot{n}_{prod}\, dt \qquad \text{(assuming 100\% recovery)} \quad \text{(C22)}$$

$$E_{TVSA} = \frac{c_p\left(T - T_{feed}\right) + \frac{\gamma}{\gamma - 1} RT \left(\left[\left(\frac{P_{high}}{P_{feed}} \right)^{\frac{\gamma-1}{\gamma}} - 1 \right] + \left[\left(\frac{P_{atm}}{P_{low}} \right)^{\frac{\gamma-1}{\gamma}} - 1 \right] \frac{y_{feed,C_2H_4}}{x_{prod,C_2H_4}} \right)}{\eta \times MW_{C_2H_4} \times y_{feed,C_2H_4}} \quad \text{(C23)}$$

C.6 Binding energies (kJ/mol) in 11 mixed-metal MM'-BTCs

Table C-13 - Calculated binding energies in 11 mixed-metal MM'-BTCs.

Cr-Mo-BTC	C_2H_4	C_2H_6
Cr-BTC	42.0	21.9
Cr @ Cr-Mo	42.8	23.4
Mo @ Cr-Mo	40.0	18.4
Mo-BTC	38.1	21.3

Cr-Cu-BTC	C_2H_4	C_2H_6
Cr-BTC	42.0	21.9
Cr @ Cr-Cu	47.1	22.8
Cu @ Cr-Cu	45.6	26.6
Cu-BTC	40.4	23.9

Cr-Ru-BTC	C_2H_4	C_2H_6
Cr-BTC	42.0	21.9
Cr @ Cr-Ru	46.3	25.9
Ru @ Cr-Ru	46.9	23.4
Ru-BTC	52.0	22.5

Cr-Fe-BTC	C_2H_4	C_2H_6
Cr-BTC	42.0	22.0
Cr @ Cr-Fe	37.3	19.2
Fe @ Cr-Fe	71.9	23.4
Fe-BTC	64.0	23.0

Cr-Mg-BTC	C_2H_4	C_2H_6
Cr-BTC	42.0	22.0
Cr @ Cr-Mg	40.1	20.0
Mg @ Cr-Mg	68.7	38.3
Mg-BTC	68.0	41.0

Cr-Mn-BTC	C_2H_4	C_2H_6
Cr-BTC	42.0	22.0
Cr @ Cr-Mn	42.1	24.4
Mn @ Cr-Mn	68.8	33.6
Mn-BTC	69.0	37.0

Cr-Zn-BTC	C_2H_4	C_2H_6
Cr-BTC	42.0	22.0
Cr @ Cr-Zn	40.1	21.7
Zn @ Cr-Zn	75.3	26.4
Zn-BTC	79.0	38.0

Cu-Zn-BTC	C_2H_4	C_2H_6
Cu-BTC	40.4	23.9
Cu @ Cu-Zn	44.3	27.0
Zn @ Cu-Zn	76.6	37.2
Zn-BTC	79.0	38.0

Table C-13 continued

Cu-Mg-BTC	C_2H_4	C_2H_6
Cu-BTC	40.4	23.9
Cu @ Cu-Mg	42.9	27.8
Mg @ Cu-Mg	69.3	44.6
Mg-BTC	68.0	41.0

Fe-Mg-BTC	C_2H_4	C_2H_6
Fe-BTC	64.0	23.0
Fe @ Fe-Mg	53.5	23.8
Mg @ Fe-Mg	62.6	32.5
Mg-BTC	68.0	41.0

Ti-Mo-BTC	C_2H_4	C_2H_6
Ti-BTC	53.0	20.0
Ti @ Ti-Mo	54.7	23.4
Mo @ Ti-Mo	36.9	20.6
Mo-BTC	38.1	21.3

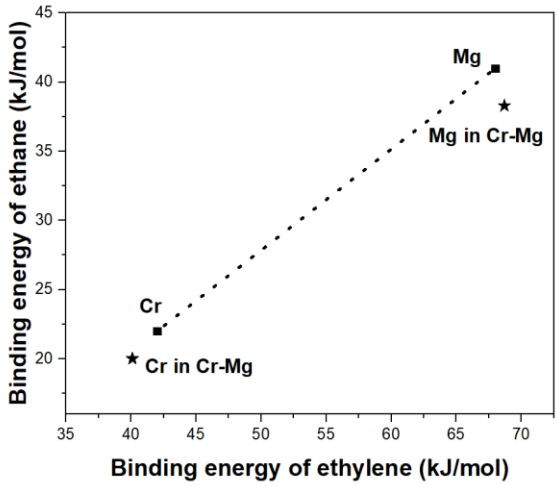

Figure C-3 - The binding energy of ethylene and ethane for Cr and Mg in mixed metal dimers of Cr-Mg-BTC and pure Cr-BTC and Mg-BTC. Mixed site binding energies, indicated by the star symbol, do not lie on the tie line between the pure Cr and Mg metal states.

C.7 Parameter values used in Full Model

Table C-14 - Properties of the adsorption bed and the adsorbent solid phase

Hollow Fiber Bed			
R_{OD} ,m	0.653×10^{-3}	w_f	0.6
R_{ID} ,m	0.275×10^{-3}	λ_f, W/m.K	0.05
ε_f	0.48	C_{pf} , J/kg.K	1142.4
τ_f	2.5	v_{fib}	0.68
R_{pore} , µm	0.17	$C_{p,bf}$, J/kg.K	4178
R_c , µm	1	h_{bf} , W/m^2.K	7268
ρ_f ,kg/m^3	802	ρ_{bf} ,kg/m^3	1000

Table C-15 - Property parameters for ethylene, ethane

	C_2H_4	C_2H_6
D_{c0A} , m^2/sec	3.8×10^{-9}	3.6×10^{-9}
D_{c0B} , m^2/sec	3.1×10^{-9}	3.9×10^{-9}
E_A , J/mol	16.97×10^{3}	23.7×10^{3}
E_B , J/mol	16.05×10^{3}	21.5×10^{3}
C_p , J/mol	51.54	65.22
C_v , J/mol	43.23	56.90
$C_{v,ads}$, J/mol	120	112
$K_{conductivity}$, W/m.K	28.9×10^{-3}	27.07×10^{-3}
σ	4.934	4.766
ω	1.24	1.24
μ_g , Pa.s	1.53×10^{-5}	

Table C-16 - Mass transfer coefficients in the packed bed and the hollow fiber bed for same interstitial bulk gas velocity (1.05 m/s) and same bed void fraction (0.32). The coefficients are calculated on the basis of a unit volume of the pellet (or hollow fiber) and the difference between the actual and the equilibrium adsorbed phase (q*) as the driving force

Mass transfer coefficients $\frac{mol/sec}{m^3_{pellet}\left(\frac{mol}{kg_{adsorbent}}\right)}$	C_2H_6	C_2H_4
	Hollow Fiber Bed	Hollow Fiber Bed
k'_{gas}	17.98	2.06
k'_{macro}	5.40	0.62
k'_{micro}	2.42×10^5	3.99×10^4

Table C-17 - Heat transfer coefficients in the packed bed and the hollow fiber bed for same interstitial bulk gas velocity (1.05 m/s) and same bed void fraction (0.32). Units: (Watt/K) / (m3 of solid phase i.e. pellet or fiber.

	$h_{adsorbent-H/C\ medium}$		$h_{adsorbent-gas}$	$\boldsymbol{h_{overall}}$
	$W/m^2.K$	$W/m^3.K$	$W/m^3.K$	$W/m^3.K$
Hollow Fiber Bed	7,268	1.15×10^5	1.14×10^7	1.15×10^7

C.8 Notation

$\Delta H_{ads,i}$	heat of adsorption of component i (J/mol)	Pr	Prandtl no.
a	area to volume ratio, pellet or fiber (1/m)	P_{tot}	total pressure (bar)
$a_{f,int}$	internal surface area/ volume fo fiber (1/m)	$P_{tot}\|_z^0$	pressure at position z at the beginning of respective step (bar)
Bi_i	Biot no. at the gas pellet (or fiber) interface	P_{TVSA}	Purity of TVSA ethylene product

$C_{g,tot}$	total bulk gas phase concentration (mol/m^3)	q_i	adsorbed phase concentration (mol/kg)
C_{gi}	bulk gas phase concentration (mol/m^3)	q_i*	equilibrium adsorbed phase concentration (mol/kg)
$C_{p,bf}$	heat capacity of bore fluid (J/kg/K)	Q_{vol}	volumetric flow rate of gas (m^3/s)
$C_{p,bf}$	heat capacity of fluid in the bore (J/kg/K)	R	ideal gas constant
$C_{p,T}$	total constant pressure heat capacity of gas (J/mol/K)	R_{bed}	radius of the bed, packed or hollow fiber (m)
$C_{p,tot}$	total pellet gas phase concentration (mol/m^3)	R_c	radius of crystal (m)
c_{pf}	heat capacity of fiber (J/kg/K)	Re	Reynold's number.
C_{pi}	macropore gas phase concentration (mol/m^3)	r_{fs}	radius of Happel's free surface (m)
$C_{v,ads,i}$	heat capacity of adsorbed phase (J/mol/K)	R_{hyd}	hydraulic radius of fiber (m)
$c_{v,i}$	constant volume heat capacity of component i (J/mol/K)	R_{ID}	inner radius of a single fiber (m)
$C_{v,T}$	total constant volume heat capacity of gas (J/mol/K)	R_{OD}	outer radius of a single fiber (m)
$D_{ax,i}$	mass axial dispersion coefficient (m^2/s)	R_{pore}	radius of mcropores in fiber (m)
$D_{c,0A,I}$, $D_{c,0B,i}$	pre-exponential factors for crystal diffusivity (m2/s)	Sc_i	Schmidt no.
$D_{c,i}$	crystal diffusivity (m^2/s)	Sh_i	Sherwood no.
$D_{fp,i}$	macropore diffusivity inside fiber (m^2/s)	t	time (sec)
$D_{p,i}$	macropore diffusivity inside pellet (m^2/s)	T_{amb}	temperature of ambient (K)
$E_{A,}$, $E_{B,i}$	activation energy for crystal diffusion (J/mol)	Tbf	bore fluid temperature (K)
h_{bf}	film heat transfer coefficient between fiber and fluid in the bore (W/m^2/K)	T_f	temperature of fiber (K)

h_f	Gas film heat transfer coefficient between gas and solid phase ($W/m^2/K$)	T_{feed}	temperature of feed (K)
$K_{conductivity,i}$	thermal conductivity of pure component i (W/m2.K)	T_g	gas temperature (K)
$k_{g,i}$	gas film mass transfer coefficient (m/s)	$time_{cycle}$	total time to complete 1 cycle (sec)
$k_{gas,i}$, $k_{macro,i}$, $k_{micro,i}$,	LDF mass transfer coefficients (1/sec)	t_{step-x}	total time required for step x (x = adsorption, blowdown etc)
$k_{gas,j}$	LDF mass transfer coefficients (1/sec)	u_{bf}	velocity of the bore fluid (m/s)
K_{mix}	thermal conductivity of gas mixture ($W/m^2.K$)	u_g	gas velocity (m/s)
L	length of the bed (m)	v_{ads}	velocity of the feed gas at inlet (m/s)
M_p , M_b	pseudo-valve coefficients during pressurization, blowdown	v_{fib}	volume fraction of bed occupied by the fibers
MW_i	molar weight of component i (kg/mole)	w_s	weight fraction of adsorbent in the fiber
N_i	flux of species i being removed from bulk gas phase (per unit volume of bulk gas)	$x_{prod,i}$	mole fraction of component i in product stream of the desaturation step
n_{prod}, n_{feed}	number of moles	$y_{ads,i}$	mole fraction of component i in the inlet
Nu	Nusselt number	$y_{feed,i}$	mole fraction of component i in feed
P_{ads} , Pinter, P_{des}	adsorption and desorption pressure (bar)	y_i	mole fraction
P_{atm}	Atmospheric pressure (1 bar)	z	axial distance along column (m)
p_i	partial pressure (bar)		

C.8.1 Greek symbols

μ_g	viscosity of gas (Pa.s)	λ_f	thermal conductivity of fiber (W/m.K)
γ	ratio of specific heats	ρ_{bf}	density of bore fluid (kg/m^3)
ε	porosity of bed	ρ_f	total density of fiber (including fiber void volume) (kg/m^3)
ε_f	porosity of fiber	ρ_g	density of gas (kg/m^3)
η	efficiency of compressor	ρ_p	total density of fiber (including pellet void volume) (kg/m^3)
λ	axial heat dispersion (W/m.K)	τ_f	tortuosity of fiber

C.9 References

[1] Sillar, K.; Sauer, J., Ab Initio Prediction of Adsorption Isotherms for Small Molecules in Metal-Organic Frameworks: The Effect of Lateral Interactions for Methane/CPO-27-Mg. *Journal of the American Chemical Society* **2012,** *134* (44), 18354-18365.

[2] Wong, M. W., Vibrational frequency prediction using density functional theory. *Chem Phys Lett* **1996,** *256* (4-5), 391-399.

[3] Shubina, T. E.; Hartnig, C.; Koper, M. T. M., Density functional theory study of the oxidation of CO by OH on Au(110) and Pt(111) surfaces. *Physical Chemistry Chemical Physics* **2004,** *6* (16), 4215-4221.

APPENDIX D. SUPPORTING INFORMATION FOR CHAPTER 4

D.1 Crystal Diffusion Model

$$-\rho \frac{q_i}{RT} \frac{\partial \mu_i}{\partial r} = -\rho \sum_j \Gamma_{ij} \frac{\partial q_j}{\partial r} = \sum_{j \neq i} \frac{x_j N_i - x_i N_j}{\mathcal{D}_{ij}} + \frac{N_i}{\mathcal{D}_i} \tag{D1}$$

$$\left(\frac{1}{\mathcal{D}_i} + \sum_j \frac{x_j}{\mathcal{D}_{ij}} \right) N_i - x_i \sum_{j \neq i} \frac{N_j}{\mathcal{D}_{ij}} = -\rho \sum_{j \neq i} \Gamma_{ij} \frac{\partial q_j}{\partial r} \tag{D2}$$

$$[B](N) = -\rho [\Gamma] \left(\frac{\partial q}{\partial r} \right) \quad \left(\text{i.e.} \quad \sum_j B_{ij} N_j = -\rho \sum_j \Gamma_{ij} \frac{\partial q_j}{\partial r} \right) \tag{D3}$$

Thermodynamic correction factor

$$\Gamma_{ij} = \frac{q_i}{p_i} \frac{\partial p_i}{\partial q_j} \tag{D4}$$

D.1.1 Converting equations to dimensionless form

$$q_i = \frac{q_i^{sat} p_i b_i}{1 + \sum_j p_j b_j} \quad \theta_i = \frac{\hat{b}_i y_i}{1 + \sum_j \hat{b}_j y_j} \tag{D5}$$

Where $y_i = \frac{p_i}{P^0}$ $\qquad \hat{b}_i = b_i P^0$

$$\Gamma_{ij} = \frac{q_i}{p_i}\frac{\partial p_i}{\partial q_j} = \frac{q_i^{sat}}{q_j^{sat}}\left(\delta_{ij} + \frac{\theta_i}{1-\sum_j \theta_j}\right) = \frac{q_i^{sat}}{q_j^{sat}}\left(\delta_{ij} + \frac{q_i / q_i^{sat}}{1-\sum_j q_j / q_j^{sat}}\right) \tag{D6}$$

$$\hat{\Gamma}_{ij} = \frac{\theta_i}{y_i}\frac{\partial y_i}{\partial \theta_j} = \left(\delta_{ij} + \frac{\theta_i}{1-\sum_j \theta_j}\right) = \delta_{ij} + \hat{b}_i y_i \tag{D7}$$

D.1.2 Final form for dimensionless crystal model:

If i = j then $B_{ij} = \frac{1}{\cancel{D}_{ij}} + \sum_j \frac{x_j}{\cancel{D}_{ij}} - \frac{x_i}{\cancel{D}_{ij}}$ else $B_{ij} = -\frac{x_i}{\cancel{D}_{ij}}$ (D8)

$$\hat{\cancel{D}}_{ij} = \frac{\cancel{D}_{ij}}{\cancel{D}_{11}} \qquad \hat{B}_{ij} = B_{ij}\cancel{D}_{11} \qquad \hat{B}_{ij}^{-1} = \frac{B_{ij}^{-1}}{\cancel{D}_{11}} \tag{D9}$$

$$(N) = -\rho[B]^{-1}[\Gamma]\left(\frac{\partial q}{\partial r}\right) \qquad (N) = -\rho[\cancel{D}]\left(\frac{\partial q}{\partial r}\right) \tag{D10}$$

$$[\cancel{D}] = [B]^{-1}[\Gamma]$$

$$-\frac{N_i}{\rho} = \sum_j \sum_k B_{ik}^{-1}\Gamma_{kj}\dot{q}_j = \sum_j \sum_k \hat{B}_{ik}^{-1}\hat{\Gamma}_{kj}\dot{\theta}_j\left(\cancel{D}_{11} q_j^{sat}\frac{q_k^{sat}}{q_j^{sat}}\right) = \sum_j \sum_k \hat{B}_{ik}^{-1}\hat{\Gamma}_{kj}\dot{\theta}_j\left(\cancel{D}_{11} q_k^{sat}\right) \tag{D11}$$

$$q_i^{sat}\frac{\partial\theta_i}{\partial t}=-\frac{1}{\rho}\frac{1}{r^2}\frac{\partial}{\partial r}\left(r^2N_i\right)$$

$$\left(\frac{\partial q}{\partial t}\right)=-\frac{1}{\rho}\frac{1}{r^2}\frac{\partial}{\partial r}\left(-r^2\rho[B]^{-1}[\Gamma]\left(\frac{\partial q}{\partial r}\right)\right) \tag{D12}$$

$$\frac{\partial\theta_i}{\partial\left(\frac{t}{R_c^{\,2}}D_{11}\right)}=\frac{1}{\rho}\frac{1}{\hat{r}^2}\frac{\partial}{\partial\hat{r}}\left(\hat{r}^2\rho\sum_j\sum_k\left(\frac{q_k^{sat}}{q_i^{sat}}\hat{B}_{ik}\right)^{-1}\left(\delta_{kj}+\frac{\theta_k}{1-\sum_m\theta_m}\right)\frac{\partial\theta_j}{\partial\hat{r}}\right) \tag{D13}$$

D.1.3 Boundary Conditions:

At r = R_c

$$\theta_i=\theta^*{}_i=\frac{\hat{b}_i y_i}{1+\sum_j\hat{b}_j y_j}\left(where,\hat{b}_i=b_iP_{tot},y_i=\frac{p_i}{P_{tot}}\right)$$
$$=\frac{\tilde{\hat{b}}_i y_i}{\frac{1}{\hat{b}_1}+\sum_j\tilde{\hat{b}}_j y_j}\left(where,\tilde{\hat{b}}_i=\frac{b_i}{b_1},\hat{b}_1=b_1P_{tot},y_i=\frac{p_i}{P_{tot}}\right) \tag{D14}$$

At r =0

$$\frac{\partial\theta_i}{\partial r}=0 \tag{D15}$$

D.2 Material property parameters

D.2.1 Constant properties

Table D-18 – Value of input material property parameters considered constant in analysis

	Component 1	Component 2
E_c (kJ/mol)	16	22
ΔH (kJ/mol)	-37.8	-32
$q^{sat}{}_1$ (mol/m^3 adsorbent crystal)	2640	
$D_{c1}{}^0$ (m/s^2)	4.09×10^{-8}	

D.3 MAP-Elites Algorithm description

The algorithm begins with a random selection of genomes and determining their performance and features. Samples are placed into cells to the feature bin to which they belong based on these results. If multiple genomes map to the same bin, only the highest performer is retained. This is followed by repeated iterations of the following steps till termination criteria is satisfied (such as allowed computational resources or time). (1) From the current map a sample is randomly selected and mutated via mutation and/or crossover. (2) Features and performance of the offspring are evaluated. Suitable bins are determined based on these evaluations. The offspring is placed in the bin if it is unoccupied or out-performs the previous occupant (in this case the previous occupant is discarded). A pseudocode for the algorithm is provided in Figure D-4.

```
procedure MAP-elites algorithm
  (P = [ ];  X = [ ] )      (Create an empty, N-dimensional map of elites: {solutions X and their performances P})
  for iter = 1 to I do                  (Repeat for I iterations)
     if iter < G then
       x′ = random_solution()           (Initialize by generating G random solutions; all subsequent
                                                    solutions are generated from elites in the map)
     else
       x = random selection(X)          (Randomly select an elite from the map)
       x′ = random_variation(x)         (Generate offspring x′ through random mutation and/or crossover of x)
     b′ = feature_descriptor(x′)        (Simulate candidate solution x′ and record its feature descriptor b′ )
     p′ = performace(x′)                (Record performance p′ of x′)
     if P(b′) = [ ] or P(b′) < p′ then  (if appropriate bin is empty or its occupant's performance is ≤ p′)
       P(b′) = p′
       X(b′) = x′                  (store solution x′ and performance p′ according to its feature descriptor b′)

  return feature-performance map (P and X)
```

Figure D-4 - Pseudocode for MAP-elites algorithm.

D.4 SAIL Algorithm

SAIL initiates by creating a Gaussian Process model from precisely evaluated samples, selected randomly from the genotype space *x*. The UCB estimate form the GP is then used as performance metric to run MAP-elites as described in the section above. An *acquisition map* is generated with maximizes the acquisition function in each bin of the feature space. Underlying predicted optimal *genotype* parameters, form a few randomly selected *feature bins* are precisely evaluated using the underlying system model. These evaluations are added to the GP estimate which is again used to generate an *acquisition map*. A schematic representation of these steps is shown in Figure D-5**Error! Reference source not found.**, for an example function. The iterations are repeated till we run out of a user defined precise evaluation budget. The final iteration of SAIL used the *mean* (μ) instead of the UCB to run MAP-elites which results in the final *prediction map* of elite

values for each bin in the feature space. If the feature functions are also complex, their mean value may be estimated using independent GP models for each.

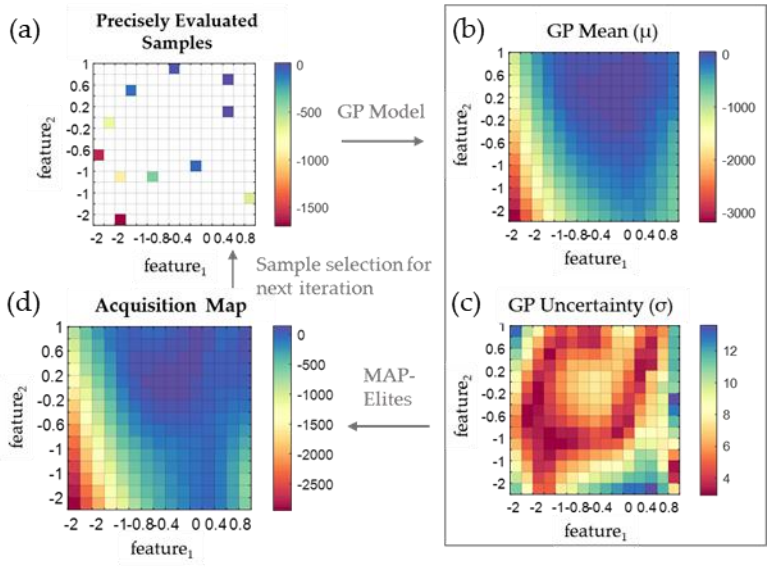

Figure D-5 - Schematic of a single iteration in the SAIL algorithm for an example function. (a) Indicates the initial samples selected randomly for precise evaluation of performance and features. (b) & (c) represents the mean and uncertainty predicted by fitting a Gaussian Process model to the precisely evaluated samples (d) represents the acquisition map generated by applying MAP-elites algorithm on the GP Upper Confidence Bound (UCB) estimate for performance. Random samples are selected from this map for precise evaluation and so the next iteration repeats the above steps. This continues till termination criteria.

D.5 Calculating p from q

$$\frac{dP_0(\mathrm{i})}{d\varepsilon} = \frac{\mathrm{q}_0(1)/\mathrm{P}_0(1)}{\mathrm{q}_0(\mathrm{i})/\mathrm{P}_0(\mathrm{i})} \tag{D16}$$

Where $P_0(i)$ are the hypothetical pressures at which each component exerts the same modified spreading pressure (π). $q_0(i)$ is the single component loading in equilibrium with $P_0(i)$. Integrating the above set of ODEs from an intial condition of $P_0(i) = 0$, till the

following stopping criteria enables calculation of $P_0(i)$ corresponding to a given multi-component loading.

$$\sum_i \frac{x_i}{q_{0_i}} = \frac{1}{q_{tot}} \tag{D17}$$

x_i is the loading fraction of each component, q_{tot} are the total component loadings, and are known values.

D.6 Analytical Jacobian

$$\begin{aligned}
x &= \frac{q_i}{\sum_i q_i}; \qquad P_{0_i} = \frac{P_i}{x_i}; \quad q_{0_i} = f\left(P_{0_i}\right) \\
w_i &= \frac{\sum_i q_i}{q_{0_i}}; \qquad \mathrm{w} = \mathrm{col}(\mathrm{w}_i); \quad W = diag(w); \quad e^T = [1...1] \\
\sigma &= \sum_i \left(w_i P_i \sum q \frac{d}{dP_{0_i}} \left(\frac{1}{q_{0_i}} \right) \right) \\
J &= \left(\left(\mathrm{I} - \left[xw^T \right] \right) \left(\mathrm{I} - \left[Wxe^T \right] \right) - \sigma \left[xe^T \right] \right) \left(diag \left(\frac{\sum q}{P_{0_i}} \right) \right)
\end{aligned} \tag{D18}$$

D.7 Comparison of Langmuir approximation of Γ to full calculation when using IAST

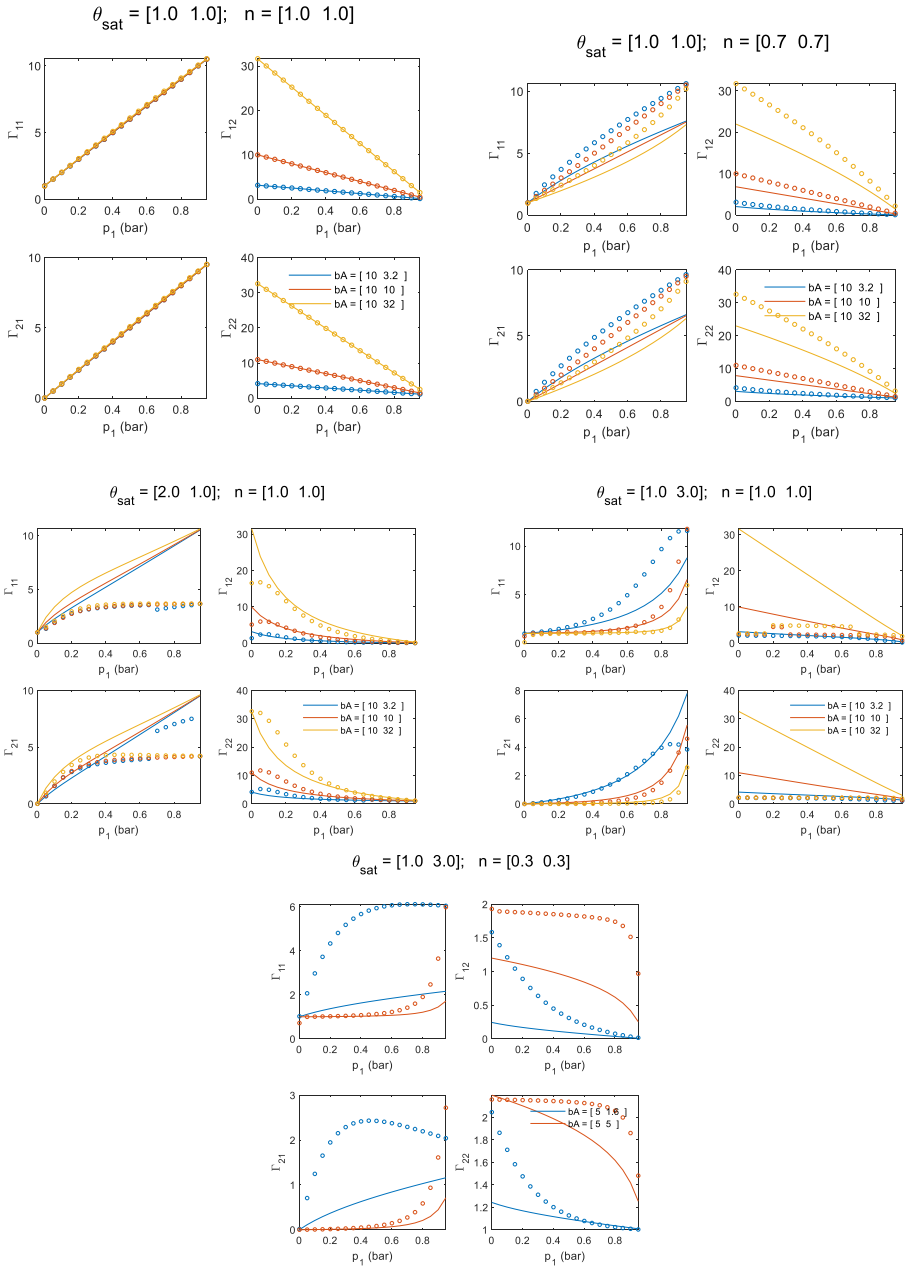

Figure D-6 - The solid lines indicate Γ calculated using competitive Langmuir isotherm, the open circles indicate exact Γ calculation using IAST calculations for Toth isotherms.

APPENDIX E. SUPPORTING INFORMATION FOR CHAPTER 5

E.1 Detailed isotherm model:

The detailed isotherm model is presented in equations E1-E13. Parameter values used to fit experimental data are listed in Table E-1. The transition pressure is given by equation E1.

$$p_{step}(T) = p_{step,0} \exp\left(\frac{-\Delta H_{step}}{R} \left(\frac{1}{T_0} - \frac{1}{T} \right) \right) \quad \text{(E1)}$$

The sigmoidal CO_2 isotherm of MMEN-Mg_2(dobpdc) is modeled using the method outlined by Hefti et al.[1] with some modifications. Total adsorption is sum of two adsorption mechanisms denoted by $q_1{}^*$ and $q_2{}^*$. Adsorption of CO_2 below the step partial pressure, p_{step} is represented by a modified Langmuir isotherm q_{low}. A combination of a Langmuir and Henry's isotherm q_{high} is used after the transition step.

$$q_{total} = q_1^* + q_2^* \quad \text{(E19)}$$

$$q_1^* = q_{low}(1-w) + q_{sat} w \quad \text{(E20)}$$

$$q_2^* = \left(q_{high} - q_{sat} \right) w \quad \text{(E21)}$$

$$q_{low} = \frac{q_L (b_L p)^{n_L}}{1 + (b_L p)^{n_L}} \qquad \text{For } p < p_{step} \tag{E22}$$

$$q_{high} = \frac{q_H b_H p}{1 + b_H p} + q_U p \quad \text{For } p > p_{step} \tag{E23}$$

$$q_{sat} = \frac{q_L (b_L p_{step})^{n_L}}{1 + \left(b_L p_{step}\right)^{n_L}} \tag{E24}$$

A smooth function (w) is used to switch between the low-pressure Sips and the high pressure Langmuir-Henry isotherms, shown here in equation E8. Parameters in the isotherm are listed in Table E-1.

$$w = \left(\frac{exp\left(\frac{log(p) - log(p_{step})}{\sigma} \right)}{1 + exp\left(\frac{log(p) - log(p_{step})}{\sigma} \right)} \right)^{\gamma} \tag{E25}$$

The temperature dependences of the affinity and heterogeneity parameters and the switching function are presented in the equations E9-E13

$$b_L = b_{L0} \exp\left(\frac{\Delta H_L}{R T_g} \right) \tag{E26}$$

$$b_H = b_{H0} \exp\left(\frac{\Delta H_H}{RT_g}\right) \tag{E27}$$

$$q_U = q_{U0} \exp\left(\frac{\Delta H_u}{RT_g}\right) \tag{E28}$$

$$n = n_0 \exp\left(\frac{\Delta H_n}{RT_g}\right) \tag{E29}$$

$$\sigma = \lambda_1 exp\left(\lambda_2\left(\frac{1}{T_0} - \frac{1}{T_g}\right)\right) \tag{E30}$$

E.2 Model for the mass transfer in the bed:

Dimensionless numbers and corresponding equations are given by equations E14-E28. Parameters are listed under *Notations*.

$$\mathrm{Re} = \frac{2R_p \rho_g v}{\mu_g} \tag{E31}$$

$$Sc_i = \frac{\mu_g}{\rho_g D_{mol,i}} \tag{E32}$$

$$\mathrm{Pr} = \frac{\mu_g}{K_{mix}} \frac{C_{p,tot}}{MW_{mix}} \tag{E33}$$

Table E-1 - Parameters used to fit the experimental isotherms along with their temperature dependence.

Parameter	Values used in the simulation	Parameter	Values used in the simulation
T_0	313.5 K	q_{U0}	$5.27\times10^{-7}\ mol/kg\ .\ mbar^{-1}$
p_0	$0.80\ mol/kg$	λ_1	1.74×10^{-2}
q_L	$28.25\,mol/kg$	ΔH_{step}	$-62.49\,kJ/mol$
b_{L0}	$2.51\times10^{-15}\ mbar^{-1}$	ΔH_L	$70.74\ kJ/mol$
n_0	0.518	ΔH_n	$1.35\,kJ/mol$
q_H	$3.46\ mol/kg$	ΔH_H	$67.72\,kJ/mol$
b_{H0}	$2.42\times10^{-11}\ mbar^{-1}$	ΔH_u	$18.67\,kJ/mol$
		λ_2	$6.53\,kJ/mol$

$$K_{m,i} = \frac{Sh_i D_{mol,i}}{2R_p} \tag{E34}$$

$$Sh_i = 2 + 1.1 Re^{0.6} Sc_i^{0.33} \tag{E35}$$

$D_{mol,i}$ is calculated from the Chapman-Eskog equation for gas molecular diffusion coefficient.

$$\frac{1}{D_{p,i}} = \frac{\tau}{\varepsilon}\left(\frac{1}{D_{mol,i}} + \frac{1}{D_{knud,i}}\right) \tag{E36}$$

Where, $D_{knud,i}$ stands for Knudsen diffusion.

$$P_{tot} = \sum p_i,\ \ p_i = C_{g,i}RT_g,\ \ C_{g,tot} = \sum C_{g,i} \tag{E37}$$

The Ergun equation is used for the estimation of pressure drops,

$$-K_{mbar\to Pa}\frac{\partial P_{tot}}{\partial z} = 150\frac{\mu_g(1-\varepsilon)^2}{\varepsilon^3(2R_p)^2}u_g + 1.75\frac{(1-\varepsilon)\rho_g}{2R_p\varepsilon^3}u_g{}^2 \tag{E38}$$

$$\frac{\partial C_{g,i}}{\partial t} = D_{ax,i}\frac{\partial^2 C_{g,i}}{\partial z^2} - \frac{1}{\varepsilon}\frac{\partial(u_g C_{g,i})}{\partial z} - \frac{1}{\varepsilon}Ni_i \tag{E39}$$

For He, $Ni_i = 0$ (E40)

For CO_2,

$$Ni_i = \frac{(1-\varepsilon)aK_{m,i}}{1+Bi_i}\left(C_{g,i} - C_{part,i}\right) \tag{E41}$$

$$a = \frac{3}{R_p},\ \ Bi_i = \frac{K_{m,i}R_p}{5\varepsilon_p D_{p,i}} \tag{E42}$$

$$\frac{\partial C_{part,i}}{\partial t} = \frac{15 D_{p,i}}{R_p{}^2} \frac{Bi_i}{1+Bi_i}\left(C_{g,i} - C_{part,i}\right) - \frac{\rho_p}{\varepsilon_p}\left(\frac{\partial q_1}{\partial t} + \frac{\partial q_2}{\partial t}\right) \tag{E43}$$

E.3 Boundary conditions

$$C_{g_{in}} = y_{ads} \frac{P_{tot}\big|_0}{RT\big|_0} \tag{E44}$$

$$-\varepsilon D_{ax,i} \left.\frac{\partial C_{g,i}}{\partial z}\right|_0 = u_{g_0}\left(C_{g,i_{in}} - C_{g,i}\big|_0\right) \tag{E45}$$

$$\left.\frac{\partial C_{g,i}}{\partial z}\right|_L = 0 \tag{E46}$$

E.4 Estimation of the dispersion coefficient in the bed.

Dispersion in the bed is modeled using the Wakao & Funazkri[2] empirical correlation given by equation E30-E31.

$$D_{ax} = \left(20 + 0.5 Sc\,\mathrm{Re}\right)\frac{D_{mol}}{\varepsilon} \tag{E47}$$

$$\lambda = (7 + 0.5\,\mathrm{Pr}\,\mathrm{Re})K_{mix} \tag{E48}$$

E.5 Breakthrough profiles at different flowrates

The linear driving force equation with a single LDF constant was used to predict breakthrough profiles at different flowrates. As shown in the Figure E-1, the same wave concentration was observed for all flowrates.

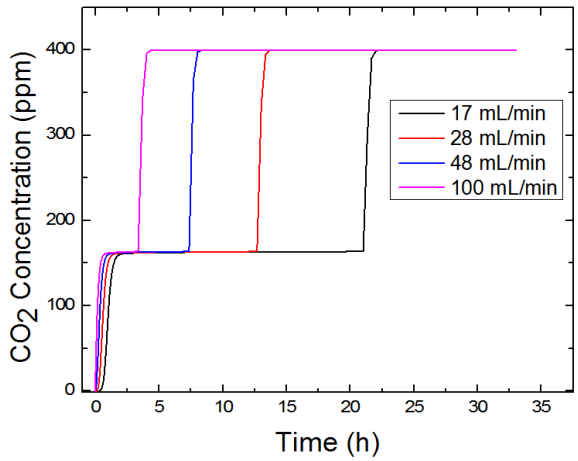

Figure E-1 - Predicted breakthrough profiles at different flowrates using linear driving force model with single mass transfer coefficient.

Table E-2 - Avrami rate constant and coefficient for different concentrations of CO_2.

p_{CO_2} (mbar)	Avrami rate constant, k_A (s^{-1})	Avrami coefficient n_A
0.4	4.36×10^{-5}	1.50
1	3.80×10^{-4}	1.55

10.02	4.22×10^{-3}	1.75

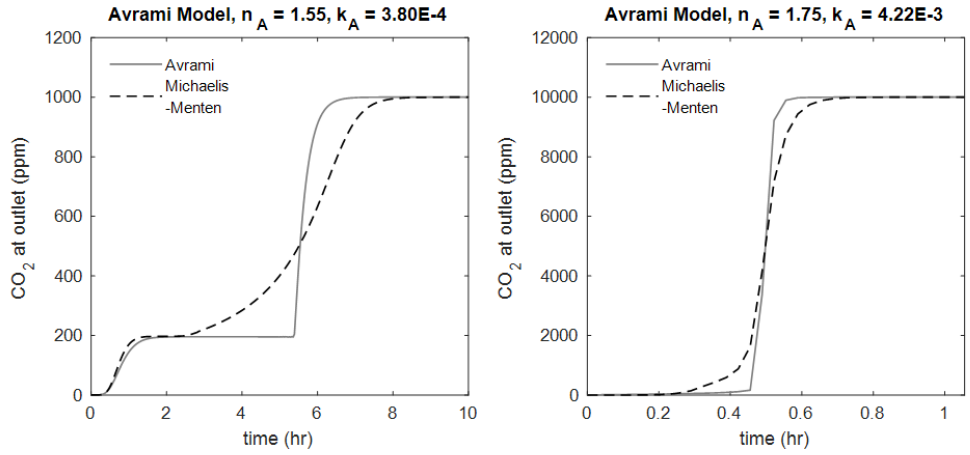

Figure E-2 - Predicted breakthrough profiles using the hybrid Avrami model (solid lines) vs Michaelis-Menten analogue model (dashed lines) at 1000 PPM (left) vs 10020 PPM (right) feed concentrations. These results are simulated for a feed flowrate of 17.2 NmL/min.

E.6 Effect of temperature on the breakthrough profile

The CO2 adsorption profiles at temperatures of 23 °C, 49 °C, and 70 °C are presented in Figure E-3 for the flowrate of 17.2 NmL/min and 0.4 mBar partial pressure. As the Pstep is expected to be beyond 0.4 mBar for both 49 °C and 70 °C, a shockwave - dispersive wave - shock wave breakthrough profile was not observed. The breakthrough profile at 23 °C is hown only in the initial range to highlight the differences between the profiles at different temperatures.

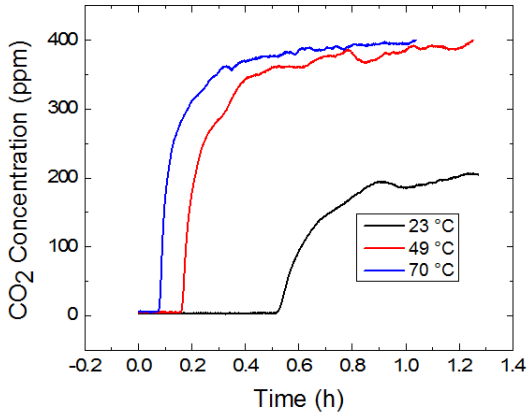

Figure E-3 - CO_2 Breakthrough profiles at 23 °C, 49 °C and 70 °C for the feed partial pressure of 0.4 mBar and a flowrate of 17.2 NmL/min.

E.7 Thermal effects on the breakthrough profile

To understand thermal effects, CO_2 adsorption in packed bed adsorption was simulated under both adiabatic and near isothermal conditions in Figures E4-E6 for two different CO_2 concentrations of 400 PPM and 5660 PPM. A small temperature (~0.6 °C) increase was predicted at 17.2 NmL/min feed with 400 PPM CO_2 concentration for the case of adiabatic bed. This resulted in a slightly higher concentration of the dispersive wave in the breakthrough than the isothermal case. At 100 NmL/min, the temperature rise was smaller than at 17.2 NmL/min for the case of an adiabatic bed and the breakthrough profile was almost identical with the near isothermal case. A higher increase in the bed temperature (~7 °C) was predicted in case of 17.2 NmL/min feed at 5660 PPM CO_2 concentration. This suggests that at higher concentrations, thermal effects are more prominent in this system.

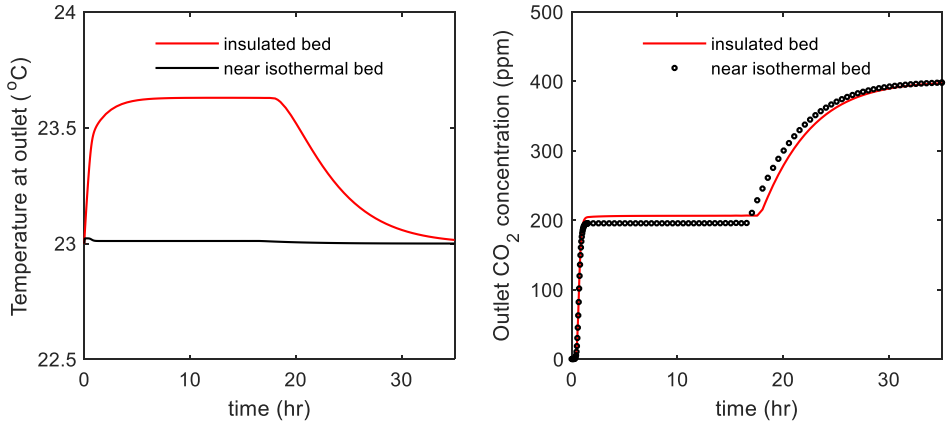

Figure E-4 - Simulated thermal profile in the bed (left) and exit CO_2 concentration as a function of time for feed with CO_2 concentration of 400 PPM at 17.2 NmL/min. Red curve indicates an adiabatic bed while the black curve indicates a near isothermal bed.

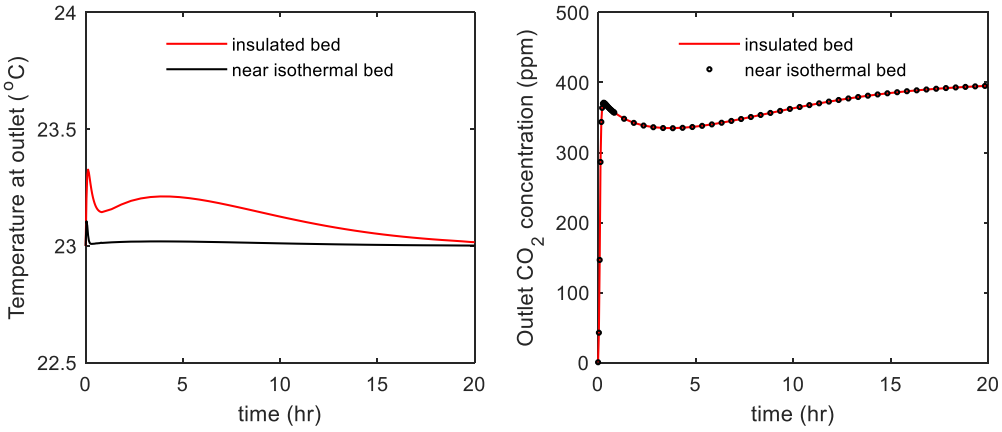

Figure E-5 - Simulated thermal profile in the bed (left) and exit CO_2 concentration as a function of time for the CO_2 feed concentration of 400 PPM at 100 NmL/min. Red curve indicates an adiabatic bed while the black curve indicates a near isothermal bed.

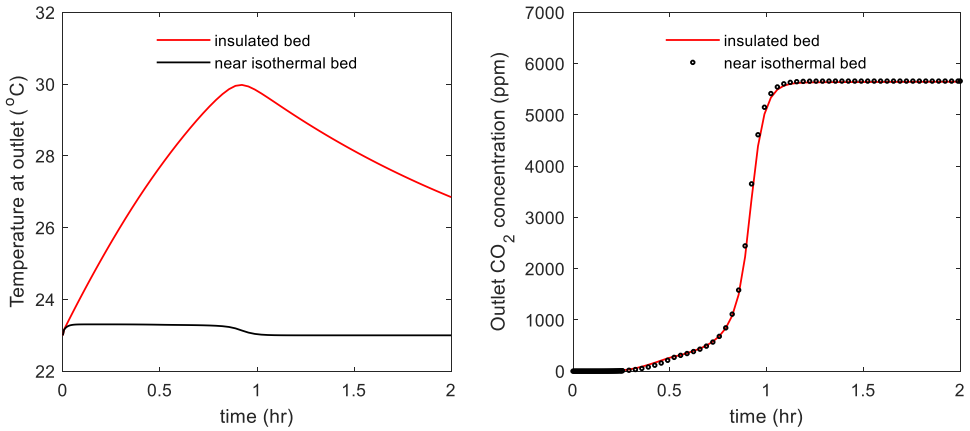

Figure E-6 - Thermal profile in the bed (left) and exit CO_2 concentration as a function of time for feed CO_2 concentration of 5660 PPM at 17.2 NmL/min. Red curve indicates an adiabatic bed while the black curve indicates a near isothermal bed.

E.8 Effect of dead volume on the breakthrough profile.

The deadtime of the system was measured using a helium tracer and was found to be less than 1 min for experimental conditions. Additionally, we simulated the effect of dead volume (1*bed volume vs 100*bed volume) on the spreading of the breakthrough for a CO_2 concentration of 5660 PPM at 17.2 NmL/min flowrate (Figure E-7). The dead volume can be analyzed as a packed bed system with boundary conditions connecting before and after the bed. The overall system can be simulated as a series of packed bed systems using equations E32-E34. As shown in the figure, it can be seen that a significant spreading of the breakthrough curve is not observed for smaller dead volumes in the system.

(Assumption: No pressure drop, isothermal dead volumes)

$$u_g = Q_{feed} \,/\, Area \tag{E49}$$

$$\frac{\partial y_{dead,i}}{\partial t} = D_{ax,i}\frac{\partial^2 y_{dead,i}}{\partial z^2} - u_g\frac{\partial y_{dead,i}}{\partial z} \tag{E50}$$

BC's for front end

$$y_{dead\_front,i}\Big|_0 = y_{feed,i} \tag{E51}$$

$$\left.\frac{\partial y_{dead\_front,i}}{\partial z}\right|_{L\_dead\_front} = 0 \tag{E52}$$

BC connecting front end to bed

$$y_{in,i} = y_{dead\_front,i}\Big|_{L\_dead\_front} \tag{E53}$$

BC's for back end

$$y_{dead\_back,i}\Big|_0 = y_i\Big|_L \tag{E54}$$

$$\left.\frac{\partial y_{dead\_back,i}}{\partial z}\right|_{L\_dead\_back} = 0 \tag{E55}$$

Final concentration at outlet of setup:

$$y_{out,i} = y_{dead\_back,i}\Big|_{L\_dead\_back} \tag{E56}$$

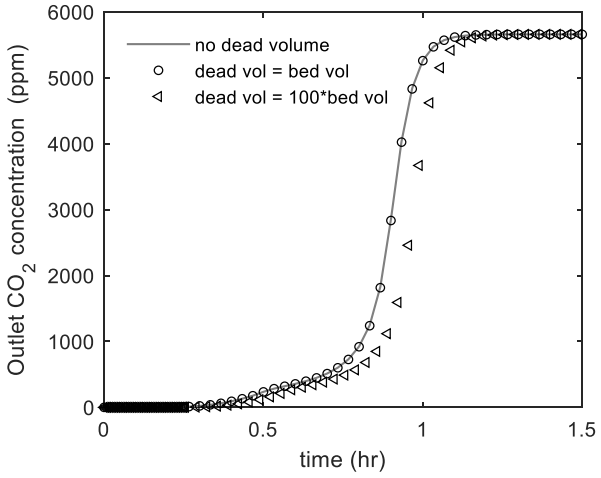

Figure E-7 - Breakthrough curves at different dead volumes. Solid line is without any dead volume, Hollow circles and triangles are for cases where the dead volume is equal to the bed volume and 100 times the bed volume, respectively. Our analysis suggests that a significant spreading of the breakthrough curve is not observed for smaller dead volumes in the system.

E.9 Notation

$\Delta H_{ads,i}$	heat of adsorption of component i (J/mol)	P_{tot}	total pressure (mbar)
a	area to volume ratio, pellet or fiber (1/m)	$P_{tot}\|_z^0$	pressure at position z at the beginning of respective step (mbar)

Bi_i	Biot no. at the gas pellet (or fiber) interface	q_1, q_2	adsorbed phase concentration (mol/kg)
C_{gi}	bulk gas phase concentration (mol/m^3)	q_{total}	equilibrium adsorbed phase concentration (mol/kg)
$C_{part,i}$	macropore gas phase concentration (mol/m^3)	R	ideal gas constant
$D_{ax,i}$	mass axial dispersion coefficient (m^2/s)	Re	Reynold's number.
$D_{p,i}$	macropore diffusivity inside pellet (m^2/s)	R_p	radius of pellet (m)
$K_{mbar \rightarrow Pa}$	conversion factor for pressure (mbar to Pa)	Sc_i	Schmidt no.
$K_{m,i}$	gas phase mass transfer coefficients (m/sec)	Sh_i	Sherwood no.
K_{mix}	thermal conductivity of gas mixture ($W/m^2.K$)	t	time (sec)
L	length of the bed (m)	T_g	gas temperature (K)
MW_{mix}	molar weight of mixture (kg/mole)		
N_i	flux of species i being removed from bulk gas phase (per unit volume of bulk gas)	u_g	superficial gas velocity (m/s)
P_{ads}	adsorption pressure (mbar)	y_{ads}	mole fraction in the inlet

p_i	partial pressure (mbar)	z	axial distance along column (m)
Pr	Prandtl no.		

E.9.1 Greek Letters

μ_g	viscosity of gas (Pa.s)	ρ_b	bulk density of the packed bed (kg/m^3)
ε	porosity of bed	ρ_g	density of gas (kg/m^3)
ε_p	porosity of pellet	ρ_p	total density of pellet (including pellet void volume) (kg/m^3)
		τ	tortuosity of pellet

E.10 References

[1] Hefti, M.; Joss, L.; Bjelobrk, Z.; Mazzotti, M. On the Potential of Phase-Change Adsorbents for CO_2 Capture by Temperature Swing Adsorption. *Faraday Discuss.* **2016**, *192* (0), 153–179.

[2] Wakao, N.; Funazkri, T. Effect of Fluid Dispersion Coefficients on Particle-to-Fluid Mass Transfer Coefficients in Packed Beds: Correlation of Sherwood Numbers. *Chem. Eng. Sci.* **1978**, 33, 1375 − 1384.